A THESIS

entitled

KINETICS AND EQUILIBRIA OF ION-MOLECULE ASSOCIATION REACTIONS STUDIED USING TEMPERATURE VARIABLE HIGH PRESSURE ION SOURCES

by

RICHARD THOMAS GALLAGHER, B.Sc.

Submitted to the University of Warwick in fulfilment of the requirements for the award of the degree of Doctor of Philosophy.

November 1987

To my mother and father

CONTENTS

Acknowledgement

Over the last three years I spent at the University of Warwick as a postgraduate student I made many friends and colleagues whom I wish to thank.

I would first like to thank Prof.Keith Jennings for all his help and encouragement, and for always making the answers to the many problems I encountered seem so obvious. Dr.Rod Mason for his endless patience and enthusiasm and for also teaching me the art of mass spectrometry. Dr.Anthony Wickham for making my stay at Berkeley Nuclear Laboratories so interesting and enjoyable. Thanks also to my good friend and fellow student Maria Teraza Fernandez, who helped share the frustrations and enjoyment of the many hours in lab. C101.

Acknowledgement to Ron, Harry, Ted and Norman from the workshops who assisted me many times during my research. Apologies to Alex Colborn for my constant interruption of his tea breaks, but thanks for the endless supply of '741 op. amps.'. I would also like to thank Phillip Pring and Michael Brown for sharing with me some of their greater knowledge, and to Josie Lloyd for the excellent typing of this thesis.

Finally may I thank Kate Heath for the invaluable aid of her dictionary and without who's constant support the writing of this thesis may never have been completed.

Financial assistance from the Science and Engineering Research Council and the Central Electricialy Generating Board is also acknowledged.

Declaration

Parts of the work described in this thesis have been presented at the following Mass Spectrometry Conferences:

10th International Mass Spectrometry Conference, University College of Swansea, UK, 1985.

'Low Energy Ion/Molecule Reactions', K.R.Jennings.

15th meeting of the British Mass Spectrometry Society, University of Sussex, UK, 1986.

Talk No.23, 'Kinetics and Equilibria of Ion-Molecule Association Reactions using Temperature Variable High Pressure Ion Sources'.

R.T.Gallagher, R.S.Mason, K.R.Jennings and A.J.Wickham.

35th ASMS Conference on Mass Spectrometry and Allied Topics, Denver, CO, USA, 1987.

'Kinetics and Equilibria of Ion Molecule Reactions'.

R.T.Gallagher, R.S.Mason, K.R.Jennings and A.J.Wickham.

Abstract

Interest in termolecular association reactions of the type shown below, stems from their importance in the chemistry of planetary atmospheres, gas-cooled nuclear reactors and gas-phase cluster ions. This study is concerned with evaluating the rate constants of such

$$X^{+\cdot} + X + M \text{ ------> } X_2^{+\cdot} + M \qquad k_3 \qquad (1)$$

reactions as both a function of temperature and of the third body M. The values of the third order rate constant k_3 are expressed conventionally in terms of $k_3 = CT^{-m}$ where T is the temperature and C and m are constants characteristic of the reaction which depend also on the nature of M. Literature now shows a general measure of agreement on values of C and m in several studies for which X = M, however, inconsistent values have been reported on the M = He system. This thesis describes an investigation of the two systems X = N_2, CO and M = the reactant or a rare gas.

Experiments were conducted in a conventional high pressure ion source and a pulsed drift ion source fitted to an updated Kratos MS9 mass spectrometer.

Results obtained for the one component studies show good agreement with other literature values for the temperature dependence, m. In general, for both N_2 and CO systems, He was found to have the same efficiency as the parent molecule as a third body at 300K, but the temperature dependence of k_3 is markedly lower. Ar was found to behave very similarly to the parent molecule in both systems. For the CO system, although good agreement is found for the temperature dependence result with literature, there is still an uncertainty of about a factor of 2 in the room temperature values of k_3.

List of Figures

List of Tables

List of Abbreviations and Symbols

α	polarisability of molecule
α_T	first order diffusion decay constant
β	collision efficiency
ΔH^o	enthalpy change of reaction
ΔS^o	entropy change of reaction
ΔT_{eff}	change in temperature of ions in gas due to drift electric field.
∇n	variation in ion concentration
θ	angle between dipole and centre of collision for colliding ion-molecule pair
λ_D	characteristic diffusion length for reaction vessel
μ	reduced mass
μ_D	dipole moment
μsec	microsecond (10^{-6} seconds)
ν	frequency of collision factor
ρ	density of vibrational energy states
σ	collision cross section
Ω	Ohms
Ω	collision integral
AADO	Average Angular Momentum-Dipole Orientation Theory
ADO	Average Dipole Orientation Theory
ADC	Analogue to Digital Converter
AGR	Advanced Gas Cooled Nuclear Reactor
AQO	Average Quadrupole Orientation Theory

$\underline{b}$	impact parameter
$\underline{b_c}$	critical impact parameters
B	magnetic field strength
CEGB	Central Electricity Generating Board
CI	Chemical Ionisation
CPD	Characteristic Pore Dimension
cm	centimeter
D	diffusion coefficient
D_i	free diffusion coefficient of species i
D_L	longitudinal diffusion coefficient
D_o	dissociation energy
D_T	transverse diffusion coefficient
DC	direct current
e	charge of electron
eV	electron-Volts
E	electric field strength (V/cm)
EI	electron impact ionisation
F(E)	energy distribution function
F(r,t)	fraction of ions passing through ion-exit aperture of radius r and at time t
g	gain of electron multiplier (detector)
GCMS	Gas Chromatography Mass Spectrometry
h	voltage height of detector signal response
h	Planck's constant
HPPS	High Pressure Pulsed electron beam ion source
$i(r_c,t,z)$	ion current passing through plane z at time t and collected through an aperture r_c

i(t,z)	ion current passing through plane z at time t
I	electric current
ICR	Ion Cyclotron Resonance mass spectrometry
J	angular momentum
J	ionic flux density
k	rate constant
k_a	rate constant for formation of an excited association complex
k_b	rate constant for dissociation of an excited association complex
k_c	rate constant for collision process (microscopic rate constant)
k_f	rate constant for overall formation process
k_L	Langevin rate constant (macroscopic rate constant)
k_{LD}	locked dipole rate constant
k_S	rate constant for stabilisation of excited association complex
kJ	kilo-Joules
kVolt	kilo-Volts
K	Kelvin
K	mobility
K_{eq}	equilibrium constant
K_i	mobility of species i
K_o	reduced mobility
L	classical angular momentum
m	mass of ionic species or netural species
m	temperature dependence
m_b	mass of buffer gas
m_r	mass or reactant ion
mol	mole

M	bath gas
MCA	Multi Channel analyser
MS/MS	Mass Spectrometry-Mass Spectrometry
n_i	concentration of species i
n_T	total number density
N	gas number density
N	number of atoms in complex
psi	pounds per square inch
P	pressure
P^+	primary ion
PG	pulse generator
PST	Phase Space Theory
ppm	parts per million
q	charge on ion (2.7)
q*	pseudo partition function
Q	total charge from ion detector
r	radius of magnet (2.3)
r	interacting ion-molecule separation (2.6)
r	number of degrees of rotational freedom
R	gas constant
R	electrical resistance
RF	radio frequency
RRK	Rice, Ramsberger and Kassel Theory
RRKM	Rice, Ramsberger, Kassel and Marcus Theory
s	second
s	effective number of oscillators in complex
sec	second

S	slope of late afterglow region from ln ion intensity vs reaction time profile
S^+	secondary ionic species
SIFT	Selected Ion Flow Tube
SIMON	Simulation of Ion Trajectories program
t	time (seconds)
t_d	average drift or residence time of ions in drift source
t_{NR}	measured residence time of non-reactive species
t_R	measured ion residence time of reactive species
T	temperature (Kelvin)
Td	Townsends
TST	Transition State Theory
v	velocity of ionic species
v_d	drift velocity of ion
vpm	volumes per million
V	accelerating voltage
V_{es}	electrostatic potential energy
w	width (seconds) of ion detector signal response
z	drift distance
z	ionic charge
k_1	Rate constant for association reaction 5.1
k_{-1}	Rate constant for dissociation reaction 5.4(iii)
k_2	Rate constant for association reaction 5.2
k_{-2}	Rate constant for dissociation reaction 5.12(ii)
K_3	Equilibrium constant for reaction 5.3
k_4	Rate constant for association reaction 5.4(i)

k_5 Rate constant for association reaction 5.12(iii)

k_6 Rate constant for charge exchange reaction 5.13

k_7 Rate constant for association reaction 6.5

k_{-7} Rate constant for dissociation reaction 6.6

k_8 Rate constant for association reaction 6.12

k_{-8} Rate constant for dissociation reaction 6.12

k_9 Rate constant for association reaction 6.13

k_{-9} Rate constant for dissociation reaction 6.13

k_{10} Rate constant for association reaction 6.14

k_{11} Rate constant for dissociation reaction 6.16

$k(N_2)$ Rate constant for nitrogen association (reaction 5.1)

k(CO) Rate constant for carbon monoxide association (reaction 5.2)

k_3 General third order rate constant

k_f Rate constant for any association reaction (reaction 6.2)

k_f Rate constant for any dissociation reaction (reaction 6.3)

Chapter One

Introduction

Over the last twenty years the use of a variety of experimental techniques has provided an abundance of data on the reactivity of gaseous ions. Most ionic species have been found to be extremely reactive in the gas phase, often reacting with unit efficiency during collisions with molecules.

A problem which can arise and influence results obtained by various experimental methods is the possibility of internally exciting the reactant ions under investigation. This excitation can markedly effect the reactivity of charged species. In high pressure experiments, (> 1 Torr), and to a lesser extent in afterglow studies, the ionic species undergo many collisions with the surrounding gas molecules before any reactive interactions occur. It is possible for ions, even after multiple collisions, not to be fully thermalised as many ionic species possess metastable vibrational and electronic internal energy states. However, those ions which experience multiple bath gas collisions are more likely to be truly thermalised: possess a Maxwellian velocity distribution with their internal states populated according to Boltzmann statistics[1], than ions in 'collisionless' or low gas density experiments.

Rate coefficients and product distributions of ion-molecule reactions are also extremely temperature sensitive. Consequently, collision-dominated experimental techniques are used for the study of ion-molecule reactions in gaseous environments. These studies normally fall into two groups: high and low temperature conditions. Low temperature investigations are used to aid the understanding of processes occurring in the Earth's ionosphere and other planetary atmospheres[2,3,4] and also interstellar gas clouds[5,6]. Higher temperature studies have been used to model laser plasma[7] and industrial problems such as graphite corrosion in advanced gas cooled nuclear reactors (AGR)[8,9].

In the latter case, which is the basis for this thesis, the corrosion of the graphite moderator by oxidising species which occurs in the reactor core is of major concern to industries involved in this area, such as the Central Electricity Generating Board (CEGB).

The process of corrosion weakens the graphite structurally by pore enlargement and decreases its efficiency as a neutron moderator in the fusion process. It is the structural condition of this moderator which is one of the major factors in determining the operational lifetime of an AGR.

The coolant gas used in the reactor core is high pressure carbon dioxide gas chosen for its stability to ionising radiation. The typical composition of the coolant gas comprises of 415vpm CH_4, 300vpm H_2O and 300vpm H_2, where these additivies are corrosion inhibitors and/or impurities in the carbon dioxide. For example, 1% CH_4 in the CO_2 will reduce corrosion by up to 50%, but further additions have no change on this original reduction. The overall oxidising process can be simply stated as:

$$C + CO_2 \longrightarrow 2CO \qquad (1.1)$$

Positive ions, negative ions and radicals are formed under the high ionising radiation flux found in the reactor core. A clear understanding of radiolytic graphite oxidation is therefore central to the understanding of the corrosion processes occurring. The basic positive ion chemistry of CO_2 and CO_2/CO mixtures is well documented [10-14] and is not discussed here. These studies help to determine which ion molecule processes dominate the chemistry inside the reactor and thus which ionic species can be expected to be present, and hence take part in graphite corrosion and/or inhibition of oxidising species. The results of Headley[15] show that under the conditions experienced in a reactor core $CO_2^{+\cdot}$ and $(CO_2)_2^{+\cdot}$ ions will exist but not the trimer or any higher cluster species. As yet however, the proportions of the carbon monoxide clusters expected to be formed have not been evaluated since all attempts to obtain the equilibrium conditions for these processes have been unsuccessful.

This thesis is devoted to studying the temperature dependence of several ion molecule reactions. High pressure mass spectrometric techniques were engaged for this investigation. Two different high pressure ion sources were constructed as chambers in order to conduct

these experiments. This work enabled both a comparison of the performance of each ion source and comment on their ability to produce reliable data.

The initial systems studied in this thesis by both high pressure ion sources were the one component carbon monoxide and nitrogen association reactions:

$$CO^{+\cdot} + 2CO \longrightarrow (CO)_2^{+\cdot} + CO \qquad (1.2)$$

$$N_2^{+\cdot} + 2N_2 \longrightarrow (N_2)_2^{+\cdot} + N_2 \qquad (1.3)$$

Although studied by many groups, there are still many discrepancies found in the reported literature values of the negative temperature dependence of the forward association reactions. This study is conducted to help rationalise this present situation.

The carbon dioxide equilibrium system (1.4) was also investigated in both high pressure ion sources to aid in the evaluation of source performance.

$$CO_2^{+\cdot} + 2CO_2 \rightleftharpoons (CO_2)_2^{+\cdot} + CO_2 \qquad (1.4)$$

The second section of this thesis is devoted to investigating the effect of using different third body or bath bases in the following systems:

$$CO^{+\cdot} + CO + He \longrightarrow (CO)_2^{+\cdot} + He \qquad (1.5)$$

$$CO^{+\cdot} + CO + Ne \longrightarrow (CO)_2^{+\cdot} + Ne \qquad (1.6)$$

$$CO^{+\cdot} + CO + Ar \longrightarrow (CO)_2^{+\cdot} + Ar \qquad (1.7)$$

$$N_2^{+\cdot} + N_2 + He \longrightarrow (N_2)_2^{+\cdot} + He \qquad (1.8)$$

$$N_2^{+\cdot} + N_2 + Ar \longrightarrow (N_2)_2^{+\cdot} + Ar \qquad (1.9)$$

The reaction mechanism for these termolecular association reactions involves the initial formation of an excited intermediate complex, denoted as $(AB^{+})^{*}$ below. This complex may

then either dissociate back to the original reactants or be collisionally stabilised by a third body M.

$$A^{+\cdot} + B \rightleftharpoons (AB^{+\cdot})^{*} \qquad (1.10)$$

$$(AB^{+\cdot})^{*} + M \longrightarrow AB^{+\cdot} + M \qquad (1.11)$$

The temperature dependence of the overall third order rate coefficients were measured for the systems 1.5-1.9. These results were compared to the one component studies to evaluate the collision efficiency of the inert gases helium, neon and argon with respect to the parent gas.

Gas mixtures with particular interest to the chemistry occurring in advanced gas cooled reactors were also investigated. These systems were mixtures of the two gases CO and CO_2, with CO present at 0.3, 0.9 and 1.5% by volume. It was the intention that the enthalpy change for the equilibrium shown below could be measured by this study.

$$CO^{+\cdot} + CO + CO_2 \overset{k_{eq}}{\rightleftharpoons} (CO)_2^{+\cdot} + CO_2 \qquad (1.12)$$

However, even using the large operating pressure and temperature range of both ion sources this could not be achieved. It was also found that with residual water present in the gases, even after drying to less than 3ppm H_2O, that the dominate ion produced in this system was the $HCO^{+\cdot}$ species. This is believed to be formed by the proton transfer reaction shown below which dominates all other processes in this system. The dimer carbon monoxide ion,

$$H_3O^{+\cdot} + CO \longrightarrow HCO^{+\cdot} + H_2O \qquad (1.13)$$

$(CO)_2^{+\cdot}$ was observed but unfortunately the ion abundance was too low to be measured accurately.

As part of the CASE award requirements for this work three months were spent working for the CEGB at the Berkeley Nuclear Laboratories, Berkeley, Gloucestershire. The aim of this study was to evaluate a new image analysis technique for the determination of graphite pore-structure. Such information on the size and shape of the pore structure is essential in the study of radiolytic graphite oxidation as the oxidation rate has been found to depend upon competitive gas-phase and surface reactions within the pores.

Previous methods used in determining the "characteristic pore dimension" (CPD) have used liquid metal impregnation techniques for which gold, bismuth and mercury have been used by varying amounts of success.[9] The image analysis technique was carried out on various graphite moderator samples after impregnation into the pores of the graphite with a fluorescent pigment which fluoresces under ultra-violet light. The impregnation technique is outlined in Appendix A. The impregnated samples were then studied under a microscope at various magnifications. Appendix B shows some example photographs of the typically observed graphite pore structure. As shown in B1, virgin graphite has only a few large pores with little fine structure around circular dark areas with no accessible pores. The dark areas are grist particles and the surrounding area is binder. After irradiation to 2.3% weight loss a few of the grist pores are now open. By 21% weight loss there is extensive opening of the grist particles which now consist of an 'onion-skin' type structure of pores of about 7μm CPD, see B2. The second two photographs B3 and B4 show how the graphite pore structure may vary between different graphite production techniques.

Eight different graphite samples were studied in total using the imaging technique described in detail in Ref.9. The results obtained for a typical graphite moderator sample, code MP4, is shown in Appendix C. This plot of the cumulative pore area versus the pore dimension shows how different magnification lenses, X6 and X63, discriminate between small and large pores in a graphite sample. This occurs as low magnification lenses are unable to resolve small pores and higher magnification lenses have a much smaller analysis frame and thus 'cut up' large pores. However, the total envelope of results obtained using

different magnification lenses yields a very good representation of the pore structure of the graphite moderator. For comparison a mercury impregnation result is also shown. This latter technique calculates the total open pore volume very accurately although as shown, is poor in representing the true distribution of pore sizes. It is known that under the high pressure required for the mercury impregnation technique (1000 Kg cm^{-2}) that damage occurs to the graphite pore structure.[9] In fact the mercury actually cracks open any small necks present in the structure and then fills up the large internal areas.

The pore structure distributions obtained from these studies have been used in predicting weight-loss to graphite moderator samples by graphite oxidation with some success.[9] In summary the technique of fluorescence impregnation with image analysis shows much promise in successfully predicting corrosion rates for graphite moderators of widely differing pore structure. These results can also be used to confirm mean ranges and rate constants for reactions of oxidation species found in reactor gas mixtures. It is hoped that future developments of this technique will allow pore structure enlargement, which occurs in graphite during radiolytic oxidation processes, to be modelled.

Chapter Two

Recent Advances in Gas-Phase Ion-Molecule Chemistry

2.1 Introduction

From the earliest days of mass spectrometry evidence was found for the occurrence of secondary processes which were generally agreed to result from collisions between ions and neutral species. In 1916 Dempster[16] observed an ion at a mass to charge ratio of three, which was correctly identified as H_3^+. By 1925, the reaction leading to its formation was well established[17,18] as:

$$H_2^+ + H_2 \longrightarrow H_3^+ + H\cdot \qquad (2.1)$$

The mass spectrometer ion source serves as a very convenient reactor for the study of ion-molecule reactions because the mass spectrometer provides a means to quantitatively determine both the reactant and product ions. The measurement of appearance energies provides, in many instances, a convenient and ready method of relating a precursor to its product. As the field strength in an ion source is known, the residence time of the detected ions formed in the source may be measured and the rates of the various ion-molecule reactions may be determined.

The aim of this chapter is to outline recent developments in the theory of bimolecular and termolecular association processes, but first, developments of experimental techniques used in the investigation of ion-molecule reactions will be reviewed.

2.2 Advances in Experimental Techniques

The applications of mass spectrometry in analytical, organic and physical chemistry have grown steadily since the initial use of a single focusing magnetic sector instrument by the oil industry in the early 1940's. The advantage of high mass resolution and accurate mass

measurement were realised by the 1950's and double sector instruments, which combined an electric sector with a magnetic sector, were introduced for this work. The last twenty years has seen a continuous improvement in the performance and versatility of such instruments.

The technical advances of the past ten years have led to a vast increase in the use of mass spectrometers for the investigation and categorisation of ion-molecule reactions. It is now possible to study ion-molecule reactions at higher pressures and over a wider temperature range than before. This has meant that many slow reactions hitherto undetectable in a standard low-pressure source, can be investigated. Such studies have led to the realisation that many ion-molecule reactions display third-order kinetics. The main techniques used in these studies at low pressure (< 1 Torr) involve drift tubes, flowing afterglow methods, selected ion-flow mass spectrometry and ion cyclotron resonance techniques (see following sections).

2.2(i) Basic Mass Spectrometry

Mass spectrometry is mainly used as an analytical tool for the determination of compound structures. Ions of the neutral species are formed from the sample molecules by various methods, of which only the two most common are considered here. Ion sources that use the electron impact (E.I.) method of ionisation operate at source pressures of 10-5 to 10-6 Torr. Ions are formed by the inelastic collisions of electrons, emitted from a hot metal filament, with molecules in the gas phase. The electrons normally have initial energies of around 70eV on entering the ion chamber and due to the low sample pressures used, single collision conditions are obtained. As the energy transferred from the electrons usually exceeds the ionisation energy of the sample molecules, bond cleavages and rearrangements may also occur, resulting in the formation of many fragment ions.

A study by Meisels[19] in 1982 has considered fragment patterns produced in mass spectrometry using a standard 70eV electron impact ion source and compared them to the

patterns obtained by radiation chemistry studies. The correlation of the results obtained by the two methods has led to a better understanding of radiation chemistry processes.

The study of ion-molecule reactions was initially promoted because of their importance to radiation chemistry was recognized. It has been suggested that the results obtained from radiolysis experiments on hydrogen in the presence of minor additives, led to the currently important analytical method of chemical ionisation[20,21]. Thus ion-molecule reactions with relevance to radiation chemistry can be studied at pressures of the order of 10^{-1} Torr with a collision frequency of 10^6 sec^{-1}; i.e. in a conventional mass spectrometer, although a knowledge of kinetics and thermodynamics is required when extrapolating results to higher pressures.

Chemical Ionisation (CI) is the name given to the process in which sample molecules are ionised by reaction with bath gas ions, already formed in an ion source by a 'normal' EI process. An example is methane chemical ionisation:

	Chemical Ionisation	Electron Impact Ionisation
(1)	$CH_4 + e^- \longrightarrow CH_4^{+\cdot} + 2e^-$	$M + e^- \longrightarrow M^{+\cdot} + 2e^-$
(ii)	$CH_4^{+\cdot} + CH_4 \longrightarrow CH_5^{+\cdot} + CH_3^{\cdot}$	
(iii)	$CH_5^{+\cdot} + M \longrightarrow MH^{+\cdot} + CH_4$	

The energy transferred in step (iii) to the sample molecule M is normally less than that transferred to in step (i) of EI ionisation. Hence, CI is often referred to as a 'soft' ionisation technique as the fragmentation produced may be quite limited compared to EI mass spectrometry.

After the ions have been produced they are made to drift out of the ion sources where they are rapidly accelerated by a potential difference in the order of 4 to 8 kVolts between the source block and the tube unit, the latter being held at earth potential. The ions are accelerated to a velocity of ~ 10^5 $msec^{-1}$ requiring only a few microseconds to transverse the analyser tube and reach the detector. The detector is normally an electron multiplier which has the properties of a very rapid response to ion impact and normally amplifies the initial signal by a

factor of 106. The mass spectrum is recorded as a function of ion beam intensity versus magnetic field strength, from which mass may be determined. This data is either output directly as raw data to an ultra-violet recorder or as a mass spectrum via a computer data system.

Mass separation is conventionally achieved using a magnetic sector between the source and ion detection system. The magnetic sector separates a beam of ions according to the momentum-to-charge ratios of the ions contained within it. The kinetic energy of an accelerated ion of charge z and mass m entering the magnetic sector can be related to its initial potential energy (zV) in the source by the expression:

$$zV = 1/2\ mv2 \qquad (2.2)$$

where v is the ion velocity. In a magnetic field of strength B, an ion will experience a centripetal force Bzv which is balanced by a centrifugal force of mv2/r, where r is the radius of the circular path followed by the ion as it traverses the magnetic field.

$$Bzv = mv2/r \qquad (2.3)$$

Eliminating the velocity term from expressions 2.2 and 2.3 gives:

$$m/z = B2r2/2V \qquad (2.4)$$

The ion beam may also be passed through an electric sector before detection. Here the ions pass through two large concentric cylindrical metal plates, of uniform separation with an electric field across them. This separates a beam of ions according to their energy to charge ratios. If all ions formed in the source receive the same translational energy upon acceleration then the electrostatic sector produces no mass separation. If it is used in combination with

another unit such as a magnetic sector, then the detected ions can be both mass and energy selected, resulting in higher mass resolution and sensitivity at the detector.

Instruments in which the electrostatic analyser precedes the magnetic sector, where both sectors deflect the beam by 60° or 90°, are known to have Nier-Johnson geometry[22] (Figure 2.1).

2.2(ii) Quadrupole Mass Analyser

Quadrupole mass spectrometers[23] were first developed in the late 1950's. They have the advantage of a particularly fast speed of scanning, up to 1000 daltons sec^{-1} and were the first mass analysers to be computer controlled. The analyser for this instrument is made up of four cylindrical rods fixed at the angles of a square and electrically insulated from each other. They are connected alternately to form two couples to which are applied D.C. and R.F. potentials with charges of opposite sign. The accelerated ions enter the analyser and begin to oscillate in a complex manner according to the m/z and RF/DC ratios. For every value of these ratios only one mass is able to pass completely through the filter and impinge on the collector. Thus, this is the only one of the three units so far described that separates an ion beam according to the mass-to-charge ratio of the ions contained in it.

The sensitivity of the quadrupole, unlike that of conventional sector instruments, is mass dependent. Although the sensitivity is high at low masses, it falls rapidly above a value of 500 daltons. In addition, the upper limit of the currently available quadruples is only 1200 to 1500 daltons. This disadvantage to 'normal' sector instruments has not halted the commercial success of these analysers, as the advantages of compactness, relative inexpensive and fast scanning capabilities have led to their use in many GCMS applications.

2.2(iii) Ion-Molecule Equilibria

There are three thermodynamic conditions which must be satisfied before gas phase ion equilibria can be measured by mass spectrometry techniques. Firstly, the reactants and

Fig. 2.1 BASIC LAYOUT OF MASS SPECTROMETER (NIER-JOHNSON OPTICS).

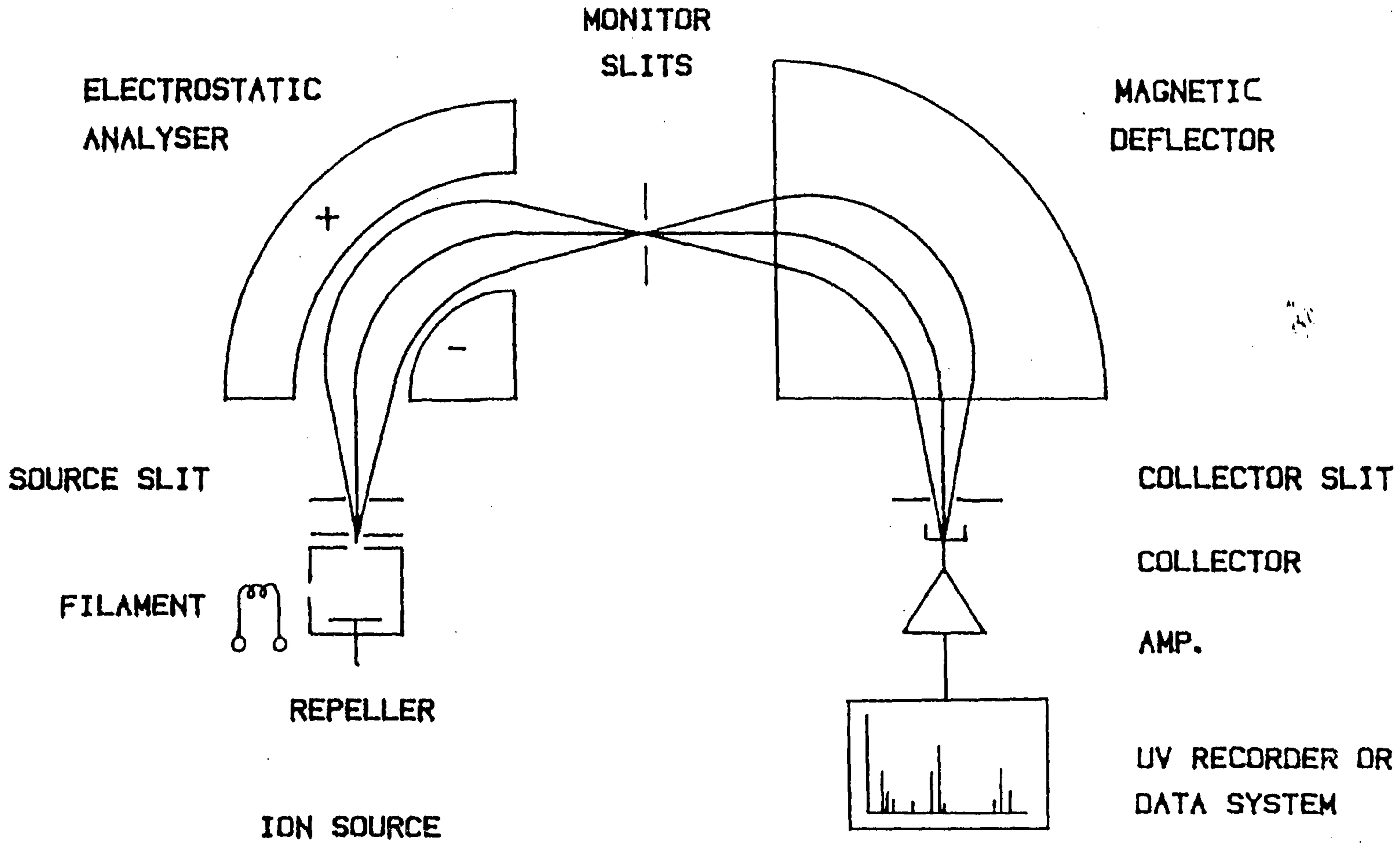

products must be in thermal equilbrium with their surroundings. Secondly, the reaction pathways which lead to equilibrium must be appreciably faster than all other processes occurring in the source which may effect the concentration of the ions. Finally, the system must be given sufficient time to allow equilibrium to be established. These conditions will be examined in more detail in chapters three and five.

Different types of apparatus have been successfully applied to the measurement of ion equilibria and reaction rates. The three most successful areas are the pulsed electron-beam high pressure ion source[24], flow tubes[25], and ion cyclotron resonance mass spectrometry[26,27]. These experimental methods will now be considered.

2.2(iv) <u>High Pressure Mass Spectrometry</u>

A pulsed electron-beam high pressure ion source consists of a reaction chamber which may operate in a pressure range of 0.1 to 10 Torr. This ensures that the ions formed by a short pulse, (5 to 50 μsec duration) of high energy electrons (200 to 500eV) are truly thermalised before detection, by allowing many collisions to occur with the bath gas. Collection of a mass selected ion with a multichannel scaler gives a peak profile of the selected ion intensity against reaction time. The shape of such peaks yields information on the energetics and diffusion properties of ions and are of fundamental importance to the physical chemist. Ratios of ion concentrations can be measured as a function of time and progress towards equilbrium monitored. Advantages of this method are the temperature control of the ion source, 20 to 700K, and the assured thermal ion distribution[25,28,29]. Disadvantages are the possibility of mass discrimination at the sampling slits; acceleration can lead to collisionally-induced decompositions of the ions and, as the ions and neutrals are in one source, undesired 'side' reactions may also occur.

2.2(v) Flow Tubes[25,30]

a) The Flowing Afterglow This technique was first introduced in 1966 and is used for determining ion mobilities and thermal rate constants for many gas phase reactions[31]. The essence of the technique is that ionisation is created upstream in a fast flowing carrier gas and an afterglow plasma is distributed along a flow tube remote from the source of ionisation. The ions are sampled downstream in the flow by a standard electron multiplier. Advantages of the system are that the neutral reactant gas is never exposed to the extreme conditions of the ionisation source but only to the thermalised afterglow plasma. Significant internal excitation is minimised and, by sequential addition of gases at different positions along the length of the afterglow column, a wide variety of ion types can be generated. In rate coefficient measurements it is necessary to operate with small charge densities in the reactor zone to minimise loss of ions due to recombination of positive ions with electrons. Typical values of ion densities used are of the order of 10^7 sec^{-1}. In some negative-ion studies, however, some anomalous rate coefficients have been obtained due to variations in the diffusive loss rate of the ions from transitions between electron-ion and ion-ion plasmas.

b) The Flow-Drift Tube There are many restrictions on the temperature range over which the flowing afterglow technique can be used and hence, restrictions over the mean energy range 0.01 to 0.1eV, which the ions may be given. The drift-tube technique[25] bridges the energy gap between the flowing afterglow and beam experiments and has the potential of allowing ion-neutral collisions to be studied.

The principle of the technique is that the average energy of a swarm of ions in a non-reactive buffer gas is increased by the application of a uniform electric field. With the addition of relatively small amounts of a reactive gas, ion-neutral reaction rates, as a function of energy, can be determined. The chemical versatility of the flowing-afterglow has been united with the energy range of the drift-tube to form the flow-drift tube; Figure 2.2(ii). The upstream section is the ion production region and is simply a flowing afterglow ion source of thermalised ions. Downstream of the ion production region, the flow walls are segmented

Fig. 2.2 DIFFERENT FLOW TUBE APPARTUS[25]

(i) Flowing Afterglow

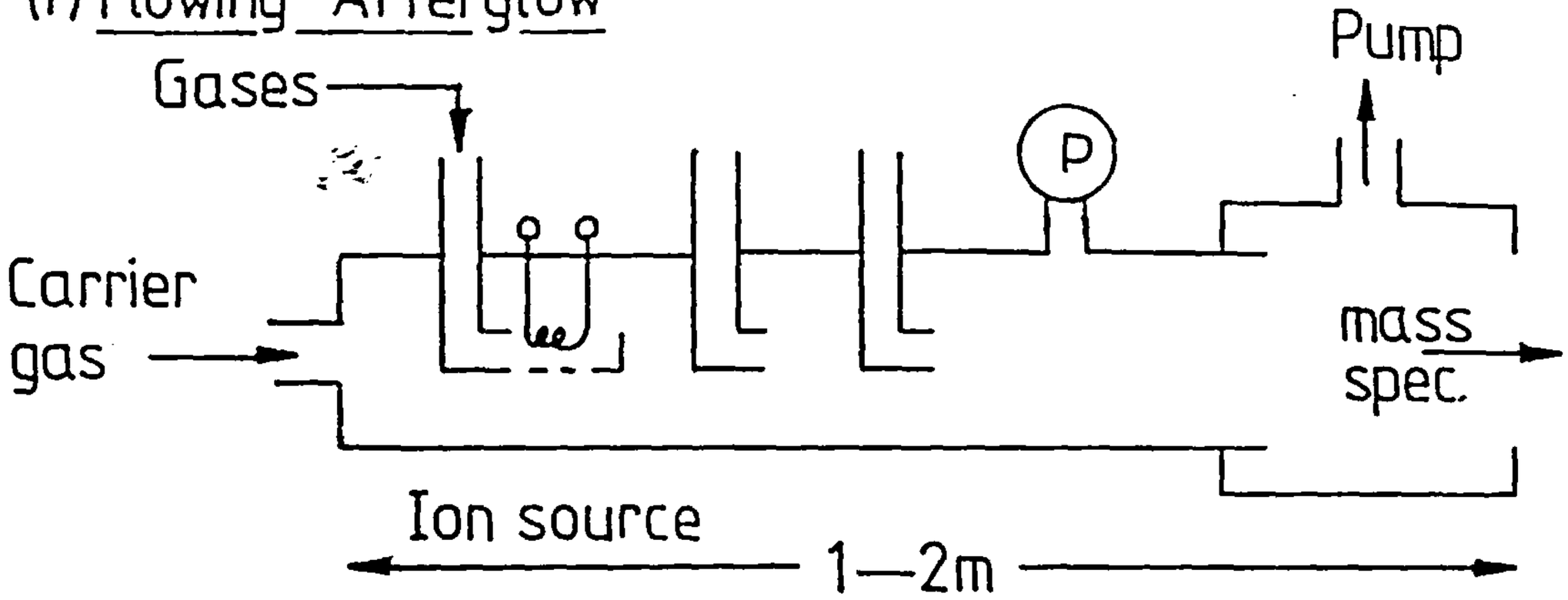

(ii) Flow-Drift Tube

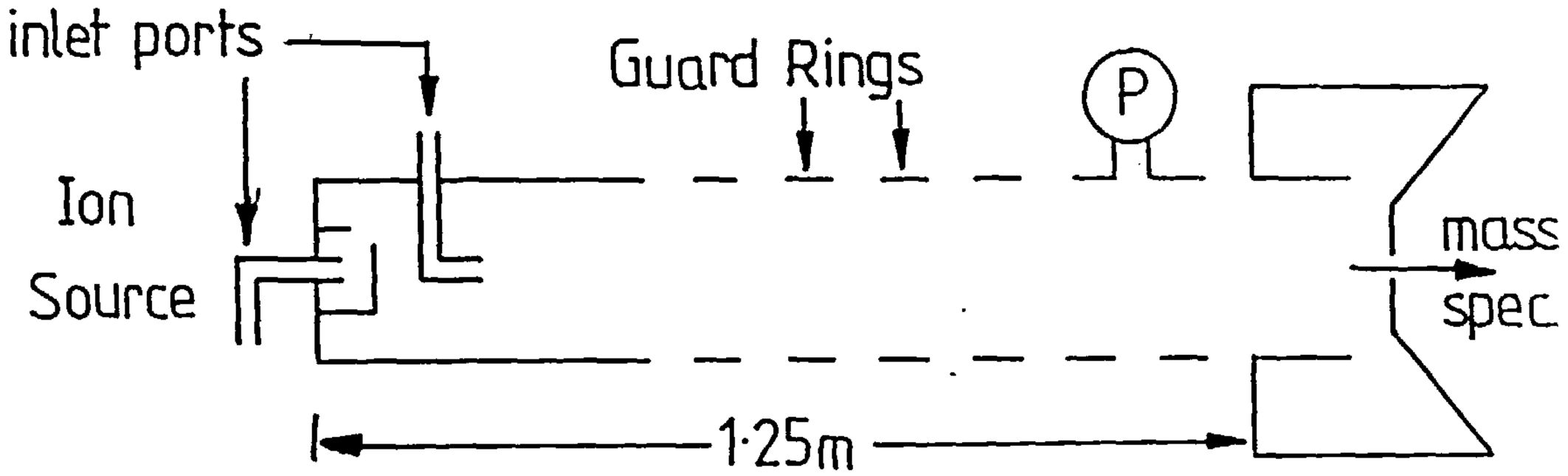

(iii) SIFT Apparatus

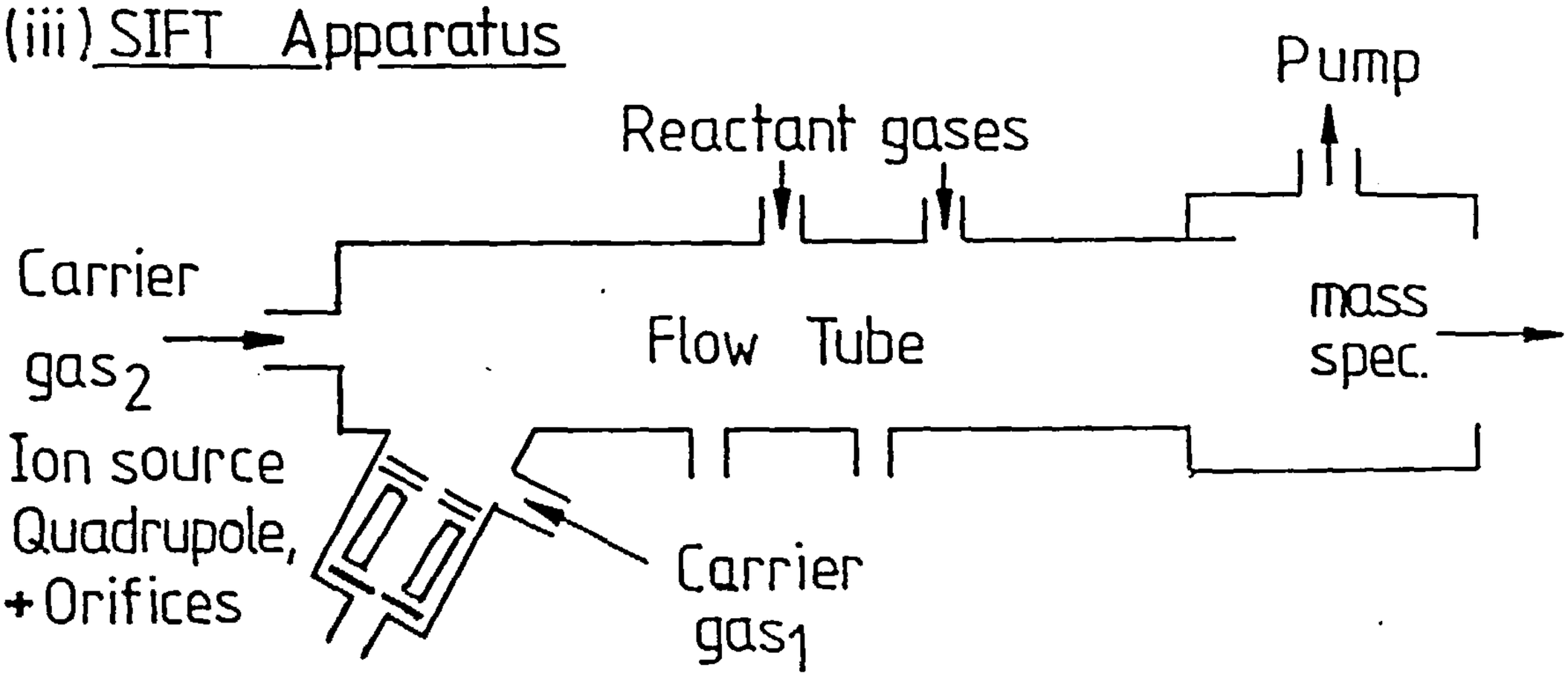

into nearly 100 guard-rings, each insulated from its neighbour and coupled together with the appropriate resistors to form the required electric field. Separation of positive and negative ions in the plasma occurs in the ion production section as a consequence of the axial electric field. Rate coefficients can be readily determined as a function of E/N, where E is the electric field strength, and N is the number density of ions. Flow-drift techniques give excellent agreement with results from cross beam measurements for rate coefficients.

The most recent developments of this technique can be seen in the work of Rayment and Moruzzi (1978) on negative ion studies[32]. The main different in their apparatus is that the drift electric field is directed along a diameter of the flow tube that is normal to the gas flow direction. Any excited neutral species generated by electron collisions are swept out of the drift region and therefore cannot interfere with the negative ion-molecule reaction under study.

c) Selected Ion Flow Tube (SIFT) The main disadvantages of the two previous experimental techniques are that the source gas and primary ions under study can undergo competing reactions which can compete with the reaction being investigated. In thermoneutral reactions, the reverse reaction may also occur resulting in a slower decay of the primary ion signal. The presence of primary ions other than those of interest and possible metastable excited species can lead to erroneously low rate constants if the ion under study is a product of a simultaneous reaction of another primary ion. These complications can be effectively avoided by producing the ions of interest in a remote ion source and injecting a single mass selected ion species into a flowing carrier gas. This is the principle of SIFT[25,33], in which the chosen ion is selected in a quadrupole mass filter, Figure 2.2(iii). There are no electrons present in the SIFT to neutralise the diffusive wall current of the positive ions. Sampling is easier for both positive and negative ions since no plasma sheath, a cause of negative ion sampling problems in stationary afterglow and also to a lesser extent in flowing afterglow, is formed.

We can summarise this section by underlining the fact that flow-drift tubes now allows the variation of the amount of translational energy transferred to ions before reaction. The SIFT method has extended the flow-tube technique to study a wider range of ions in a cleaner reactive medium compared to high pressure pulsed source methods.

2.2(vi) Ion Cyclotron Resonance Mass Spectrometry (ICR)

ICR[32,26], is a mass spectrometric technique which operates at source pressures of 10^{-6} to 10^{-7} Torr, much lower than found in conventional mass spectrometry. Generated ions, formed by electron impact in a magnetic sector, are irradiated with cyclotron radiation. The ions move in a cycloidal motion within the source due to the joint effect of these fields. Detection is accomplished by altering the incident radiation so the ions impinge on a detector.

In a conventional drift cell ICR the ion residence time is ~ 10^{-3} secs while ions in trapped cells can be stored for periods up to the order of seconds. Early studies with ICR had several severe limitations. Mass resolution was limited to about 1amu at a $^{m}/_{z}$ of 200 daltons, and an upper mass range of 280 daltons. In addition the scan rate was very slow. Recent developments employing Fourier Transform Techniques[27] and a one region ICR cell have largely removed these limitations and provide a wide mass range and ultra-high mass resolution.

Ion-molecule reactions involving positive and negative ions may be studied by Fourier Transform ICR[34] , although some concern has been expressed as to whether the ions are in true thermal equilibrium with their surroundings at these low pressures. Also as the source is positioned in the middle of the magnet, temperature variable reactions cannot be performed.

2.2(vii) Tandem Mass Spectrometry

Tandem mass spectrometry or MS/MS has grown in importance in recent years particularly in the areas of biochemistry where structural investigation of large organic molecules is required[35,38]. Tandem mass spectrometry makes it possible to first select the

ion of interest in the first mass spectrometer and to deduce its structure by analysing the collision-induced fragments of the parent ion in the second[36]. The major advantage of this technique is the efficient suppression of the 'chemical noise' present in the primary spectrum. Besides these analytical aspects, the excitation and fragmentation dynamics of polyatomic ions can be studied by this technique[37].

Several developments in instrumental MS/MS have evolved in recent years, where the main interest was directed towards accurate mass measurement for the fragment ions. Triple quadrupole instruments have been built, combining a high transmission with greater flexibility and ease of operation[39]. These types of instruments, however, have a limited mass range, resolution and usually only operate at low collision energies (< 100eV).

Various sector instrument combinations have been developed, utilising high mass range, resolution and collision energies (10 KeV). Hybrid instruments of EBQQ[40] and BEQQ-geometry[41,42] have been designed and operated successfully. For these types of instruments high energy collision studies are possible, although the mass range of the second stage is limited to about 2000 daltons.

2.3 Advances in Ion-Molecule Collision Rate Theory

This review will be concerned primarily with thermal 'clustering' reactions of the general type:

$$A^{+\cdot} + B + M \rightleftharpoons AB^{+\cdot} + M \qquad (2.5)$$

where $A^{+\cdot}$ denotes a positively charged ion, and B and M are both neutral species. As indicated most clustering or association reactions are reversible, though not necessarily appreciably so for all experimental conditions. The bonding between the ion and 'solvent' molecule is relatively weak compared to a 'normal' chemical bond, typically in the order of 200 kJ mol^{-1} or less. This type of bonding is derived primarily from electrostatic forces such

as ion-dipole interaction and it is this type of electrostatic forces that make collisions between ion-molecule pairs so different compared to those for neutral species. The pure polarisation theory was first developed by Langevin in 1905 for bimolecular processes[43]. This theory has since been developed by many groups[44,45], the latest being by Su and Bowers in 1979 for ion-molecule pairs[46].

2.4 Bimolecular Ion-Molecule Collision Theory

The electrostatic potential energy, V_{es} between a pair of interacting molecules considered as point charges will vary with separation r, according to the general law:

$$V_{es} = - a/r^n \qquad (2.6)$$

where a is a constant depending on the charges on one or both of the molecules, dipole moments and polarisabilities of the species. This is positive for all cases except similarly charged ions. The superscript 'n' denotes the total number of the orders of the poles plus one, such that:

n=1 for ion-ion interactions,

n=2 for ion-dipole interactions,

n=3 for dipole-dipole interactions,

n=4 for ion-induced dipole (polarisable molecule) interactions,

n=5 for dipole-induced dipole interactions

and so on. When the preceding equation is applied to an ion-molecule reaction, the relationship obtained is:

$$V_{es} = -\alpha q^2/2r^4 \qquad (2.7)$$

where q is equal to the charge on the ion and proportional to the polarisability of the molecule providing that the molecule does not have a permanent dipole moment.

The effect of these attractive forces on the course of collisions has been depicted in Figure 2.3, by considering the motion of a molecule relative to that of an ion and then by drawing trajectories of the motion for various values of the impact parameter $\underline{b}$ for a fixed relative velocity. At large values of $\underline{b}$ as described by line (i) , Figure 2.3, the molecule is virtually undeflected and no close collision occurs. Line (ii) denotes a collision parameter where the value of $\underline{b}$ is very small and the molecule undergoes a collision with the ion. At a moderate value of $\underline{b}$, Figure 2.3 line (iii), the molecule is captured by the electrostatic field of the ion and spirals into the ion to undergo a close collision, or alternately it escapes after suffering appreciable deflection, line (iv). The critical value of the impact parameter $\underline{b}_c$, separates close collisions from the rest and can be clearly calculated as a function of the relative velocity by using classical mechanics and a known potential energy function, equation (2.7). If the impact parameter exceeds $\underline{b}_c$ by a small margin, it may be shown that the closest approach of the molecule and ion is a distance $\underline{b}_c/\sqrt{2}$. This minimum distance of approach and hence $\underline{b}_c$, are governed by the fact that in this critical orbit, the attractive ion-molecule force balances the outwardly-directed centrifugal force for the motion in a circle of radius $\underline{b}_c/\sqrt{2}$. Equating these two forces leads to the result:

$$\underline{b}_c^2 = (2q/v)\sqrt{(\alpha/\mu)} \qquad (2.8)$$

where v is the initial relative velocity at large separations and μ is the reduced mass of the ion-molecule pair. If one assumes that the ion is spherically symmetrical the effective collision cross section σ can be obtained by rotating Figure 2.3 about the line $\underline{b}$ equals zero, this gives $\sigma=\pi\underline{b}_c^2$. This value of σ is the effective capturing area presented to the approaching molecule by the ion, and is clearly velocity dependent as shown in equation

Figure 2.3

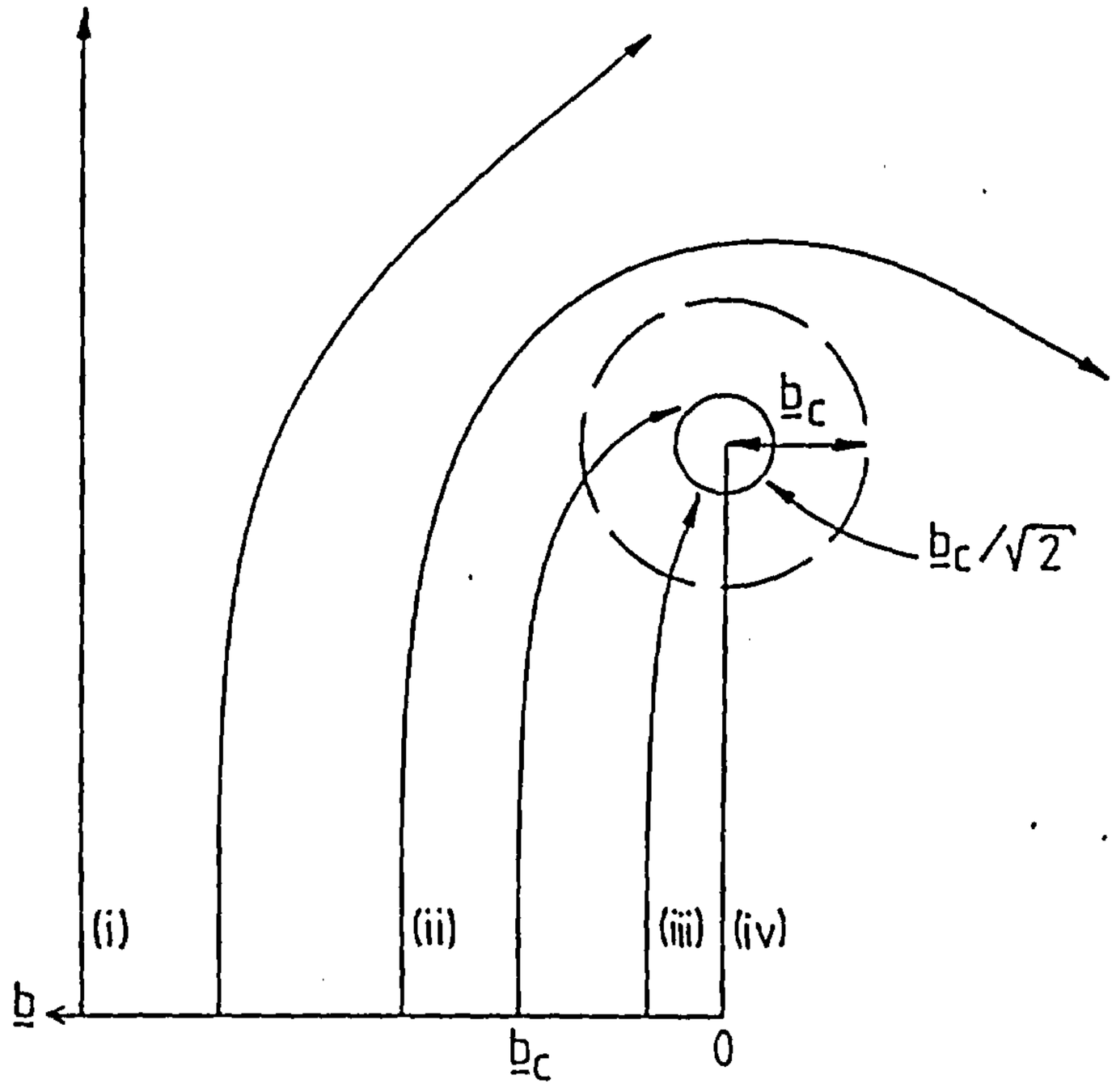

Some trajectories of collisions between a molecule and an ion.[47]

Figure 2.4

Energy relationships between reactants and reaction complex; D_o is the dissociation energy of the complex and E is the internal energy in excess of the dissociation energy.[61]

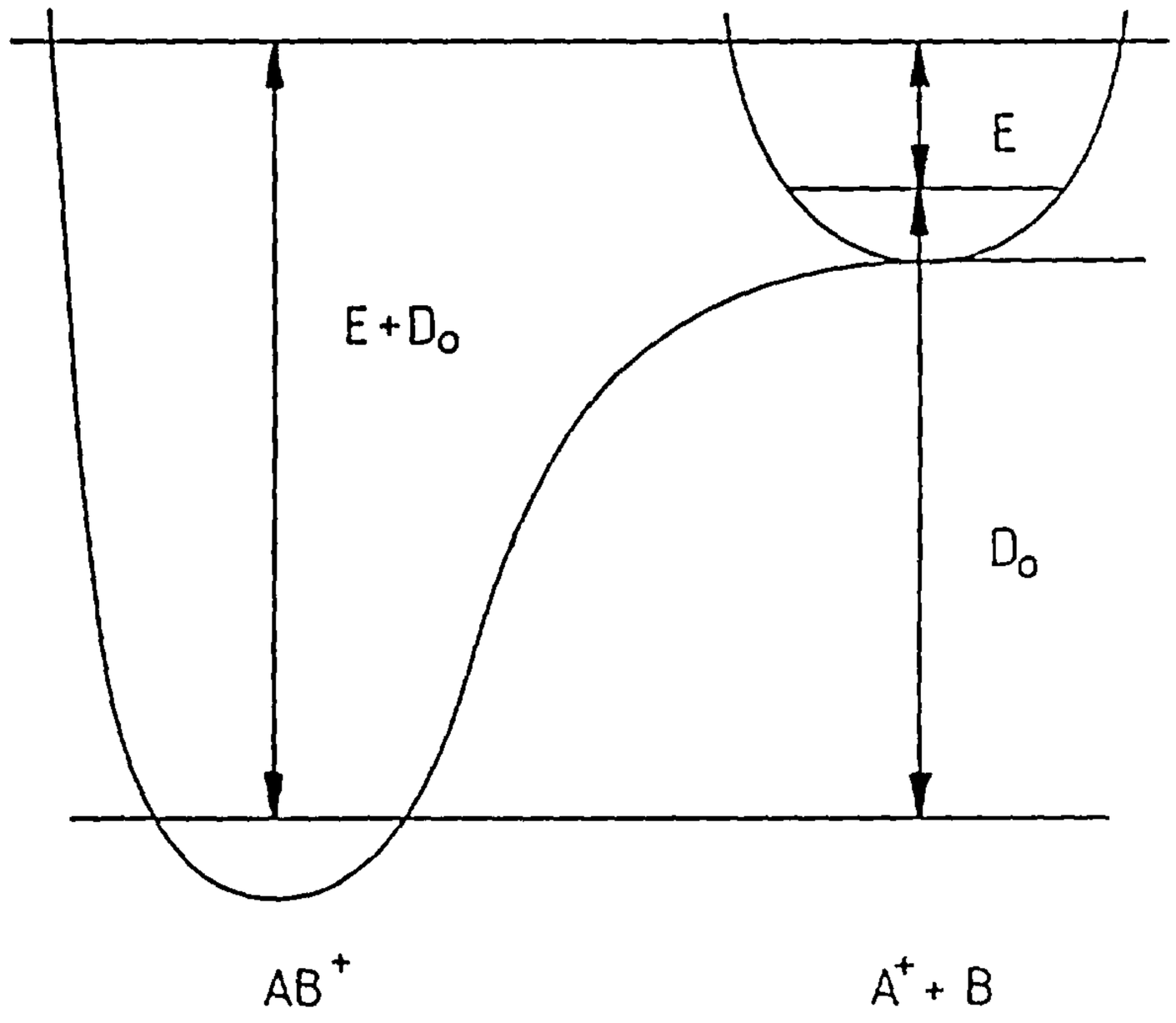

(2.8). Hence the capture cross section $\sigma(v)$, which is defined by the area of the circle radius $\underline{b}_c$ is:

$$\sigma(v) = \pi \underline{b}_c^2(v) = (2\pi q/v)\sqrt{(\alpha/\mu)} \qquad (2.9)$$

and k_c the microscopic rate constant is given by expression 2.10:

$$k_c = \sigma(v).v = 2\pi q\sqrt{(\alpha/\mu)} \qquad (2.10)$$

The macroscopic or Langevin rate constant k_L, is obtained by summing the k_c values over a velocity distribution f(v):

$$k_L = \langle\sigma(v).v\rangle = \frac{\int f(v).\sigma(v).v \, dv}{\int f(v).dv} = 2\pi q\sqrt{(\alpha/\mu)} \qquad (2.11)$$

This model is limited to low energy ion-molecule collisions as at the high energy limit equation 2.9 is zero. This is indicative of a value of r above which the capture cross-section σ is less than that predicted by the hard sphere gas cross-section model. This pure polarisation theory also predicts the capture cross section to be inversely proportional to v, and the capture rate constant independent of v. Hence, k_L is independent of temperature.

Equation 2.10 has been found to predict reasonably well the maximum rate constant for ion-molecule pairs involving non-polar molecules, but underestimates rate constants where polar molecules are involved. Work by Moran and Hamill[48] in 1963, considered ion-dipole forces between interacting molecules and yielded an analogous equation to number 2.7 of:

$$V_{es} = (L2/2\mu r2) - (\alpha q2/2r4) - (\mu_D q \cos\theta/r2) \qquad (2.12)$$

L is the classical angular momentum of the two particles, μ_D the dipole moment and θ the angle the dipole makes with the centre of collision. A simplification was made by Hamill which suggested that the dipole 'locks on' to the ion such that θ is zero. The capture collision rate constants for this 'locked dipole' orientation k_{LD}, was given by:

$$k_{LD} = (2\pi q/\sqrt{\mu}) [\sqrt{\alpha} + (\mu_D/v)] \qquad (2.13)$$

and thus, k_{LD} is dependent on the relative velocity of the pair. For a Maxwell-Boltzmann distribution of velocities the expression 2.13 changes to:

$$k_{LD} = (2\pi q/\sqrt{\mu}) [\sqrt{\alpha} + \mu_D\sqrt{(2/\pi k_B T)}] \qquad (2.14)$$

where k_B is the Boltzmann constant and T the absolute temperature.

Work by Su and Bowers in 1973 concluded that expressions 2.13 and 2.14 overestimated the ion-dipole effect on Ion-Molecule rate constants, i.e. that the 'locking in' effect does not occur[49]. A more realistic expression was derived by these workers who considered the average dipole orientation between the interacting species. This theory, known as ADO theory, gives the expression for k as:

$$k_{ADO} = (2\pi q/\sqrt{\mu}) [\sqrt{\alpha} + C\mu_D\sqrt{(2/\pi k_B T)}] \qquad (2.15)$$

where C is a dipole locking constant with values between zero (for no alignment) and one ('locked on'). Many studies have been proformed on proton-transfer reactions[49,50,52] which conclude that ADO theory does adequately predict the maximum rate constant for ion-polar-molecule reactions. Several groups have refined this form of Langevin theory even further to consider the conservation of angular momentum (AADO Theory[52]) and to include ion-

quadrupole interactions (AQO Theory[53]), although results show that these considerations have only small effects on the theoretical values of k derived by ADO theory.

2.5 Termolecular Association Reactions

2.5(i) Intermediate Complex or Ligand Switching Mechanism

The features of termolecular association reactions, third order kinetics and a negative temperature dependence can be accounted for by the model known either as the Intermediate Complex or Ligand Switching Mechanism[64]. The reaction between two species A and B in a bath gas M, is considered and the mechanism proposed is outlined in the sequence below:

$$A^{+\cdot} + M \underset{k_{-1}}{\overset{k_1}{\rightleftharpoons}} (AM^{+\cdot})^* \overset{M}{\rightleftharpoons} AM^+ + M \qquad (2.16)$$
$$k_2$$
$$AM^{+\cdot} + B \text{ ------> } AB^{+\cdot} + M$$

The transient species $(AM^{+\cdot})^*$ is a true molecular entity and not an activated complex. As the interaction between the atom and the third body is relatively weak, the complex $(AM^{+\cdot})^*$ is a short lived species, so a steady-state approximation can be applied to it:

$$\frac{d[(AM^{+\cdot})^*]}{dt} = k_1[A][M] - k_{-1}[(AM^{+\cdot})^*] - k_2[(AM^{+\cdot})^*][B] \approx 0 \qquad (2.17)$$

This results in the expression:

$$[(AM^{+\cdot})^*] = \frac{k_1[A][M]}{k_{-1} + k_2[M]} \qquad (2.18)$$

Thus, the rate of product formation k_f, is given by the relationship:

$$\frac{d[AM^+]}{dt} = k_2[AM^+][B] = \frac{k_1k_2[A][B][M]}{k_{-1} + k_2[M]} = k_f \qquad (2.19)$$

Any weak complex formed is more likely to dissociate than survive to react and hence k_{-1} will be much greater than $k_2[A]$ and equation (2.19) becomes:

$$k_f = \frac{k_1k_2}{k_{-1}}[A][B][M] = k_2K_{eq}[A][B][M] \qquad (2.20)$$

where $K_{eq} = k_1/k_{-1}$, the equilibrium constant for the formation of $(AM^+)^*$. From the van't Hoff relationship: ln K = (- $\Delta H^o/RT$)- ($\Delta S^o/R$) where: ΔH^o is the heat formation of the complex, ΔS^o the entropy change on formation, R is the Gas Constant and T the temperature, it can be observed that a linear relationship for the Ligand Switching Mechanism of ln K versus 1/T can be obtained.

2.5(ii) Energy Transfer Mechanism

This mechanism, which was first proposed by Rabinowitz[54] in 1937 for atom recombination reactions, is generally considered applicable to most ion-molecule reactions[30,44,45]. The mechanism is usually considered to follow the scheme:

$$A^{+\bullet} + B \underset{k_b}{\overset{k_a}{\rightleftharpoons}} (AB^{+\bullet})^* \qquad (AB^{+\bullet})^* + M \underset{}{\overset{k_s}{\rightleftharpoons}} AB^{+\bullet} + M \qquad (2.21)$$

The rate constant for formation of the excited association complex k_a, is often equated with the collision rate constant $k_c(A^{+\bullet} + B)$, which is calculated from Langevin[43] or Average Dipole Orientation (ADO) Theory[49]. The stabilisation rate constant k_s, is approximated to the collision rate constant between $(AB^{+\bullet})^*$ and M. This assumption is justified on the basis that the removal of a fraction of the excitation energy from $(AB^{+\bullet})^*$ by a collision with M makes

the dissociation of the complex to A^+ and B sufficiently slow to allow for the eventual stabilisation of $(AB^{+\cdot})^*$. The third body M, varies in stabilisation efficiency:

$$k_s = k_c\beta \qquad (2.22)$$

where β is the stabilisation efficiency and k_c the collision rate constant. β allows for a fraction of the collisions to remove only sufficient energy to de-energise $(AB^{+\cdot})^*$. When $\beta=1$ this corresponds to a strong collision assumption where all the collisions result in back reaction. Considering the mechanisms 2.21, k_f the rate constant for the forward reaction of $AB^{+\cdot}$, is given by:

$$k_f = \frac{k_a k_s[M]}{k_b + k_s[M]} \qquad (2.23)$$

At low pressures, however, $k_s[M]$ is much less than k_b, such that k_f approximates to:

$$k_f = \frac{k_a k_s}{k_b}[M] \qquad (2.24)$$

The second order rate constant k_f, is linearly dependent upon the pressure M, such that at low pressures the overal reaction exhibits third order behaviour. k_a and k_s are represented by the corresponding collision rates and are therefore considered to be only weakly temperature dependent. The major cause of any temperature dependence of k_f will be attributed to k_b. This is in fact an over simplification since the Lindemann mechanism is not entirely correct as k_b is pressure dependent and varies in the following way. At low pressures, most complexes decompose to reactants and the average lifetime of those which decompose is generally long, in other words k_b is large. At high pressures a fraction of the complexes are collisionally stabilised and hence, the average lifetime of those which escape

collision is reduced and k_b is small. This problem is accommodated in the Unimolecular Rate Theory statistical treatment of Rice, Ramsperger55 and Kassel56, (RRK Theory). The fundamental concepts of this theory assume strong coupling collisions, which allow the energy distribution of the activated molecule to be determined directly from statistical considerations. Secondly, rapid intermolecular vibrational energy redistribution is allowed. The macroscopic rate constant is evaluated by integrating the microscopic rate constant k(E), over the appropriate energy distribution function F(E):

$$\frac{d(AB^{+})}{dt} = \frac{d(AB^{+})^{*})}{dt} = \int_0^\infty \frac{k_s[M]}{k(E)+k_s[M]} \cdot F(E)dE \qquad (2.25)$$

The main consequence of these assumptions is that a plot of $1/k_f$ versus $1/P$ is no longer linear, and hence k_b cannot be derived from such plots. k_b may be written in terms of the RRK treatment as:

$$k_b = \nu(rRT/(D_o + rRT))s\text{-}1 \approx \nu(rRT/D_o)s\text{-}1 \qquad (2.26)$$

where ν is a frequency factor, D_o the dissociation energy of the complex, RT is the average thermal energy per oscillator, r is proportional to the number of degrees of freedom and s is the effective number of oscillators in the complex. This predicts:

$$k_b \alpha Ts\text{-}1 \alpha Tn \quad \text{and hence:} \quad k_f \alpha T\text{-}n \qquad (2.27)$$

Consequently plots of log k_f versus log T are linear, with a slope equal to: -n = -(s-1), where s = 3N-6, when N is the number of atoms in the complex. However, deviations from linearity have been observed in some systems recorded at temperatures less than 150K and these are believed to be due to the activation energies of the complexes becoming increasingly important under such conditions57.

In conclusion, we observe that the Energy Transfer and Ligand Switching Mechanisms both explain the third order kinetics and the negative temperature dependence of thermolecular association reactions. Although these temperature tests are indirect, they are useful as the two mechanisms cannot be distinguished by pressure studies.

2.6 Statistical Phase Space Theory

2.6(i) Introduction

In recent years Statistical Phase Space Theory has been applied by many groups[59-60] to ion-molecule association reactions. This theory is based on the Energy Transfer Mechanism:

$$A^{+\cdot} + B \underset{k_b}{\overset{k_a}{\rightleftharpoons}} (AB^{+\cdot})^* \qquad (AB^{+\cdot})^* + M \xrightarrow{k_s} AB^{+\cdot} + M \qquad (2.28)$$

The rate constants for complex formation and excited complex dissociation, k_a and k_b respectively, are both determined by the collision rates derived by Langevin[48] and ADO theory[49]. Once more, depending on the bath gas M, k_s is taken to be only a fraction of the collision rate k_c, such that $k_s = k_c\beta$, where β represents the stabilisation efficiency. The binary and tertiary rate constants are defined by considering the overall reaction in (2.28):

$$A^{+\cdot} + B \xrightarrow{k_2} AB^{+\cdot} \qquad k_2 = \frac{k_a k_c \beta [M]}{k_b + k_a k_c \beta [M]} \qquad (2.29)$$

$$A^{+\cdot} + B + M \xrightarrow{k_3} AB^{+\cdot} + M \qquad k_3 = \frac{k_a k_c \beta}{k_b + k_a k_c \beta [M]} \qquad (2.30)$$

Statistical Phase Space Theory may be applied to either the unimolecular decomposition of $(AB^+)^*$ to give k_b, or to the bimolecular association process to yield k_2. If assumed values

of k_a, k_b and β are used, the values of k_b, k_2 and k_3 can be calculated once one of the latter has been determined by this statistical theory.

A modified thermal treatment has been recently developed by Herbst[59] and Bates[60] which is essentially a simplified Phase Space Theory at the limiting low pressures will also be considered.

2.6(ii) Phase Space Theory

In this model two basic assumptions are made; firstly, all rotations of molecules are considered in the classical motion and secondly, symmetric and asymetric tops are approximated to spherical tops. If we consider the Energy Transfer Mechanism, but this time on a microcanonical level:

$$\begin{aligned} &\text{(i)} && A^{+\cdot} + B \xrightarrow{k_a F(E,J)} AB^{+\cdot}(E,J)^* \\ &\text{(ii)} && AB^{+\cdot}(E,J)^* \xrightarrow{k_b(E,J)} A^{+\cdot} + B \\ &\text{(iii)} && AB^{+\cdot}(E,J)^* + M \xrightarrow{k_s} AB^{+\cdot} + M \end{aligned} \qquad (2.31)$$

E is the energy of the complex in excess of its bond dissociation energy D_o, see Figure 2.4 and J is the angular momentum of the complex. $AB^{+\cdot}(E,J)^*$ represents a complex which is capable of back dissociation, and $AB^{+\cdot}$ complexes which are stabilised. F(E,J) is a distribution function of the thermal $A^{+\cdot}$ and B activation process and $k_b(E,J)$ a microcanonical rate constant for back dissociation of the complex state (E,J). It should be noticed that k_s, the rate constant for stabilisation, is not considered on a microcanonical level and is derived by equation 2.22 since it is independent of the internal state of the complex. The Phase Space Theory[61] expression for F(E,J) and $k_b(E,J)$ are:

$$F(E,J) = \frac{2Jexp(-E/k_BT)G(E,J)}{\int_0^{\infty} dEexp(-E/k_BT) \int_0^{J^*(E)} dJ2JG(E,J)} \quad (2.32)$$

and

$$k_b(E,J) = \frac{SG(E,J)}{h2J\rho\nu(E + D_o - BJ^2)} \quad (2.33)$$

where, G(E,J) is the sum of the states at the orbiting transition state,

S is the ratio: $\frac{\text{symmetry numbers of complex}}{\text{symmetry numbers of reactants}}$

h is Planck's constant,

BJ^2 is the classical energy of a spherical top,

$(E + D_o - BJ^2)$ is the vibrational density of states for the complex.

and $\rho\nu\ (E + D_o - BJ^2)$ is the vibrational energy of states.

The tertiary rate constant is given by the relationship:

$$k_3 = \frac{k_ak_c\beta}{k_bk_ak_c\beta[M]} = k_ak_c\beta \cdot \int_0^{\infty} dE \cdot \int_0^{J^*(E)} dJ \frac{F(E,J)}{k_b(E,J) + k_c\beta[M]} \quad (2.34)$$

the temperature dependence arising from the F(E,J) factor. At low pressures the expression, $k_c\beta << k_b(E,J)$, is assumed valid for all (E,J) states accessible from the reaction 2.31(i). The relationship for k_3 may be simplified to yield:

$$k_3 = \frac{k_ak_c\beta h}{S} \cdot \frac{q^*(AB^{+\cdot})}{q^*(A^{+\cdot} + B)} \quad (2.35)$$

where q^* terms are the pseudo-partition functions defined by:

$$q^*(AB^{+\cdot}) = \int_0^\infty dE \exp(-E/k_BT) \cdot \int_0^{J^*(E)} dJ(2J)^2 p\nu(E + D_o \cong BJ^2) \qquad (2.36)$$

$$q^*(A^{+\cdot} + B) = \int_0^\infty dE \exp(-E/k_BT) \cdot \int_0^{J^*(E)} dJ 2J\, G(E,J) \qquad (2.37)$$

the expression for k_3 is generally applicable to any temperature and pressure. The pseudo-functions have the general form of a partition function, but only the states that are consistent with angular momentum conservation and which are capable of passage across the centrifugal barrier are included.

2.6(iii) Modified Thermal Treatment

The main assumptions of this treatment are:

(i) the low limit pressure conditions are satisifed,

(ii) $AB^{+\cdot}$ is considered as diatomic,

(iii) the number of states available to $A^{+\cdot}$ and B in forming AB^+ is not significantly affected by assumption (ii),

(iv) the vibrational density of states for $AB^{+\cdot}$ is independent of energy over the range populated by $A^{+\cdot} + B \longrightarrow AB^+$;

(v) vibrational modes of $A^{+\cdot}$ and B do not contribute significantly to the total $(A^{+\cdot} + B)$ density of states.

Assumption (i) leads to consideration of the reaction mechanism:

$$A^{+\cdot} + B \xrightarrow{k_a} (AB^{+\cdot})^* \quad \text{and} \quad (AB^{+\cdot})^* \xrightarrow{k_b} A^+ + B$$

as a chemical equilibrium, giving k_3 as:

$$k_3 = \frac{k_c \beta q(AB^{+\cdot})}{q(A^{+\cdot})q(B)} \qquad (2.38)$$

where q becomes the simple partition function. Consideration of the remaining assumptions leads to this treatment defining a new expression for k_3 as:

$$k_3 = \frac{k_c \beta q^*(AB^{+\cdot})}{q^*(A^{+\cdot} + B)} \qquad (2.39)$$

The temperature dependencies of $q^*(AB^{+\cdot})$ and $q^*(A^{+\cdot} + B)$ are given by:

$$q^*(AB^{+\cdot}) \propto T^{3/2} \text{ and } q^*(A^{+\cdot}B) \propto T^{(3/2+r/2)} \qquad (2.40)$$

This leads to k_3 being proportional to $\propto T^{-(r/2)}$, where 'r' is the number of rotational degrees of freedom.

2.6(iv) Comparison with Experimental Results

Selected Ion Flow Tube experiments (SIFT - see section 2.2(v) conducted by Smith and Adams[33]), have been used to study the termolecular reactions occurring in the systems;

$$A^{+\cdot} + B + He \longrightarrow AB^{+\cdot} + He \qquad (2.41)$$

where $A^{+\cdot}$ is CH_3^+ or CD_3^+; and B is H_2, D_2, N_2, 0_2, CO or CO_2. The Modified Thermal Treatment predicts n the temperature dependence of these reactions to be equal to 2.5 for all of these systems, whereas experimental results range from 2.3 to 3.4. These apparently anomolous results have been attributed to a temperature dependence in k_c, the collisional stabilisation rate constant[63]; alternatively they indicate the shortcomings of this treatment.

Divergences from the predicted result of n = 2.5, tend in the most to be greatest for complexes with large well depths and large numbers of low frequency vibrations and internal rotations. The low pressure limit, $k_c\beta[M] << k_b(E,J)$ depends on the dissociation rate of the complex over the various (E,J) states populated by equation 2.3(i). The dissociation rate $k_b(E,J)$, defined by equation 2.33, is a strong function of D_o, the well depth, and hence the low pressure limit is not satisfied by complexes with a large well depth.

The results obtained from Statistical Phase Space Theory show that the $k_3 \alpha$ T-n approximation is valid only at low pressures and deviations occur at high temperatures due to the reactant vibrational modes becoming more significant. Also as the pressure rises, the assumption $k_b >> k_c\beta$ is no longer valid, and deviations from linearity occur for complexes with large well depths. However, agreement between Phase Space Theory and experimental results are accurate enough to show no signficant temperature dependence for collisional stabilisation.

In conclusion we see that Phase Space Theory considers the decomposition of a strong coupling collision complex. One of the important properties of this theory is that it is not highly 'parameterised', and requires only a knowledge of the initial and final properties of the reaction systems.

Chapter Three

The High Pressure Ion Source, Instrumentation and Experimental Procedure

3.1 Introduction

Pulse methods for the determination of rate constants of ion-molecule reactions were first developed as early as 1960 by Tal'roze and Frankevich[65]. The development of the pulsed high pressure and drift mass spectrometry ion sources have provided valuable instruments for studying the kinetic behaviour of ion-molecule reactions. In this chapter the experimental procedure and instrumentation used in conjunction with the high pressure ion source are considered with the treatment of the experimental data used for the determination of rate and equilibrium constants.

3.2 The Pulsed Electron Beam, High Pressure Ion Source

The pulsed high pressure ion source used in this work was modelled on a version originally built by Kebarle[24] in 1974 and later developed by Headley[29,66,67] in 1981. A diagram showing the general features of this source is given in Figure 3.1. The main source unit consisting of the block and focusing plates, were constructed out of stainless steel. This material was preferred as the copper source block of Headley was 'soft', leading to the stripping of threads during assembly. This choice of material has also done away with the need for nickel flashing and gold plating on the inside surface of the block in order to produce an inert surface. The source reactor is essentially a one cm^3 chamber with two openings in it, the electron entrance and ion exit apertures. Several different metal foils were tested for use in the construction of these apertures, of which gold foil (0.025mm thickness, 99.95% purity, light tight, Goodfellow Metals Ltd.) was found to be the most durable. A new method for forming these apertures has been developed: Gold discs of approximately

Figure 3.1 Cross-section of High-Pressure Ion Source.

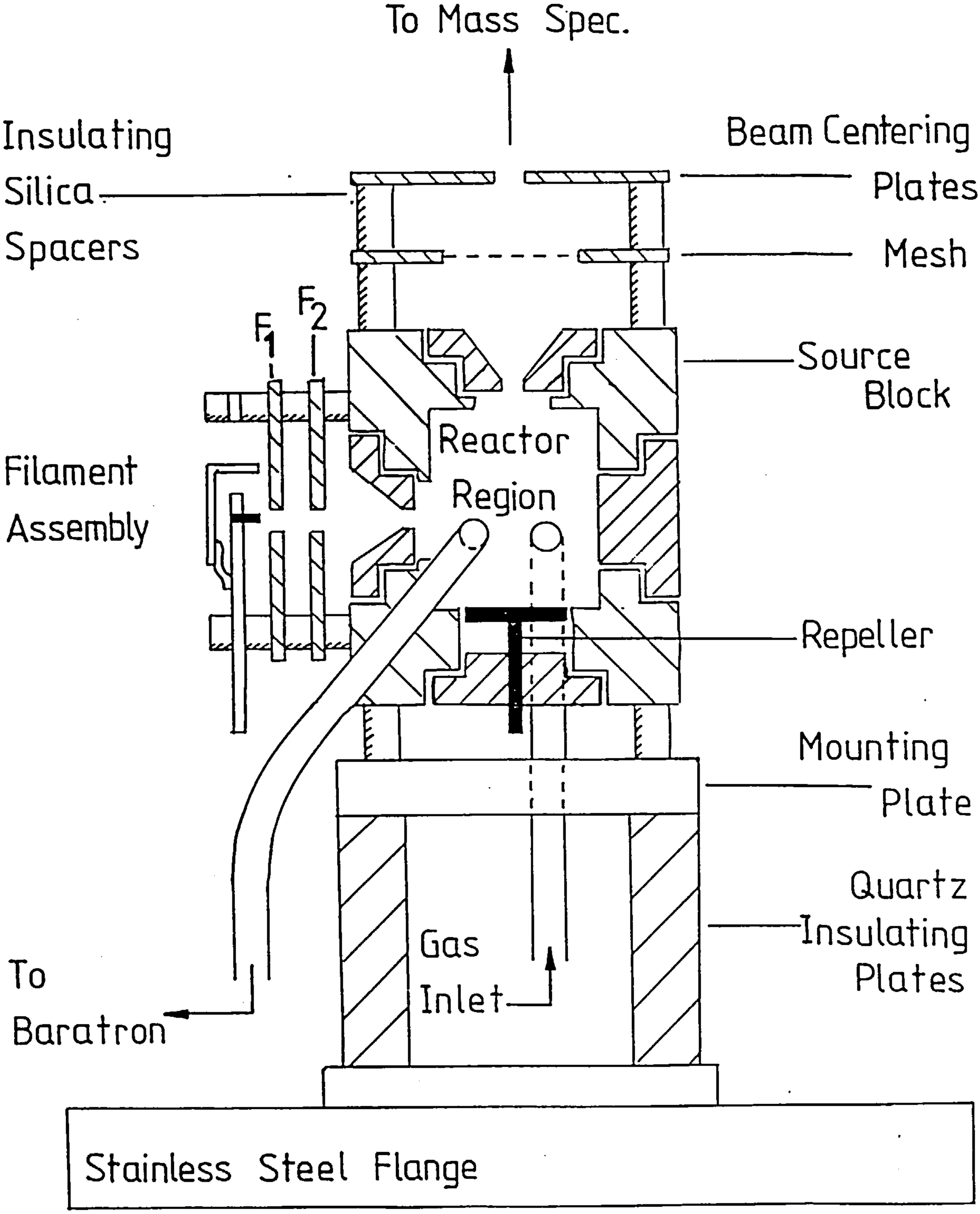

10mm diameter are cut out using a specially constructed die. A hole is then formed in the centre of the disc using a spark eroder to great accuracy. The holes formed have a diameter in the range of 0.013 to 0.025cm. The whole inside of the source block including the gold discs, are coated with Aquadag, a colloidal graphite in water suspension, Acheson Ltd., to prevent an electric charge building up on the sides of the chamber during source operation.

Two focusing plates for the electron beam are positioned between the Rhenium filament and the electron entrance aperture. On the outside of the ion exit hole was positioned a wire mesh (40 wires cm^{-1}, 81% transmission) insulated by silica spacers between the block and the beam centering plates. The main purpose of the mesh is to reduce any electric field penetration into the reaction chamber. It also aids the channelling away of gas streaming from the ion exit hole and thus reduces the degree of collisional-induced ion decompositions in the emergent ion beam. The whole source assembly is held in position on the flange by two quartz insulating plates. All electrical connections are made via ten insulated solid feedthroughs in the flange. There are also three hollow feedthroughs; one used for the thermocouple leads for temperature measurement and the other two sealed with 1/8" 'cajon' fittings, provide the inlet for gas samples to the reaction chamber and the source pressure meter (see below).

3.3 Pressure Measurements

Experiments were conducted at various source pressures between 0.5 and 6.0 Torr, although the source was capable of operating at pressures up to ten Torr. The pressure was controlled by an automatic pressure control valve (Granville Philips, Series 215, Bakable) and monitored by an NKS.Inc. 'Baratron' capacitance pressure meter (type 77). The pressure was shown on a Chell digital meter to an accuracy of $\pm$0.01 Torr. This was not regarded as a significant source of error in this work as it contributes less than the measured scatter of the experimental data recorded.

The whole source housing was kept at a pressure of around 2.10^{-7} Torr before sample introduction by a 15cm diameter diffstak (Mk II, Edwards M160/700) via a 15cm wide pumping elbow connected to the source housing by a 7.5cm diameter port. During source operation the housing pressure rose to around ~ 10^{-5} Torr and the analyser pressure from 2.10^{-8} Torr to a maximum of 2.10^{-7} Torr.

3.4 Temperature Measurement

The source block temperature can be varied by the use of a heating coil (25V, 50Watts, Rosemount Eng.Co.Ltd.) attached to the repeller side of the block. The temperature is controlled by use of a specially constructed control unit via a platinum resistance sensor fixed into the block unit. Normal operating temperatures range from 310 to 620K and were measured by means of a thermocouple (type K, Radio Spares Ltd.) connected to the block and a digital temperature meter (Jenway, Model 7500). Great care was taken in making this measurement. Numerous thermocouples were connected to various parts of the block and these indicated that temperature gradients in this source were only $\pm$1K across the block, ion exit port to repeller side, which are considered to be negligible.

3.5 Introduction of Gas Samples

A gas inlet system was constructed and is shown schematically in Figure 3.2. The system consists of a large glass flask of known volume ~ $5dm^3$, which is situated in a double skinned oven made of 'sindanyo', an asbestos-like material, and heated to around 380K. All valves used in the oven were an all-metal bakable type made from stainless steel (Vacuum Generators Ltd.). All gases used were of research grade (BOC Ltd., 99.95% pure). Some gas mixtures were made up at the Gamma Ray Laboratory, Berkeley[68], using a special rig built for this purpose. These mixtures were pressurised and transported to Warwick in cylinders at ~ 600p.s.i. where the gases were dried further before storing in the reservoir inlet system.

Fig. 3.2 THE HEATED RESERVOIR INLET SYSTEM

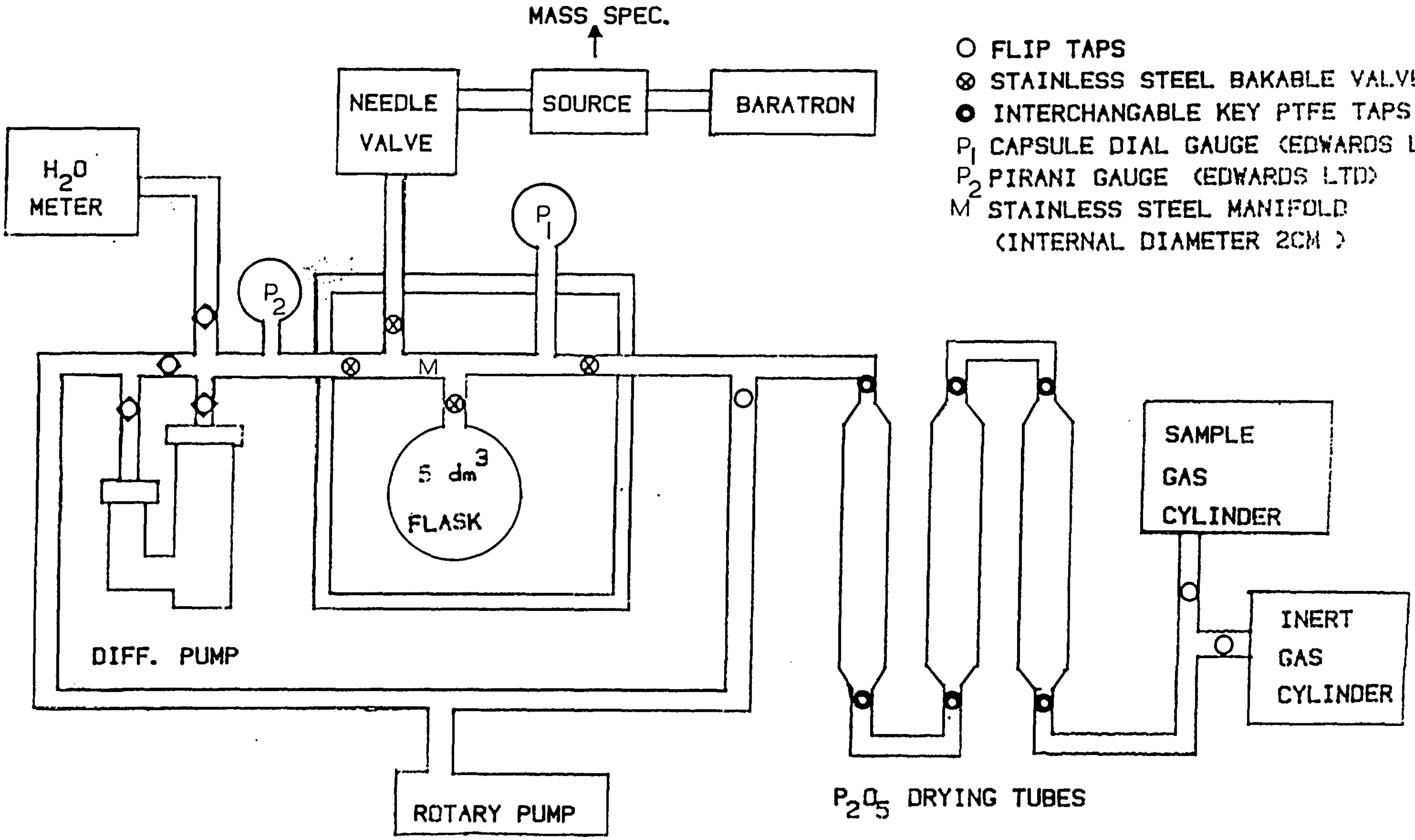

Many different drying agents were tested on the gases, such as $Mg(ClO_4)_2$, $CaSO_4$ and silica gel. Eventually three tubes of granular P_2O_5 (with moisture indicator, BDH Ltd.) were found to be most successful in reducing the water level down to less than 5vpm. It was discovered that allowing the gas to pass through the system at a low flow rate of ~ $2cm^3$ min^{-1}, for several hours, would reduce the water level content to an acceptable level, 3vpm. This water content was measured on a moisture meter (Engelhard) on loan from the C.E.G.B[68].

The whole inlet system can be evacuated to a pressure below 10^{-5} Torr by means of a small diffusion pump (Metrovac 022A). The sample gases are introduced into the source chamber via the automatic pressure control needle valve and 'Baratron' pressure meter previously described in Section 3.3.

3.6 Instrumental Layout and Experimental Procedure

The main hardware used for experimentation is listed below and shown schematically in Figure 3.3.

(i) MS9 mass spectrometer, Kratos Analytical Ltd., updated with a Mass Specrometry Services (MSS) console.

(ii) Pulse Generators : Thandor TG105, 5Hz to 5MHz and a Farnell P.G.System (P.G.1 and 2 respectively in Figure 3.3).

(iii) Mini-computer: Minc-11 (PDP-11), Digital Electronics Corporation, with a Digital Decwriter IV printer.

(iv) Bryans X-Y plotter, Model 26000.

(v) EG & G Ortec multichannel analyser (MCA), model 7450, with an Ortec minibin power supplies and ratemeter.

Experiments are conducted on the MS9 mass spectrometer using a high pressure source by the following procedure. The filament and Focus 2 are held at -400 and +27.5V respectively with respect to the source block potential. Focus 1 is normally held at a relative

Figure 3.3 Layout of Pulsed Source Experiment.

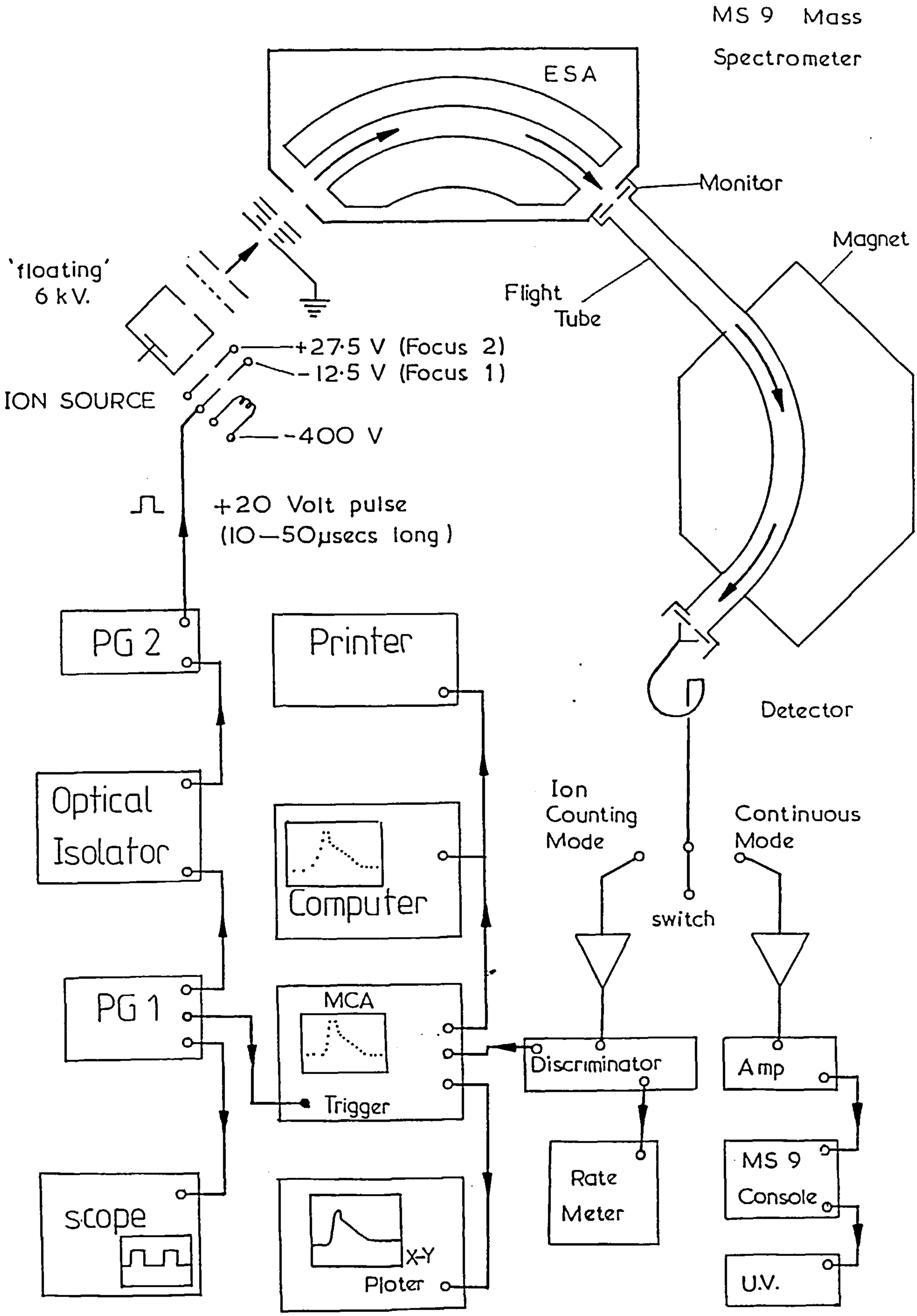

potential of -12.5V and therefore restricts any electrons from entering the reaction chamber. A high intensity of ions is initially produced by firing a short burst of electrons into the ion chamber. This is achieved by P.G.1 transmitting a triggering pulse simultaneously to the Ortec MCA and via an optical isolator to the second pulse generator P.G.2. The latter is necessary as the whole source assembly is floating at around 6KV with respect to earth. P.G.2 is then triggered to transmit a short (10-50μsec) square pulse of +20V amplitude to Focus 1 which allows a short burst of electrons into the source. The filament is then blocked off for 10μsec during which time ion-molecule reactions occur in the chamber and reactant and product ions diffuse to the walls or out of the source through the ion exit aperture. The ion chamber is a field free region in which the pressures used are sufficiently high (> 0.5 Torr) for the ions produced to be thermalised. They are then accelerated, focused and analysed in the conventional manner, although for rate measurements a chosen ion peak intensity is monitored as a function of time, see Figure 3.5. Normally 10 to 25 kilocycles are required until an acceptable signal to noise ratio is obtained. The ions are detected on a single channel electron multiplier (Mullard, type X919AL) with a typical gain of 1.8×10^8 at 2.5KV.

3.7 Mass Discrimination at the Detector

The possibility of mass discrimination caused by the unequal response of the detector to ions of differing $^m/_z$ ratios was investigated. The average response of the detector to 256 ions was averaged for each mass by measuring the signals produced from the electron multiplier via both the MS9 console amplifier and the 'pulse-counting' pre-amplifier. The average signal response was monitored on an oscilloscope and the corresponding peak height h (in volts) and width w (in seconds) were measured. For the current I, measured via the 'pulse-counting' pre-amplifier set to a gain of ten, the detected total charge Q is equal to:

$$Q = It = (V/R)t = (h/R)\,(^w/_2) \qquad (3.1)$$

fig. 3.4 Electron Multiplier response to ions of varying m/z ratios.

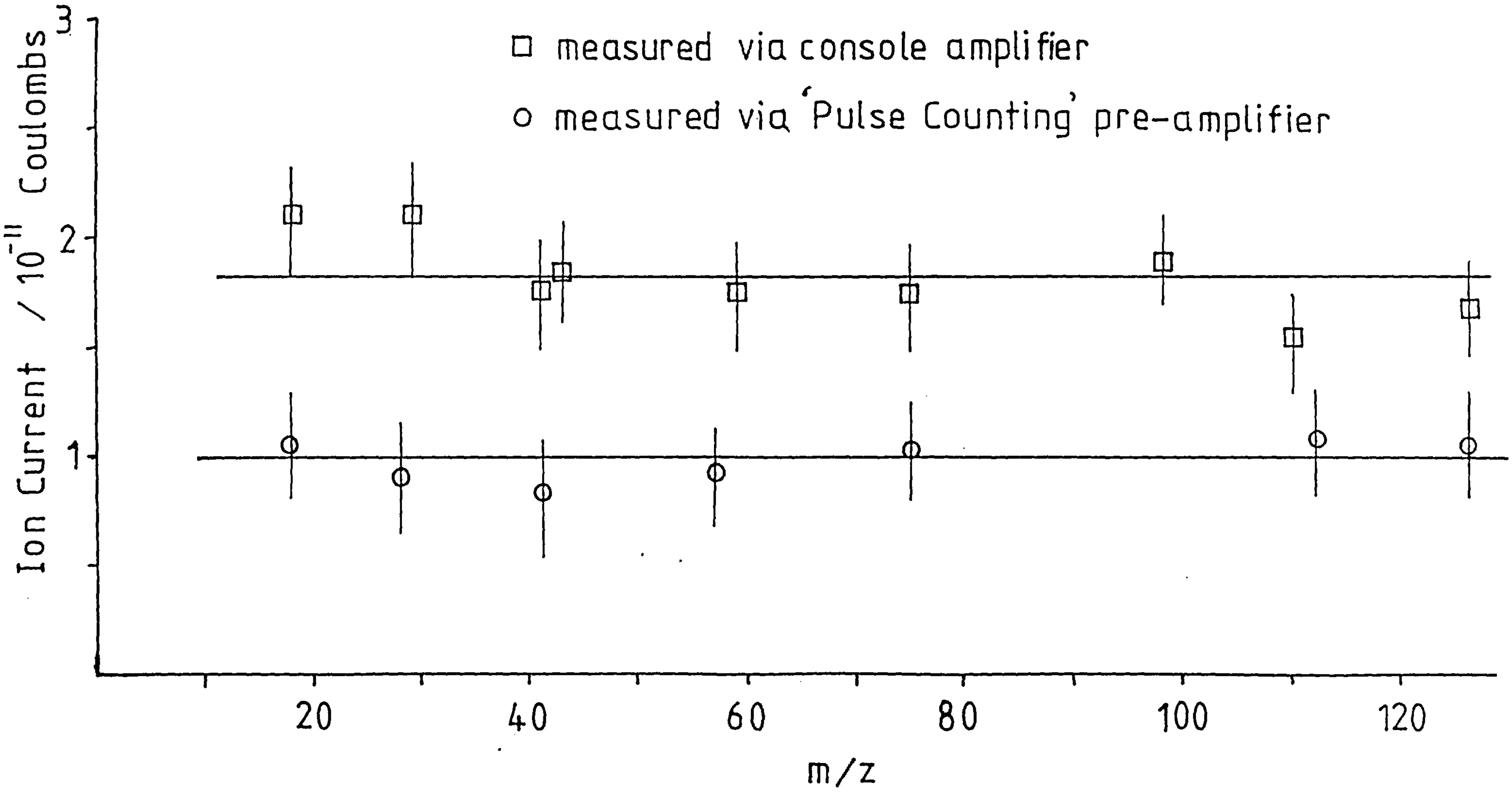

where V is the measured voltage and R is the resistance of the pre-amplifier (50Ω). The duration of the detected electron pulse via the console amplifier was of the order of 280 μsec compared to 30 nanosec via the pulse counting amplifier. The detected voltage from the console amplifier and hence the total charge Q was determined in the same manner using the known console amplifier resistance of $10^7\Omega$. The charge detected via both sources is plotted against $^m/_z$ over the mass range 18 to 126 daltons, see Figure 3.4. The good linearity of the data shows that no unequal response and thus no significant mass discrimination is found over the mass range studied. Mass discrimination was therefore ignored in all subsequent experiments.

The gain g of the electron multiplier can thus be determined as:

$$g = Q_{av}/q \qquad (3.2)$$

where Q_{av} is the average charge produced per ion striking the detector and q is the charge of the ion. The resulting gain was determined at 1.10^8 at an electron multiplier voltage of 2.08KV.

3.8 Ionic Behaviour in the Reaction Chamber

When the transmission of electrons into the ion chamber has been halted by the appropriate potential being applied to Focus 1, the electrons disappear from the plasma by one or more of the following processes:

(a) diffusion to the walls of the chamber,

(b) recombination in the plasma with positive ions to form neutral species,

(c) attachment to a neutral particle to form negative ions.

This last case is not assumed to occur to any great extent as no negative ion spectra were recorded in the systems studied. The recombination of the electrons with the positive ions at the walls of the chamber is a very effective process since the molecules or atoms of

the surface are always present as third bodies which can take up the liberated energy of neutralisation. The concentration of charged particles at the walls is negligible since the particles arriving there are neutralised very rapidly. Hence, the characteristics of the disappearance of electrons and ions in a high pressure source can be discussed by assuming a zero density at the walls. This phenomenon of wall recombination thus affects the concentration gradient of charged particles in the source chamber.

The diffusion velocity of the electron is large with respect to that for ions. The electrons can build up a negative space charge in the outer parts of the chamber and leave a positive space charge in the inner parts of the plasma. Under low charge densities, the space charge effect is small and its influence on the motion of charged particles can be disregarded. Thus, the electrons and ions move by free diffusion. However, for high charge densities, as found in this ion source, free diffusion is initially prevented by the field which is created by the space charges. This field has two effects, first it retards the electron diffusion and secondly, accelerates the positive ion diffusion until the electrons and ions move with the same average velocity. This type of diffusion, influenced by space charge is known as 'ambipolar' diffusion[69]. Studies of decaying plasmas have been published by several authors[70,71]; the most recent by Hiraoka[72] in 1986. These studies, conducted in high pressure ion sources, confirms that the production and decay of ions, positive and negative, in a plasma produced by a pulsed electron beam is diffusion controlled, and highly dependent on the gradient of space charges.

A typical peak profile is shown in Figure 3.5, its shape which contains three distinct regions can now be explained. The first region A to B, corresponds to the time of flight of the ions from the ion source to the detector which includes any electronic delays added by the system and also varies in duration depending on the m/z ratios of the ions. In the region B to C there is an initial sharp rise in signal due to the electron burst and the corresponding rapid rise in ion formation. Over the remaining part of this section, B to C, there is a high ion and electron density and ambipolar diffusion occurs along with electron-ion recombination and

Fig. 3.5 ION INTENSITY vs REACTION TIME PROFILE FOR THE $CO^{+\cdot}$ ION IN HELIUM AT 487 K AND 3.6 TORR.

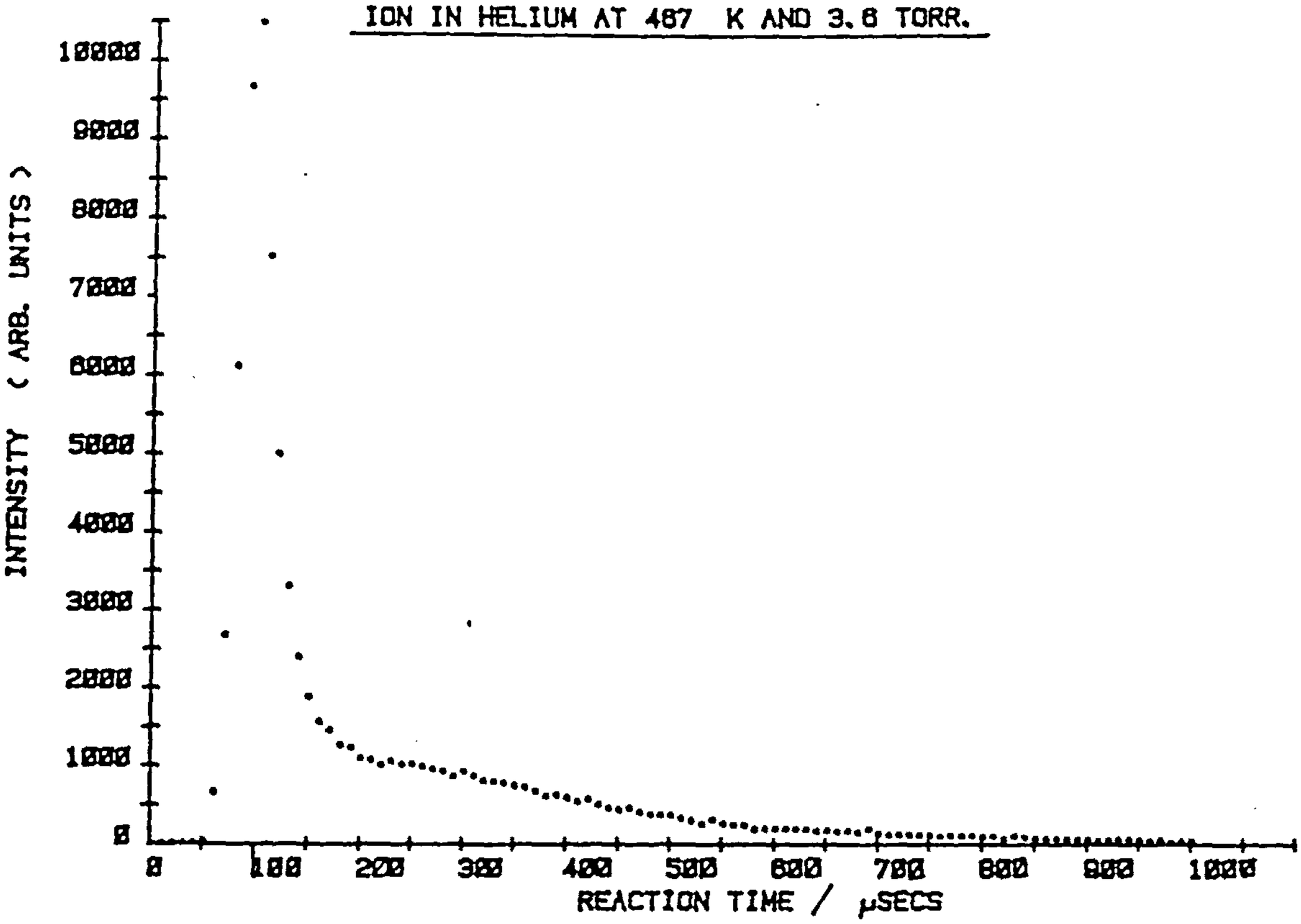

Fig. 3.5 (i) Ln INTENSITY vs REACTION TIME PROFILE.

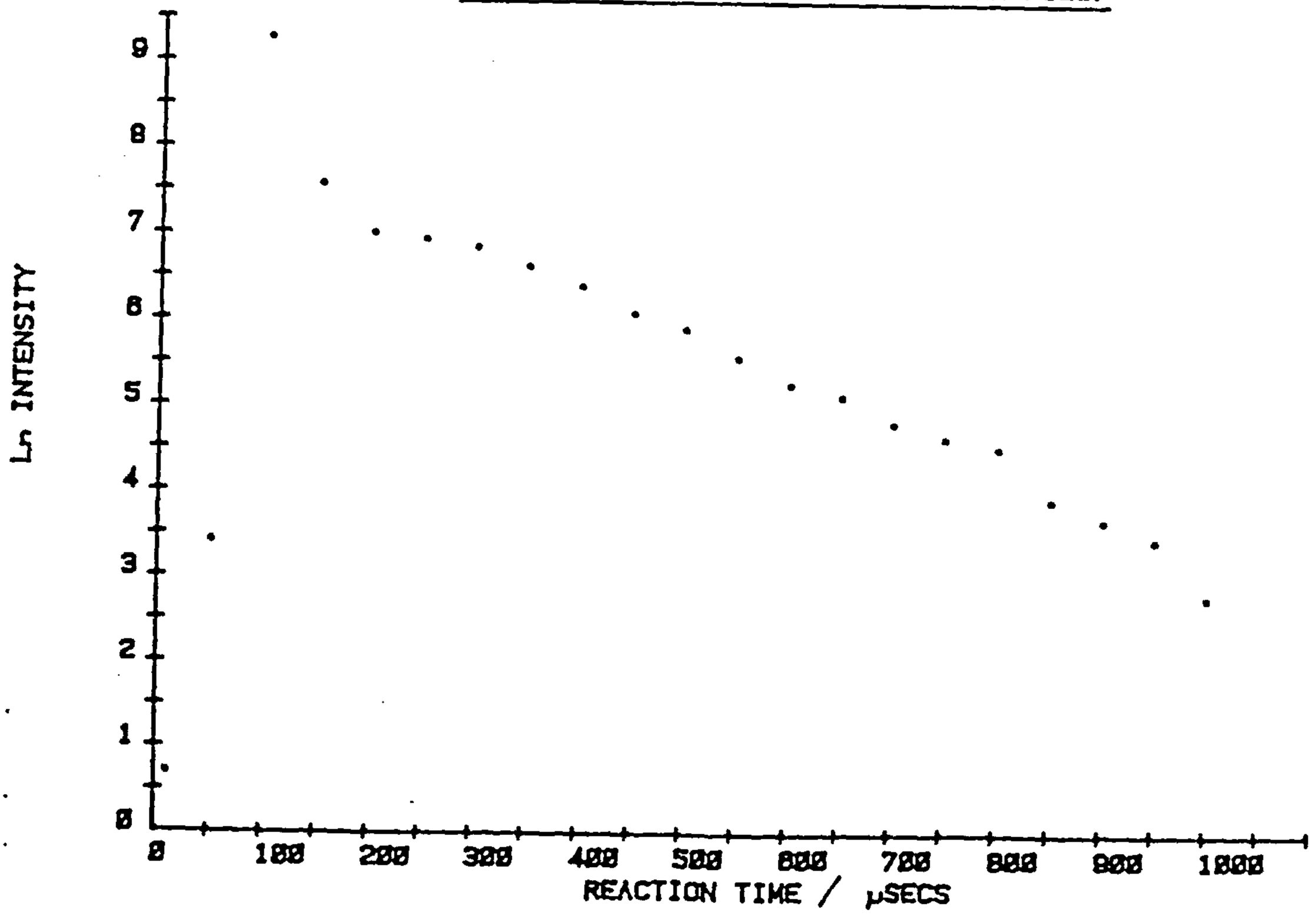

ion-molecule reactions. When sufficient electrons have been lost in the source, such that the ion-neutral gas mixture no longer constitutes a plasma, there is a sudden decrease in the ion decay rate as the ions experience a change from ambipolar diffusion to free diffusion. This is represented in Figure 3.5 at point C. The long tail-off region lasting 200-300 μseconds is the exponential free diffusion region where all kinetic and equilibria data are taken.

In the afterglow region C to D of the ion profile, the measured diffusion current Γ_i of the ionic species i is given by the relationship:

$$\Gamma_i = - D_i \nabla n_i + n_i K_i E \tag{3.3}$$

where D_i is the free diffusion coefficient, n_i is the concentration of the species under investigation, K_i its mobility and E the electric field the species i experiences in the source due to the surrounding charged particles. The diffusion current is the sum of the free diffusion term and a mobility term.

Under conditions of ambipolar diffusion:

$$\Gamma_+ = \Gamma_e \equiv \Gamma_a \quad \text{and} \quad n_+ = n_e \equiv n_a \tag{3.4}$$

where Γ_+,Γ_e and Γ_a are the ion, electron and ambipolar diffusion currents and n_+,n_e and n_a the corresponding number density of each. The ambipolar diffusion current Γ_a, is thus given by:

$$\Gamma_a = \frac{D_+ K_e + D_e K_+}{K_+ + K_e} \nabla n_o \equiv D_a \nabla n_o \tag{3.5}$$

where K_e and K_+ are the mobility of the electron and positive ion. If one assumes the diffusion coefficient of the electron is much greater than the diffusion coefficient of the positive ion, $D_e >> D_+$ and by using the Einstein relationship:

$$K_i/D_i = e/k_BT \tag{3.6}$$

where k_B is the Boltzmann constant we can arrive at an approximation for D_a of:

$$D_a \simeq 2D_+ \tag{3.7}$$

This is observed in Figure 3.5 for the $CO^{+\cdot}$ion in Helium. The slope, and corresponding ambipolar diffusion coefficient, of the late B to C section is approximately twice that of the late aferglow region C to D of the free diffusion region.

3.9 Determination of Rate Constants

3.9(i) One Component Systems

Consider a one component system undergoing an association reaction with the formation of its dimer at constant pressure and temperature:

$$A^{+\cdot} + 2A \xrightarrow{k_1} A_2^{+\cdot} + A \tag{3.8}$$

$$A^{+\cdot} \xrightarrow[\text{diff}]{a'} \text{lost on walls} \tag{3.9}$$

Considering the rate of loss of the parent ion A^+; yields:

$$-\frac{d[A^{+\cdot}]}{dt} = k_1[A^{+\cdot}][A]^2 + a'[A^{+\cdot}] \tag{3.10}$$

letting $k_1' = k_1[A]^2$ and rearranging equation (3.10) gives:

$$-\frac{d[A^{+\cdot}]}{[A^{+\cdot}]} = (k_1[A]^2 + a')dt = (k_1' + a')dt \tag{3.11}$$

As the ion intensity $I(A^{+\cdot})$ is proportional to $[A^{+\cdot}]$, and by integrating the above expression we obtain:

$$I(A^{+\cdot})_t = I(A^{+\cdot})_{t=0} \exp[-(k_1' + a')t] \qquad (3.12)$$

Therefore a plot of ln $I(A^{+\cdot})t$ versus time should give a straight line over the whole of the later afterglow region, see Figure 3.5. The diffusive rate constant a' is inversely proportional to pressure, and k_1' is proportional to the square of the pressure. The slope of the afterglow region S from equation (3.12):

$$S = k_1' + a' \qquad (3.13)$$

can now be expressed in the form:

$$S = k_1[A]^2 + a/[A] \qquad (3.14)$$

Multiplying by [A] gives:

$$S[A] = k_1[A]^3 + a. \qquad (3.15)$$

Hence a plot of S[A] versus $[A]^3$ should be linear of gradient k_1 and intercept a. This has been investigated for the nitrogen system (see Figure 3.6 and Chapter five), and the values of k thus calculated at various temperatures. The back reaction:

$$A_2^{+\cdot} + A \xrightarrow[b']{k_2} A^{+\cdot} + 2A \qquad (3.16)$$

$$A^{+\cdot} \xrightarrow[diff]{} \text{lost on walls}$$

Fig. 3.6 SEPARATION OF N_2^+ REACTION RATE AND DIFFUSIVE LOSS CONSTANTS IN NITROGEN AT 548 K.

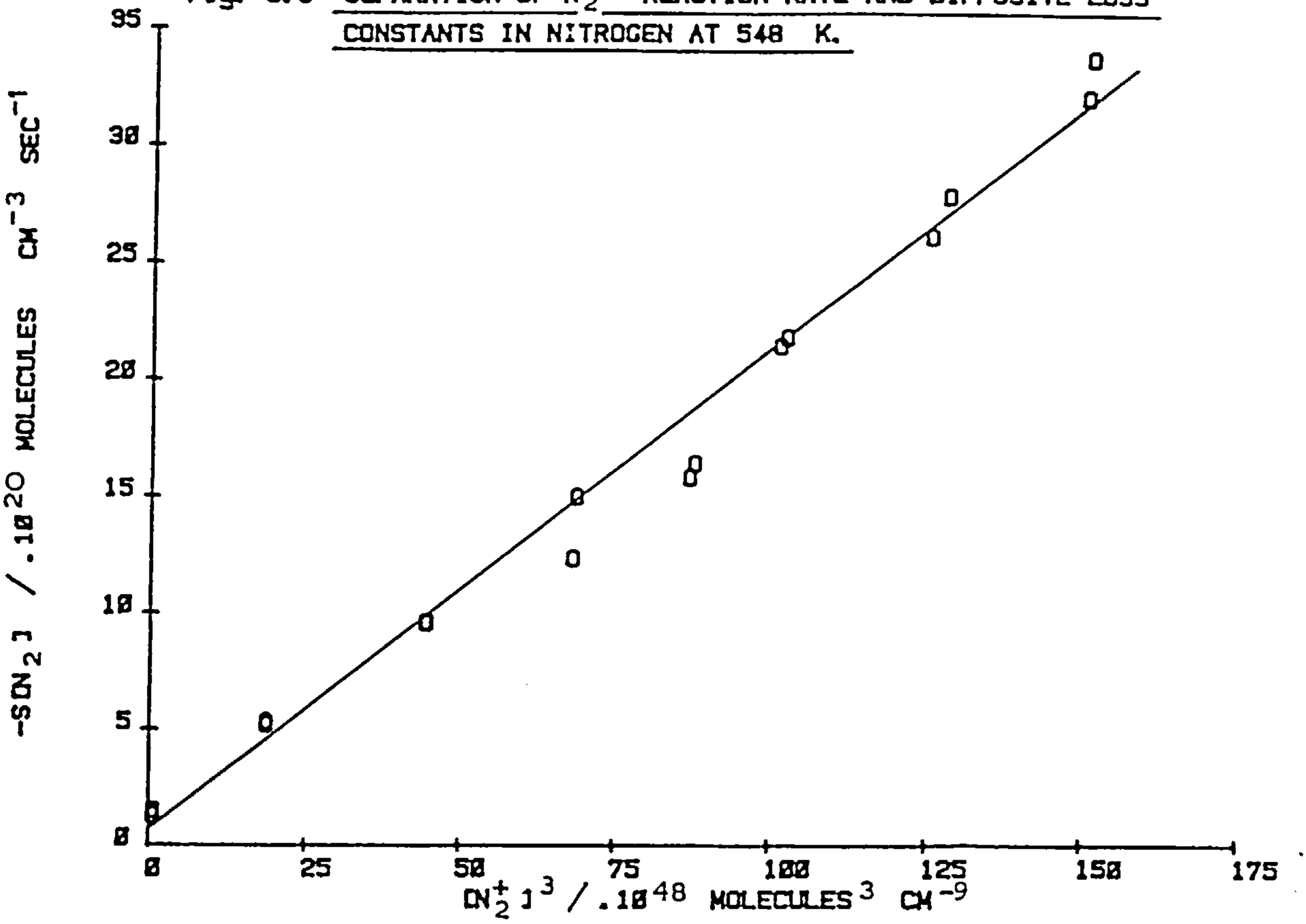

Fig. 3.7 SEPARATION OF CO^+ REACTION RATE AND DIFFUSION LOSS CONSTANTS IN HELIUM AT 400 K.

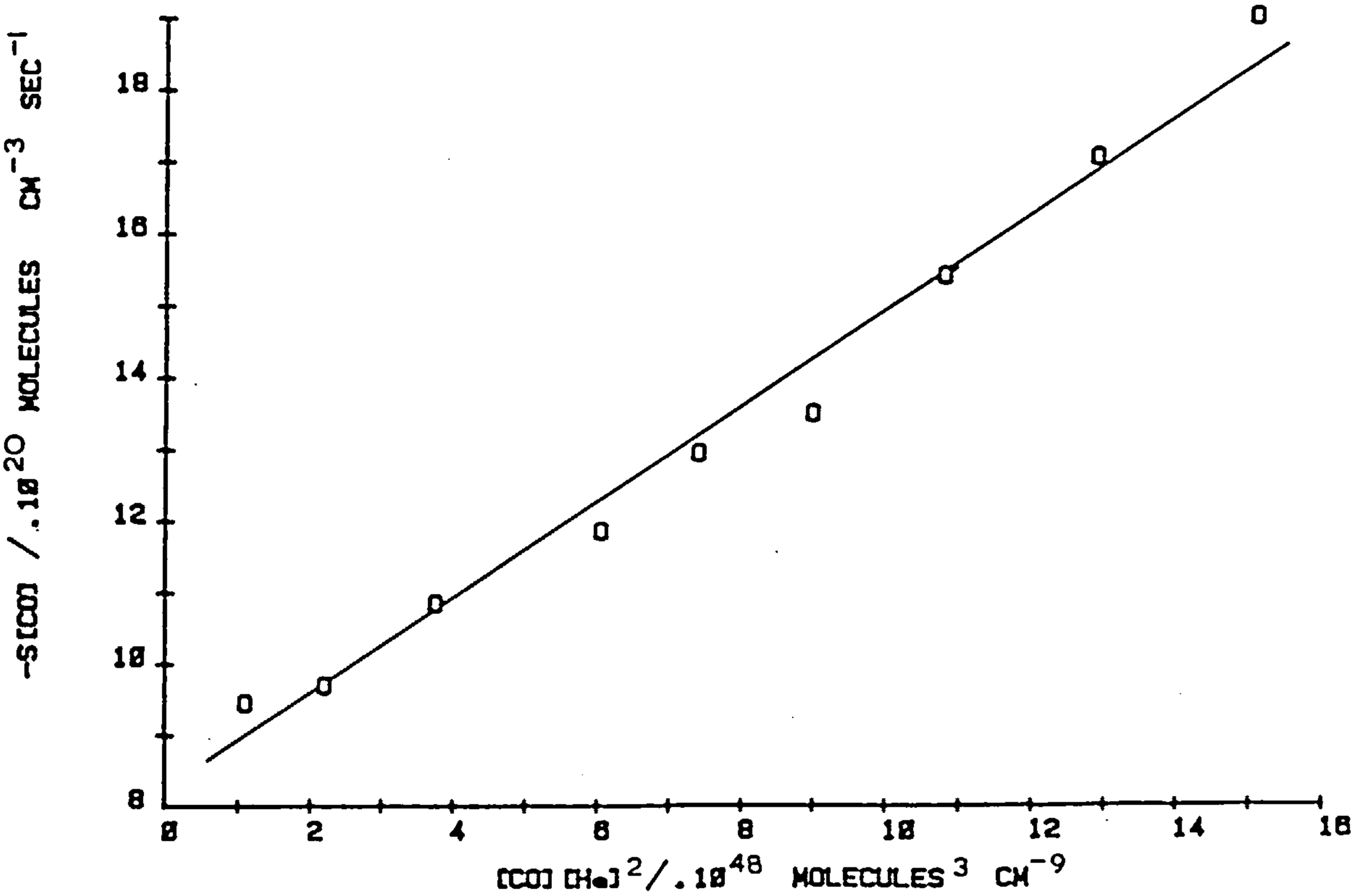

has also been investigated by a similar method. Using similar arguments to those used in the forward reaction, we arrive at the relationship:

$$S = k_2[A^2] + b/[A] \qquad (3.17)$$

Values of S at various pressures were measured and a plot of S[A] versus $[A]^2$ produced, (see Chapter 5 for this investigation).

3.9(ii) Two Component Systems

Considering a two component system where $A^{+\cdot}$ is undergoing an association reaction with A in a bath gas M:

$$A^{+\cdot} + A + M \xrightarrow{c'} A_2^{+\cdot} + M \qquad (3.18)$$

$$A^{+\cdot} \xrightarrow[(diff)]{} \text{lost on walls}$$

following the same scheme and considerations as in Section 3.9(i) we obtain the expressions:

$$-\frac{d[A^+]}{dt} = k_3[A^+][A][M] + c'[A^+] \qquad (3.19)$$

which on rearrangement and on integration yields:

$$I(A^+)_t = I(A^+)_{t=0} \exp[-(k_3' + c')] \qquad (3.20)$$

where $k_3' = k_3[A][M]$.

The slope derived from the plot of equation 3.20 is given by:

$$S = k_3' + c' = k_3[A][M] + c/([A] + [M]) \quad (3.21)$$

Rearranging yields:

$$S([A] + [M]) = k_3[A][M]([A] + [M]) + c \quad (3.22)$$

For all two component systems studied in this work the concentration of the species under interest, A, was under 1% of the total pressure. Hence $[A] + [M] \approx [M]$. This gives a new expression for equation (3.22) as:

$$S[M] = k_3[A][M]^2 + c \quad (3.23)$$

A plot of $S[M]$ versus $[A][M]^2$ is linear and shown in Figure (3.7) for the carbon monoxide association in helium.

The reverse reaction is similarly investigated and dealt with in Chapter six.

3.9(iii) Computer Treatment of Data

After collection of a peak profile on the multi-channel analyser, the data was transferred to the PDP-11 microcomputer. The program constructed for data manipulation was written in 'Digital' Basic language and consisted of four main sections:

(1) A section of the baseline before the start of the peak-region, normally about forty channels, was selected by the operator. This section was averaged, and the value obtained for the background noise was then subtracted from the remaining ion peak intensity. This was to obtain the true ion intensity above the baseline.

(2) Secondly the peak profile was displayed in a natural logorithmic form so as the late-afterglow exponential region, now a straight line section, could be seen more clearly (see Figure 3.5).

(3) A section of the late-afterglow region is now selected and its slope determined.

(4) The data was either saved on disc or output on a line printer.

3.10(i) Determination of Equilibrium Constants

Considering a one component system undergoing reaction:

$$A^{+\cdot} + 2A \xrightarrow{k_4} A_2^{+\cdot} + A \qquad (3.24)$$

$$A_2^{+\cdot} + A \xrightarrow{k_5} A^{+\cdot} + 2A \qquad (3.25)$$

$$A^{+\cdot} \xrightarrow[\text{(diff)}]{d'} \text{lost on wall} \qquad (3.26)$$

$$A_2^{+\cdot} \xrightarrow[\text{(diff)}]{e'} \text{lost on wall} \qquad (3.27)$$

If the back reaction (3.25) is sufficiently fast an equilibrium is established thus:

$$A^{+\cdot} + 2A \underset{}{\overset{Keq}{\rightleftharpoons}} A_2^{+\cdot} + A \qquad (3.28)$$

The concentration of the ionic species is again considered proportional to the ion intensities $I_A^{+\cdot}$ and $I_{A2}^{+\cdot}$ and the equilibrium constant Keq is defined as:

$$Keq = \frac{I_{A2}^{+\cdot}}{I_A^{+\cdot}} \cdot \frac{1}{[A]} \cdot \frac{S_A^{+\cdot}}{S_{A2}^{+\cdot}} \qquad (3.29)$$

where $^1/[A]$ is the mole ratio of the neutral parent species and $S_A^{+\cdot}$ and $S_{A2}^{+\cdot}$ is the number of sweeps over which the data profiles were collected.

Equilibrium is known to be established when the ratio of the ion intensities becomes constant with respect to time (see Figure 3.8). An equilibrium constant is also found to be pressure independent, see Chapter five for examples. The same expression may also be used for two component systems.

3.10(ii) Computer Treatment of Raw Data

After both peak profiles for the system in equilibrium had been collected on the MCA, they were both transferred over to the Minc for computer manipulation.

(1) First a baseline intensity was determined from the first forty channel counts for both profiles and subtracted to give the true ion intensity.

(2) Secondly, the time of flight was calculated for each ionic species and each profile shifted the appropriate number of channels to compensate for this. This is necessary so as the true ion intensity at equivalent reaction times were compared.

(3) A section of the afterglow region was selected and the ion intensity ratio determined over this section.

(4) The average ion intensity in the plateau region was selected and Keq determined from expression (3.29).

(5) The data was either saved on disc or plotted out on a printer.

3.10(iii) Thermodynamic Data

Once equilbrium has been established for an ion-molecule system at various temperatures the standard heat of formation of the association product ΔH^o, can be determined from the van't Hoff equation:

$$\ln K = \frac{-\Delta H^o}{RT} + \frac{\Delta S^o}{R} \qquad (3.30)$$

Fig. 3.8 SELECTED REGION OF THE $CO^{+\cdot}$ AND $(CO)_2^{+\cdot}$ PEAK PROFILES FOR EQUILIBRIUM DETERMINATION.

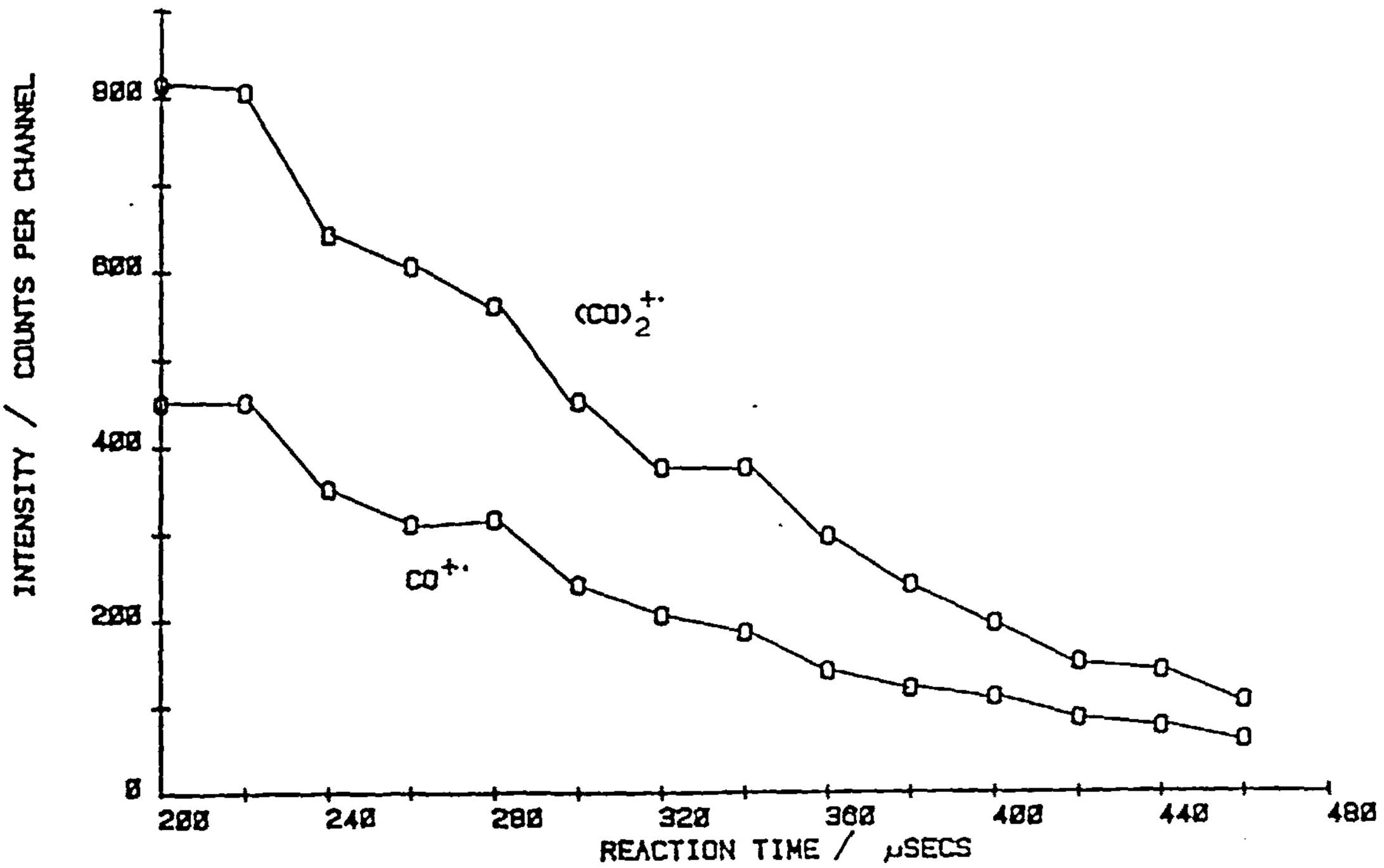

CORRESPONDING ION INTENSITY RATIO $[I_{(CO)_2^{+\cdot}} / I_{CO^{+\cdot}}]$ FOR ABOVE REGION.

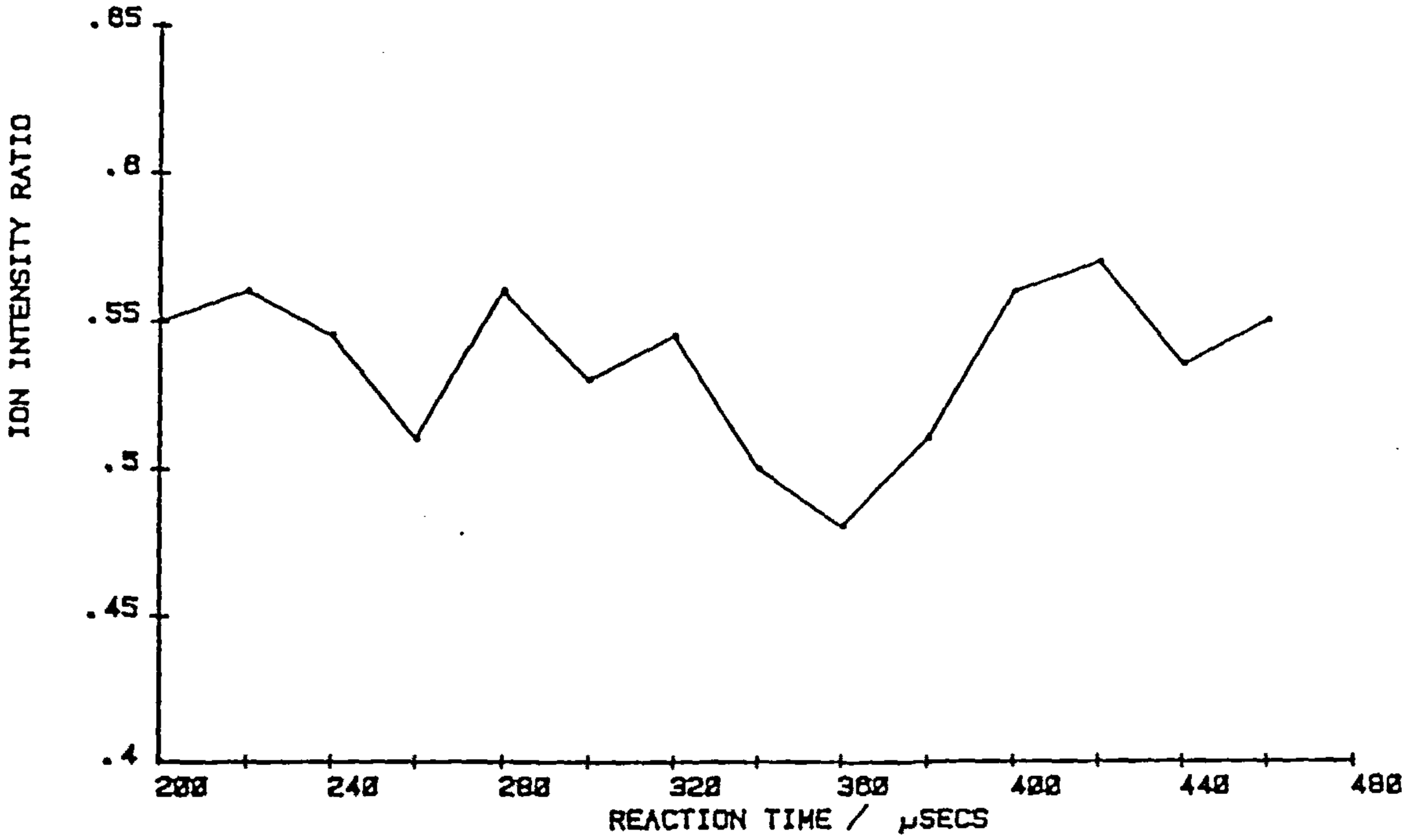

A plot of ln K versus $^{1}/T$ is linear with a slope of $-\Delta H^{o}/R$, where R is the molar gas constant. The intercept $\Delta S^{o}/R$ yields ΔS^{o} the corresponding entropy change for the reaction, (see Chapter five).

Chapter Four

The High Pressure Pulsed Electron Beam Drift Source, Instrumentation and Treatment of Data

4. 1 Introduction

A new mass spectrometer ion source has been constructed to study high pressure ion molecule kinetics and equilibria as a function of temperature. Controversy still exists regarding the temperature dependence of association reactions since it is not unknown for different experimental techniques, such as those discussed in chapter two, to produce conflicting data. This drift ion source built at Warwick is based on a version presently used by Bowers et al[73], which itself was modelled on a version first developed by Illies and Meisels[74]. From the drift ion source, ion arrival time spectra, ion velocities, diffusion coefficients and reaction rates can be determined.

4.2 The Pulsed High Pressure Drift Ion Source

This new ion source was built for use in conjunction with the MS9 mass spectrometer (Kratos Analytical Ltd), previously described in chapter three, and by making use of existing source flanges. A schematic diagram of the source is shown in Figure 4.1. The source is cylindrically symmetrical with an inside diameter of 1.42cm and a drift length of 2.03cm. The electron entrance and ion exit apertures are holes of 0.04cm diameter. The ion exit or ion extraction plate was made out of a phosphor-bronze alloy of 0.05cm thickness. The whole source block assembly including focusing and mounting plates were constructed out of stainless steel.The internal source pressure led to conditions where the ions drift through the source at a constant velocity.

The source temperature is varied by four cylindrical heaters 3.35cm by 0.3cm diameter positioned in the aligning holes of the block. The temperature range from 300 to 610K is controlled with the aid of a platinum resistance temperature sensor connected to one side of

Figure 4.1. Cross Sectional Diagram of the High Pressure Drift Source.

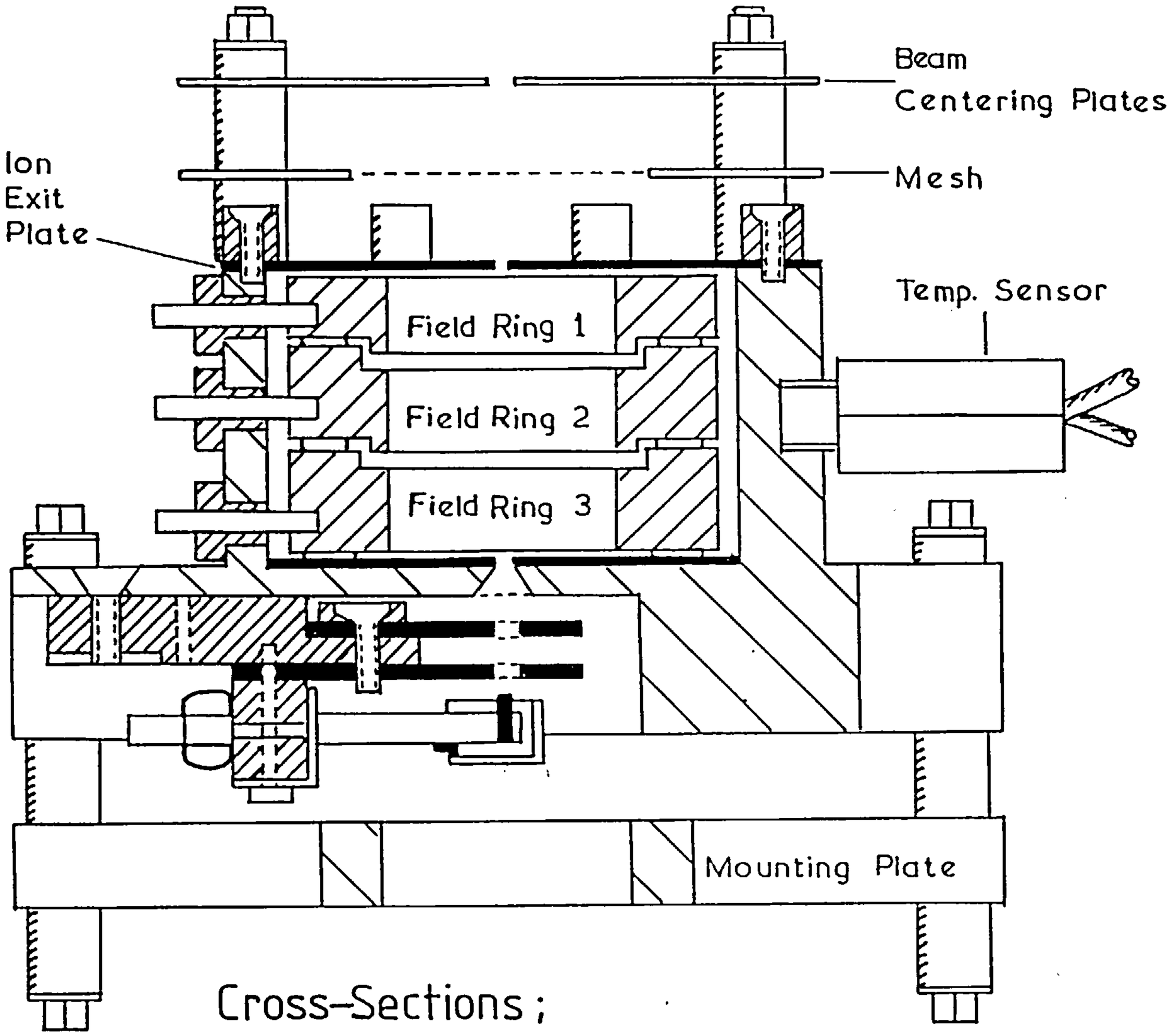

Cross-Sections ;

Ion Exit, Electron Entrance, Focus 1 and Focus 2.

Source Block and Mounting Plate.

Copper Field Rings.

'Vespel' and Ceramic Spacers.

the block. Extensive testing of the block was performed to measure for possible temperature gradients. The largest difference was found between the ion exit and the filament sides of the block due to heating effects from the filament. This effect decreased with increasing block temperatures from a maximum of 3 degrees at 300K to only one degree at 600K. This error was taken into account in all subsequent calculations and experiments.

The pressure range of the source is from 0.3 to 1.5 Torr and was measured by the aid of a capacitance manometer connected directly to the source, and controlled by an automatic needle valve (see chapter three).

To obtain the constant potential gradient across the ion chamber a resistor chain was employed and connected between the ion extraction plate, the field guard rings and the source body, as shown in Figure 4.2a. The 'conventional' repeller plate supplies of -10 to +30 Volts, from the mass spectrometer console were used to obtain the drift field. This allowed field strengths of +15 to -5Vcm^{-1} to be obtained and proved sufficient for the systems subsequently studied. A computer simulation of the internal source field was modelled using the SIMION ion trajectory/potential line plotting program[75]. For a typical drift field of 5Vcm^{-1} the obtained field potential lines are shown in Figure 4.2b. The good linearity and parallel spacing of these potential lines in the centre of the chamber show that the ions produced in this region will experience a uniform field gradient as they traverse between the electron entrance and ion extraction plate.

4.3 Source Operation

The experimental technique used is identical to that described in chapter 3.6. Data collection is carried out on a multichannel analyser as before, but treatment of data to deduce kinetic information is different. Several parameters such as filament source voltage, drift voltage and optimum pressure range for operation had to be determined before any reactive systems could be investigated, and it is the evaluation of these that is described in the next section.

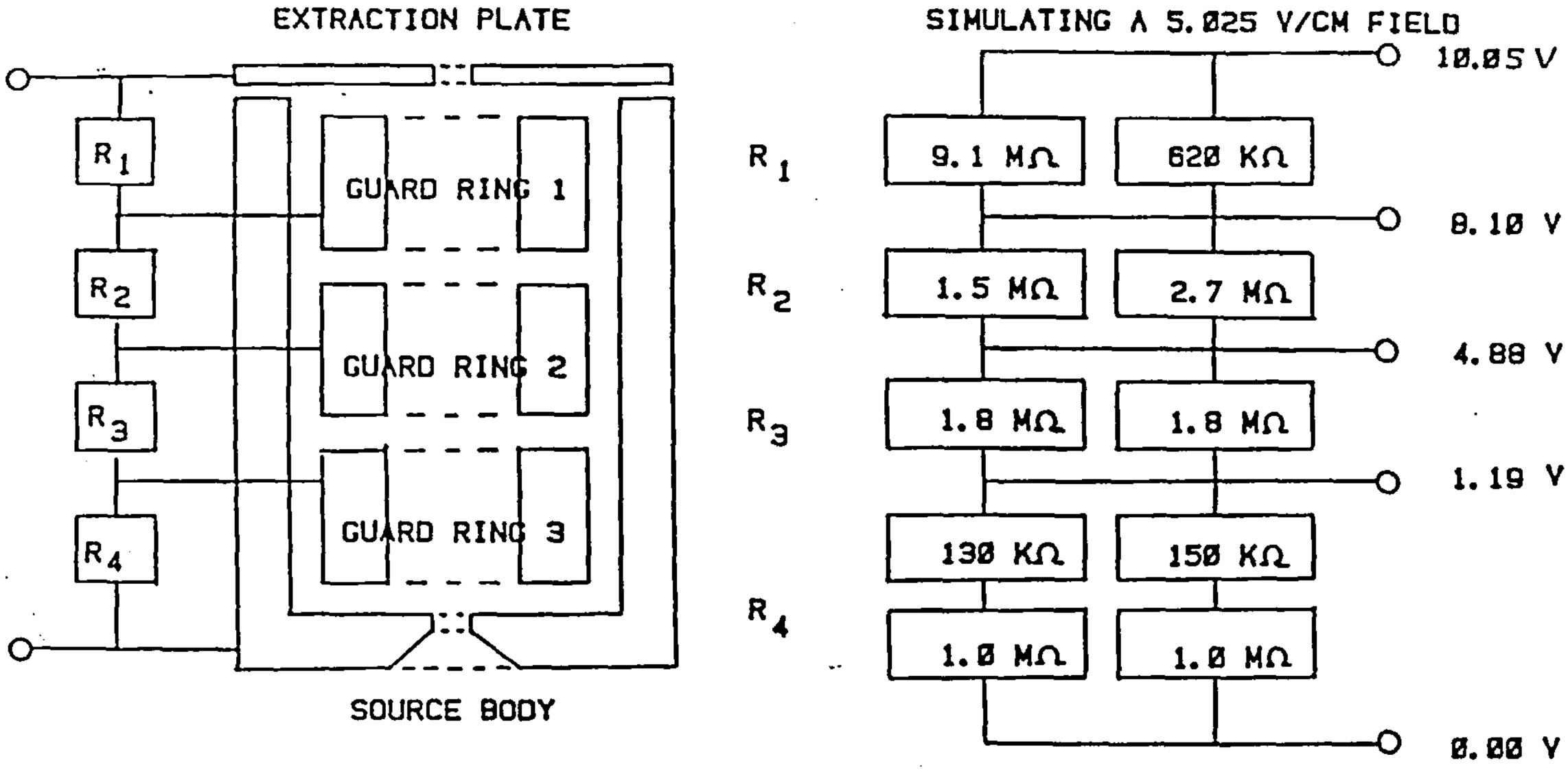

$R_1 \equiv 580\ K\Omega$
$R_2 \equiv 971\ K\Omega$
$R_3 \equiv 928\ K\Omega$
$R_4 \equiv 570\ K\Omega$

Fig. 4.2a DROPPING RESISTORS USED TO OBTAIN CONSTANT POTENTIAL GRADIENT ACROSS SOURCE.

fig.4.2b: Equipotential lines obtained for the Drift Source for an extraction Field of $5\ V\ cm^{-1}$ [Drift length = 2cm]

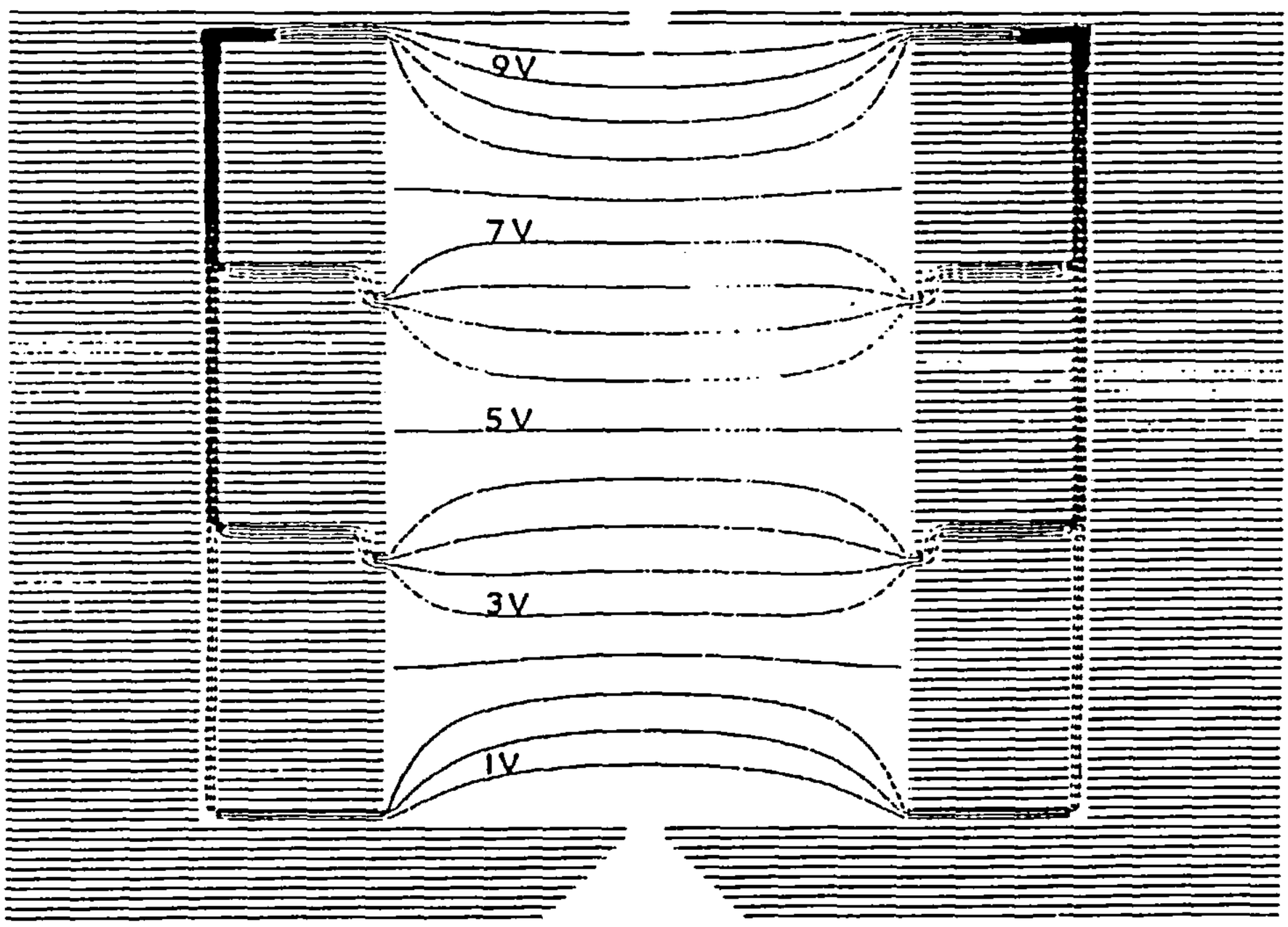

4.4 Drift Source Testing

The drift velocity v_d of an ion moving through a neutral gas under the influence of an electric field E is directly proportional to the field strength:

$$v_d = K.E \qquad (4.1)$$

where K the proportionality constant is known as the ion mobility[76]. The mobility of an ion in a gas can be calculated in this ion source by examining the residence time distribution using the relationship:

$$K = v_d/E = (z/t_d)/E \qquad (4.2)$$

where z is the drift distance and t_d is the average drift or residence time, see chapter seven. The drift distance is defined as the separation between the electron entrance and ion-exit plates and is known exactly from the source dimensions. Under normal source operation the electron beam is pulsed so as to obtain an arrival time distribution, an example is shown for the Ar^+ in argon system as a function of extraction field in Figure 4.3. As the extraction field is reduced the beam intensity decreases as the ions spend more time in the reaction chamber and hence their chances of neutralisation increase. These spectra also illustrate the increasing effects of peak broadening by longitudinal diffusion (i.e. the diffusion along the direction of the applied field) and intensity loss due to transverse diffusion as the effective drift distance is increased (i.e. E is decreased). In general, deviations from the peak shape shown in Figure 4.3 are to be expected if the detected species undergoes reaction at a significant rate as it drifts through the gas, or if the detected ion is a secondary species formed by reaction of the primary ions along the drift length[76].The distribution is essentially symmetrical with only a 5% spread of ion intensity towards longer times. Therefore, we can take the peak maximum as an indication of the average arrival time of the ions. The quantity measured in these

Figure 4.3. Experimental Residence Time Distributions of $Ar^{+\cdot}$ in Argon as a Function of Field Strength at 200 °C and 0·49 torr.

PEAK	ELECTRIC FIELD V/CM
a	4·70
b	4·30
c	3·89
d	3·46
e	3·05
f	2·63
g	2·15
h	1·82

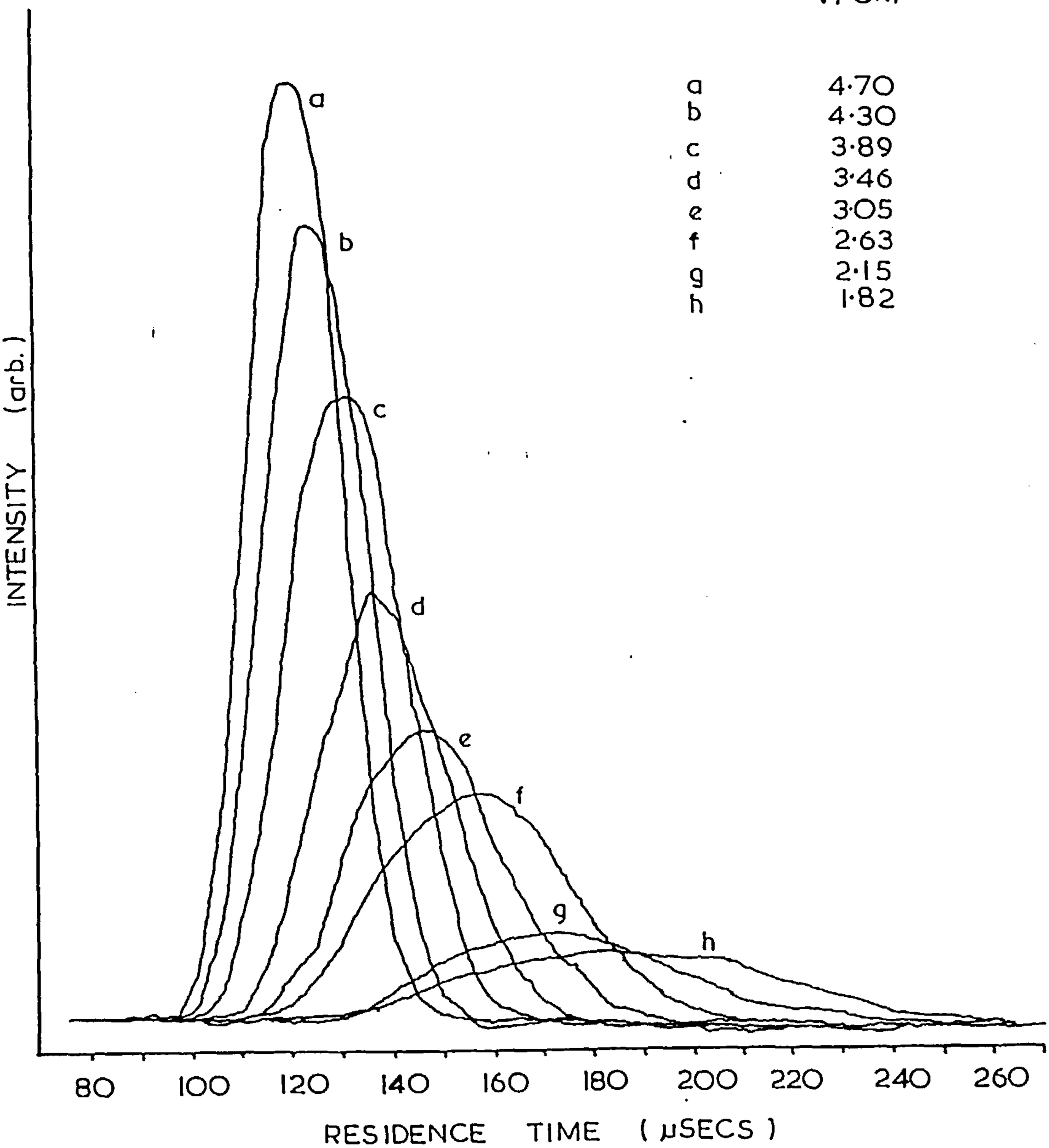

experiments is comprised of the average drift time t_d, and the analyser time t_a, which includes the ion's time of flight through the mass spectrometer and any electronic delays. This analyser time must be measured and subtracted from the observed arrival time average to obtain the true residence time. To find t_a, the source was set at low operating pressure and high electron energy(~0.05 Torr and 500eV). Under these conditions ionisation takes place throughout the source chamber and ions formed at the exit plate spend no time in the source. Their arrival time, which shows up as a sharp increase in intensity in the peak profile, corresponds to their time of flight.

The drift velocity is also given by equation 4.3[77]:

$$v_d = z/t_d = K_o(760.E/P)(T/273) \qquad (4.3)$$

where K_o is the reduced mobility of the ion, see chapter seven, P is the source chamber pressure in Torr and T the temperature in Kelvin. Under low field conditions the calculations of Wannier[78] shows that v_d and the ratio E/P remain directly proportional to each other and the expression 4.3 is valid. A plot of the average arrival time versus $(E/P)^{-1}$ has an intercept which corresponds to the time of flight of the ion under investigation. Figure 4.4 illustrates this for the $Ar^{+\cdot}$ in argon system at various source pressures. The plot has an intercept corresponding to a time of flight of 13.6 μsecs which is in good agreement with the calculated result of 10.7 μsecs from equation 2.2.

The ion intensity-residence time profiles were found to be dependent on the ionising electron energy, Figure 4.5, showing the observed change over just a small electron-volt range. The profile's geometrical centre along the time axis is found to coincide with the peak maximum only in the small energy range of 16 to 19 eV. At higher beam energies the electrons penetrate further into the ion chamber and the peak maxima consequently now occur at lower residence times. The opposite effect is found for a variation in the time duration of the electron pulse. As the electron pulse becomes longer the $Ar^{+\cdot}$ peak profile

Fig. 4.4 EVALUATION OF TRANSIT TIME FOR $Ar^{+\cdot}$ IN ARGON AT 416 K USING 15.5 eV ELECTRONS FROM 0.25 TO 1.00 TORR.

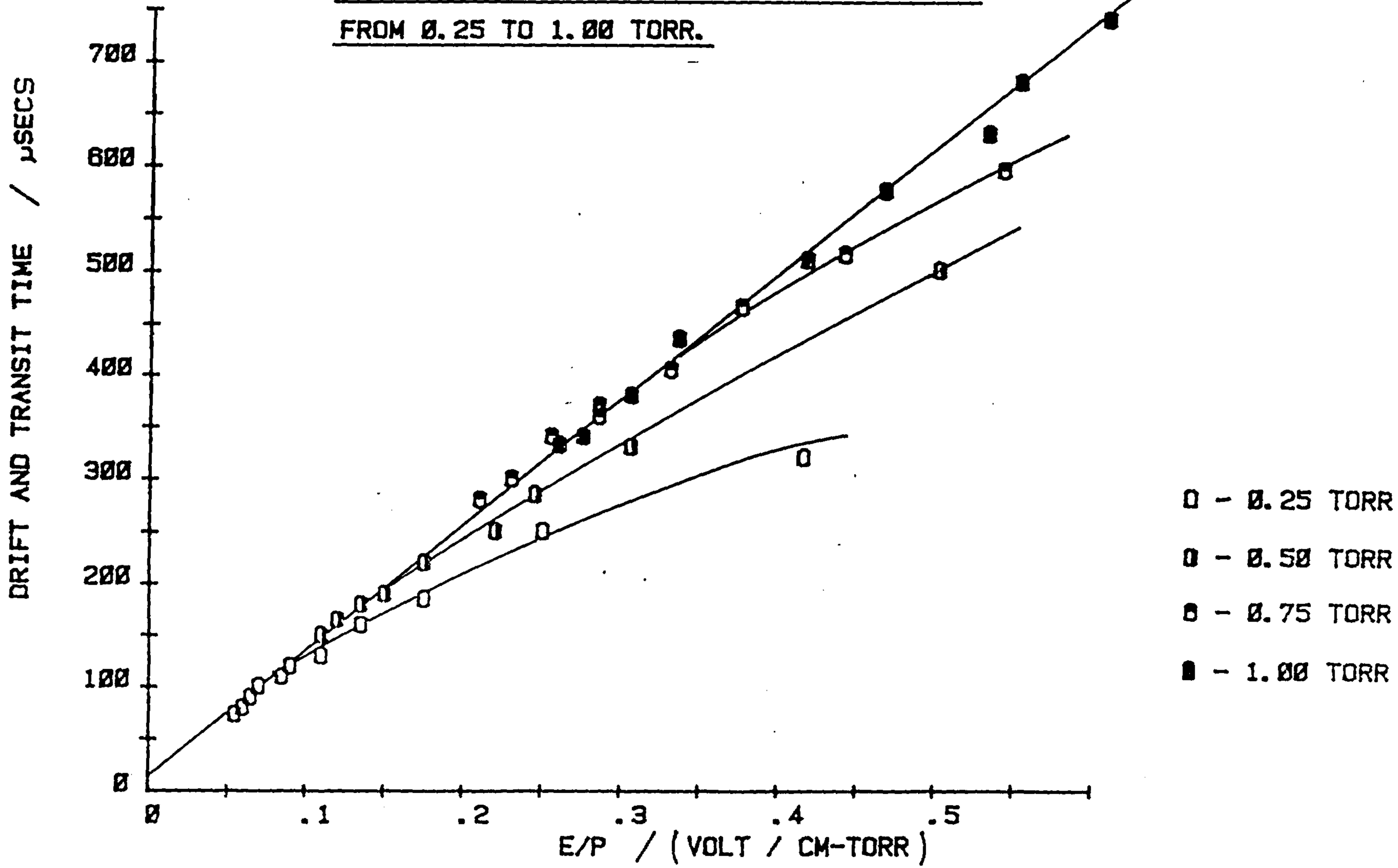

Fig. 4.5a RESIDENCE TIME OF Ar^{+}'ve ELECTRON VOLTS AT 0.5 TORR 386 K AND E=4.70 V/CM

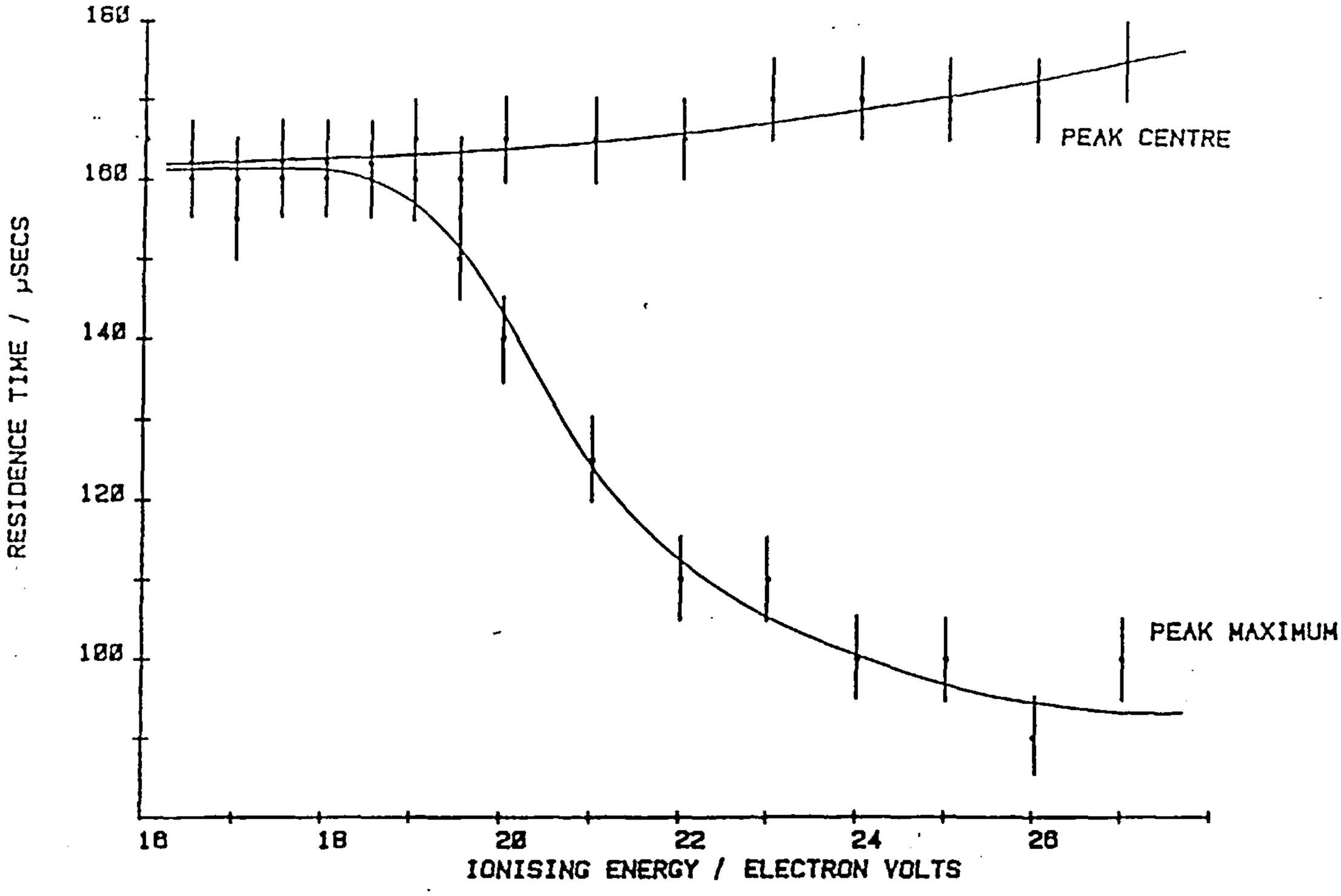

4.5b VARIATION IN PEAK PROFILE WITH RESPECT TO IONISING ENERGY.

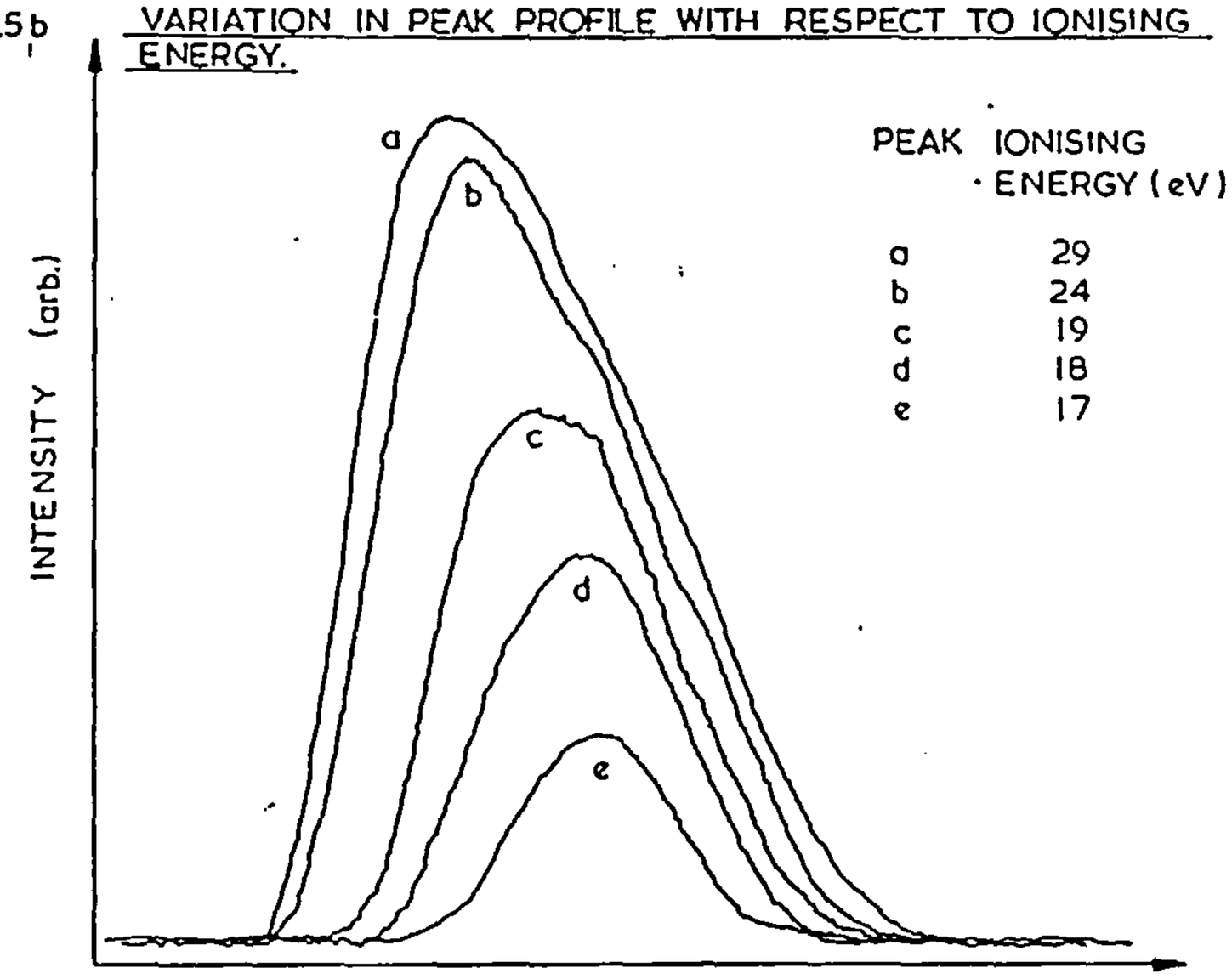

broadens such that now the peak maxima and geometric centre occur at higher residence times, see Figure 4.6. Thus it can be observed that the maxima and geometric centre of the time profiles coincide at the same residence time only when small pulse widths and low energy ionising electrons are used.

The variation in t_d against source pressure over the small operating energy range is illustrated in Figures 4.7 and 4.8. No significant difference can be observed over this pressure range in the Ar^+ residence time, although a marked difference in the ion beam intensity was noted, Figure 4.8. Throughout all experiments conducted in the drift source in order to keep electron penetration to a minimum ionising energies of 16 to 18eV and pulse widths of 5 to 10μsecs were employed. Operating at these low energies also ensures that secondary electrons have an insufficient energy to cause further ionisation in the chamber.

The variation in the measured drift velocities of $Ar^{+\cdot}$ in argon with increasing E/P for various argon pressures is shown in Figure 4.9. The solid line was obtained for measurements at high source pressures of 1.25 and 1.50 Torr. The data at 1.0 Torr agree very well with the other high pressure results. For low pressures the apparent drift velocities at low values of E/P deviate from the expected values. At the higher E/P values however, the measured velocities agree well with the high pressure results. These results established a lower limit of the order of 0.5 Torr for the source operating pressure to obtain reliable measurements. It is possible to operate at pressures below this limit as measurements at high E/P values indicate that equation 4.3 still holds. This is also observed in Figure 4.4 where the measured time average is plotted against $(E/P)^{-1}$ for $Ar^{+\cdot}$ in argon. At 0.25 Torr significant deviations from the higher pressures results are observed at low values of E/P. This trend is also observed although at a decreasing amount for both the 0.5 and 0.75 Torr results. The consequence of this was that during the drift source operation the highest possible source pressure was always used so as to minimise this effect.

Fig. 4.6a EFFECT OF ELECTRON PULSE WIDTH ON PEAK SHAPE.

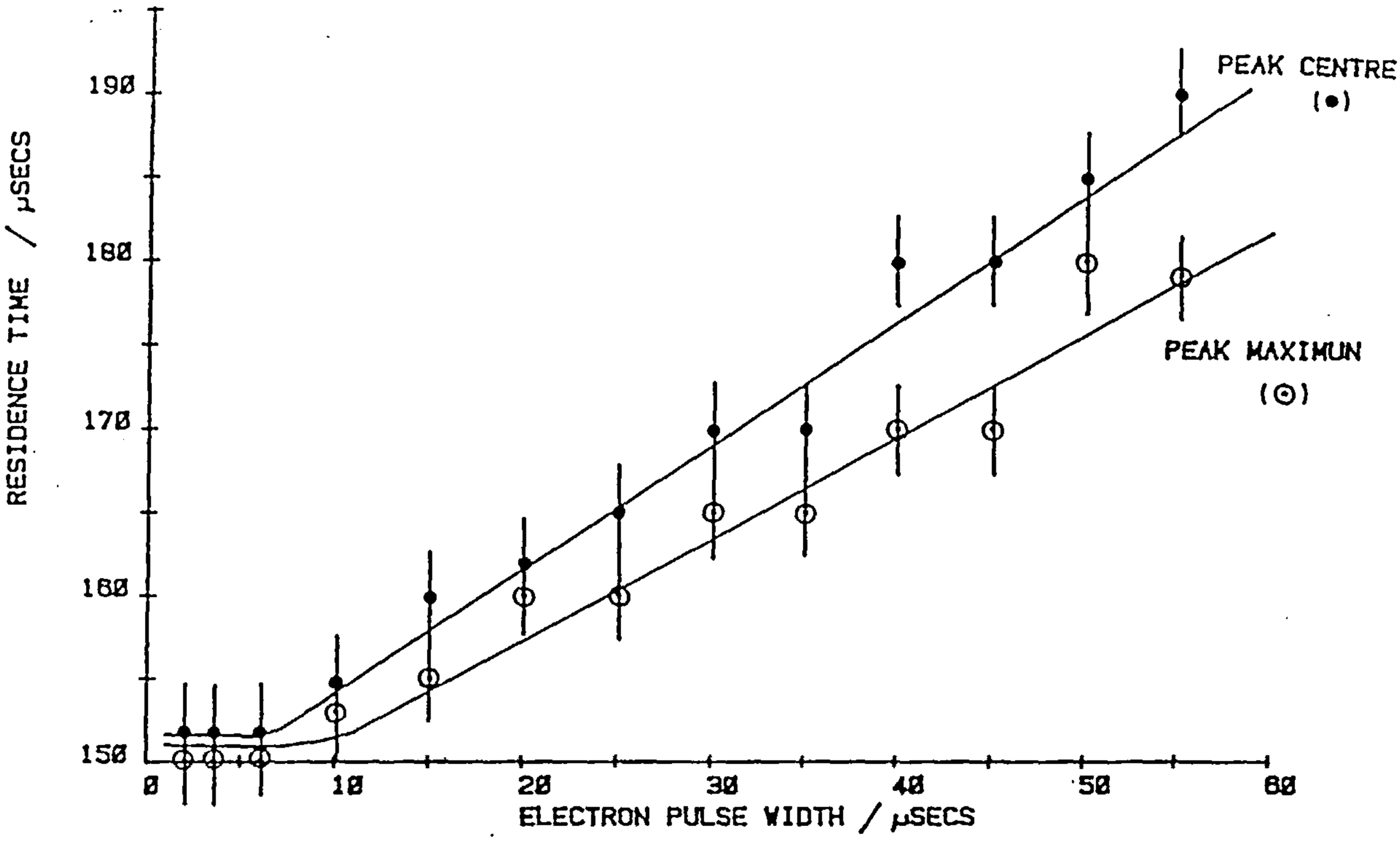

4.6 b VARIATION IN PEAK PROFILE WITH RESPECT TO IONISING ELECTRON PULSE DURATION.

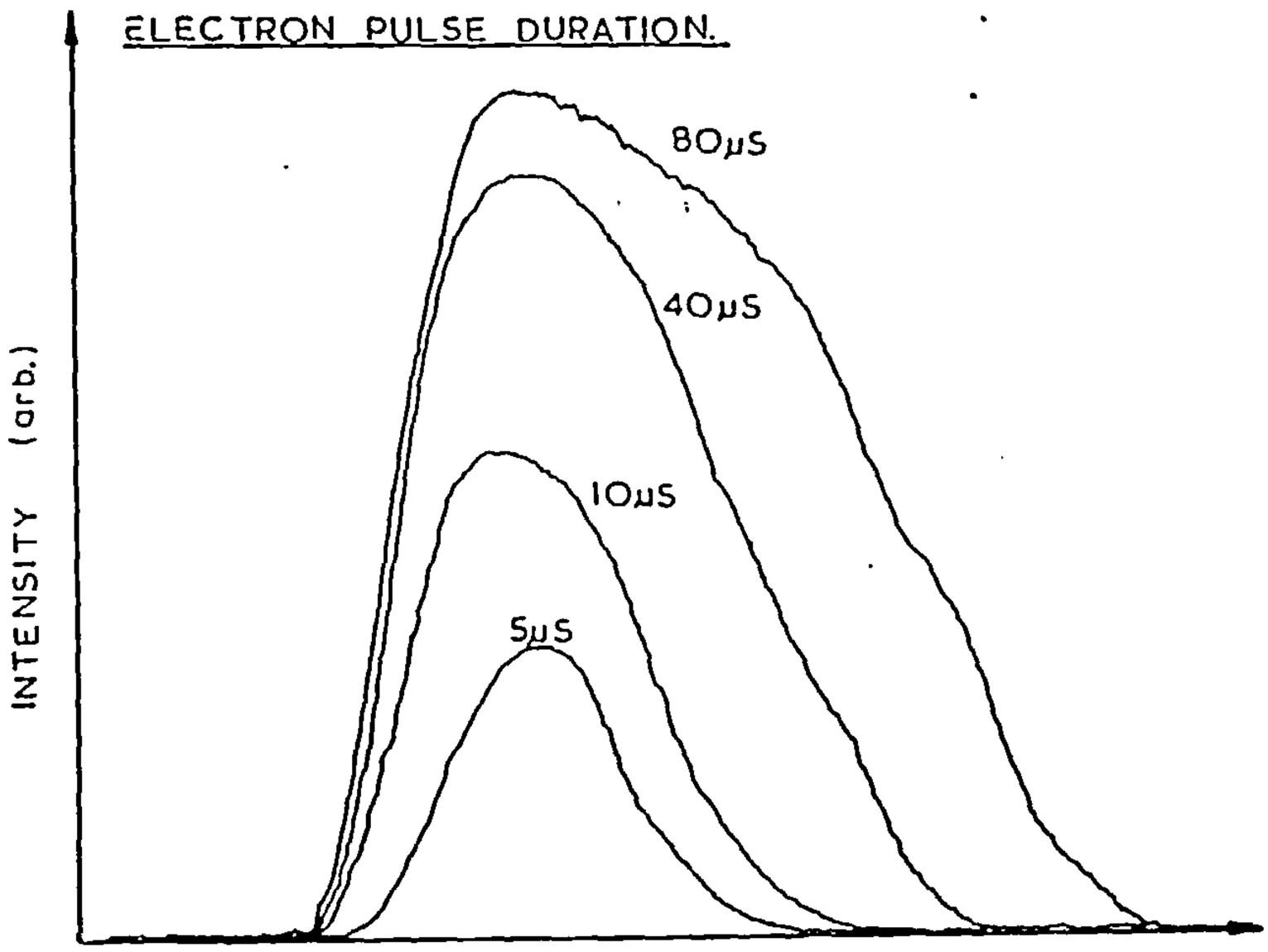

Fig. 4.7 RESIDENCE TIME vs PRESSURE FOR $Ar^{+\cdot}$ IN ARGON FOR DIFFERENT IONISING ENERGIES AT 380 K AND A FIELD STRENGTH OF 4.78 V/CM.

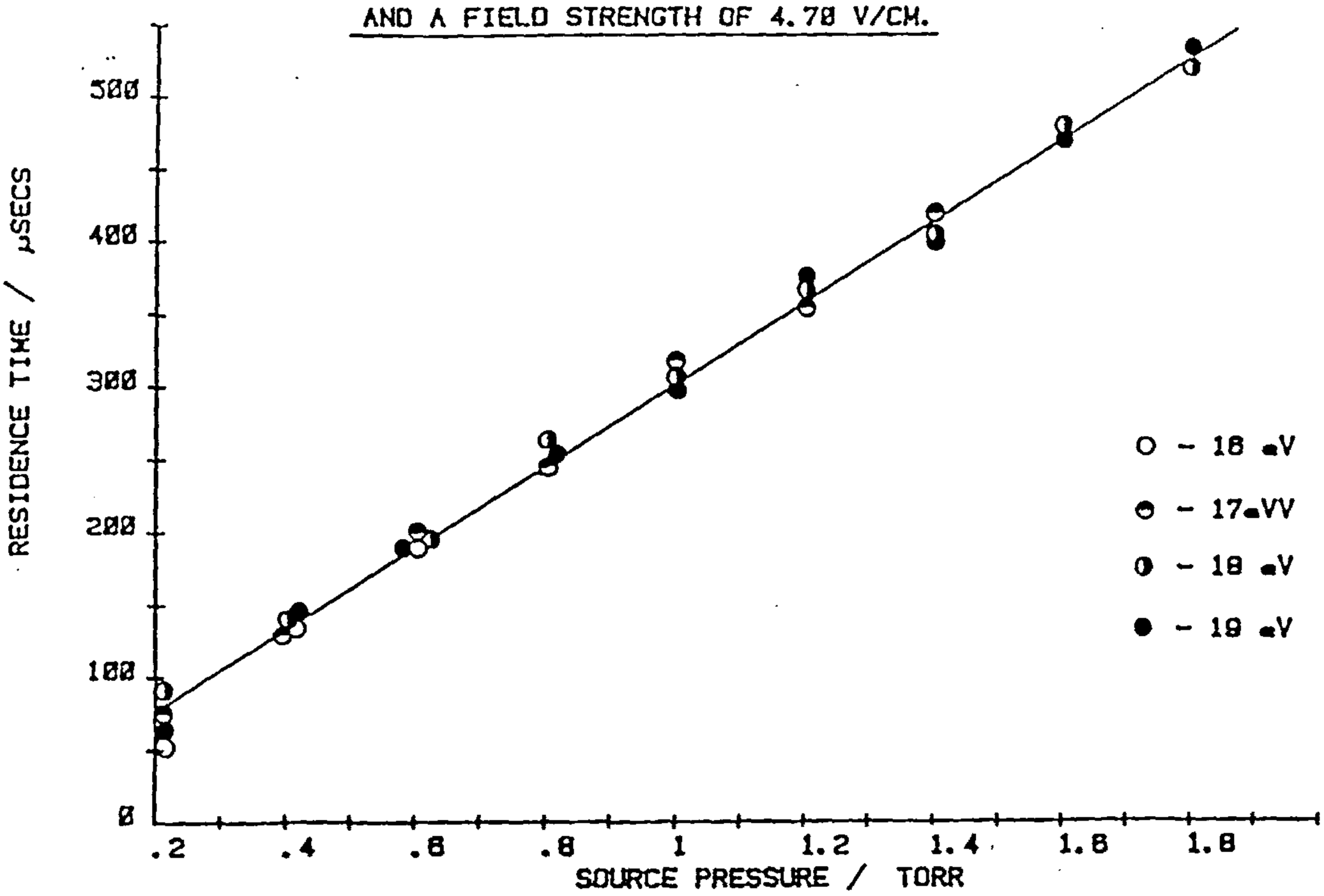

fig. 4.8

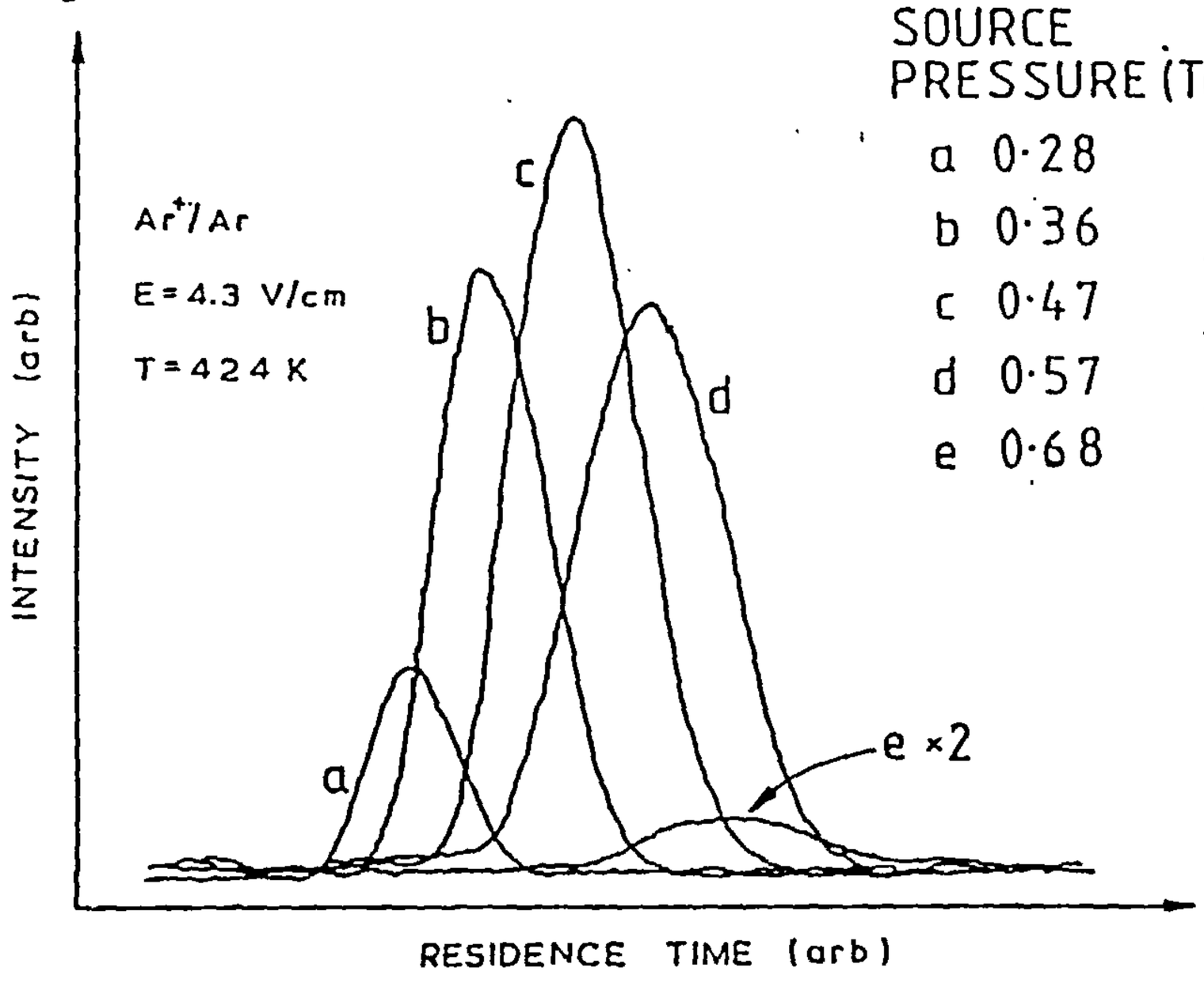

SOURCE PRESSURE (Torr)

a 0·28
b 0·36
c 0·47
d 0·57
e 0·68

Variation in Peak Profil
Intensity with respect t
Source Pressure.

Fig. 4.9 MEASURED DRIFT VELOCITIES WITH INCREASING VALUES OF E/P FOR $Ar^{+\cdot}$ IN ARGON AT 415 K USING 15.5 eV ELECTRONS.

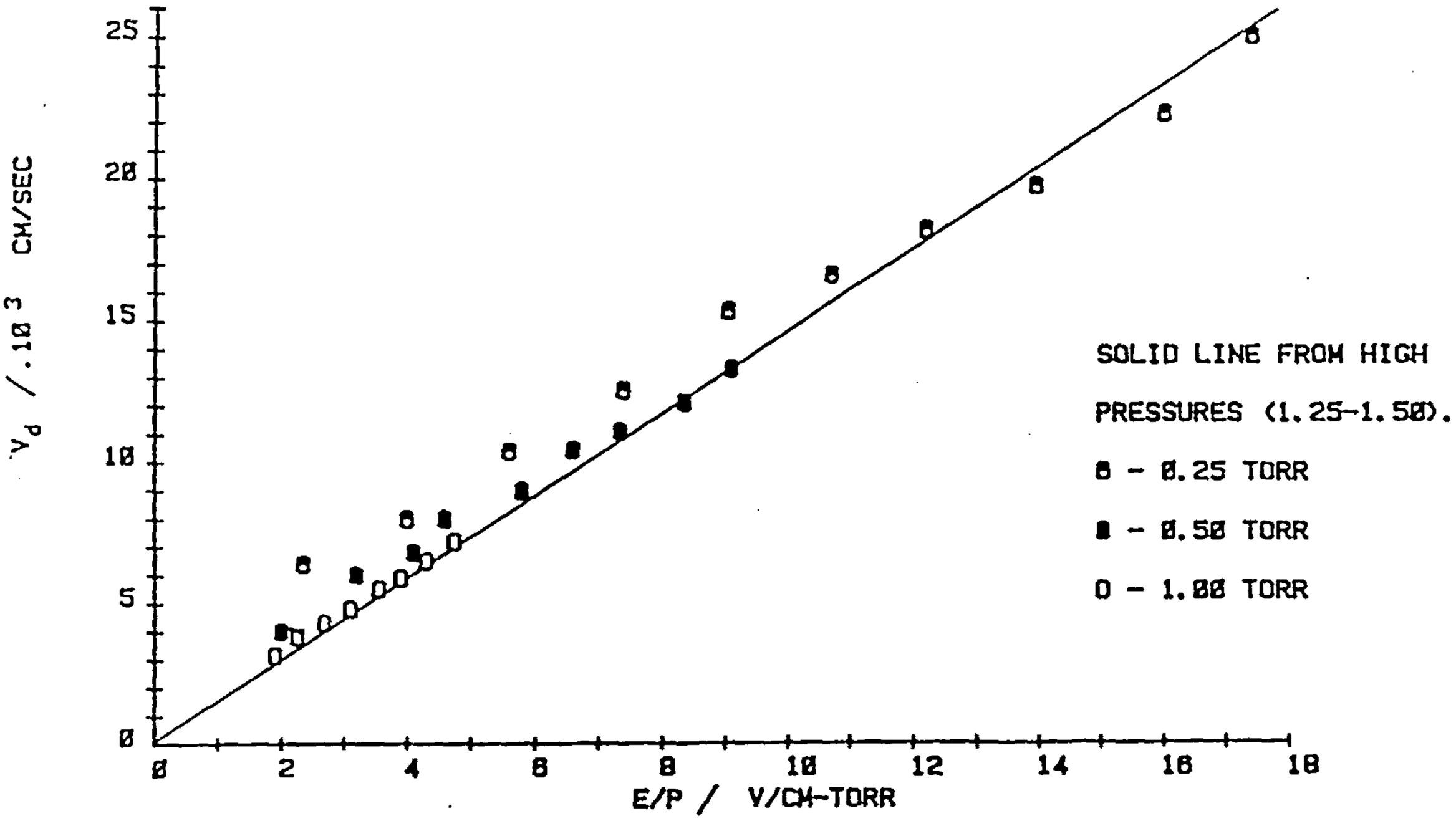

Fig. 4.10 EVALUATION OF RATE CONSTANTS FOR THE NITROGEN ASSOCIATION FROM DRIFT SOURCE RESIDENCE TIME DISTRIBUTIONS.

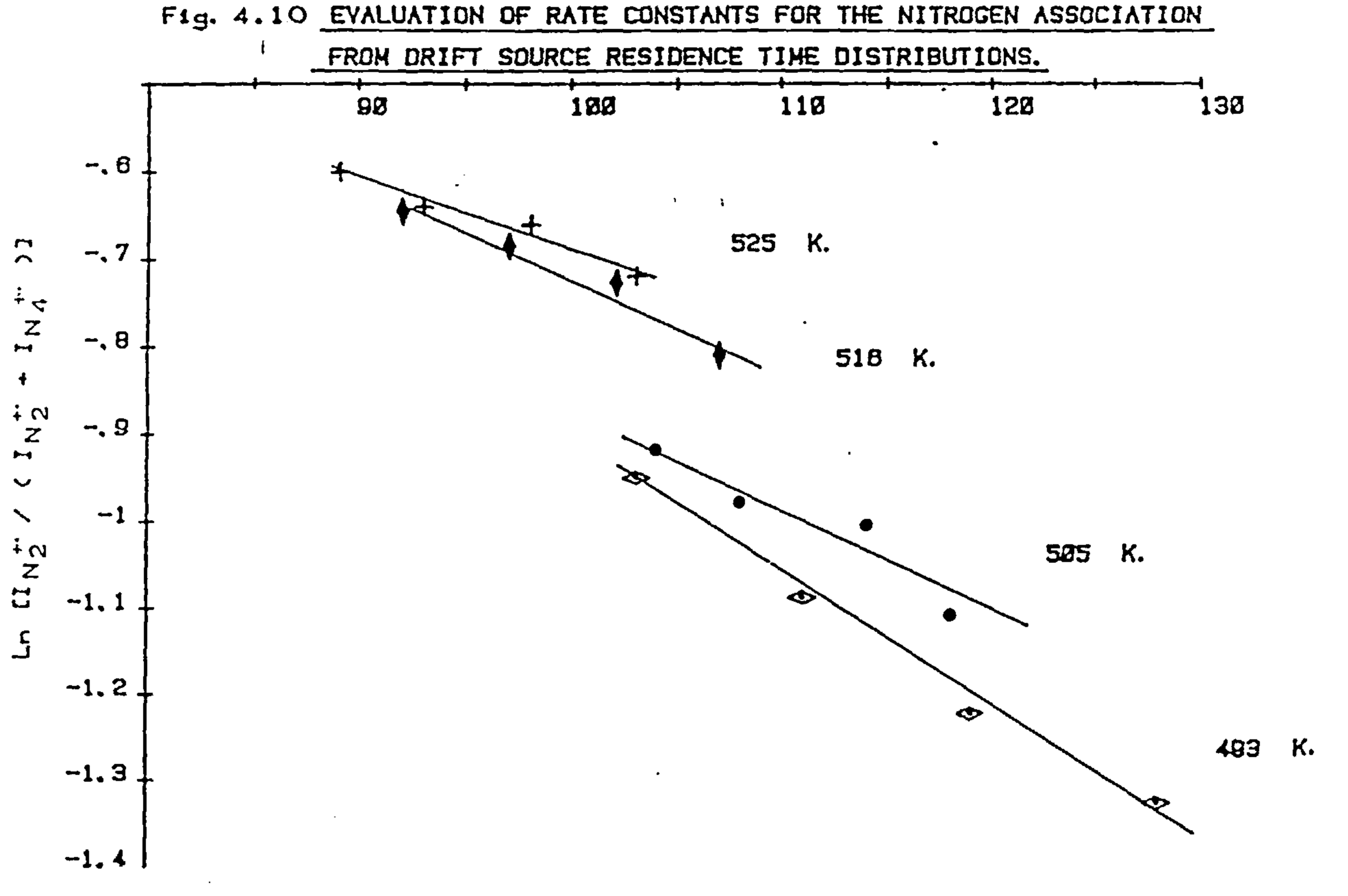

4.5 Measurement of Rate Constants

The original purpose for building the drift source was to measure the temperature variation of ion-molecule reaction rate and equilibrium constants. To obtain the rate constant of a particular system requires measuring how far a reaction has proceeded as a function of time, the measured ion source residence time.

Consider the following one component system:

$$A^{+\cdot} + 2A \xrightarrow{k_3} A_2^{+\cdot} + A \qquad (4.4)$$

The reaction mechanism is normally regarded as a two step process in which an energy-rich dimer is collisionally-stabilized:

$$A^{+\cdot} + A \underset{k_b}{\overset{k_a}{\rightleftharpoons}} (A_2^{+})^* \qquad (4.5)$$

$$(A_2^{+})^* + A \xrightarrow{k_s} A_2^{+\cdot} + A$$

Applying the steady state approximation to the intermediate species $(A_2^{+})^*$ yields:

$$d[(A_2^{+})^*]/dt = k_a[A^+][A] - k_b[(A_2^{+})^*] - k_s[(A_2^{+})^*][A] \approx O \qquad (4.6)$$

$$\therefore \quad [(A_2^{+})^*] = \frac{k_a[A+][A]}{k_b + k_s[A]} \qquad (4.7)$$

The rate of loss of the initial ionic species $A^{+\cdot}$ can be described as:

$$-\frac{d[A^+]}{dt} = k_a[A^+][A] - k_b[(A_2^{+})^*] - k_c[A^+] = \frac{k_b k_a[A+][A]}{k_b + k_s[A]} \qquad (4.8)$$

Rearranging this expression gives:

$$-\frac{d[A^+]}{[A^+]} = k_a[A] - \frac{k_b k_a[A]}{k_b + k_s[A]}\,dt \qquad (4.9)$$

Integrating this expression and noting that when t = O, $[A^+]_t = [A^+]_o$ yields:

$$\log([A^+]_t/([A^+]_o) = \left(k_a[A] - \frac{k_b k_a[A]}{k_b + k_s[A]}\right) t \qquad (4.10)$$

This expression may be simplified to:

$$\log([A^+]_t/[A^+]_o) = \frac{k_a k_s[A]^2 t}{k_b + k_s[A]} \qquad (4.11)$$

As the only ionic species formed in the source are the parent ion and its dimer, $[A^+]_o$ may be expressed as:

$$[A^+]_o = [A^+]_t + [A_2^+]_t \qquad (4.12)$$

At low pressure the assumption that $k_b >> k_s[A]$ is valid leads to the simplification of (4.12) to:

$$\log\left[\frac{[A^+]_t}{[A^+]_t + [A_2^+]_t}\right] = \frac{k_a k_s}{k_b}[A]^2 t \qquad (4.13)$$

Thus, a plot of $\ln([A^+]/([A^+] + [A_2^+))$ versus reaction time leads to a slope of $k_3[A^+]^2$ where k_3 is the third order rate constant given by $k_a k_s/k_b$. Examples of this plot are shown in Figure

4.10 for the pure nitrogen system. The concentration of the ionic species is measured by calculating the net area under each peak profile. The net area is defined as the integral of a region whose area extends from an imaginary baseline to all data points above the baseline, in this way the background data are stripped from the calculation. The baseline is determined by averaging the three data points on each side of the selected region and then performing a linear extrapolation between these two points. This procedure can be performed for the operator by the Ortec multichannel analyser by one of the preprogrammed routines stored in its memory.

The effect of the initial electron energy and drift field on the measured ion ratios and on the final rate constant must be considered. Figure 4.11a shows the effect of increasing the ionisation energy on the primary to total ion intensity ratio for the pure nitrogen system. As the ionising energy of the electron pulse is increased a subsequent increase in this ratio is observed. This is due to the initial formation of a greater number of primary ions. Over the ionising energy range of 16 to 18eV this ratio is constant, indicating that the system is capable of producing a subsequent larger number of secondary ions. Above 18eV the ratio increases, Figure 4.11a, for two reasons. First, as stated above a greater electron energy pulse results in the formation of more primary ions. Secondly, excess energy in the system leads to a reduction in the rate of formation of the association product. The rate constant for the vibronic quenching of the excited intermediate complex will be considered in more detail in the following chapter.

Increasing the E/N ratio is analogous to increasing the system's temperature. This is shown in Figure 4.11b, again for the nitrogen system. The corresponding decrease in the measured rate constant is expected as the system under study has a negative temperature dependence. This effect can be predicted by the Wannier expression[78]:

$$\Delta T_{eff} = \frac{1}{3k_B} \cdot v_d^2 \, m_r \left(\frac{m + m_b}{m + m_r} \right) \qquad (4.14)$$

Fig. 4.11a EFFECT OF IONISING ENERGY ON THE PRIMARY ION CURRENT.

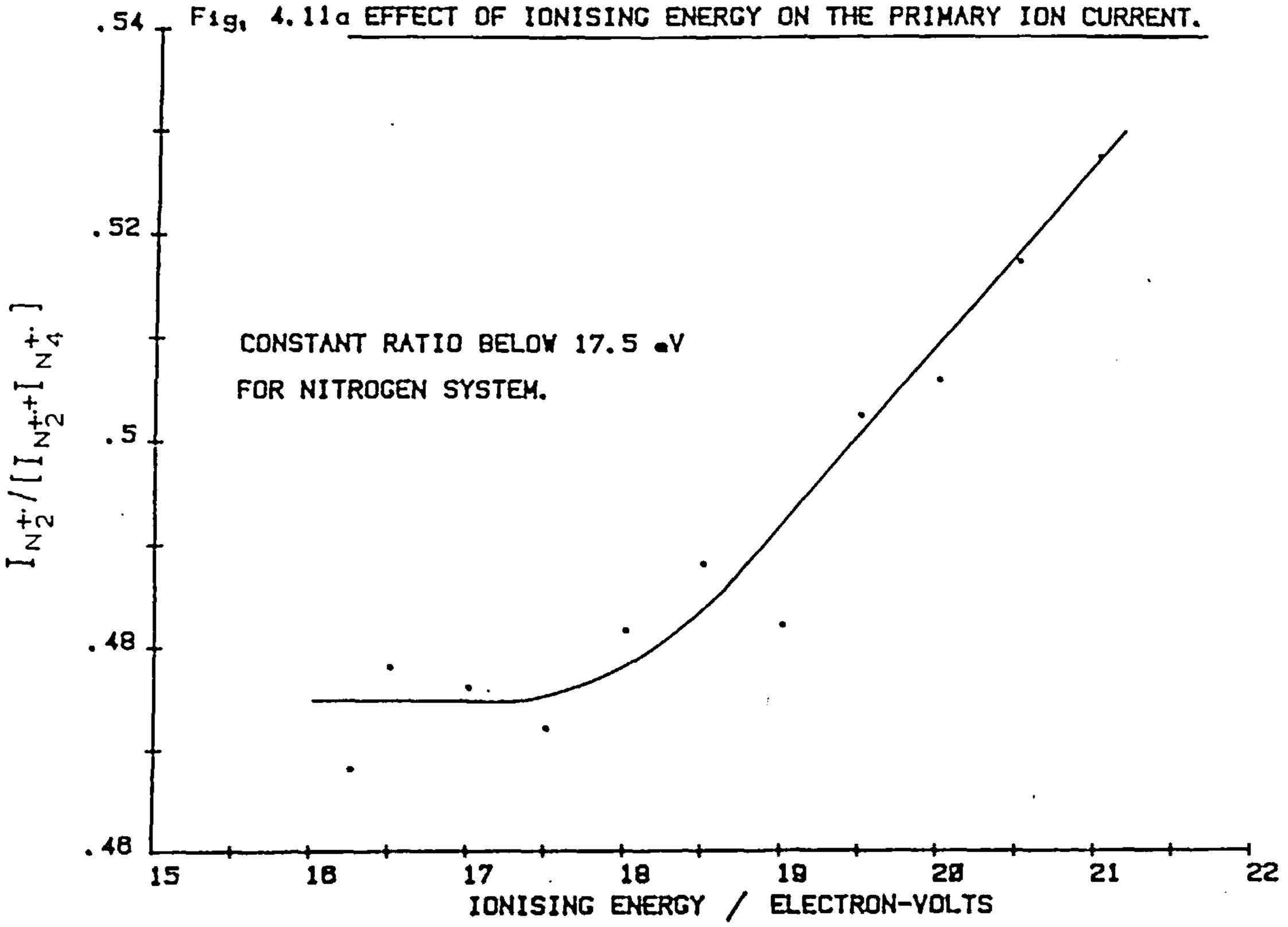

4.11b EFFECT OF INCREASING ELECTRIC FIELD ON MEASURED RATE CONSTANT FOR THE NITROGEN ASSOCIATION AT 375 K.

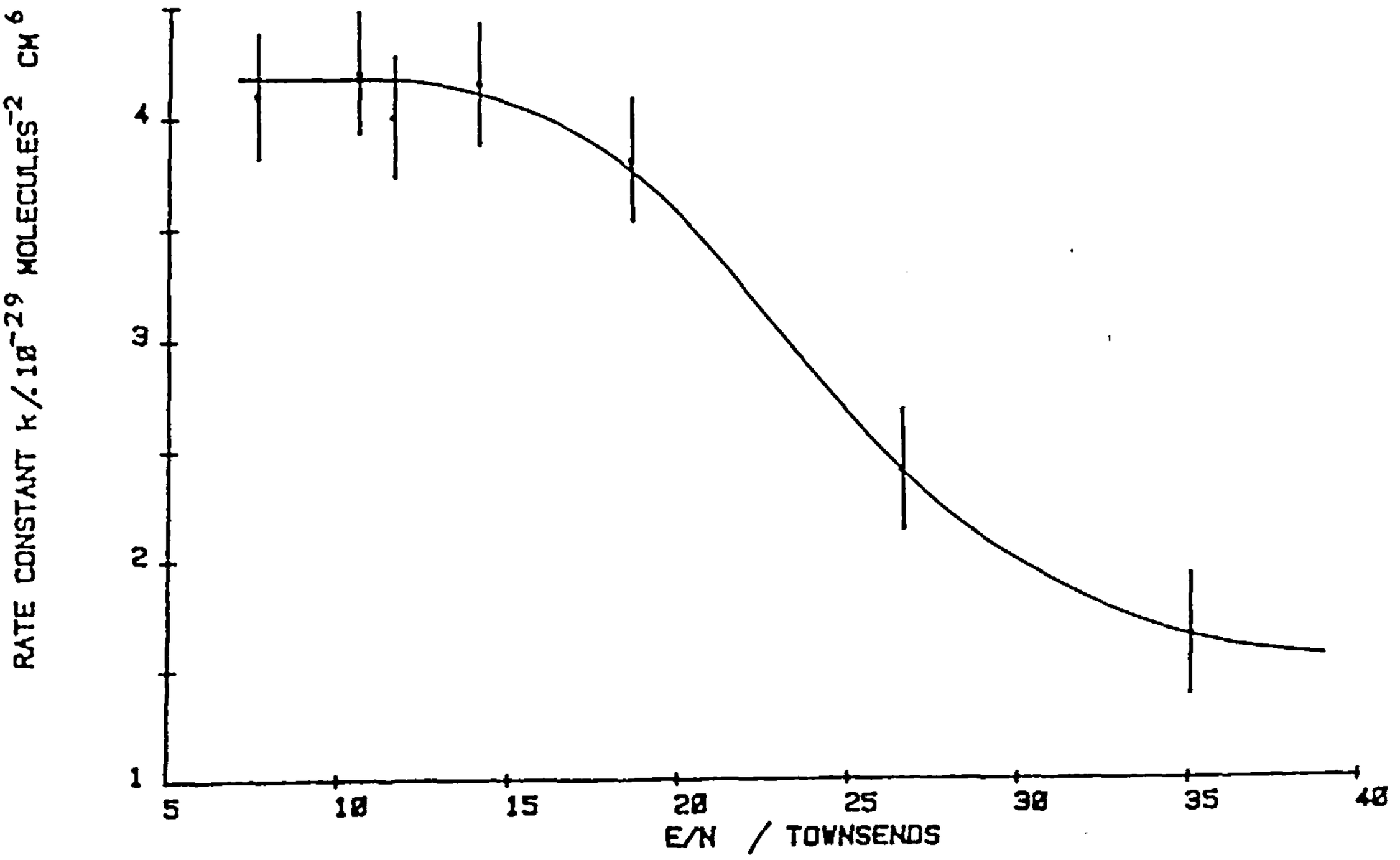

where k_B is the Boltzmann constant and m, m_r and m_b are the masses of the neutral, reactant ion and buffer gas respectively. As the drift velocity v_d approaches zero in the thermal limit, then the effective temperature change on the system ΔT_{eff} also approaches zero. In this work ΔT_{eff} normally lies between 0.5 and 2.0K maximum.

4.6 Determination of Equilibrium Constants

The systems studied for the evaluation of the source's performance in measuring equilibrium constants was the carbon dioxide system:

$$CO_2^{+\cdot} + 2CO_2 \underset{}{\overset{Keq}{\rightleftharpoons}} (CO_2)_2^{+\cdot} + CO_2 \qquad (4.15)$$

As with the high pressure source the equilibrium constant is calculated by the expression:

$$Keq = \frac{I(co_2)_2^{+\cdot}}{I(co_2^{+\cdot})} \cdot \frac{1}{[CO_2]} \qquad (4.16)$$

For this work the actual ion intensity was measured (the area under the peak profile), rather than just the ratio of dimer to monomer ion currents (section 3.10). Equilibrium can be monitored by two methods; first Keq must be pressure independent and secondly, the two peak profiles of the primary to secondary ions must overlap completely. Chapter five shows the results obtained in this study and compares the performance of the two ion sources.

It was found necessary to determine Keq under low field conditions as Keq is a function of E/N, see Figure 4.12. Similarly to the rate constant determination (section 4.5) increasing the electric field has a subsequent decrease in the measured equilibrium constant. Thus, all the Keq values determined are by extrapolation of the linear section to zero field conditions.

Fig. 4.12 THE EFFECT ON THE EQULIBRIUM CONSTANT FOR THE CARBON DIOXIDE ASSOCIATION WITH INCREASING E/N AT 501 K.

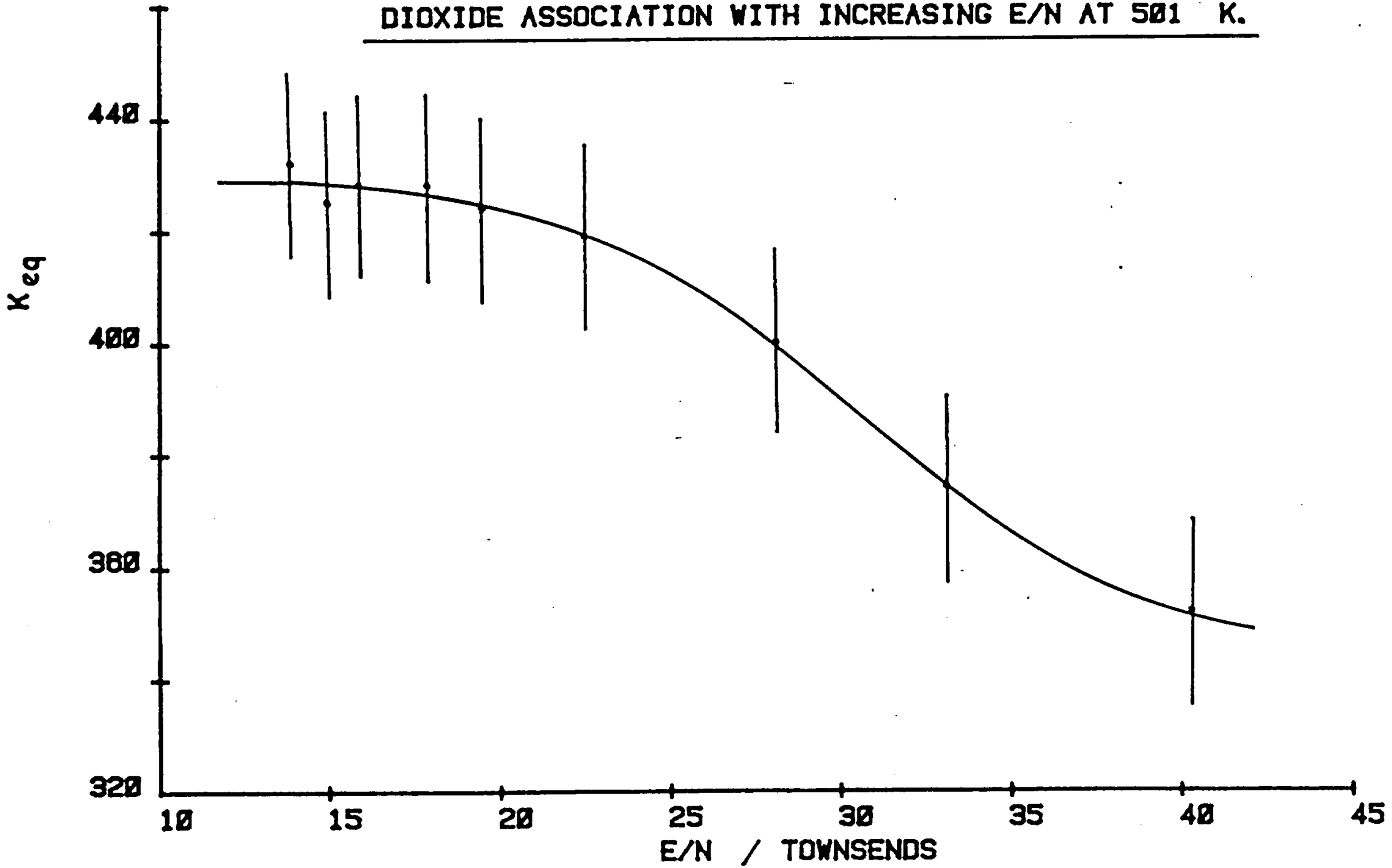

4.7 Error Assessment of the Drift Source

Possible sources of error in the measurements of residence time distributions are caused by difficulties in obtaining a uniform electric field over the entire drift region and electron penetration into the source, both discussed in section 4.4. Drift velocities measured by using a single drift length are often in error by up to 15% because they do not permit the elimination of end effects[79]. The good agreement of the mobility results obtained in this source compared to those determined in a variable length drift tube is good enough to indicate that end effects do not cause major difficulties in this source, see chapter seven.

Space charge effects associated with the expanding ion packet must also be considered. It is widely believed that this sort of charge expansion will have a negligible effect on such measurements as this phenomenon should be symmetrical about the midplane of the drifting ion cloud, normal to the axis of the drift region. This is strictly true only when a single type of charged species is present. McDaniel has observed for H^+ in hydrogen that this ion is 'pushed' down the drift tube due to the strong space charge of the more abundant H_3^+ ion[79]. However, for experiments conducted at low E/P conditions this effect is minimal and this effect is not regarded as a significant source of error.

Longitudinal and transverse diffusion coefficients, D_L and D_T respectively, have been measured[44] for the $N_2^{+\cdot}$ in nitrogen system over the E/P range of 3 to 1000Td. These are constant over the entire range with only D_L showing an increasing trend above 200Td. For this source, conditions were always chosen such that rate and equilibrium constant measurements were performed over the effective field range of 5 to 17 Td, and D_L and D_T can be assumed constant at any particular temperature.

The possibility of mass discrimination at the detector has already been considered in chapter three. There is however, a possibility of mass discrimination at the ion-exit aperture. This can occur when the diffusion rate of each ion differs and leads to a different number density of each species at the ion-exit hole. If we consider a packet of ions at a concentration

n_o released at time zero and at a point x=y=z=0, the three dimensional distribution function n(r,z,t) over a drift distance z, and a time t, in cylindrical polar coordinates is given by[76,78]:

$$n(r,z,t) = \frac{n_o r}{2D_L t\sqrt{(4\pi D_L t)}} \cdot \exp\left(\frac{-r^2}{4D_L t}\right) \cdot \exp\left(\frac{-(z-v_d t)^2}{4D_L t}\right) \qquad (4.17)$$

where r is the radius of the drift region. The total ion current passing through a plane is given by:

$$i(t,z) = \frac{n_o}{4} \cdot \frac{v_d + z/t}{\sqrt{(\pi D_L t)}} \cdot \exp\left(\frac{-(z-v_d t)^2}{4D_L t}\right) \qquad (4.18)$$

This relationship assumes that all ions pass through some plane at a distance z from the origin are collected. In this source the ions actually pass through a circular aperture of radius $r_c = 0.02$cm. The collected current $i_c(r_c,t,z)$ is:

$$i_c(r_c,t,z) = \frac{n_o}{4} \cdot \frac{v_d + z/t}{\sqrt{(\pi D_L t)}} \cdot \exp\left(\frac{-(z-v_d t)^2}{4D_L t}\right) \cdot \left(1-\exp\left(\frac{-r_c 2}{4D_L t}\right)\right) \qquad (4.19)$$

It is possible to assess the discrimination introduced by the aperture by calculating the fraction of ions passing through a plane at a drift distance z which exit through the aperture by the division of equation 4.19 by equation 4.18, this gives:

$$F(r_c,t) = 1 - \exp(-r_c^2/4D_r t) \qquad (4.20)$$

where $F(r_c,t)$ is the fraction of ions passing through the ion-exit aperture. In this source, $r_c^2 = 4.10^{-4}$ cm^2 and a typical value of $4D_T t$ is 0.06cm for N_2^+ in nitrogen at 425K and 0.75 Torr. Thus, the assumption that $r_c^2 << D_T t$ is valid and expression 4.20 can be simplified to:

$$F(r_c,t) \approx r_c^2/4D_T t \qquad (4.21)$$

In the measuring of reactant and product ion currents the relative discrimination due to mass sampling for the nitrogen system is:

$$\frac{F_{N2^{+\cdot}}}{F_{N4^{+\cdot}}} = \frac{(D_T)_{N4^{+\cdot}}(t_d)_{N4^{+\cdot}}}{(D_T)_{N2^{+\cdot}}(t_d)_{N2^{+\cdot}}} \qquad (4.22)$$

where t_d is the drift time and D_T is the diffusion coefficient as calculated from the Einstein equation 3.4. Over the whole pressure and temperature range studied for the N_2, CO and CO_2 systems the maximum value of this ratio was 1.02. This corresponds to a discrimination of only 2% towards the primary ion over the secondary ion and this is not considered to be significant.

The spectra obtained can be modelled theoretically by the expression:

$$i_c(r_c,t,z) = \frac{n_o}{4} \cdot \frac{v_d + z/t}{\sqrt{(\pi D_L T)}} \cdot \exp\left(\frac{-(z-v_d t)^2}{4D_L t}\right)\left(1-\exp\left(\frac{-r_c^2}{4D_L t}\right)\cdot\exp(-\alpha t)\right) \qquad (4.23)$$

which is essentially expression 4.19 with an extra term to take account of loss of the primary ion due to reaction: α is the frequency of the rate of loss of the reactant in units of sec^{-1}. The measured residence time t, is for reactive systems the time of the maximum in the reactive ion distribution. Unfortunately for rate constant determination, the average time for the non-reactive distribution is required. Thus, a correction for the shift in the average residence time due to reaction must be considered. As the residence time increases the reacant ion intensity is depleted and a shift to shorter residence times is observed. To calculate t_{NR} (residence time of non-reactive system) Bowers et al[73] have devised an iterative procedure using the measured reactive ion residence time, t_R:

$$t_R(\text{measured value}) = z/\sqrt{(v_d^2 + 4\alpha D_L)} \qquad (4.24)$$

where t_R and z are known. Using t_R, the rate constant is calculated from equation 4.13 along the α, the frequency of the rate of loss of the primary ion by fitting expression 2.23 to the observed ion profile. This value of α is then used in equation 2.24 to determine v_d, and this drift velocity subsequently used in equation 4.25 to determine t_{NR}. This procedure is then

$$t_{NR} = z/v_d \qquad (4.25)$$

repeated using this value of t_{NR} as t_R until a constant set of α and t_{NR} values are obtained. The corresponding t_{NR} is then used in the final determination of k_3. Such a method deduced an error in $t_{measured}$ of 10% at 260K falling to 4% at 455K[73]. However, this does not affect the measured value of k_3 if a constant pressure is maintained during its determination at a particular temperature. Thus the measured slope of a $\ln([P^+]/([P^+] + [S^+]))$ versus residence time is still valid, although the intercept is incorrect, where $[P^+]$ and $[S^+]$ are the primary and secondary ion intensities respectively. This error will affect mobility results as the source pressure can be varied during their determination. If a linear relationship is assumed between the measured and actual residence time for increasing temperature, an 8% error at 300K falling to zero at 580K must be used.

Chapter Five

Termolecular Association Reactions in One Component Systems and the Evaluation of Results Obtained by both Ion Sources

5.1 Introduction

As both a method of source testing and of clarification of previous work[29], the termolecular association reactions of three one component systems were studied as a function of temperature. The systems chosen have been investigated by other groups[73,80-85] but mainly at lower temperatures and pressures and by differing experimental techniques. These systems are the pure nitrogen, carbon monoxide and carbon dioxide termolecular association reactions:

$$N_2^{+\cdot} + 2N_2 \xrightarrow{k_1} N_4^{+\cdot} + N_2 \qquad (5.1)$$

$$CO^{+\cdot} + 2CO \xrightarrow{k_2} (CO)_2^{+\cdot} + CO \qquad (5.2)$$

$$CO_2^{+\cdot} + 2CO_2 \underset{}{\overset{K_3}{\rightleftharpoons}} (CO_2)_2^{+\cdot} + CO_2 \qquad (5.3)$$

Although these reactions have been studied by several groups, there are still discrepancies in the results reported. This is especially true with regard to the negative temperature dependence and it was hoped that the work reported here will help clarify this situation.

5.2 High Pressure Pulsed Source Results

5.2(i) The Nitrogen System

Using the high pressure pulsed sources (HPPS), described previously in chapter three, a number of experiments were conducted over a temperature range 360 to 580K and a pressure range of 0.5 to 3.5 Torr. The ion source was operated using an electron pulse of 200eV energy for a duration of 20μsecs. The ions formed were N^+; N_2^+; $N_3^{+\cdot}$ and $N_4^{+\cdot}$ with a small amount of impurity peaks associated with H_2O. These four ions accounted for >95% of the total ion beam intensity with the remainder of the signal consisting of small quantities of H_2O^+; H_3O^+; $NH^{+\cdot}$ and N_2H^+; whose relative intensity decreased with decreasing source pressure. The main secondary ions $N^{+\cdot}$ and $N_3^{+\cdot}$ are formed by the following routes:

$$N^{+\cdot} + 2N_2 \xrightarrow{k_4} N_3^{+\cdot} + N_2 \qquad \text{(i)}$$

$$N_2^{+\cdot} + 2N_2 \xrightarrow{k_1} N_4^{+\cdot} + N_2 \qquad \text{(ii)} \qquad (5.4)$$

$$N_4^{+\cdot} + N_2 \xrightarrow{k_{-1}} N_2^{+\cdot} + 2N_2 \qquad \text{(iii)}$$

The relative intensities of these ions are temperature and pressure dependent, see Figure 5.1. This study is primarily concerned with the reaction 5.4(ii), but first the back reaction 5.4(iii) was investigated to determine whether or not a significant concentration of $N_2^{+\cdot}$ ions was formed by this route.

There are two possible pathways by which the $N_4^{+\cdot}$ ion can react either by dissocation to the parent $N_2^{+\cdot}$ ion or by neutralisation against the walls of the source chamber:

$$N_4^{+\cdot} \xrightarrow[\text{diff}]{b'} \text{lost on walls of chamber} \qquad (5.5)$$

fig. 5.1 HIGH PRESSURE MASS SPECTRA FOR THE PURE NITROGEN SYSTEM.

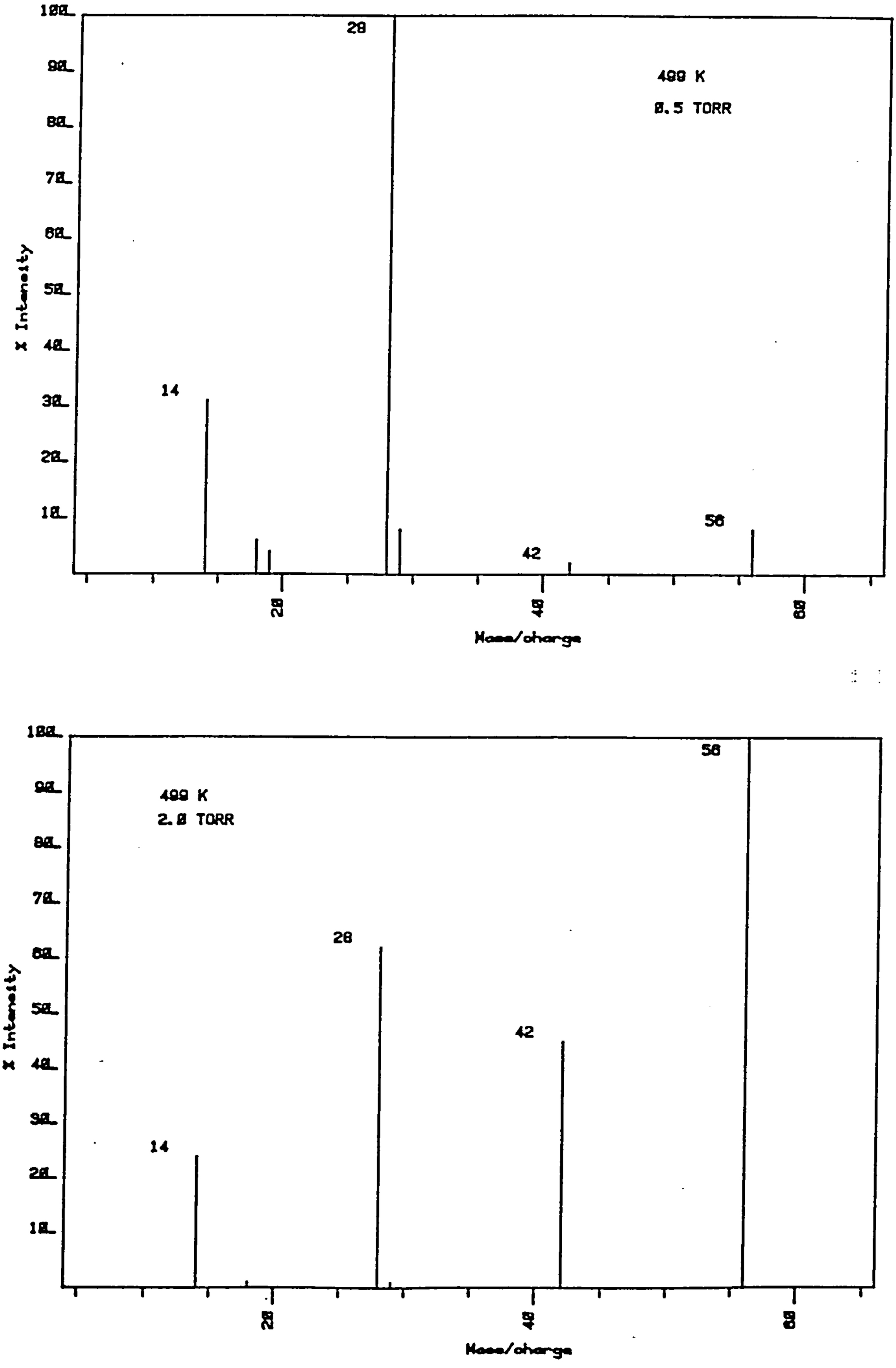

The rate of loss of $N_4^{+\bullet}$ can be determined by considering reactions 5.4(iii) and (5.5), yielding:

$$-d[N_4^+]/dt = k_{-1}[N_4^+][N_2] + b'[N_4^+] \qquad (5.6)$$

$$\therefore \qquad -d[N_4^+]/[N_4^+] = (k_{-1}[N_2] + b')dt \qquad (5.7)$$

If one assumes that the ion intensity $I_{(N4^+)}$ is directly proportional to the concentration of N_4^+, integration of expression 5.7 gives:

$$I_{(N4^+)t} = I_{(N4^+)o} \exp(-(k_{-1}[N_2] + b'))t \qquad (5.8)$$

where $I_{(N4^+)o}$ is the initial concentration of the dimer at t=O. A plot of ln $I_{(N4^+)t}$ versus time is shown to be linear with a slope of $(k_{-1}[N_2] + b')$ and an intercept $I_{(N4^+)o}$, Figures 5.2 and 5.3. If one assumes that $b' = \underline{b}/[N_2]$, and by multiplying the slope expression by $[N_2]$ one obtains:

$$-S[N_2] = k_{-1}[N_2]^2 + \underline{b} \qquad (5.9)$$

A plot of this function of $-S[N_2]$ versus $[N_2]^2$ is shown in Figure 5.4. The slope of this plot, and thus the rate constant for reaction 5.4(iii) is essentially zero and this route is assumed to be a negligible source of the primary ion N_2^+: This was found to apply over the whole temperature range studied. This function does yield the diffusive rate constant $\underline{b}$, and the temperature variation of this parameter is shown and discussed in chapter seven along with diffusion coefficient results for the other systems studied.

The derivation of the diffusive/chemical loss method for a forward association reaction has been considered in section 3.9(i). The expression obtained relating the slope S, of the

Fig. 5.2 ION INTENSITY vs REACTION TIME PROFILE FOR THE N_4^+ IN NITROGEN AT 436 K AND 1.80 TORR.

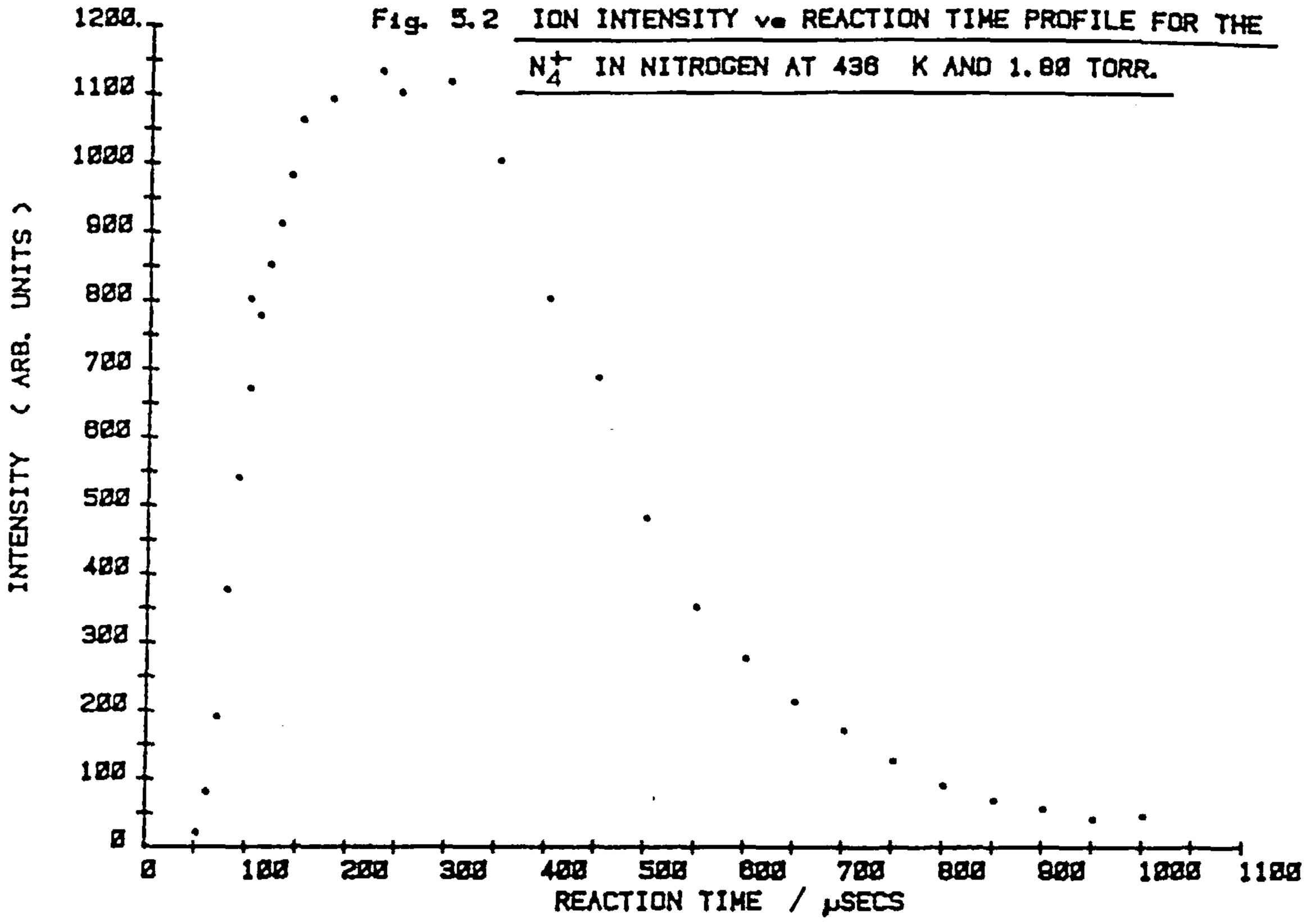

Fig.5.3 Ln INTENSITY vs REACTION TIME PROFILE.

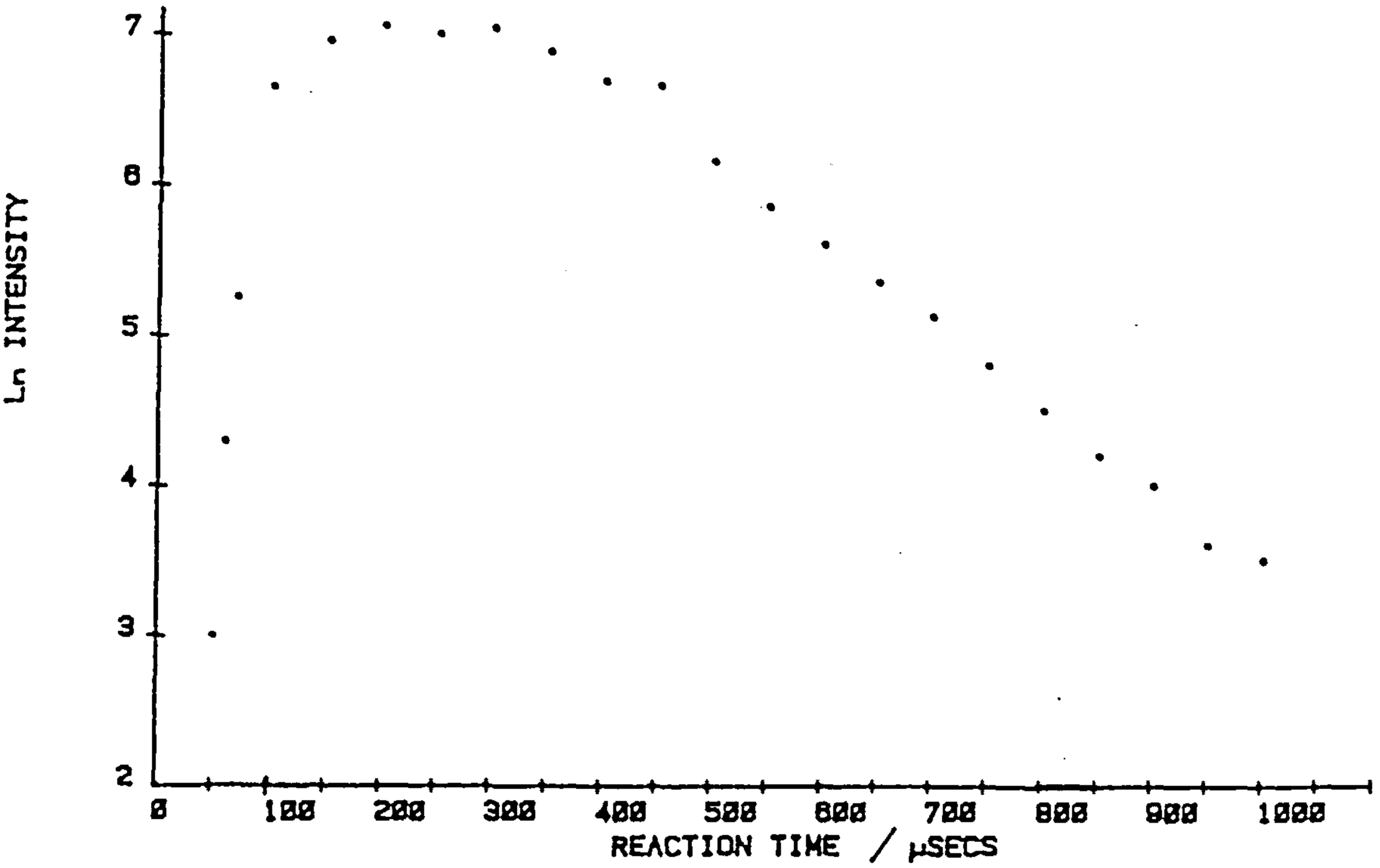

Fig. 5.4 PLOT OF $-S[N_2]$ vs $[N_2]^2$ FOR DETERMINATION OF THE RATE CONSTANT FOR THE DISSOCIATION REACTION: $N_4^{+\cdot} + N_2 \rightarrow N_2^{+\cdot} + 2N_2$

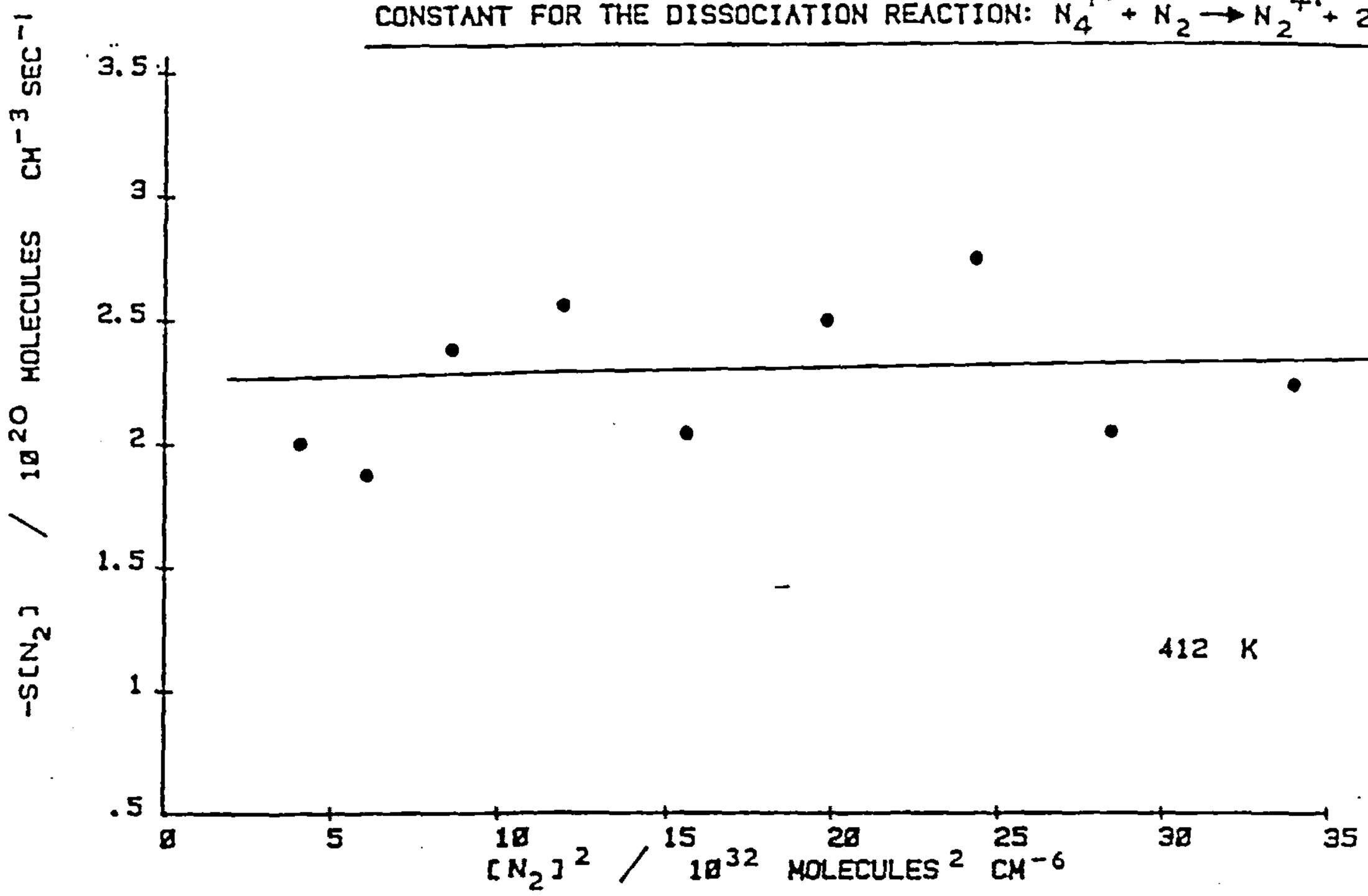

Fig. 5.5 SEPARATION OF $N_2^{+\cdot}$ REACTION RATE AND DIFFUSIVE LOSS CONSTANTS IN NITROGEN AT 424 AND 499 K.

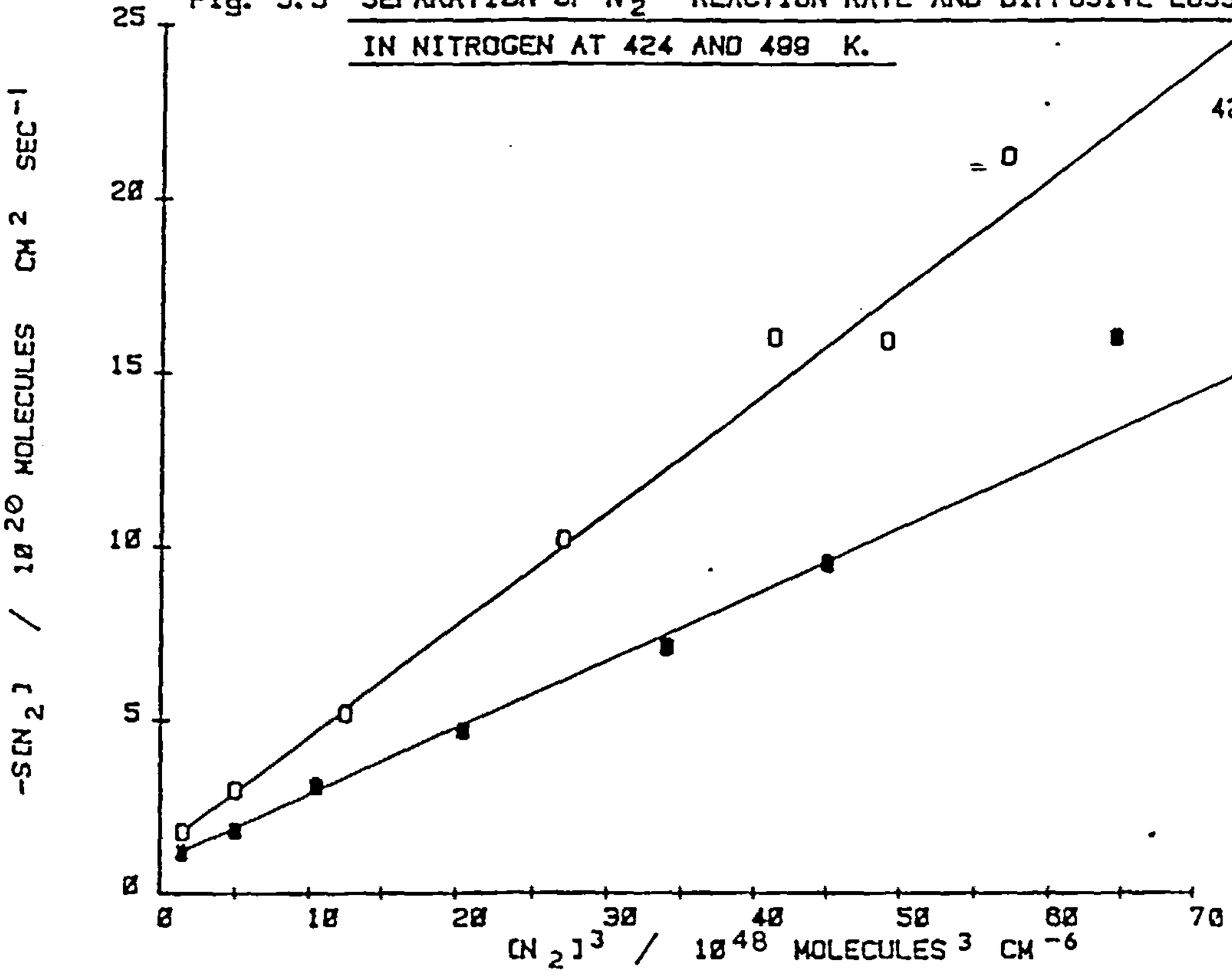

diffusive loss of the primary ion to the neutral gas pressure [A] can be expressed for the nitrogen system as:

$$S[N_2] = k_1[N_2]^3 + \underline{a}[N_2] \qquad (5.10)$$

where k_1 is the rate constant for this process and $\underline{a}$ is the diffusion rate constant. Examples of this function is shown in Figure 5.5 at two temperatures 424 and 499K.

Conventionally k_1 is related to temperature by the expression:

$$k_1 = CT^m \qquad (5.11)$$

where C and m are constants characteristic of the reaction. The previous function was used to determine k_1 at 20°C intervals and a $\log_{10} k_1$ versus $\log_{10} T$ plot employed to determine $\underline{m}$, Figure 5.6. The temperature dependence was found to be -1.95 ± 0.26 as determined from a least squares analysis fit to the data.

5.2(ii) Carbon Monoxide

This system was studied using the same method that was used for the nitrogen system. The association reaction forming the dimer $(CO)_2^{+\cdot}$ was monitored over a pressure range of 0.20 to 3.51 Torr and a temperature range of 403 to 615K. Examples of the mass spectra recorded for this system are shown in Figure 5.7. The main peaks observed occur at m/z ratios of 12,28,56 and 68 daltons and correspond to the ions C^+; CO^+, $(CO)_2^{+\cdot}$ and $C(CO)_2^{+\cdot}$ respectively. This gas was dried to a water content of <5vpm to keep the formation of the HCO^+ species to a minimum.

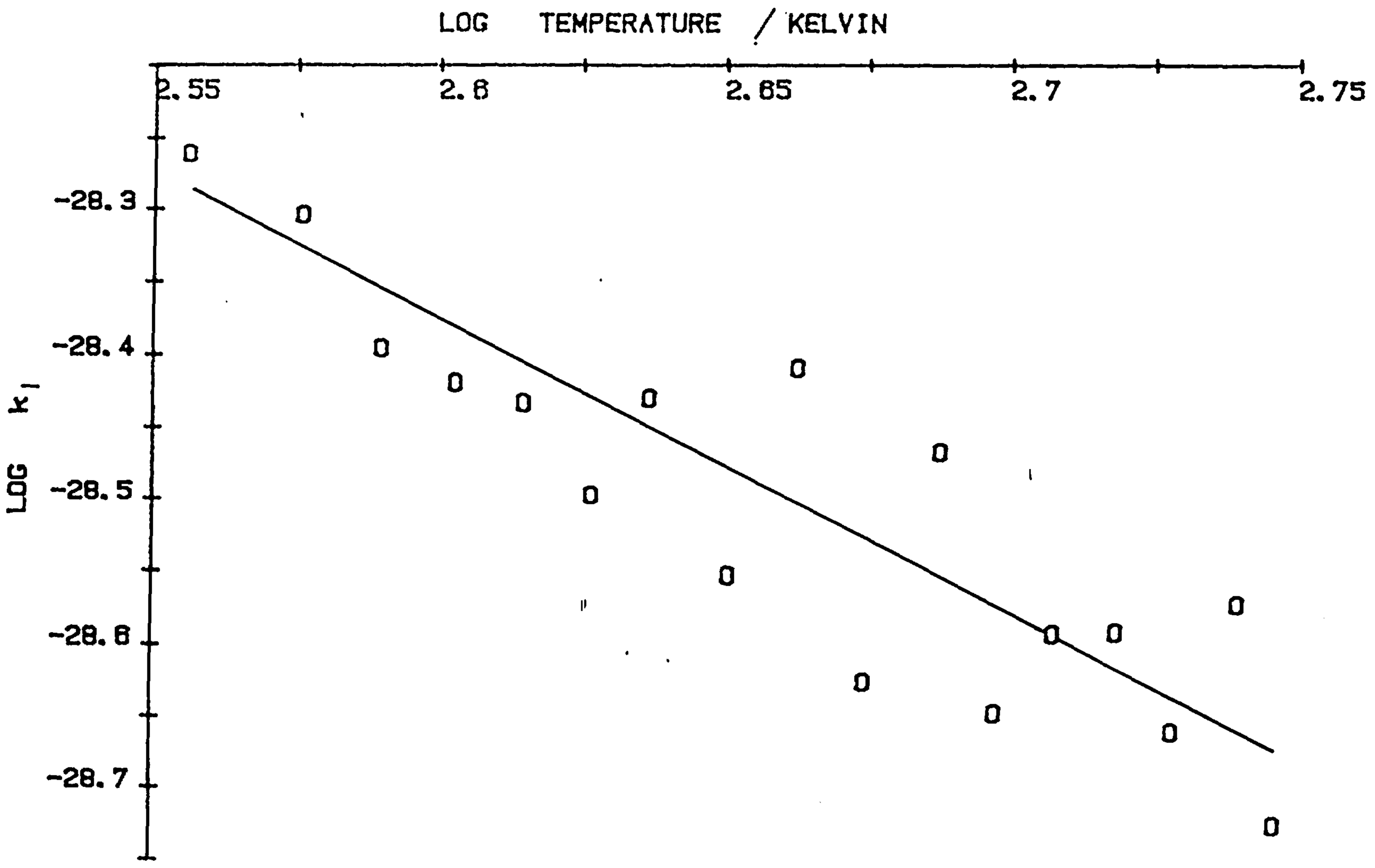

Fig. 5.6 FORWARD ASSOCIATION RATE CONSTANT k_1 AS A FUNCTION OF TEMPERATURE FOR THE NITROGEN SYSTEM (HPPS DATA).

fig. 5.7 HIGH PRESSURE MASS SPECTRA OBTAINED FOR CARBON MONOXIDE

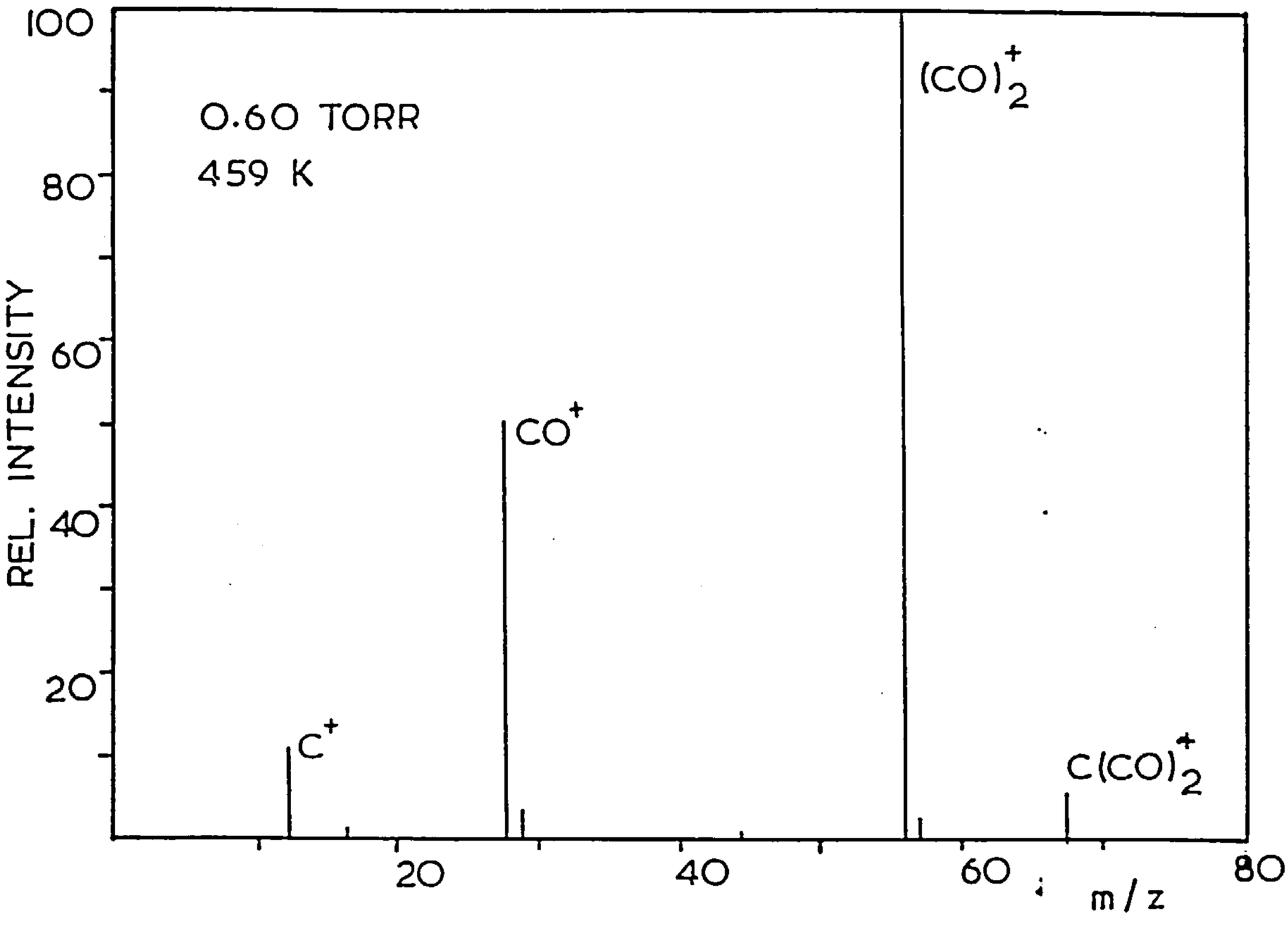

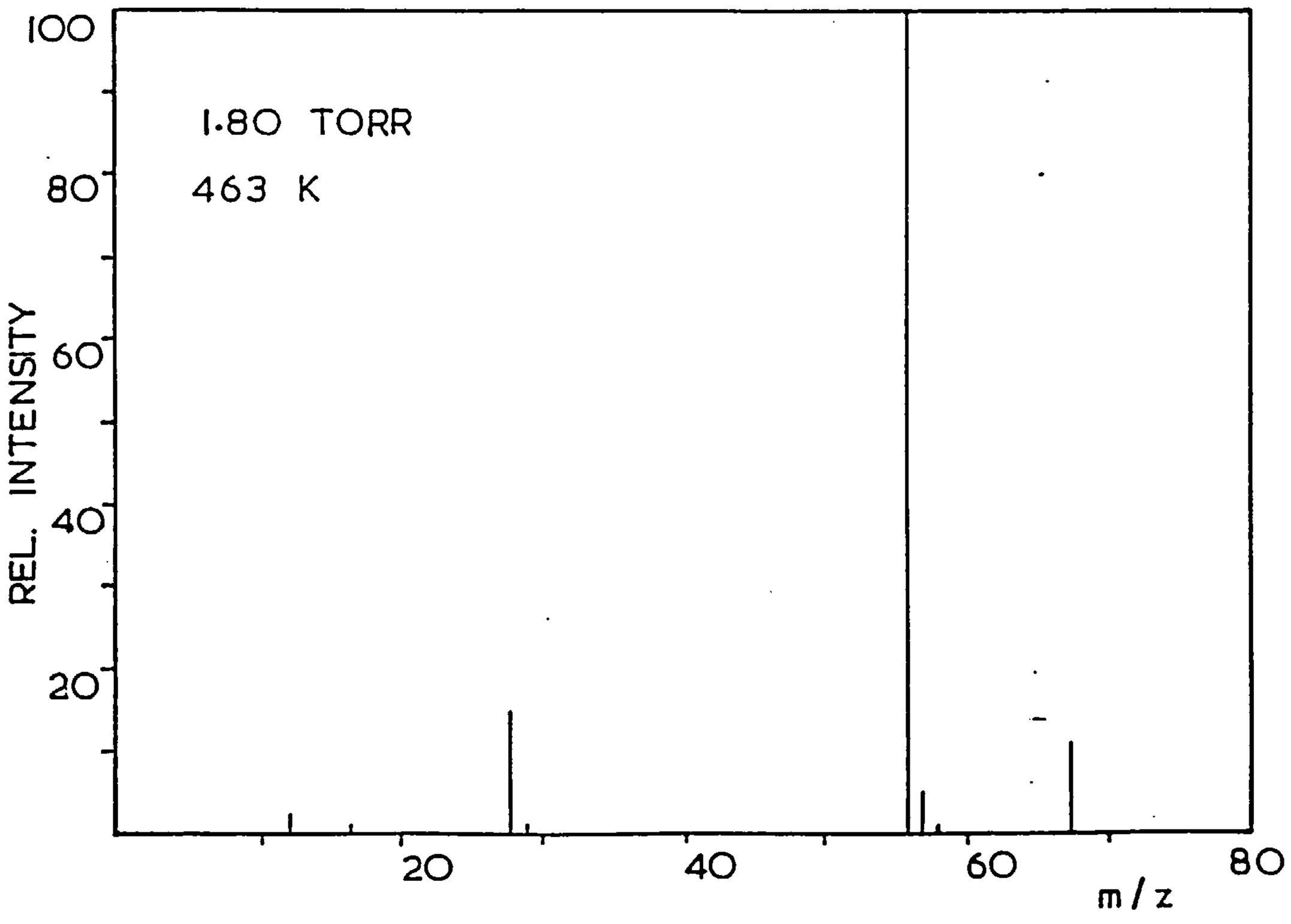

The main processes occurring in the source chamber were:

$$CO^{+\cdot} + 2CO \xrightarrow{k_2} (CO)_2^{+\cdot} + CO \qquad \text{(i)}$$

$$(CO)_2^{+\cdot} + CO \xrightarrow{k_{-2}} CO^{+\cdot} + 2CO \qquad \text{(ii)} \qquad (5.12)$$

$$C^{+\cdot} + (CO)_2 \xrightarrow{k_5} C(CO)_2^{+\cdot} \qquad \text{(iii)}$$

A small amount of carbon dioxide was also observed in the mass spectra. This is an impurity in the gas which can be ionised either initially in the source or by charge-exchange[86] with CO^+:

$$CO^{+\cdot} + CO_2 \xrightarrow{k_6} CO + CO_2^{+\cdot} \qquad (5.13)$$

As with the nitrogen system the back reaction 5.12(ii) was first measured by performing a plot of S[CO] versus $[CO]^2$, where S is the slope of the diffusive loss of the dimer ion and [CO] the pressure of the parent gas (molecule cm^{-3}). The rate constant k_{-2} was found to be negligible, Figure 5.8. The forward rate constant of the association reaction 5.12(i) was measured by the method given in 3.9(i) and the results are shown in Figures 5.9 and 5.10. The temperature dependence was determined and a value of $\underline{m} = -1.50 \pm 0.30$ was obtained.

5.2(iii) Carbon Dioxide

This system behaves differently from those described above in that under the conditions of study the carbon dioxide established an equilibrium between the parent ion and its dimer form:

$$CO_2^{+\cdot} + 2CO_2 \underset{}{\overset{K_3}{\rightleftharpoons}} (CO_2)_2^{+\cdot} + CO_2 \qquad (5.14)$$

Fig. 5.8 PLOT OF $-S[CO]$ vs. $[CO]^2$ FOR THE DETERMINATION OF THE RATE CONSTANT FOR THE DISSOCIATION REACTION $(CO)_2^{+\cdot} + CO \rightarrow CO^{+\cdot} + 2CO$

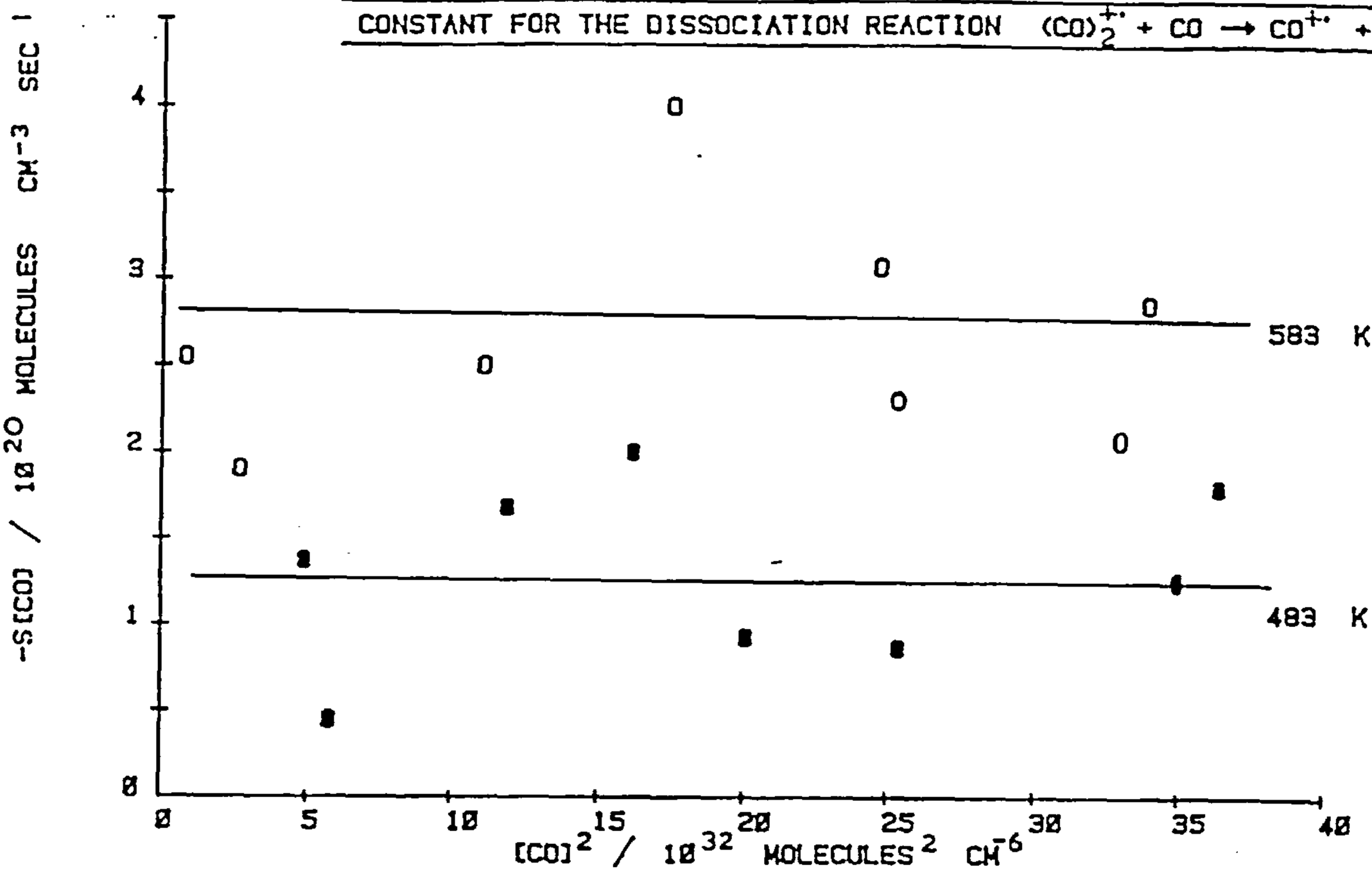

Fig. 5.8 SEPARATION OF $CO^{+\cdot}$ REACTION RATE AND DIFFUSIVE LOSS CONSTANTS IN CARBON MONOXIDE AT 403, 484 AND 516 K.

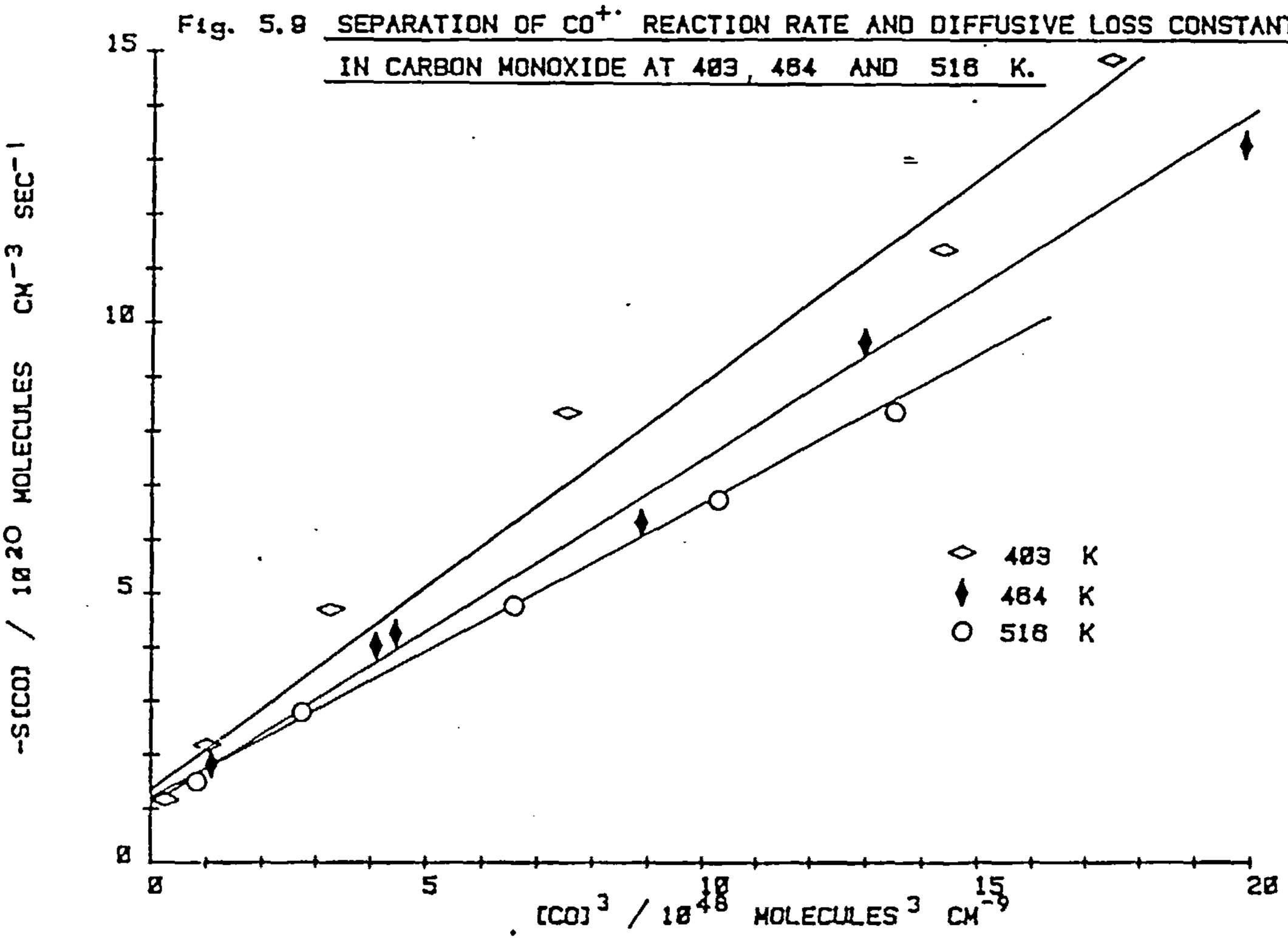

Fig. 5.10 FORWARD ASSOCIATION RATE COEFFIENT k AS A FUNCTION OF TEMPERATURE FOR THE CARBON MONOXIDE SYSTEM (HPPS DATA).

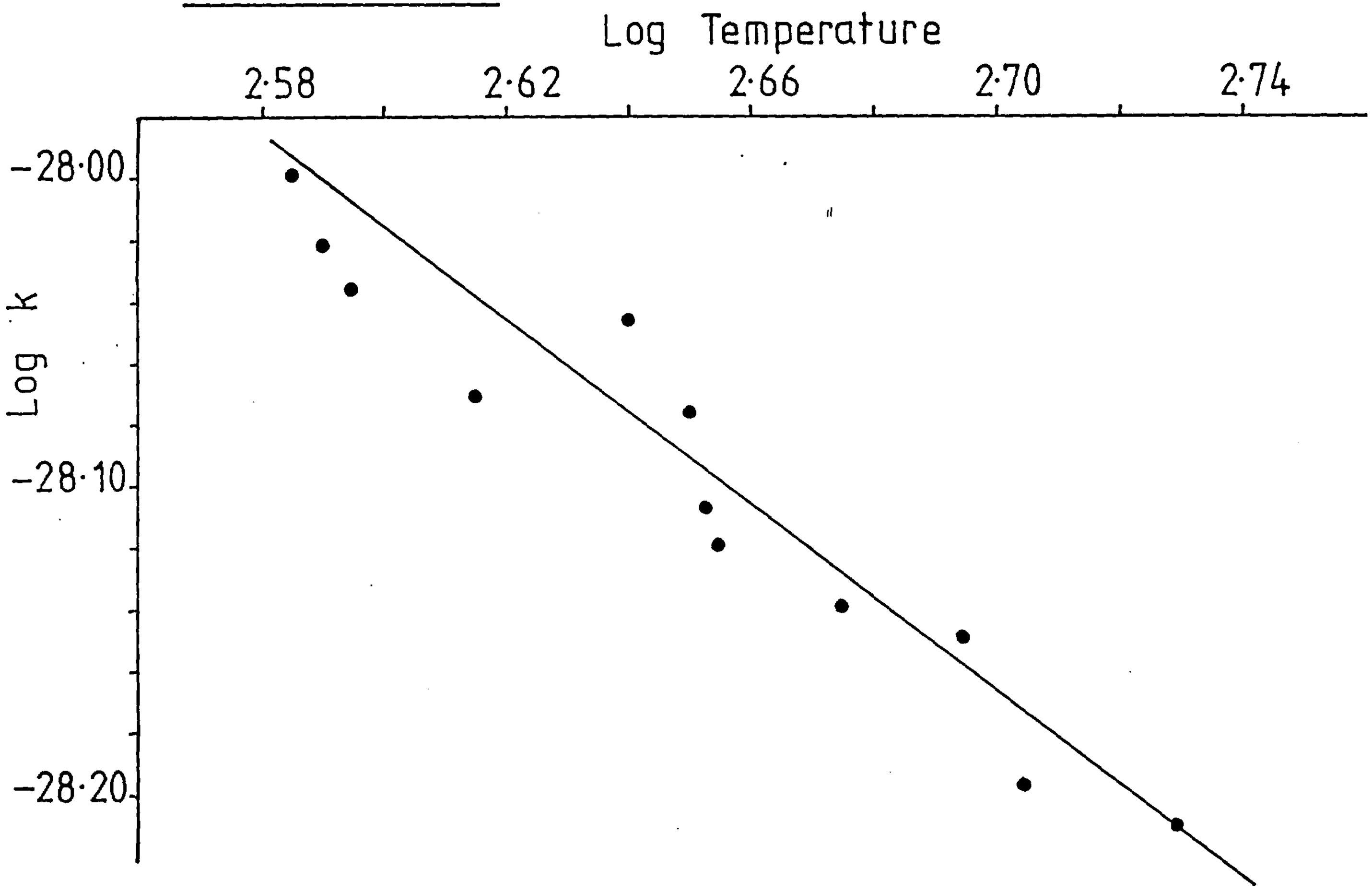

As shown in Figure 5.11 the two main peaks of the spectrum are the parent and dimer ion, m/z = 44 and m/z = 88 respectively. Some other clusters were also observed although in much lower concentration. These are believed to be formed by the following schemes:

$$(CO_2)_2^{+\cdot} + H_2O \longrightarrow (CO_2H_2O)^{+\cdot} + CO_2 \quad \text{(i)}$$

$$O_2^{+\cdot} + 2CO_2 \longrightarrow (O_2CO_2)^{+\cdot} + CO_2 \quad \text{(ii)} \qquad (5.15)$$

$$(O_2CO_2)^{+\cdot} + H_2O \longrightarrow (O_2H_2O)^{+\cdot} + CO_2 \quad \text{(iii)}$$

$$H_2O + H_3O^{+\cdot} \longrightarrow (H_2OH_3O)^{+\cdot} \quad \text{(iv)}$$

The mechanism for the $O_2^{+\cdot}$ formation is not clear[66]. It is proposed, however, that considering the harsh source conditions used, $O_2^{+\cdot}$ may be produced by the dissociation of the $(O_2H_2O)^{+\cdot}$ or $(O_2CO_2)^{+\cdot}$ clusters in addition to the dissociation of the parent molecule, CO_2.

The equilibrium between the monomeric and dimeric CO_2 ions is indicated by the apparent independence of Keq with pressure over the range 0.5 to 3.0 Torr, see Figure 5.12. A van't Hoff plot of the data obtained over a temperature range of 400 to 570K was used to measure the enthalpy and entropy change for reaction. The values of ΔH^o and ΔS^o obtained from the slope and intercept of the plot were -69.6±4.9 $kJmol^{-1}$ and -87.0±10.0 $JK^{-1}\ mol^{-1}$ respectively.

5.3 The High Pressure Drift Source Results

5.3(i) The Nitrogen System

The Drift ion source was used to study the nitrogen association reaction (5.1) over a temperature range of 331 to 562K and a pressure range of 0.59 to 0.65 Torr. The source was operated using an electron pulse of 16eV energy for a 5μsec duration. The spectra obtained from 'continuous' mode operation are shown in Figure 5.14. Over 96% of the total ion

fig. 5.11 HIGH PRESSURE MASS SPECTRA OF CARBON DIOXIDE

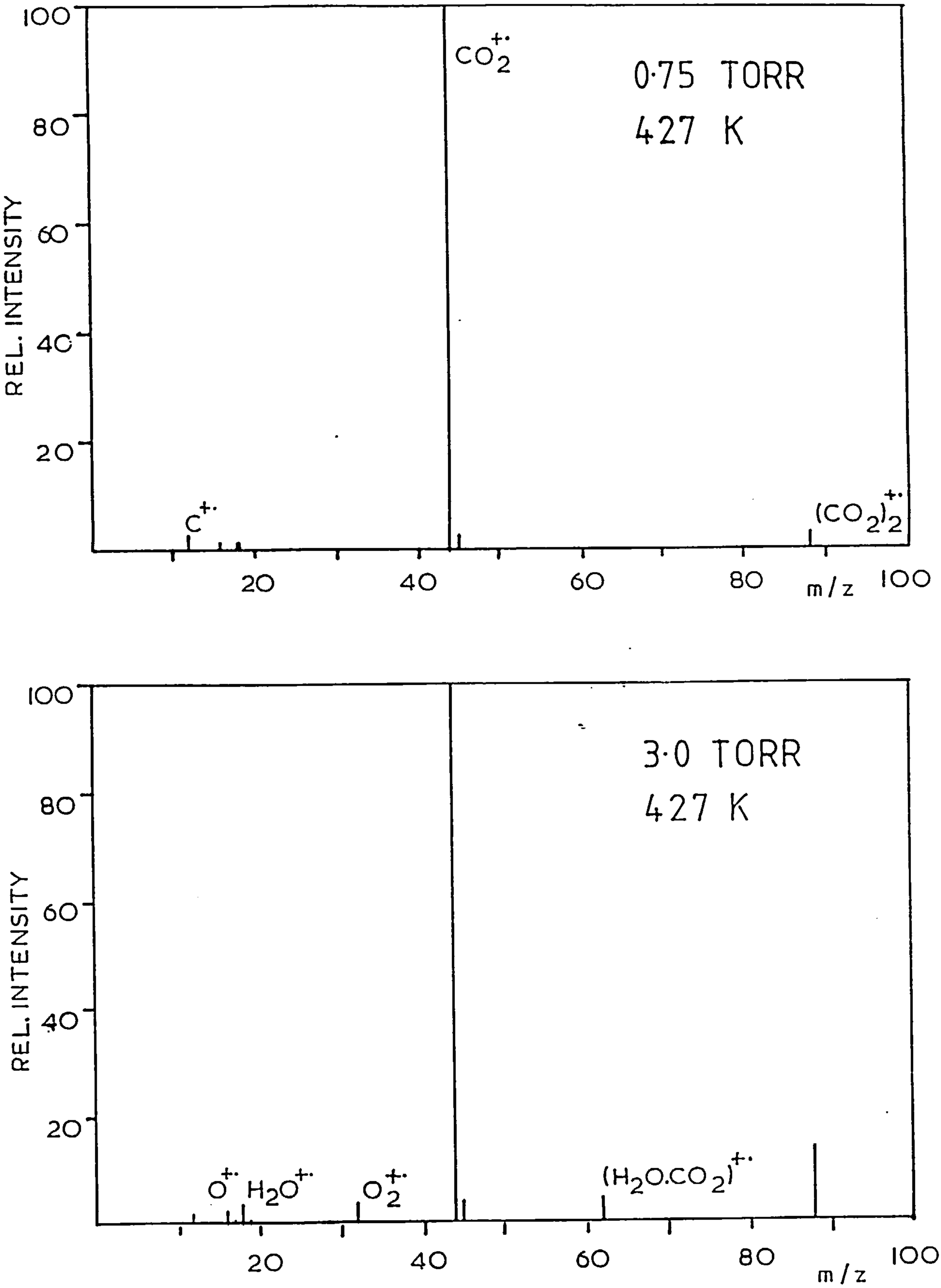

Fig. 5.12 VARIATION IN K_{EQ} WITH RESPECT TO PRESSURE FOR THE CARBON DIOXIDE ASSOCIATION AT VARIOUS TEMPERATURES.

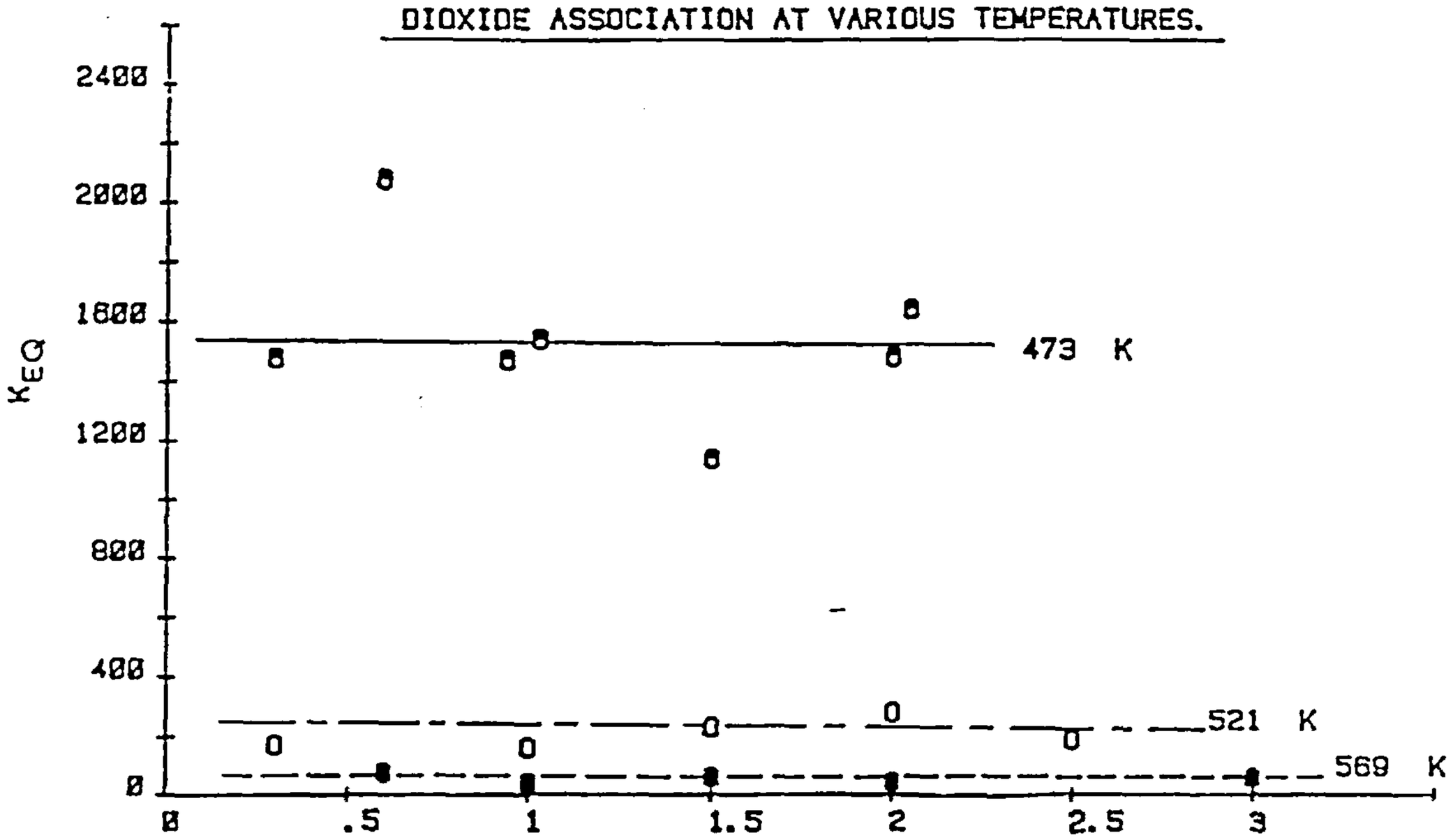

Fig. 5.13 VANT HOFF PLOT (LN K vs 1/T) FOR THE CARBON DIOXIDE SYSTEM OVER THE TEMPERATURE RANGE 475 TO 578 K.

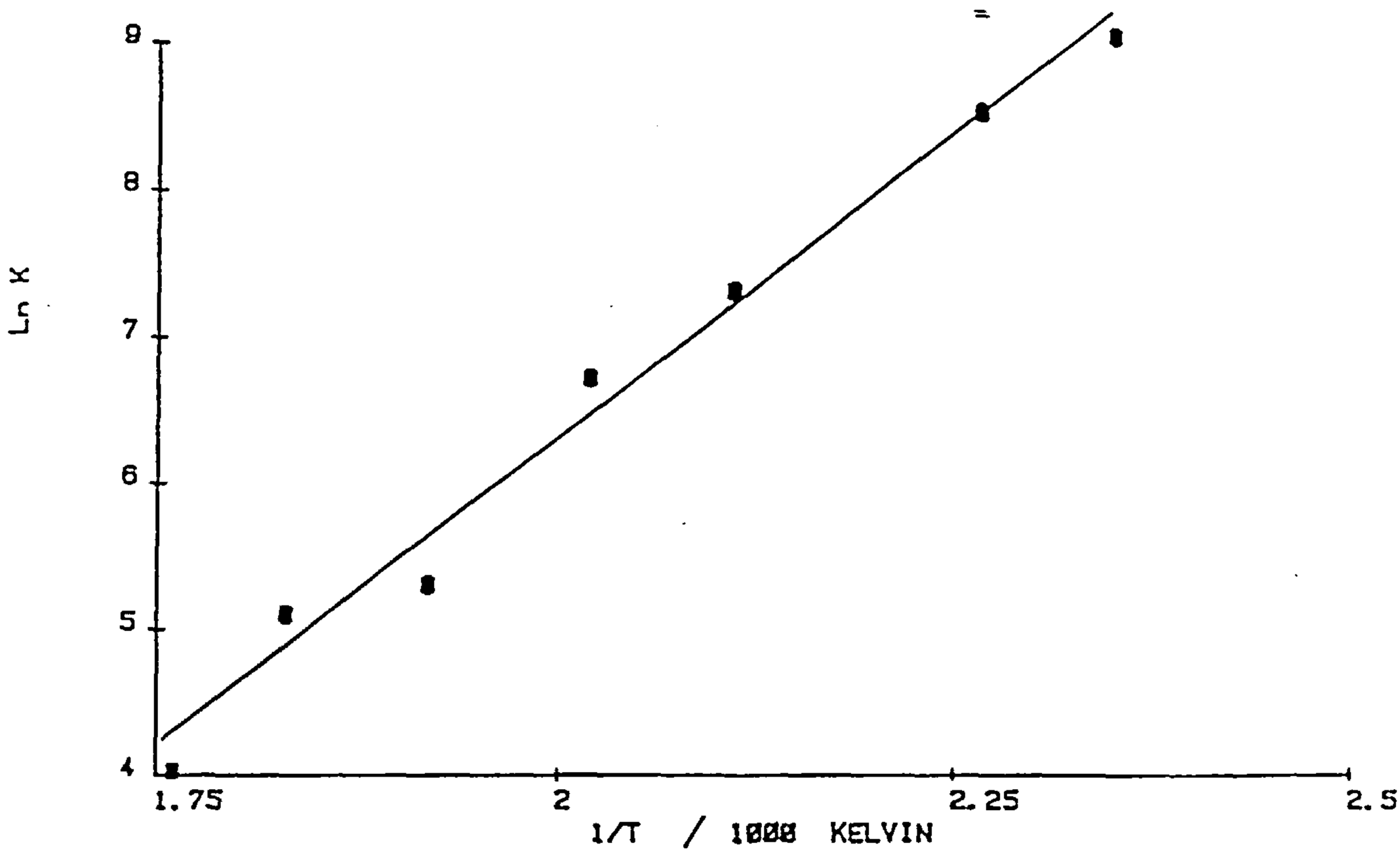

fig. 5.14 VARIATION IN MASS SPECTRA WITH RESPECT TO PRESSURE FOR THE NITROGEN SYSTEM.

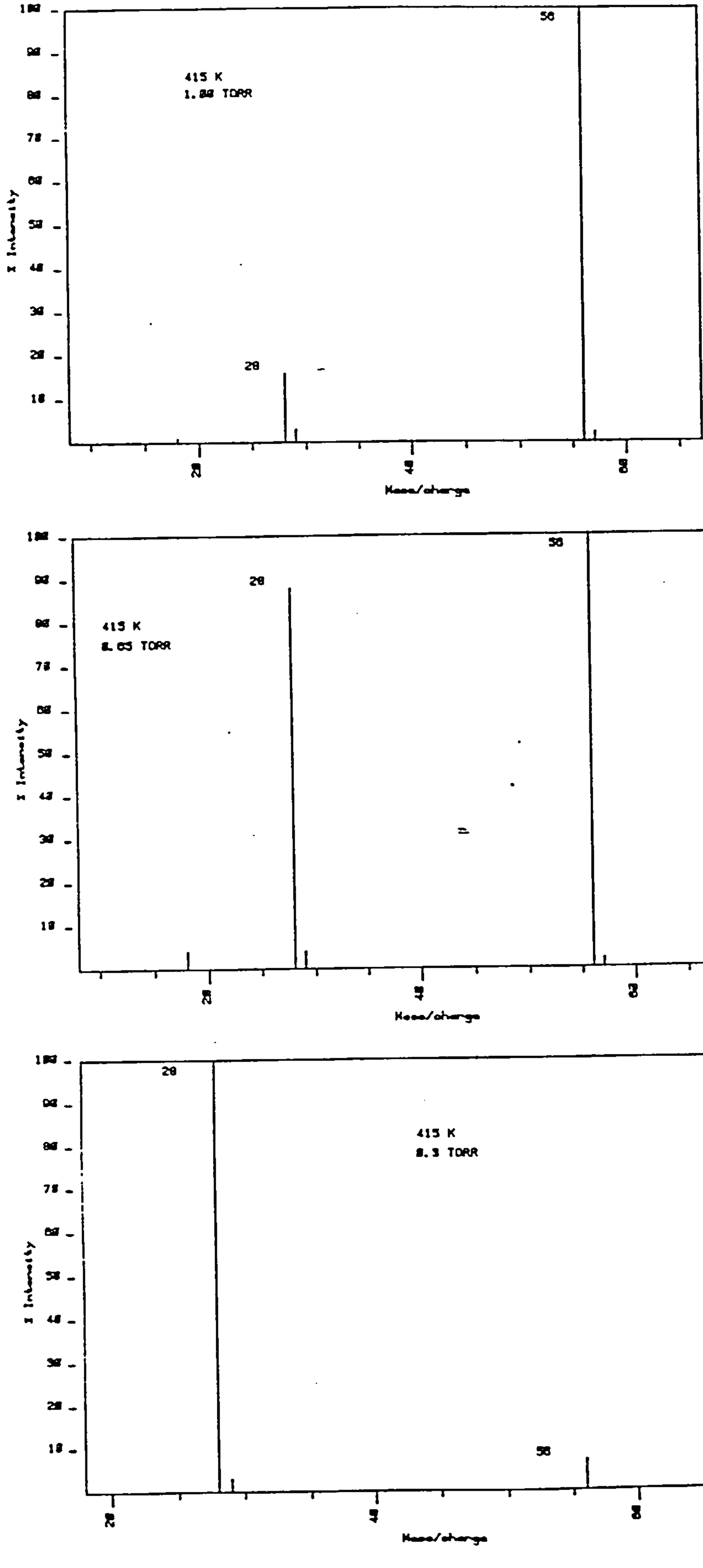

current was made up of only the parent $N_2^{+\cdot}$ ion and the association product N_4^+: The remaining ion signal consisted of H_2O^+; $N_2H^{+\cdot}$ and $N_4H^{+\cdot}$ ions.

Source operating conditions have been documented in chapter four as well as the theory behind rate constant determination. The extent of reaction, $\ln([N_2^+]/([N_2^+]+[N_4^+]))$ as a function of electric field strength, at 415K and at three different pressures is shown in Figure 5.15. The third-order rate constant is calculated by dividing the slope of this plot by the square of the gas concentration. The lines shown are the least squares fits to the data points. Although source conditions were set such that the peak maxima and centre coalesce, at high temperatures this condition was found to break down. This is due to tailing off in the peak profile towards longer reaction times, see Figure 5.16. Extra care was therefore taken in determining the true peak maximum reaction time under these extreme conditions. The third order rate constant was measured at approximately 20° intervals over the investigated temperature range and $\log_{10}k_1$ was plotted against $\log_{10}T$, see Figure 5.17. The temperature dependence of the forward association reaction was determined by a linear least squares analysis of the data and a result of -1.75 ± 0.55 obtained for the temperature dependence.

5.3(ii) The Carbon Monoxide System

The procedure described in chapter four was used in the determination of the temperature dependence of the reaction:

$$CO^{+\cdot} + 2CO \xrightarrow{k_2} (CO)_2^{+\cdot} + CO \qquad (5.16)$$

This reaction was studied at a pressure of 0.64 Torr and at 10° intervals over the temperature range 373 to 533K. The mass spectra obtained for this system show virtually pure carbon monoxide with the only major peaks present corresponding to the $CO^{+\cdot}$ and $(CO)_2^{+\cdot}$ ions, see Figure 5.18. The measured extent of reaction against source residence time is shown in Figure 5.19 at various temperatures. The dissociation reaction has already been shown to be

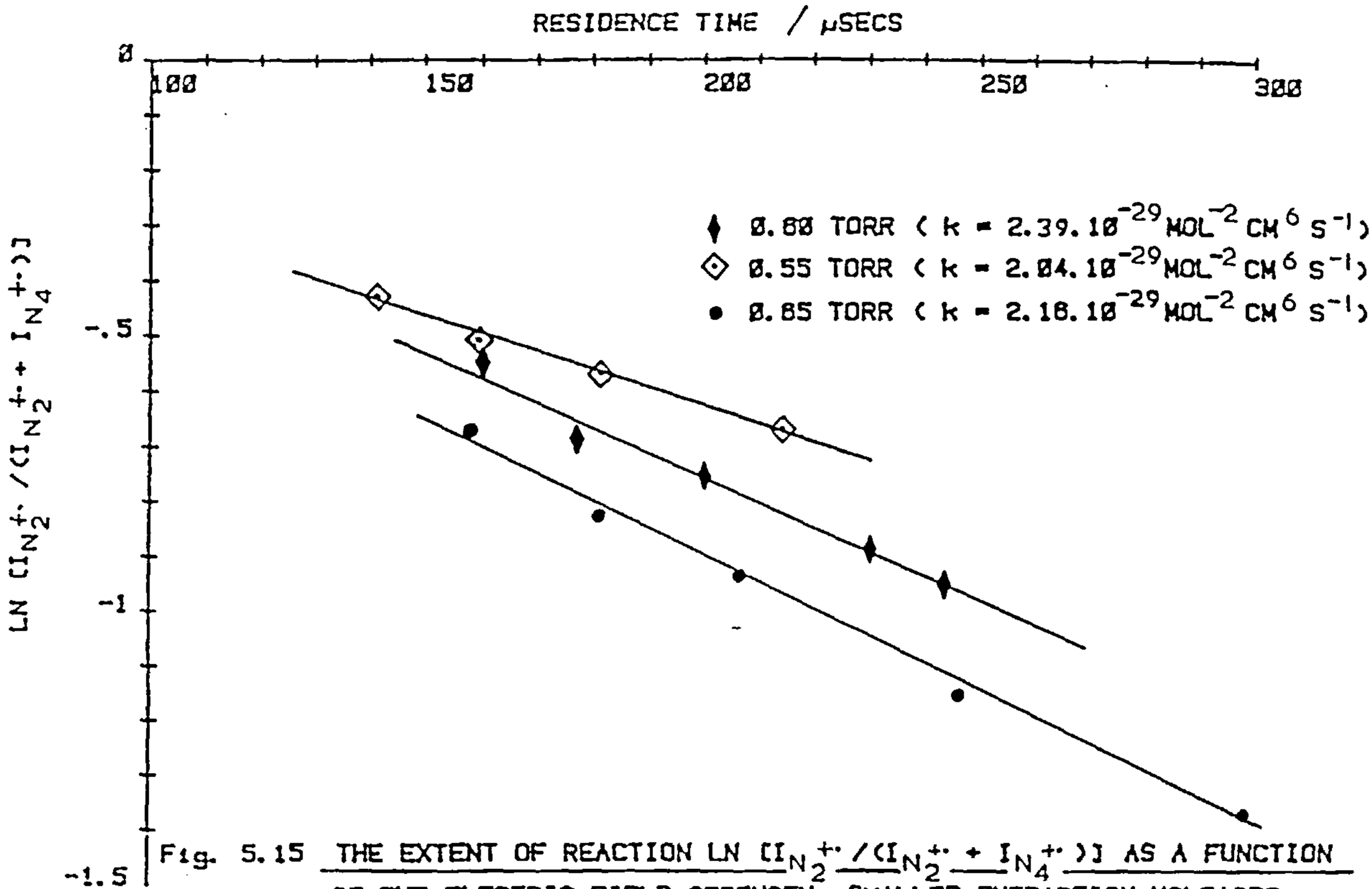

Fig. 5.15 THE EXTENT OF REACTION LN $[I_{N_2}^{+\cdot}/(I_{N_2}^{+\cdot} + I_{N_4}^{+\cdot})]$ AS A FUNCTION OF THE ELECTRIC FIELD STRENGTH. SMALLER EXTRACTION VOLTAGES CORRESPOND TO LONGER REACTION TIMES.

Fig. 5.16 VARIATION IN PEAK SHAPE WITH TEMPERATURE.

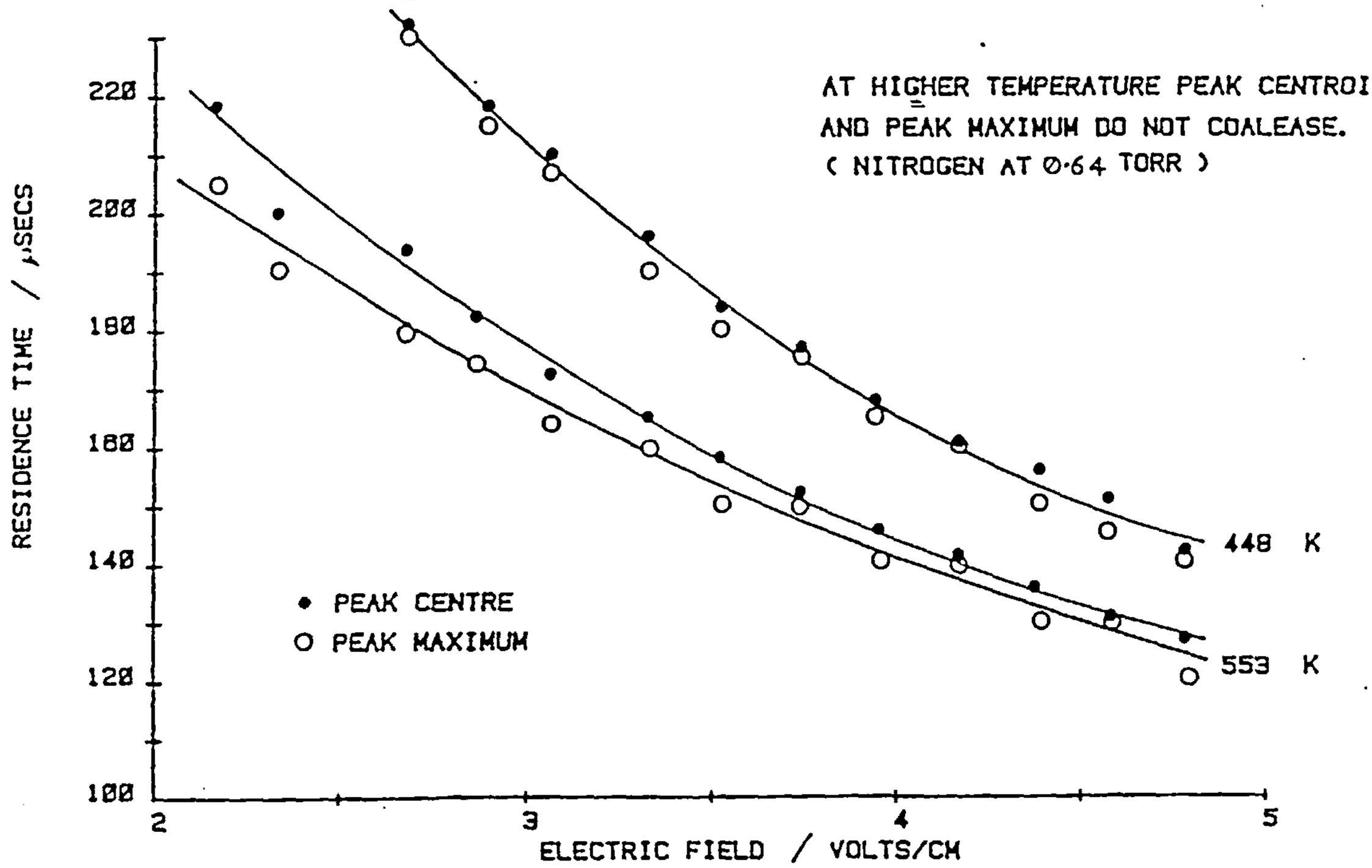

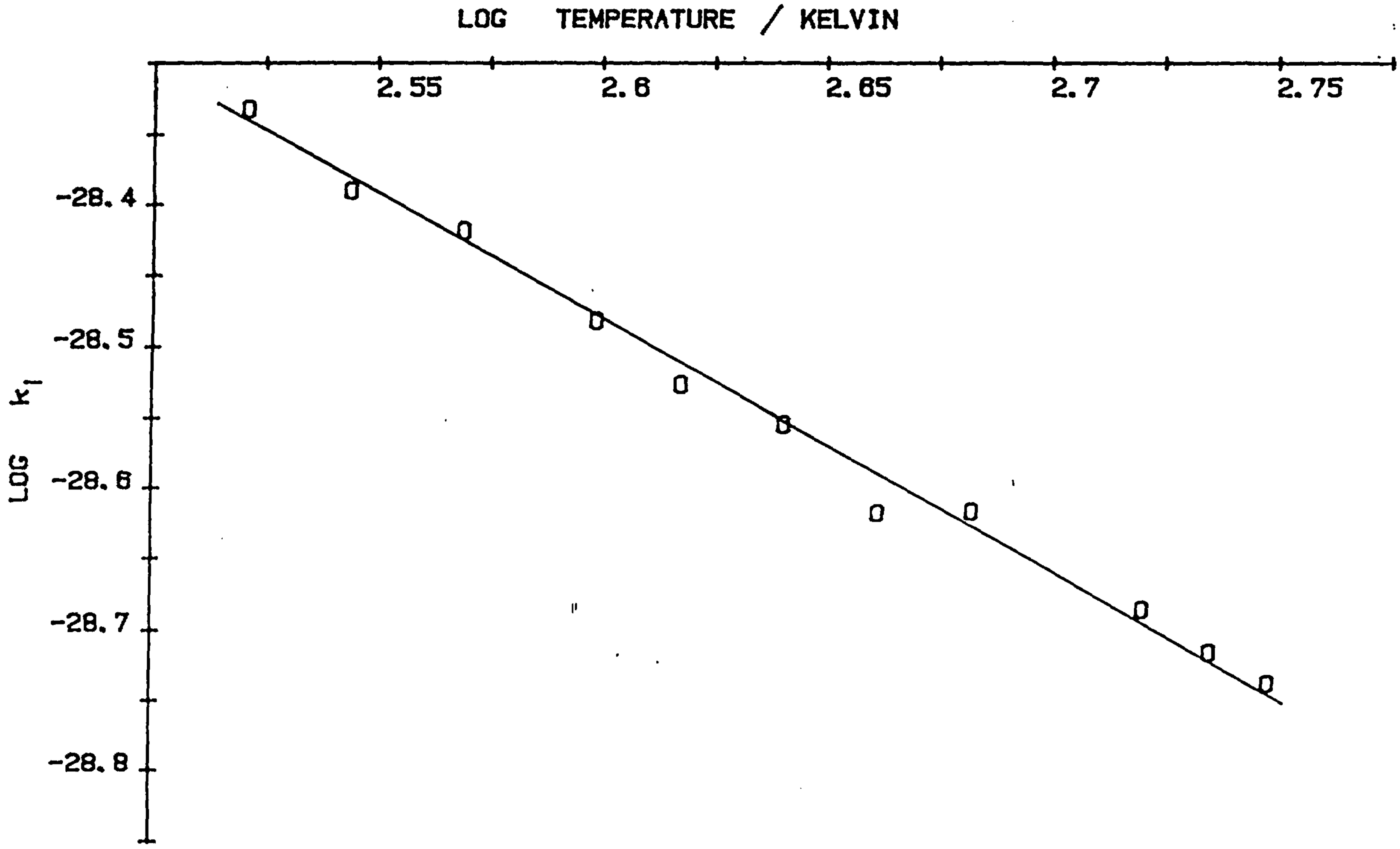

Fig. 5.17 FORWARD ASSOCIATION RATE COEFFICIENT k_1 AS A FUNCTION OF TEMPERATURE FOR THE NITROGEN SYSTEM (DRIFT SOURCE DATA).

fig. 5.18 DRIFT ION SOURCE MASS SPECTRA FOR CARBON MONOXIDE

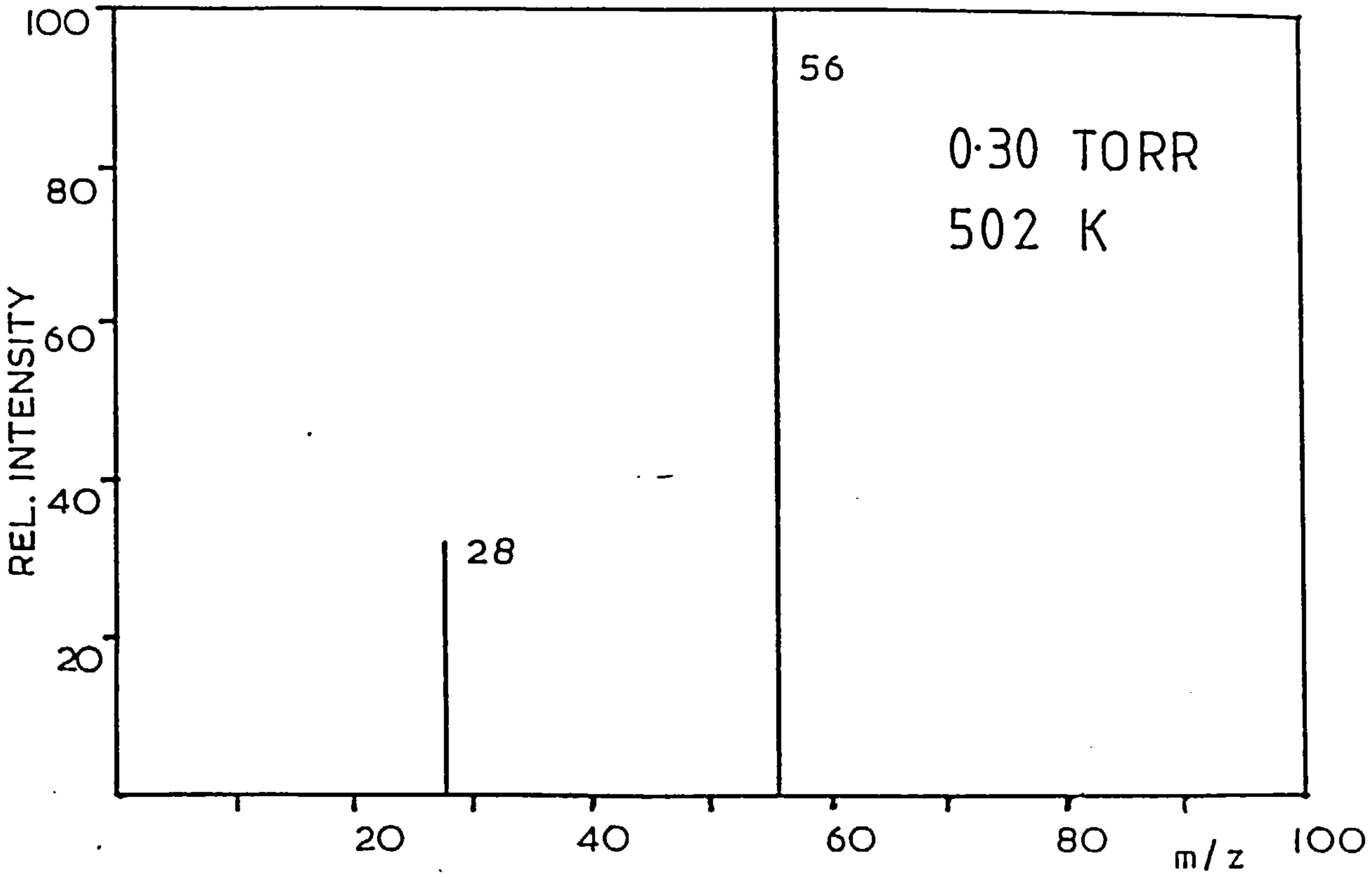

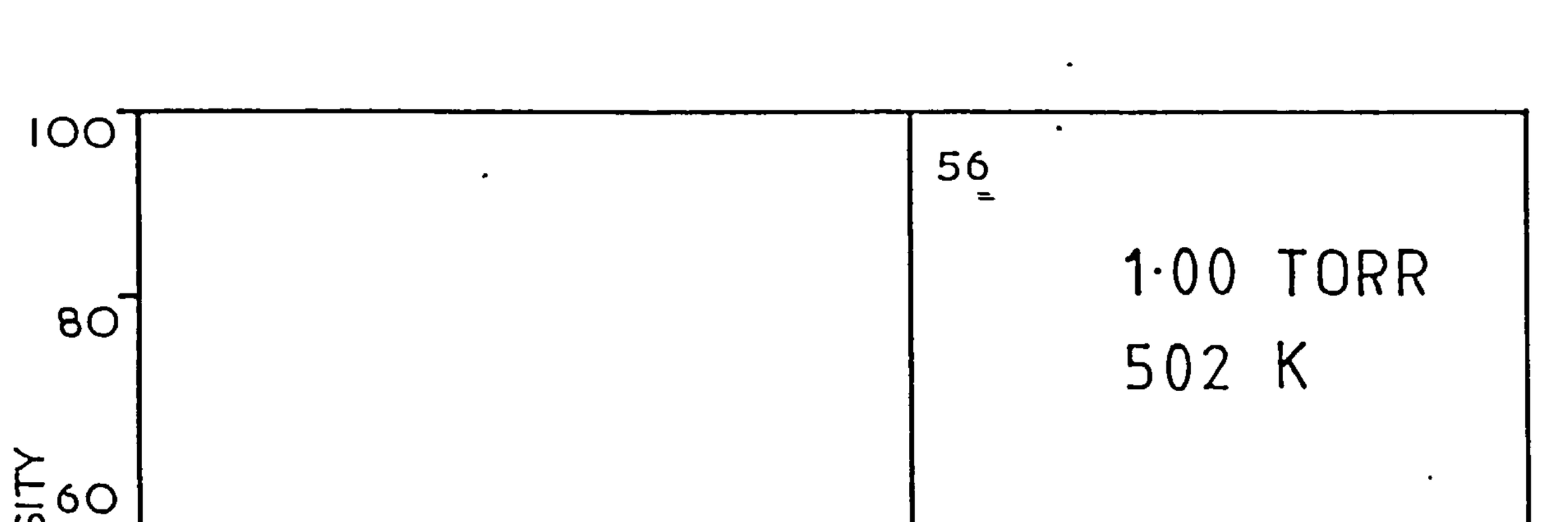

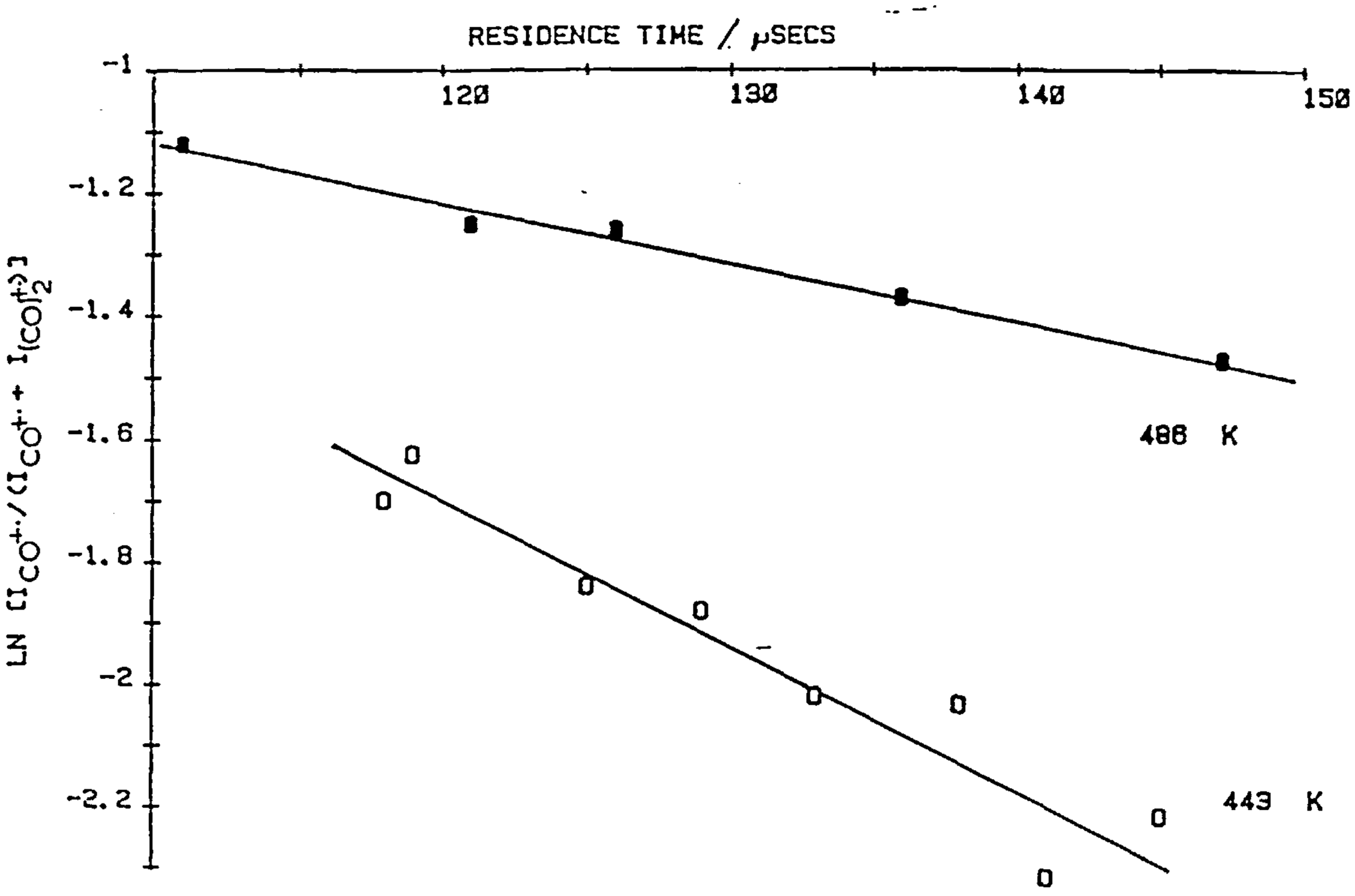

Fig. 5.19 THE EXTENT OF REACTION LN $[I_{CO^+} / (I_{CO^+} + I_{(CO)_2^+})]$ AS A FUNCTION OF THE ELECTRIC FIELD STRENGTH AT TWO TEMPERATURES.

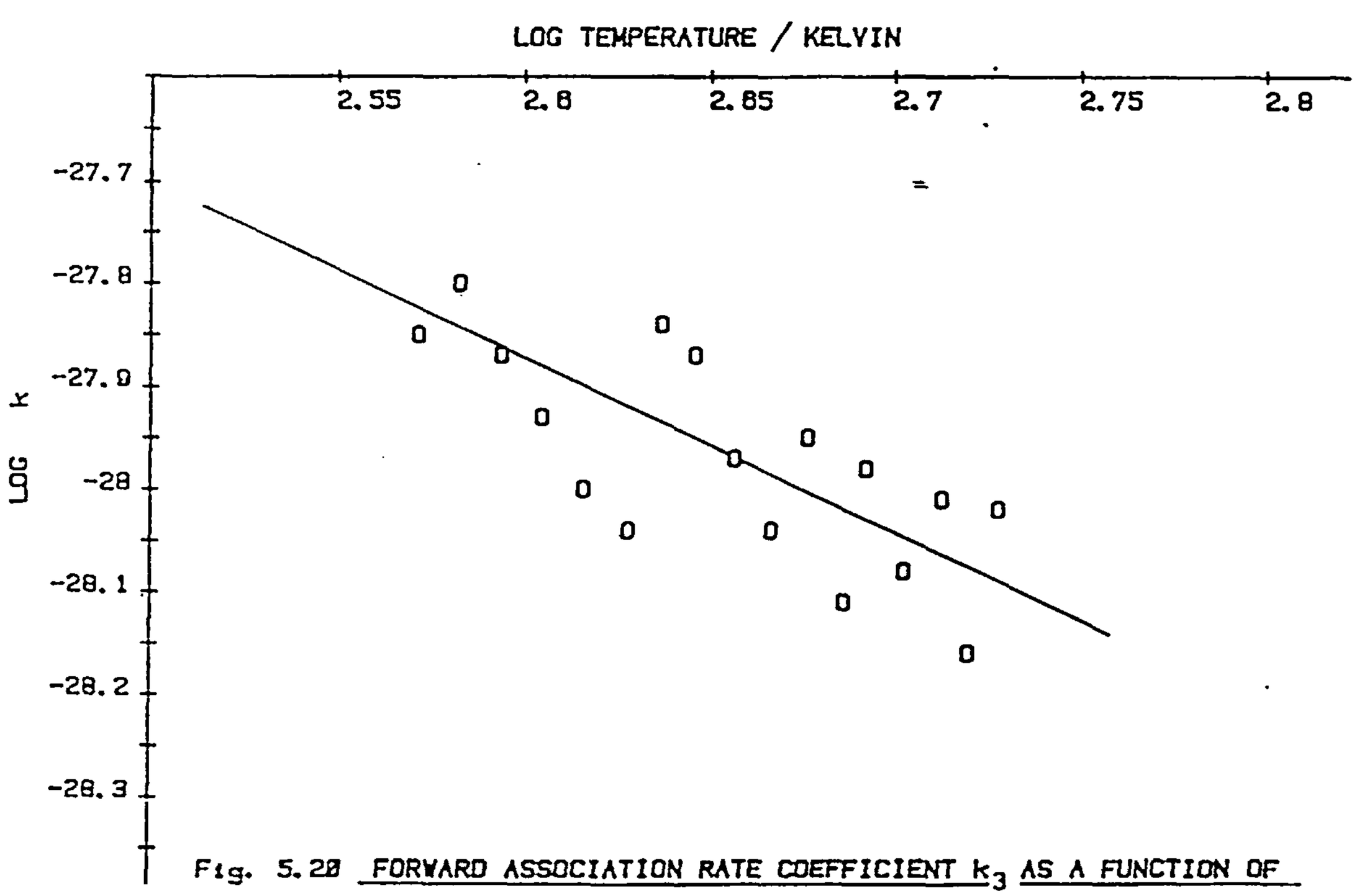

Fig. 5.20 FORWARD ASSOCIATION RATE COEFFICIENT k_3 AS A FUNCTION OF TEMPERATURE FOR THE CARBON MONOXIDE SYSTEM (DRIFT SOURCE DATA).

negligible and was thus not investigated. As in the previous system a $k=CT^m$ relationship was assumed and the corresponding log plot drawn, see Figure 5.20. The slope of this graph m was measured as -1.54±0.35.

5.3(iii) The Carbon Dioxide System

As studied in section 5.2(iii) this system is different from the first two studied in that the rate of dissociation of the complex is rapid enough to establish an equilibrium. Although the drift source operates only over a much reduced pressure range compared with that of the high pressure pulsed ion source, the very good linearity of the Keq versus pressure plot clearly indicates that equilibrium has been established, see Figure 5.22. A second test for equilibrium is the exact overlap of the primary and secondary ion residence time peak profiles[73]. This is shown in Figure 5.23 where the peak maxima coincide exactly. The Keq value was extrapolated to zero field conditions for each temperature at which it was determined within the range 460 and 580K. A van't Hoff plot was used to determine ΔH^o and ΔS^o for the reaction 5.3, see Figure 5.24. The results obtained were; $\Delta H^o = -65.9 \pm 2.3$ $kJmol^{-1}$ and $\Delta S^o = -81.6 \pm 4.3$ $JK^{-1}mol^{-1}$.

5.4 Discussion of Results

5.4(i) The Nitrogen Association

The general expression $k=CT^m$, used to describe the temperature dependence of termolecular association reactions, may be used to compare data obtained from both types of high pressure ion sources. For the pure nitrogen system the expressions obtained are:

Drift Source; $k(N_2) = 5.3.10^{-29}/(300/T)^{-1.75}$

HPPS; $k(N_2) = 7.6.10^{-29}/(300/T)^{-1.95}$

fig. 5.21 HIGH PRESSURE MASS SPECTRA OF PURE CO_2.

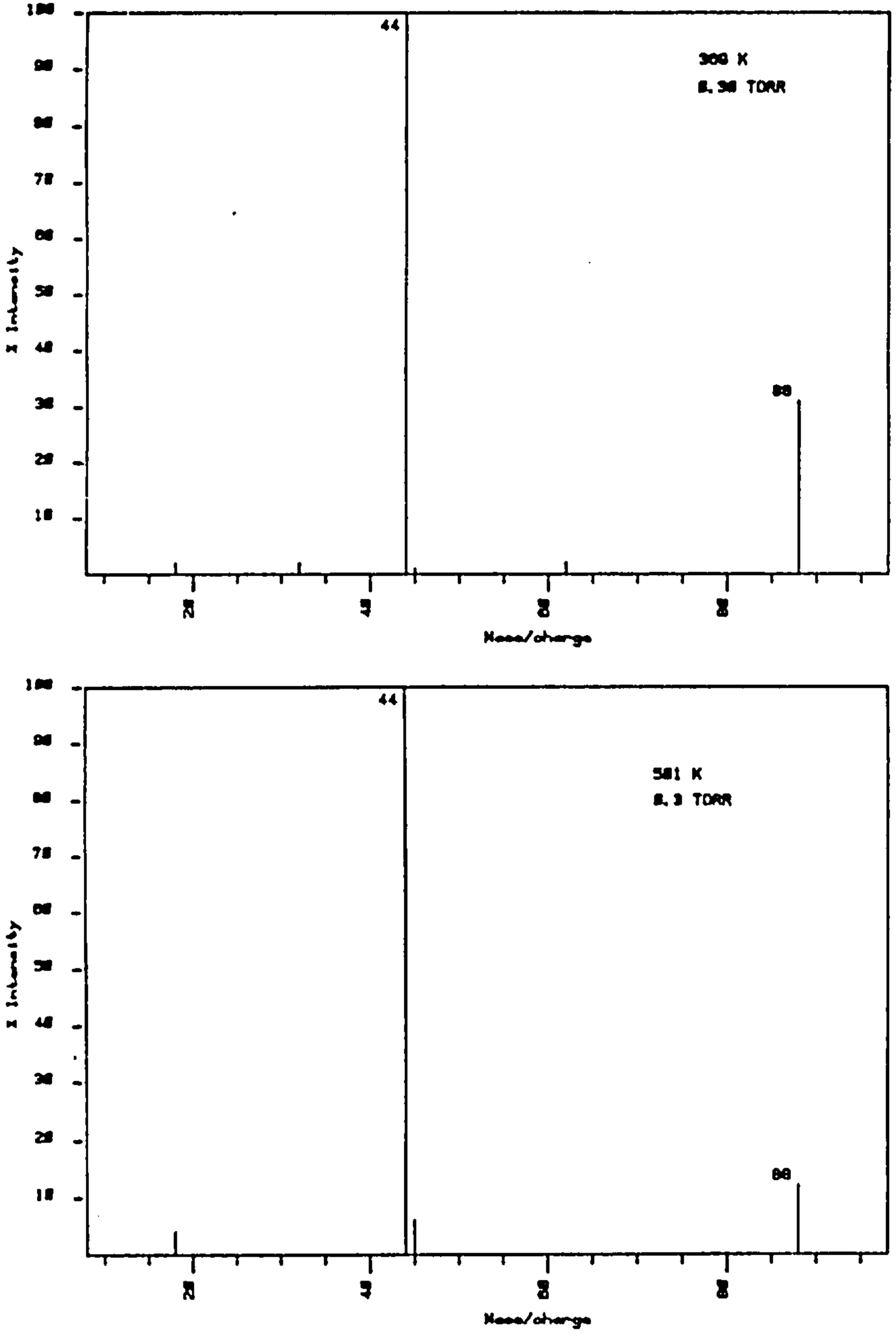

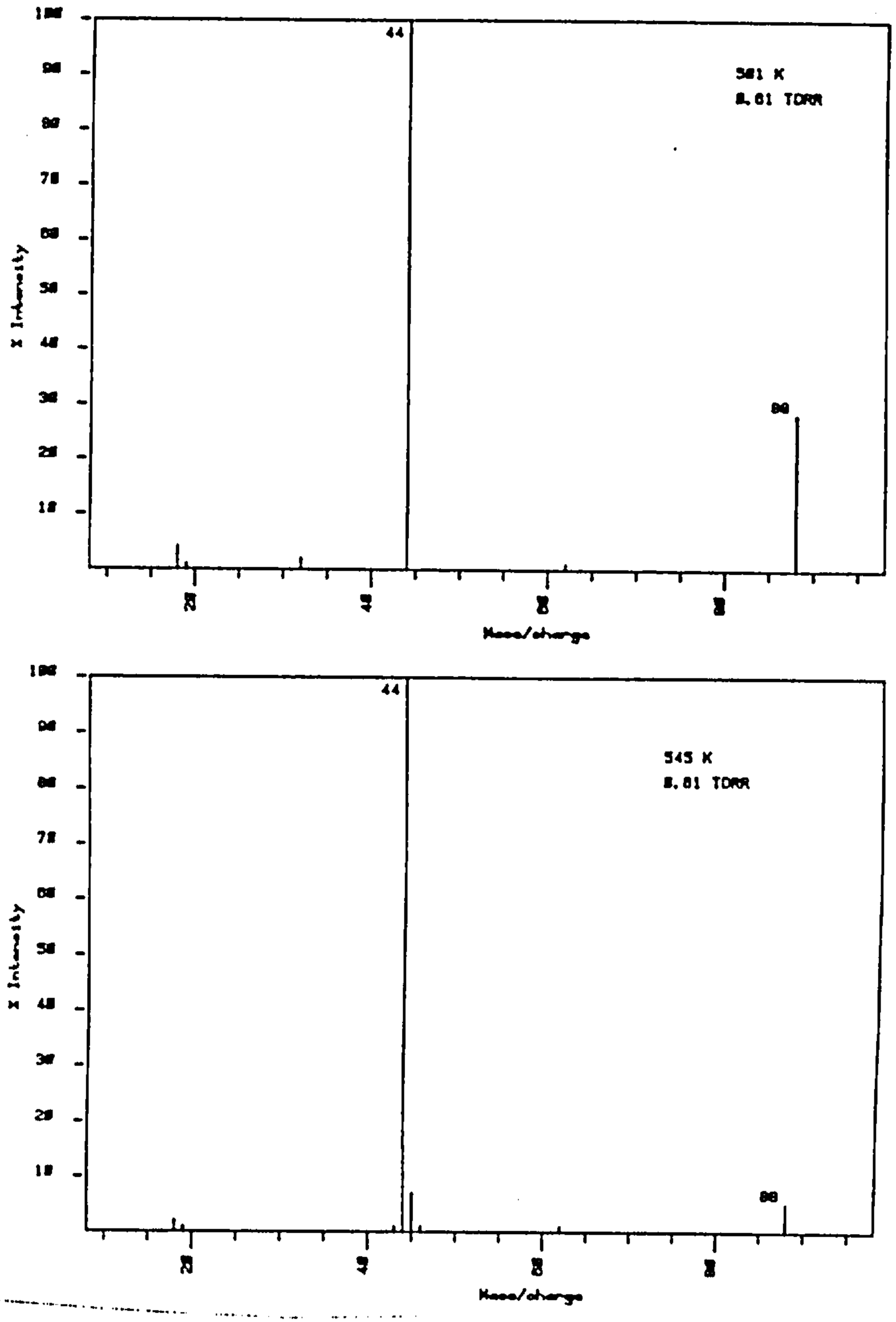

Fig. 5.22 VARIATION IN K_{eq} vs PRESSURE AT TWO TEMPERATURES FOR THE CARBON DIOXIDE ASSOCIATION.

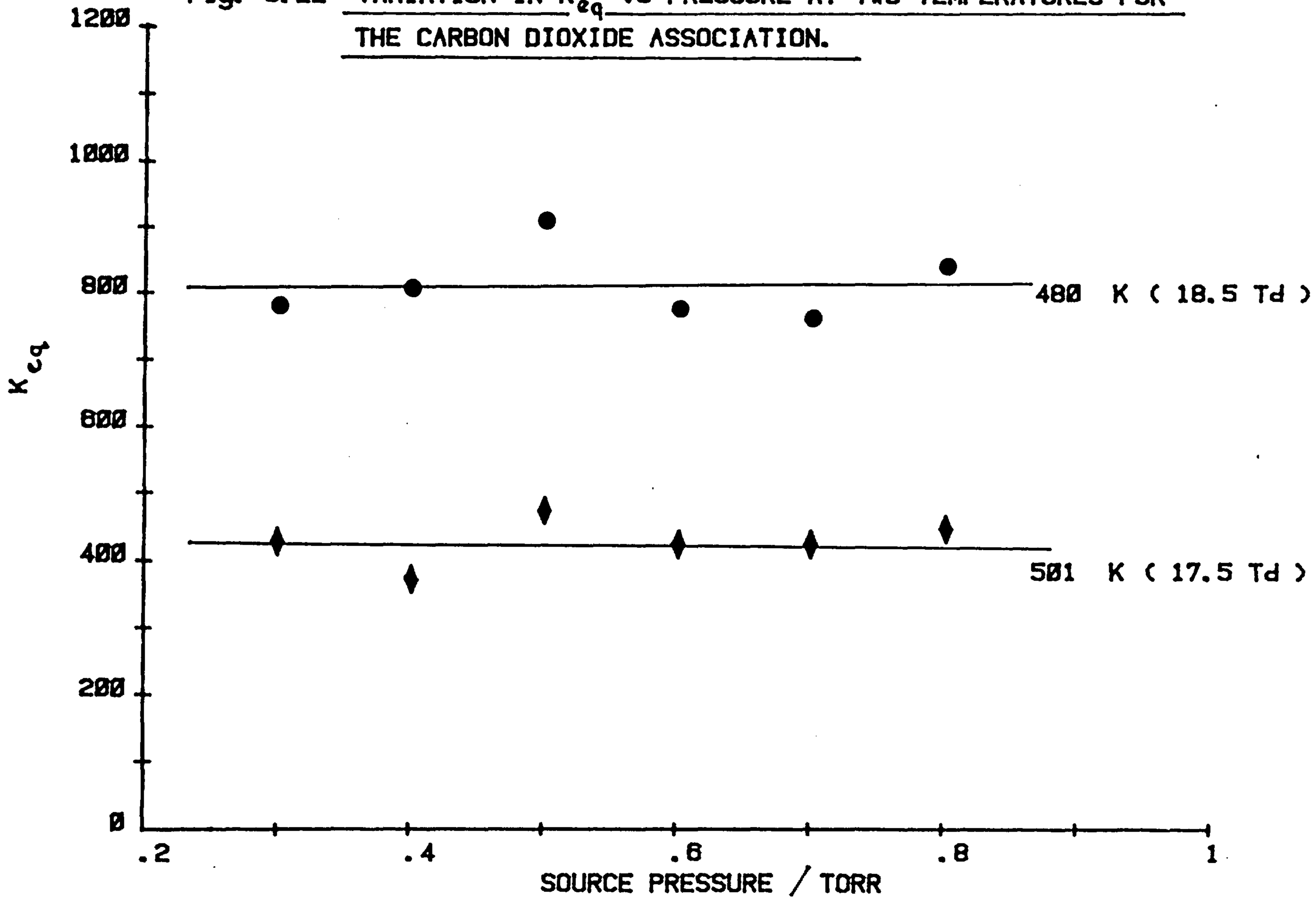

fig. 5.23 OVERLAP OF $CO_2^{+\cdot}$ AND $(CO_2)_2^{+\cdot}$ ION INTENSITY vs RESIDENCE TIME PEAK PROFILE

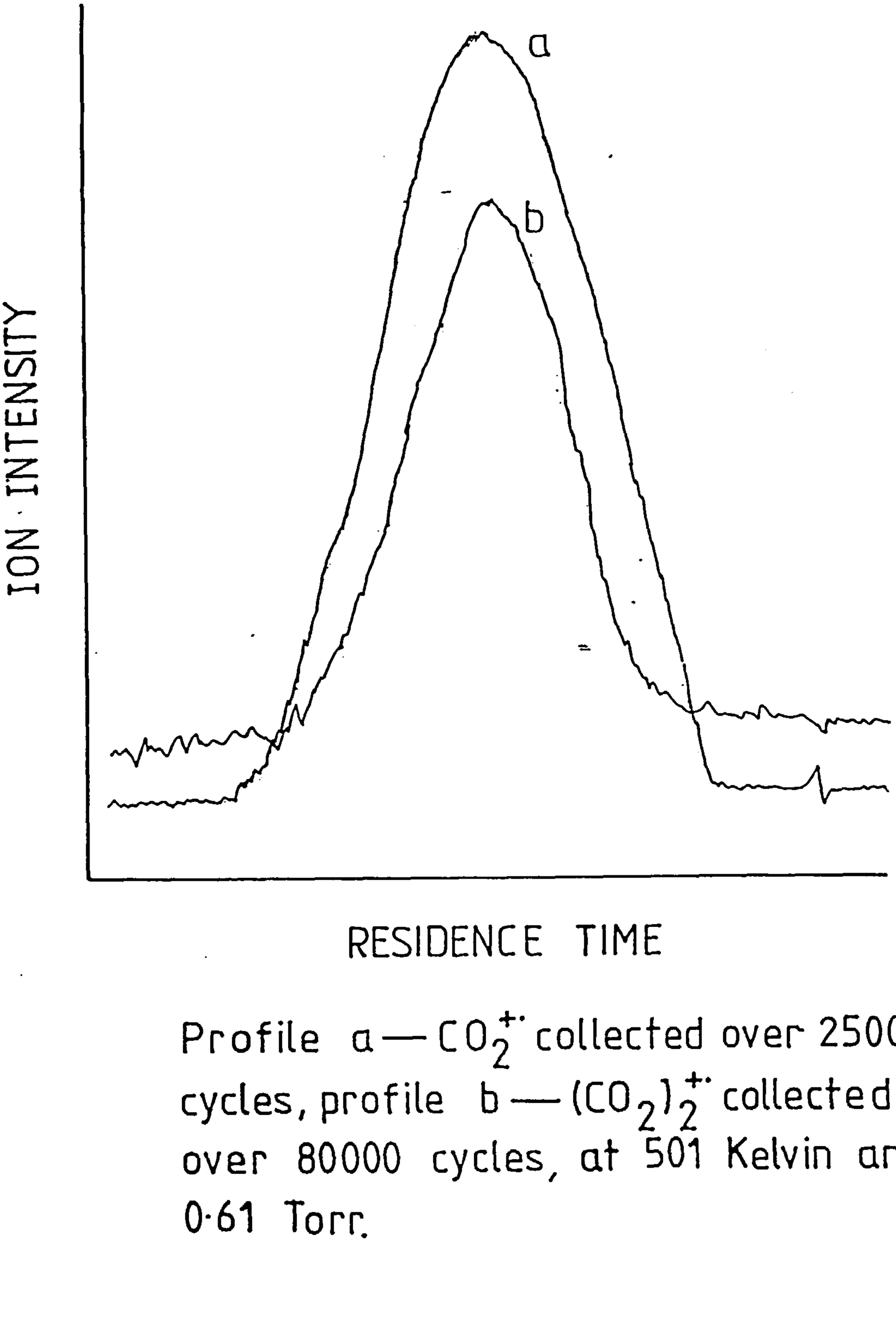

Profile a — $CO_2^{+\cdot}$ collected over 25000 cycles, profile b — $(CO_2)_2^{+\cdot}$ collected over 80000 cycles, at 501 Kelvin and 0·61 Torr.

These results were obtained over very similar temperature ranges of approximately 340 to 570K. Difficulties were experienced in collecting data at lower temperatures due mainly to heating effects from the filament. This resulted in data being collected over a small temperature gradient, of the order of 10K and was considered unreliable. The errors obtained in each temperature dependence value m were $\pm$13% for the HPPS and $\pm$31% in the case of the drift source.

Results for this system obtained by other groups are summarised in Table 5.1. The results for the temperature dependence in the four cases ref.73,80,81 and 82 range from -1.58 to -1.85 and show reasonably good internal self-consistency and are also in good agreement with the results reported here. Values of m such as 2.20[84], 3.80[67] and 4.0[85] reported by some authors are now considered to be incorrect. The results of Headley et al[67] determined over a similar temperature range to this work produce a rate constant expression of:

$$k(N_2) = 4.5.10^{-29}/(300/T)^{-3.8}$$

Although the extrapolated k value at 300K is in good agreement with the results presented here, this is now believed fortuitous as the temperature dependence for the above expression is almost twice as large as expected. This result is now believed to be incorrect as the repeat study discussed here, using similar apparatus but a new detection system has yielded a result in better agreement with other research groups. The previous detection system used a Biomac 1000 CAT for data collection. The seven bit resolution of the analogue to digital converter (ADC) of the Biomac only allowed ion current ratios of no more than 63:1 to be recorded on each cycle of data collection and thus discriminates against weaker signals. The Ortec multichannel analyser used for this work had better resolution due to a 20 bit ADC and could measure ion current ratios of 10^6:1 on each data collection cycle.

Table 5.1

Forward Rate Constants for the Nitrogen System

$$N_2^{+\cdot} + 2N_2 \xrightarrow{k_1} N_4^{+\cdot} + N_2$$

$k/.10^{-29} cm^6$ molecules$^{-2}s^{-1}$ (300 K)	Experimental Method	Temperature Dependence,m ($k=CT^m$)	Ref.
7.6	HPPS†	-1.95±0.26	This work
5.3	Drift Source	-1.75±0.55	This work
5.4	Drift Source	-1.67±0.07	73
5.0	Drift Tube	------	80
6.8	Drift Tube	-1.64	81
7.9	HPPS†	-1.70	82
6.0	CRESU‡	-1.85	83
5.0	Drift Tube	-2.20	84
4.5	HPPS†	-3.8±0.3	29,66,67
8.0	Drift Source	-4.0	85

† - HPPS - High Pressure Pulsed Ion Source

‡ - CRESU - 'Cinetique de reactions en encoulement supersonique uniform,'

The good agreement between this work and other studies and the overlapping temperature ranges at which this system has been observed means this reaction is now very well defined over a large temperature range, Figure 5.25. This is even more encouraging to observe such agreement as many differing experimental techniques were used to investigate this system. Averaging the first seven results in Table 5.1 yields a final rate constant expression for the nitrogen association of:

$$k(N_2) = 6.3.10^{-29}/(300/T)^{-1.75}$$

5.4(ii) The Carbon Monoxide Dimerisation Reaction

This system has not been as widely studied as the nitrogen system but a comparison may be made of data obtained using similarly designed ion sources. Table 2 lists the data obtained in this work with that of Meot-Ner and Field[82] and Bowers et al[84]. The very good agreement between data sets is also expressed graphically in Figure 5.26. The errors obtained for both sources are comparable at ±20 and ±23% for the HPPS and drift source respectively. The results shown for Headley et al for the temperature dependence of this reaction is approximately twice that obtained by the other groups. This is believed to be due to the error found in the detector system discussed above. The results obtained from this work may be used to express the third order rate constant in the form:

HPPS - $k(CO) = 1.43.10^{-28}(300/T)^{-1.54}$

Drift Source - $k(CO) = 2.05.10^{-28}(300/T)^{-1.54}$

These results are in very good agreement with results previously reported which are given in Table 5.2 and Figure 5.26.

An attempt was made to measure the equilibrium constant for the association:

Figure 5.25. Comparison of Experimental Results

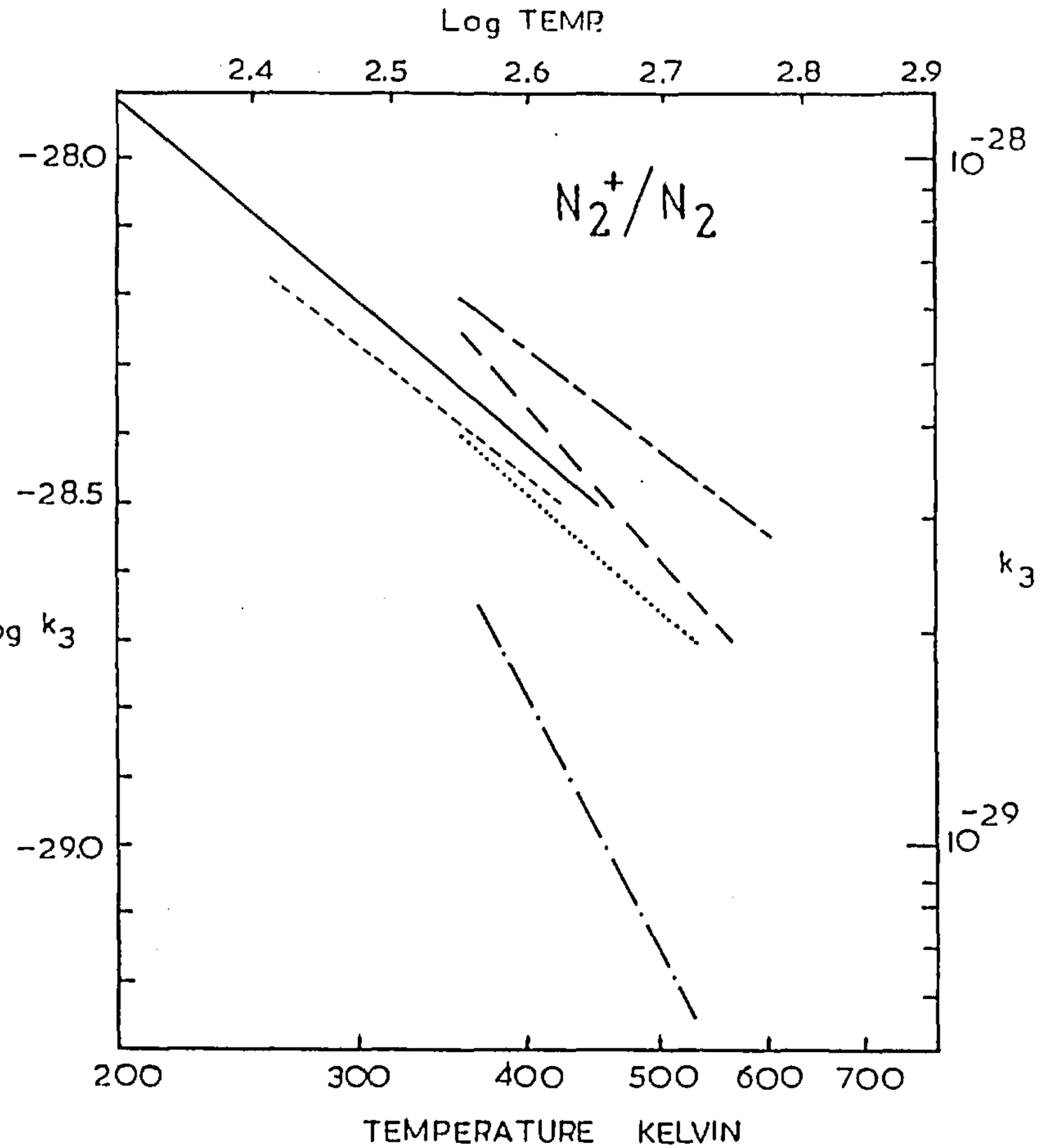

— — — — — m=-1.95 This work (HPPS)
····· m=-1.75 This work (Drift source)
---------- m=-1.67 Bowers et.al.[73]
———— m=-1.64 Böhringer and Arnold[81]
— - — - — m=-1.70 Meot-Ner and Field[82]
—·—·— m=-3.80 Headley et.al.[67]

fig. 5.26 Comparison of Experimental Results

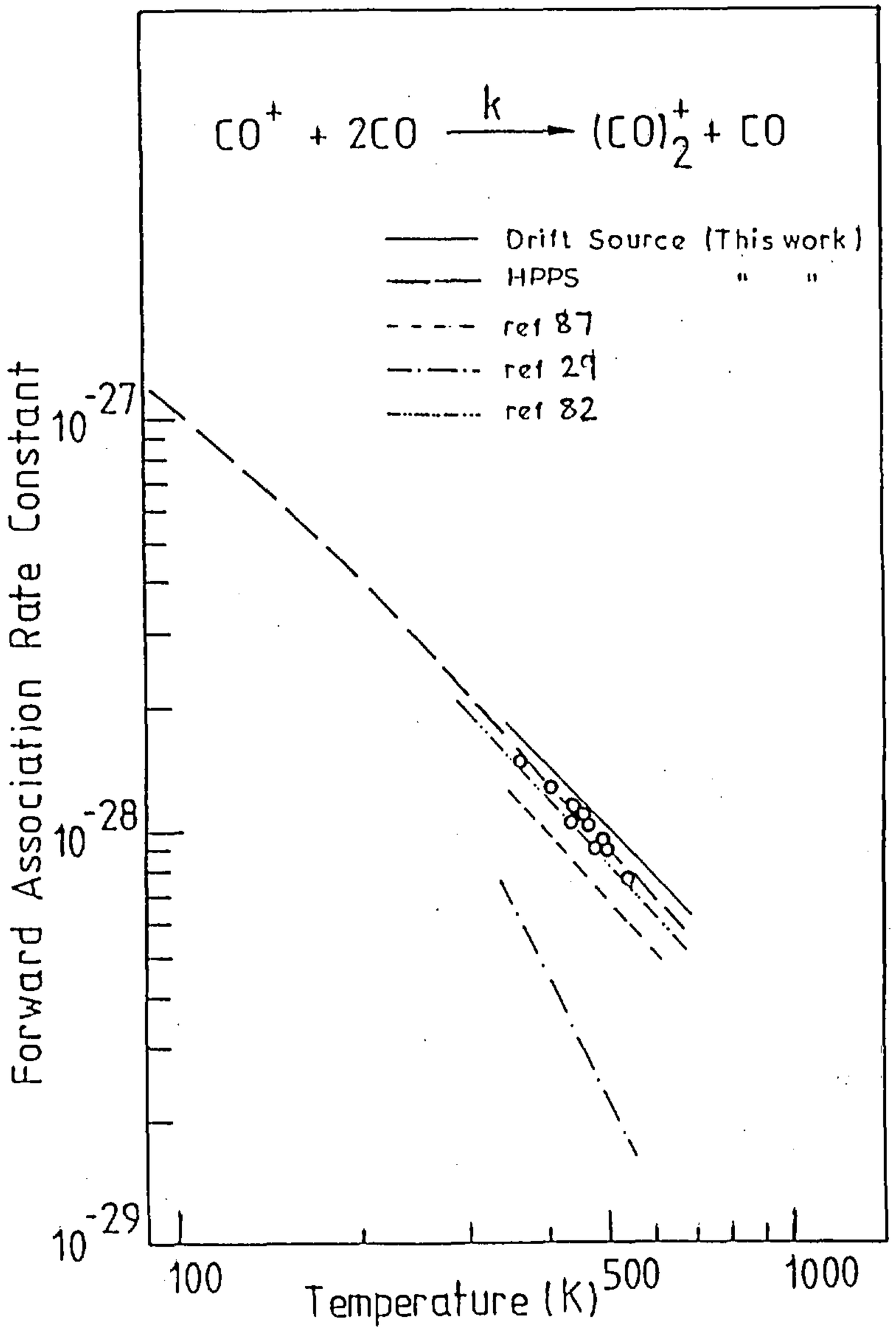

Table 5.2

Forward Rate Constants for the Carbon Monoxide System

$$CO^{+\cdot} + 2CO \xrightarrow{k_2} (CO)_2^{+\cdot} + CO$$

$k/.10^{-29} cm^6$ molecules$^{-2}s^{-1}$ (300 K)	Experimental Method	Temperature Dependence,m ($k=CT^m$)	Ref
14.3	HPPS*	-1.50±0.30	This work
20.5	Drift Source	-1.54±0.35	This work
19.7	Drift Source	-1.6±0.1	87
19.8	HPPS*	-1.5	82
12.5	Drift Tube	------	88
14.8	HPPS*	------	89
13.0	HPPS*	-3.3±0.2	29.66,67

* HPPS - High Pressure Pulsed Ion Source

$$CO^{+\cdot} + 2CO \rightleftharpoons (CO)_2^{+\cdot} + CO \qquad (5.17)$$

However, even working at the lowest possible temperatures available of 300K and investigating over a wide pressure range of 0.2 to 6.0 Torr, an equilibrium state could not be established. Removing the water impurity from the gas was essential for investigating this system. If the water content rose higher than 15vpm then $HCO^{+\cdot}$would be the major ion as a direct consequence of the high pressure used in the ion source. Operating at a water content level of less than 5vpm reduced the $HCO^{+\cdot}$ion intensity considerably, but still left the possibility of the following competing reactions occurring:

$$HCO^{+\cdot} + 2CO \longrightarrow (HCO.CO)^{+\cdot} + CO \qquad (5.18)$$

where the $HCO^{+\cdot}$species is formed by the process:

$$H_3O^{+\cdot} + 2CO \longrightarrow HCO^{+\cdot} + CO \qquad (5.19)$$

Results of Headley et al[66] and Meot-Ner and Field[82] show that the $CO^{+\cdot}$/CO association reaction (5.13) proceeds at a rate 68 times faster than the competitive reaction $HCO^{+\cdot}$/CO (5.13). The latter reaction is also less exothermic by 57.3 $kJmol^{-1}$ and consequently unlikely to compete with the reaction under study to any great extent. This is supported by the observation that under the conditions used the ions at m/z ratios of 29 and 57 accounts for less than 2% of the total ion current, as shown by Figures 5.7 and 5.18.

5.4(iii) Carbon Dioxide Equilibrium

The results for this system were obtained over a pressure range of 0.5 to 3 Torr in the HPPS as compared to 0.3 to 0.8 Torr for the drift source. The corresponding temperature ranges were more comparable however, with 400-570K to 460-580K used for the HPPS

and drift source respectively. The results obtained for the enthalpy and entropy of the dimer formation from the parent ion reaction (5.3) are:

$$\Delta H^o(HPPS) = -69.6\pm4.9 \text{ kJmol}^{-1}$$
$$\Delta H^o \text{ (Drift Source)} = -65.9\pm2.3 \text{ kJmol}^{-1}$$
$$\Delta S^o \text{ (HPPS)} = -87.0\pm10.0 \text{ JK}^{-1}\text{mol}^{-1}$$
$$\Delta S^o \text{ (Drift Source)} = -81.6\pm4.3 \text{ JK}^{-1}\text{mol}^{-1}$$

Although the drift source results were obtained over a slightly smaller temperature range the apparent accuracy of the enthalpy and entropy results are approximately one half of those obtained from the HPPS. For ΔH^o and ΔS^o, 3.5% and 5.2% standard deviation in the respective results was found for the drift source results compared to 7.0% and 11.5% standard deviation found in the HPPS data. Other literature results for this reactive system are given in Table 5.3 and in Figure 5.27; and it can be seen that there is good agreement between experimental results. It should be noted that although the temperature dependence of kinetic data obtained by Headley et al[29] was incorrect, the equilibrium data are in good agreement with literature values. It is assumed that the discrimination effects arising from the low dynamic range of the multi-channel analyser previously used, cancelled in the measurement of relative ion currents.

The data obtained for entropy changes have a larger error spread due to the long extrapolation required in ΔS^o determination, Figure 5.28. The average values of ΔH^o and ΔS^o found from this work are:

$$\Delta H^o = 67.8\pm3.6 \text{ kJmol}^{-1}; \qquad \Delta S^o = -84.0\pm7.2 \text{ JK}^{-1}\text{mol}^{-1}$$

It should be noted that these thermodynamic results are not the corresponding heat and entropy change on formation of the dimer species but the corresponding dissociation energy of $(CO_2)_2^{+\cdot}$ to CO_2^+ and CO_2. To calculate $\Delta H^o_f[(CO_2^+)]$ heats of formation of CO_2 and $CO_2^{+\cdot}$ are required and are readily obtained from the literature as -393.5 and 934.7 kJmol^{-1}

Table 5.3

Thermochemical Data for the Carbon Dioxide Equilibrium

$$CO_2^{+\cdot} + 2CO_2 \rightleftharpoons (CO_2)_2^{+\cdot} + CO_2$$

ΔH^o/kJmol^{-1}	ΔS^o/JK^{-1}mol^{-1}†	Experimental Method	Ref.
-69.6±4.9	-87.0±10.0	HPPS‡	This work
-65.9±2.3	-81.0±4.4	Drift Source	This work
-66.1±4.6	-81.6±1.3	Drift Source	73
-67.3±6.3	-88.4±8.4	HPPS‡	82
-66.1±4.6	-95.6±4.6	HPPS‡	29,66,67
-75.3±11.7	-95.4±4.6	Drift Tube	90

† - The standard deviation in ΔH^o and ΔS^o were all calculated using a least squares fit to the employed data points.

‡ - HPPS - High Pressure Pulsed Ion Source

fig. 5.27 Ln K vs 1/T for the reaction:

$$CO_2^{+\cdot} + 2CO_2 \rightleftharpoons (CO_2)_2^{+\cdot} + CO_2$$

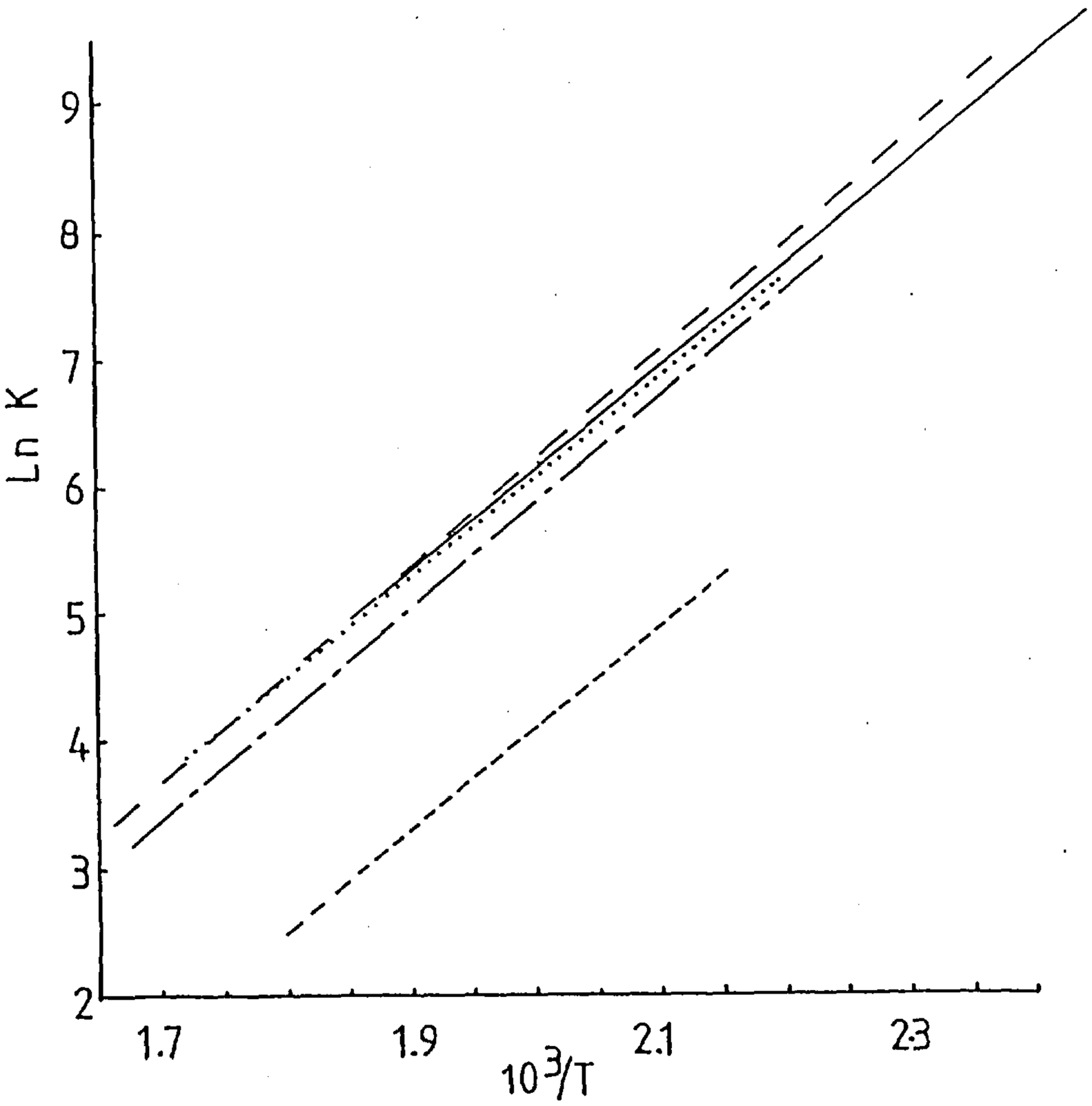

fig. 5.28 van't Hoff plots obtained for the CO_2 association.

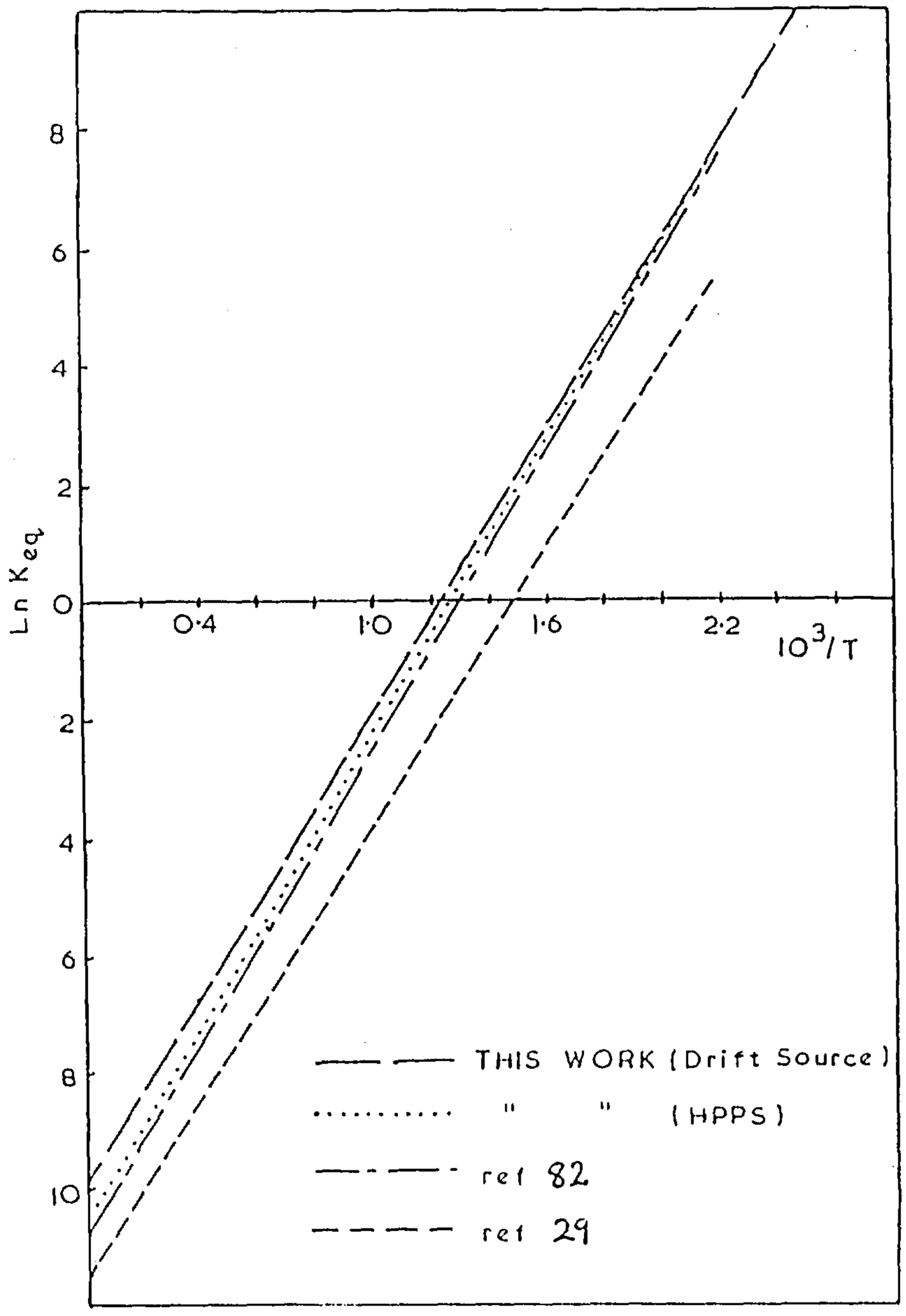

respectively. Thus, $\Delta H^o_f[(CO_2)_2^+]$ can be calculated as 474.4 $kJmol^{-1}$ as compared to 468.6±11.6 $kJmol^{-1}$ obtained by Rakshit and Warneck[90].

5.5 Discussion of Theoretical Treatments for Termolecular Association Reactions and Low Temperature Effects

Before a complete discussion on the results of this section, a quick review of recent developments in termolecular ion-molecule association reaction theory is required.

Several studies have been reported on the temperature dependence of rate constants for such reactions with encouraging agreement between experiment and theoretical results found at high temperatures (>200K). However, at lower temperatures (>100K) significant deviations in linearity of $\log_{10}k$ versus $\log_{10}T$ plots have necessitated the further developments of theory to account for this. Some authors have tackled this breakdown in the $k = CT^m$ relationship by applying phase space and RRKM theory[61,73] to this problem with some success. Other groups view that this attempt in the analysis of third-order rate constants is not valid and much simpler unimolecular rate theory is sufficiently accurate to use in predicting low temperature deviations[91].

If the results of all groups for the nitrogen association are considered over a temperature range of 20-650K we observe that at high temperatures very good agreement between theory and experimental results is obtained; Figure 5.29. This is more encouraging when it is considered that these resultes have been obtained by different groups using a variety of techniques. At low temperatures large deviations from linearity are observed for this, and other reactive systems with the exception of the results of Rowe et al[83]. For all data it was assumed that the experiments were conducted in the low pressure limit under the prevailing conditions.

The first attempt to explain the violation of the T^{-m} behaviour at low temperatures was proposed by Mickens[92] in 1983. Rather than considering the normal three body association reaction:

$$A^{+\cdot} + B + M \longrightarrow AB^{+\cdot} + M \qquad (5.20)$$

Mickens chose to consider the reverse, two body dissociation:

$$AB^{+\cdot} + M \longrightarrow A^{+\cdot} + B + M \qquad (5.21)$$

A Boltzmann energy distribution of the reactants and products is assumed owing to the decomposition reaction being 'slow'. The overall rate constant k for reaction (5.20) is then expressed as:

$$k_3 = AT^{-3} \int_0^{\infty} \exp(-E/k_B T)\sigma(E)dE \qquad (5.22)$$

where A is a constant which depends on known parameters, k_B is the Boltzmann constant and $\sigma(E)$ is the cross section for reaction (5.21) averaged over the initial and final states. If one considers the results from molecular beam experiments one may assume that σ will rise rapidly from a threshold energy E_o, to a maximum and then decrease with increasing energy to zero. The temperature dependence of k is thus determined purely by the energy dependence of $\sigma(E)$; from the threshold energy, $\sigma(E) \alpha (E-E_o)n$, as E tends towards E_o. At higher energy, $\sigma(E) \alpha E^{-m}$, as E tends towards infinity, where n,m and E_o are positive constants. The third order rate constants derived from equation (5.22) are: As T tends towards zero, $k_3 \alpha T^{n-2} \exp(-E_o/k_B T)$ and as T tends towards infinity, $k_3 \alpha T^{-m-1}$. Mickens then argues that as the temperature rises from zero, k_3 will rapidly pass through a maximum and then fall to zero with increasing temperature. The maximum k_3 value is thus a function of the threshold energy and hence different for each system studied. This theory is in excellent agreement with the results of Bohringer and Arnold[81] and Bowers et al[73] at low temperatures. However, Bates points out that this theory is based on the incorrect assumption that the cross section $\sigma(E)$ for the reverse process will depend on the energy

difference ($E-E_0$). In fact E_0 is zero because of the internal energy carried by the reactants and $n = -1/2$, due to the polarisation attraction. Ferguson[94] has recently reinforced Bates' view by emphasising that the activation energy cannot be used to explain this maximum. Comparison with results obtained by beam experiments must be viewed with great caution because of the very high energies at which such data are obtained.

Patrick and Golden[91] have also investigated these low temperature deviations from the $k_3=CT^m$ relationship, but in a much simpler way. Consider the Energy Transfer mechanism:

$$A^{+\cdot} + B \underset{k_b}{\overset{k_a}{\rightleftharpoons}} (AB^{+\cdot})^* \xrightarrow{k_s[M]} AB^{+\cdot} \qquad (5.23)$$

where $(AB^{+\cdot})^*$ represents the first-formed vibronically excited molecular state (see section 2.5(ii) for fuller account). For low pressure conditions, the rate determining step is the collisional stabilisation of the $(AB^{+\cdot})^*$ species. The nature of the transition state leading to the formation of $(AB^{+\cdot})^*$ is considered immaterial since it will equally effect both k_a and k_b and will not effect the ratio K, where $K=k_a/k_b$. Patrick and Golden then state that the overall rate constant k_3, is dependent only on the spectroscopic and thermodynamic parameters of stable molecules and may be simply calculated without the usual ambiguity in assigning transition state structures. They argue that this particular point has been overlooked by a number of groups who use phase space theory or RRKM theory in the analysis of k_3, without realising that the flux through the transition state can in no way effect the size of the temperature dependence. The results obtained by this simplified version of unimolecular rate theory are shown in Figure 5.29 and agree well with the high temperature results of this study. The theoretical results also show the substantial deviation from the third order behaviour that would be expected for this system in the commonly used HPPS experimental pressure range of 1 to 3 Torr.

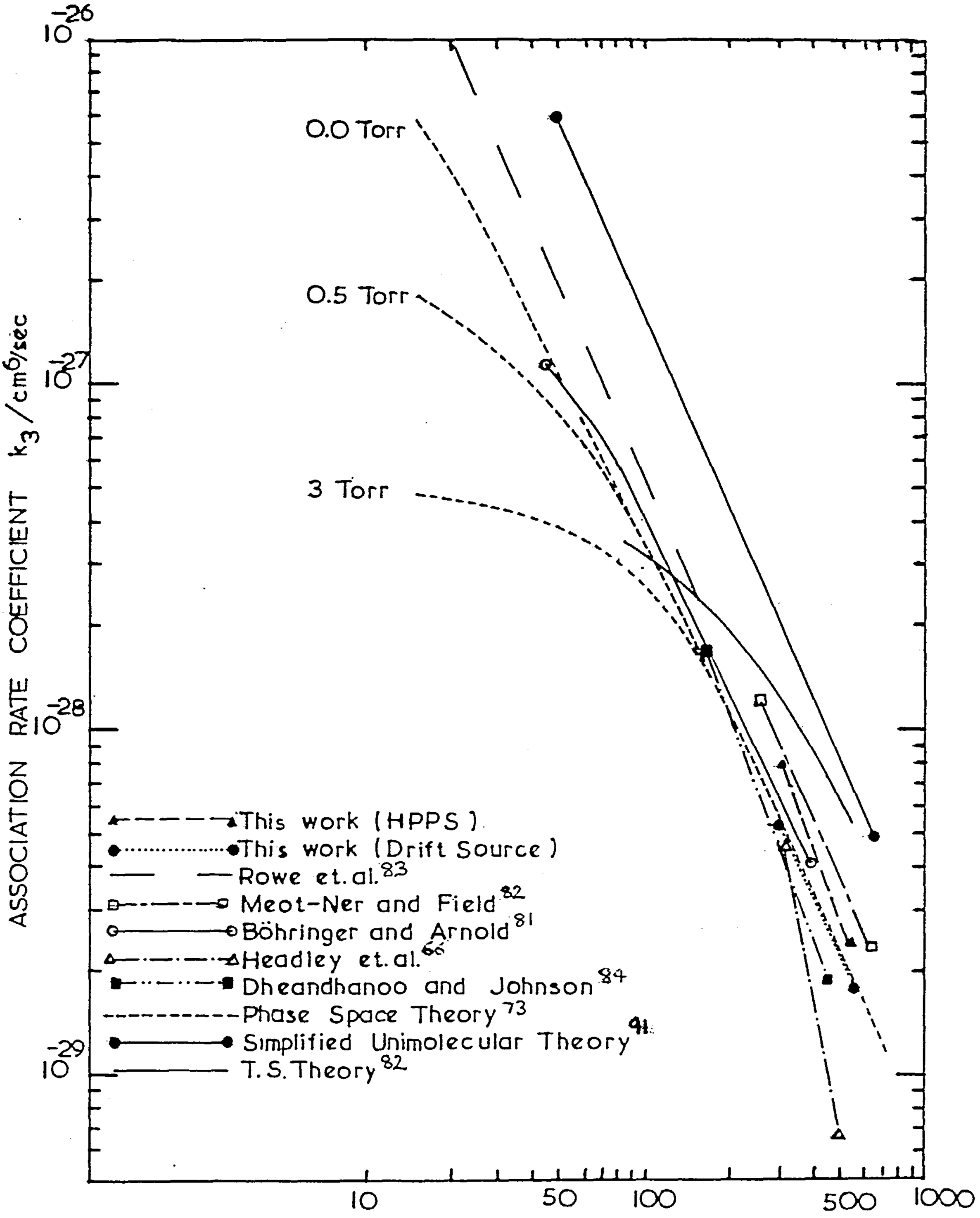

Figure 5.29. Comparison of Experimental to Theoretical Results for the Nitrogen Association.

Rowe et al[83] have recently investigated this system over the temperature range 20-160K and have shown that in their novel experimental technique that the association reaction leading to the formation of $N_4^{+\cdot}$ from $N_2^{+\cdot}$ and N_2 does not exhibit any deviations from a T^{-m} behaviour. This is believed to be due to this work being carried out at a sub-torr level so that the low pressure limit has been attained.

An older, but still reliable theoretical method used to determine the temperature dependence of a reaction is Transition State Theory as used by Meot-Ner and Field[82], and by Good[95]. Here the back dissociation of $(AB^{+})^*$ is treated in terms of RRK Theory. This leads to an equation for k_3 the overall third order rate constant of:

$$k_3 = C\left(\frac{D + rRT}{rRT}\right)^{S-2} \qquad (5.24)$$

where D is the dissociation energy of $AB^{+\cdot}$ and r is the number of square terms contributing to the internal energy of the complex, s is the number of active vibrations in RRK sense and C is a constant with respect to temperature. Applying this formula to both the N_2 and CO systems, where $D >> rRT$, a result of $s = 3.5$ for both dimeric species was deduced. This results in an expression $k_3(CO) = CT^{-1.5}$ in very good agreement with the experimental values obtained here. However, RRK Theory is now regarded as incorrect and quantitative deduction must be regarded with caution.

Although previous arguments state that phase space theory is inappropriate in describing the behaviour of these type of association reactions, it has been shown by the groups of Bowers et al[73], and Bass and Jennings[61], to be successful at low pressures and temperatures, <100K. At high temperatures (>200K) deviations occur in the expected results, since reactant vibrational modes become of greater significance. A thorough account of this treatment is given in section 2.6.

A comparison of the experimental results obtained here with various theoretical predictions of m, the temperature dependence, are shown in Table 5.4. It should be noted that the m value for Bowers' work[73] is calculated for a collinear structure for the dimer ion. Calculations were performed on all three possible structures, the colinear, T-shaped and rectangular structures. The m values obtained for each structure were within 10% of each other, showing that this treatment is rather insensitive to the various geometries in stark contrast to Meot-Ner and Field's calculations[82]. (For a review on the structure of dimeric species see ref 66). The experimental temperature dependencies are in very good agreement with the theoretical predictions of Meot-Ner and Field and Bowers. Experimental values of -1.5 and -1.85 were obtained for the pure CO and N_2 systems as compared to theoretical values of -1.5 and -1.7 which assumed linear complex structures. The temperature dependence values obtained by Patrick and Golden[91] appear somewhat higher than expected. This is believed to be due to an overestimation in the entropy of the nitrogen dimer. Another conclusion based on the above observations is that the low pressure approximation used by most experimentalists is invalid at low temperatures (<150K), although it appears to be valid enough at higher pressures.

The possibility of two body association reactions between the parent ion and neutral dimers has been discussed by Bohringer and Arnold[81]:

$$N_2^{+\cdot} + (N_2)_2 \longrightarrow N_4^{+\cdot} + N_2 \qquad (5.25)$$

Their calculations showed, however, that the density of neutral dimers was far too low to compare with the termolecular association reaction under study.

Table 5.4

Comparison of Theoretically Determined Temperature Dependencies 'm' from $k=CT^m$

Reaction Studied	H^o /kJmol^{-1}	S^o /JK^{-1}mol^{-1}	k_{-29} /10^{-29} cm^{-6}s^{-1} (300°C)	m Experimental Temperature Dependence[a]	m Predicted by T.S.T.[b] Linear Complex	m Predicted by T.S.T.[b] Non-Linear Complex	m Phase Space Theory[d] Any Structure (± 5%)	m Simplified Unimolecular Theory[e] Linear Complex
$CO_2^{+\cdot} + 2CO_2 \rightleftharpoons (CO_2)_2^{+\cdot} + CO_2$	-67.8[a]	-84.3[a]	-	-	-	-	-	-
$N_2^{+\cdot} + 2N_2 \longrightarrow N_4^{+\cdot} + N_2$	-95.5[c]	-81.7[c]	6.3[a]	$T^{-1.85\pm0.40}$	$T^{-1.5}$	T^{-1}	$T^{-1.7}$	$T^{-1.99}$
$CO^{+\cdot} + 2CO \longrightarrow (CO)_2^{+\cdot} + CO$	-106.4[b]	-	18.0[a]	$T^{-1.5\pm0.33}$	$T^{-1.5}$	T^{-1}	$T^{-1.7}$	-

a Average Experimental Value for HPPS and Drift Source

b Meot-Ner and Field (ref.82)

c Payzant and Kebarle (ref.85)

d Bowers et al (ref.73)

e Patrick and Golden (ref.91)

5.6 Comparison of the Performance of Both Ion Sources

The results obtained from the ion sources show that both are capable of producing similar and reproducible data for both ion molecule rate and equilibrium constant determination. This appears more encouraging when it is considered that both sources operate by different methods: one utilizes the free diffusion of ions out of a chamber, while the other acts essentially as a small drift tube by extracting the ions out with the aid of an appropriate electric field. Both sources have their advantages and disadvantages without either one being superior.

The temperature ranges for both ion sources are essentially the same being approximately 310 to 625K.

The pressure range of the high pressure pulsed ion source (HPPS) is very impressive, operating at up to ten Torr, although normal source conditions use pressures of 0.2 to 6 Torr. The drift source will operate up to 1.5 Torr, but under normal experimental conditions, a range of 0.3 to 0.8 Torr is used. This low pressure range is a consequence of the low energy of the ionisation electron beam used. The duration of the pulse of electrons is of the order of 5μsecs at 17eV energy. However the drift source has one major advantage over the HPPS source. The mass spectra obtained from both ion sources are very different when considering the amount of fragmentation that occurs within the parent ions. This fragmentation is limited in the drift source as a direct consequence of the low energy of the incident electron beam, Figures 5.14, .18 and .21. The HPPS source uses more vigorous initial source conditions, typically an electron pulse of 400eV for a 20μsec duration. Thus, all types of gaseous species in the source are ionised and there is a high degree of fragmentation occurring. For the 'simple' one component systems reported on so far this consideration is not important. For more complex two or three component mixtures, ionisation of the bath gas, which occurs to a great extent in the HPPS source but not at all in the drift source under suitable conditions, may be undesirable if the bath gas ions do not promptly charge-transfer to the reactant under study. Bath gas or primary ions may easily

interfere with the ion-molecule reaction under study by reacting with other neutral species present and a competition ensue. This is considered further in chapter six.

Because the drift source makes use of a low energy ionising electron beam, the intensity of ions obtained from an ion chamber is considerably reduced compared to the HPPS source. This low ion beam intensity makes it more difficult to use a large temperature range when studying certain systems since one of the ionic species may become so low in abundance that a reliable signal/noise ratio is unobtainable. However, for rate constant determination only 5% of the collected peak profile (the late afterglow region) from the HPPS source is used, as compared to the whole peak profile from the drift source.

Table 5.5 shows the main differences in the temperature and pressure ranges over which data are collected. On the whole the HPPS source has a larger pressure and temperature range for the systems studied.

Manipulation of the raw data to obtain results for rate constant determinations is very different for each ion source. Only one peak (the primary reactant ion) is monitored in the HPPS source, compared to the two required for the drift source. For the HPPS ion source, slope determination of the ln $I_{A2}^{+\cdot}$ versus reaction time is very accurate with an operating error in the slope of less than $\pm$5%. The drift source also produces reliable data although on the initial setting up of the apparatus, great care must be taken in using the correct conditions. As described in chapter 4.4 the pressure range, electron energy, pulse duration and the field strength (E/P) must all be considered before 'true' ion arrival time distributions are obtained. Primary and secondary ion currents must also be monitored in rate constant and equilibrium constant determinations. The time resolution of the multichannel analyser (MCA) was restricted to one channel, such that the residence time maximum in the peak profiles may be measured to an accuracy of $\pm$10μsecs. The peak centroid operation available in the MCA was inaccurate for these systems at the extremes of conditions owing to the tailing off of the peak profiles towards longer reaction times, thereby limiting its use.

Table 5.5(i)

Comparison of Ion Source Operating Conditions for the Pure N_2, CO and CO_2 systems

System	High Pressure Pulsed Ion Source	Drift Source
$N_2^{+\cdot}/N_2$	360 - 588K 0.50 - 3.50 Torr	331 - 562K 0.59 - 0.65 Torr
$CO^{+\cdot}/CO$	403 - 615K 0.20 - 3.51 Torr	373 - 533K @ 0.64 Torr
$CO_2^{+\cdot}/CO_2$	400 - 570K 0.5 - 3.0 Torr	460 - 580K 0.3 - 0.8 Torr

Table 5.5(ii)

General Comparisons of Ion Source Characteristics

	High Pressure Pulsed Ion Source	Drift Source
Temperature Range	Very similar for both ~ 310 - 625K	
Pressure	0.2 - 6.0 Torr Operates at any pressure in range.	0.3 - 0.8 Torr Preferable to operate at highest possible pressure.
Spectra	All gases in source ionised. Large amount of fragmentation. Much clustering observed.	Normally only two ionic species formed, the primary and any subsequently formed ions.
Peak Profile	Only the late afterflow region of profiles used in rate/equilibrium constant determination.	All of the collected peak profile required for equilibrium studies. Only peak maximum needed in rate constant determination.

Chapter Six

Termolecular Association Reactions Studied in Two-Component Systems

6.1 Introduction

The investigation of gas phase ion cluster chemistry is a current area of intense interest. Work is focused mainly on three aspects of association products; their binding energies[96], formation mechanisms[97] and the chemical reactivity of such species[98,99]. Clustering or association reactions are extremely temperature sensitive and it is thus central that if a full understanding of the mechanisms involved in cluster formation is to be achieved then their dependence must be fully characterised.

Such association reactions are believed to follow an Energy Transfer mechanism:

$$A^{+\cdot} + B \underset{k_b}{\overset{k_a}{\rightleftharpoons}} (AB^{+})^{*} \qquad \text{(i)}$$

$$(AB^{+})^{*} + M \xrightarrow{\beta k_s} AB^{+\cdot} + M \qquad \text{(ii)} \qquad (6.1)$$

which has been discussed previously (sections 2.5(ii) and 5.5), where k_a and k_s are given by classical collision theory.The area of interest in this work is to determine whether β, the collisional stabilisation efficiency, has any temperature dependence, and how β might vary as the bath gas M varies.

The systems studied in this investigation were the carbon monoxide and nitrogen dimer association reaction using helium, neon and argon bath gases:

$$CO^{+\cdot} + CO + M \xrightarrow{k_f} (CO)_2^{+\cdot} + M \qquad (6.2)$$

$$N_2^{+\cdot} + N_2 + M' \xrightarrow{k_f'} N_4^{+\cdot} + M' \qquad (6.3)$$

where M = He, Ne and Ar, and M'= He and Ar.

The advantages and disadvantages of both ion source designs have been discussed. The following results were obtained by using the high pressure pulsed electron beam ion source (HPPS) for the following reasons. It would have been desirable to use the drift source for this investigation so as to allow a direct comparison with the results of Bowers et al[73,87] who used a similarly designed ion source. Unfortunately a problem of continuous background ionisation occurred in both sources which resulted in sample gas ionisation even when the source filaments were disconnected. This is believed to be due to some form of field ionisation or to a stray discharge occurring, although a great deal of time was spent investigating this phenomenon to no avail. The problem rendered the drift source inoperable as its pulse mode of operation could not be used. However, the HPPS source was able to operate normally due primarly to the greater ion beam intensity that this source produces. The continuous ionisation problem just resulted in a noisier baseline than usual at low pressures and was completely unnoticeable at higher pressures (> 1.5 Torr).

A possible source of error that could occur in both sources is due to the Penning Ionisation phenomenon[100]:

$$m^* + P \longrightarrow m + P^{+\cdot} + e^- \qquad (6.4)$$

Here ionisation of a bath gas may result in the formation of metastable species m^* which can generate the reactant ion $P^{+\cdot}$ in the reaction chamber by the outlined Penning Ionisation

reaction. This would result in the peak profiles being tailed towards longer reaction times, and would significantly effect any data collected in the drift source unless the bath gas has a higher ionisation potential than the reagent ions. This effect would thus limit the number of species which could be investigated. In the HPPS source the reactive system is allowed to diffuse out of the chamber and there is abundant time for such reactions to occur in the ambipolar region of the profile not effecting the free diffusion section where data are obtained.

6.2 Results of the Carbon Monoxide Systems

(i) Carbon Monoxide/Helium System

The high pressure ion source was used to study reaction 6.5 over the temperature range 324 to 487K and pressure range 2 to 6 Torr. Lower pressures could not be used during data collection due to the low abundance of the primary $CO^{+\cdot}$ and secondary $(CO)_2^{+\cdot}$ ions produced. At higher pressures the background noise level became too large for an acceptable signal/noise ratio to be collected. The ion source was operated using an electron pulse of 400eV for a 20μsec duration. The predominant species formed are shown in Figure 6.1 and consist mainly of the He^+; $CO^{+\cdot}$ and $(CO)_2^{+\cdot}$ ions. Small amounts of impurity species were formed such as $HCO^{+\cdot}$ and $(H_2O.CO)^+$; but these accounted for less then 8% of the total ion beam current.

$$CO^{+\cdot} + CO + He \xrightarrow{k_7} (CO)_2^{+\cdot} + He \qquad (6.5)$$

$$(CO)_2^{+\cdot} + He \xrightarrow{k_{-7}} CO^{+\cdot} + CO + He \qquad (6.6)$$

$$CO^{+\cdot} \xrightarrow[diff]{c'} \text{lost on walls} \qquad (6.7)$$

fig. 6.1 HIGH PRESSURE MASS SPECTRA OF 1% CO IN He.

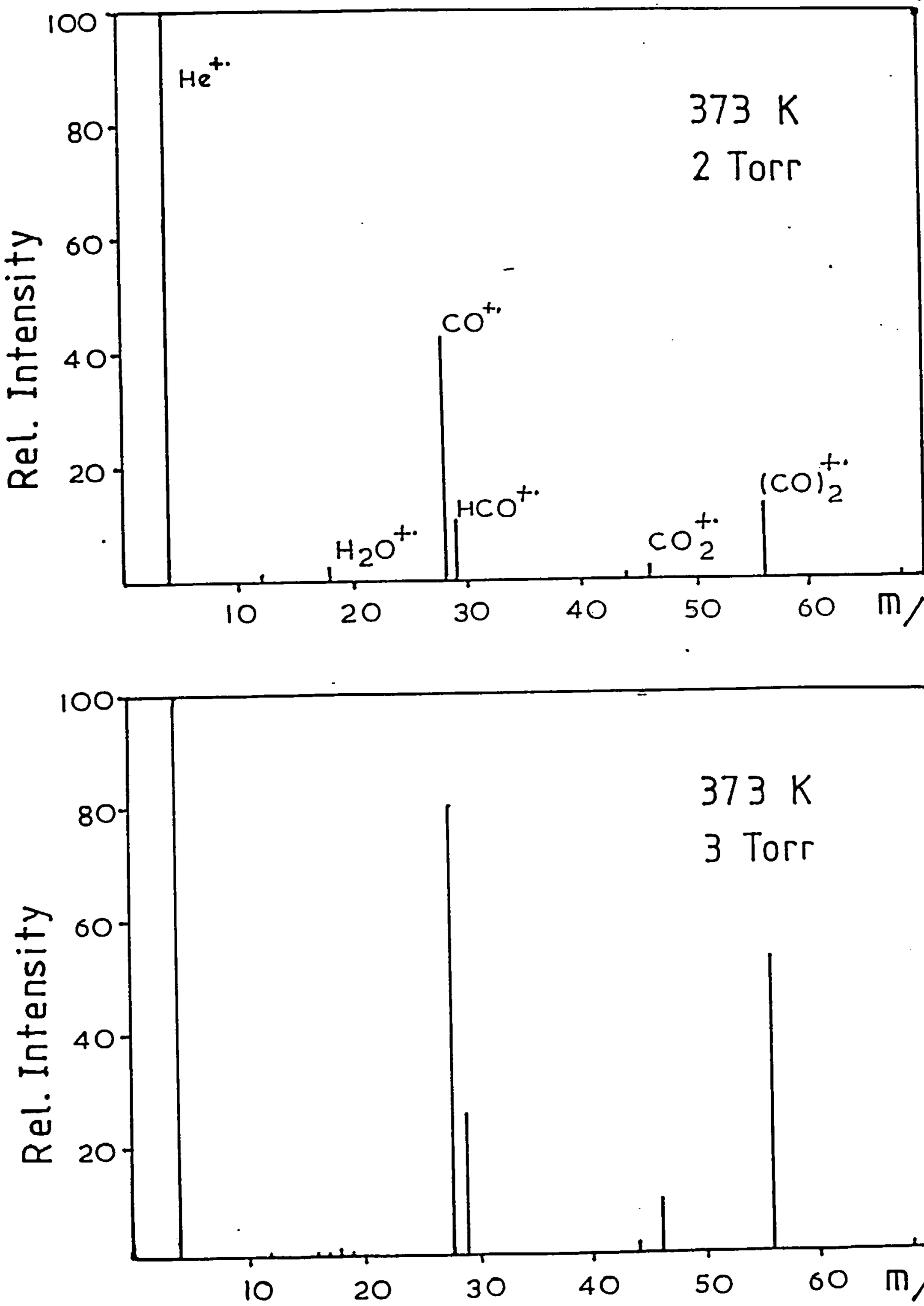

$$(CO)_2^{+\cdot} \xrightarrow[\text{diff}]{d'} \text{lost on walls} \qquad (6.8)$$

The dissociation reaction 6.6 was first investigated by use of the method outlined in section 5.2(i). For a two-component system such as this where the primary species is present at less than 1% of the total gas pressure, the expression obtained for the slope S of the ln $I_{(CO)2^{+\cdot}}$ versus reaction time is:

$$S = k_{-7}[He] + \underline{d}/[He] \qquad (6.9)$$

Thus a plot of S[He] versus $[He]^2$ is linear with a slope equal to the rate constant for the dissociation process and an intercept $\underline{d}$, the diffusive loss constant, see Figure 6.2 for an example plot. The rate constant is essentially zero and the reaction 6.6 is assumed not to form a significant amount of the primary ion CO^+:

The forward association reaction 6.5 was treated as outlined in section 3.9(ii). The expression obtained for the slope S of the ln $I_{CO^{+\cdot}}$ versus reaction time for the ion peak profile in the late afterglow region can be written in the form:

$$S[He] = k_7[CO][He]^2 + \underline{c} \qquad (6.10)$$

where k_7 is the rate constant for reaction 6.5 and c is the diffusive loss constant. An example of a rate constant determination is shown in Figure 6.3. This example at 376K is unusual as above approximately 4 Torr the slope of this plot is zero. The lower pressure region yields a rate constant of $9.8.10^{-29}$molecules^{-2}cm^{6}sec^{-1}. The levelling out of this function was also observed at higher temperatures under high gas density conditions (> 5 Torr) although to a much lesser degree.

fig. 6.2 PLOT OF S[He] vs $[He]^2$ FOR DETERMINATION OF THE RATE CONSTANT FOR THE DISSOCIATION REACTION: $(CO)_2^{+\cdot} + He \longrightarrow CO^{+\cdot} + CO + He$

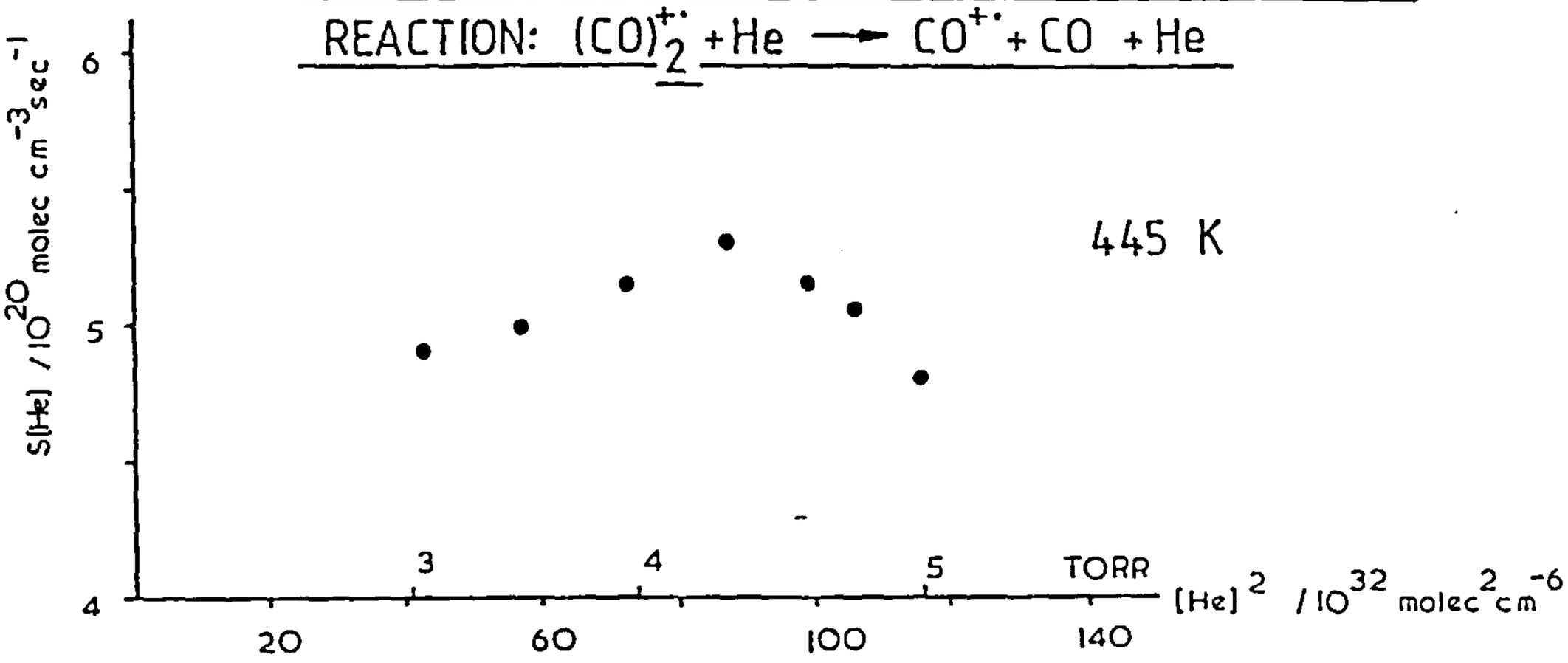

fig. 6.3 SEPARATION OF $CO^{+\cdot}$ REACTION RATE AND DIFFUSIVE LOSS CONSTANTS IN 1% CO IN He AT 376 K.

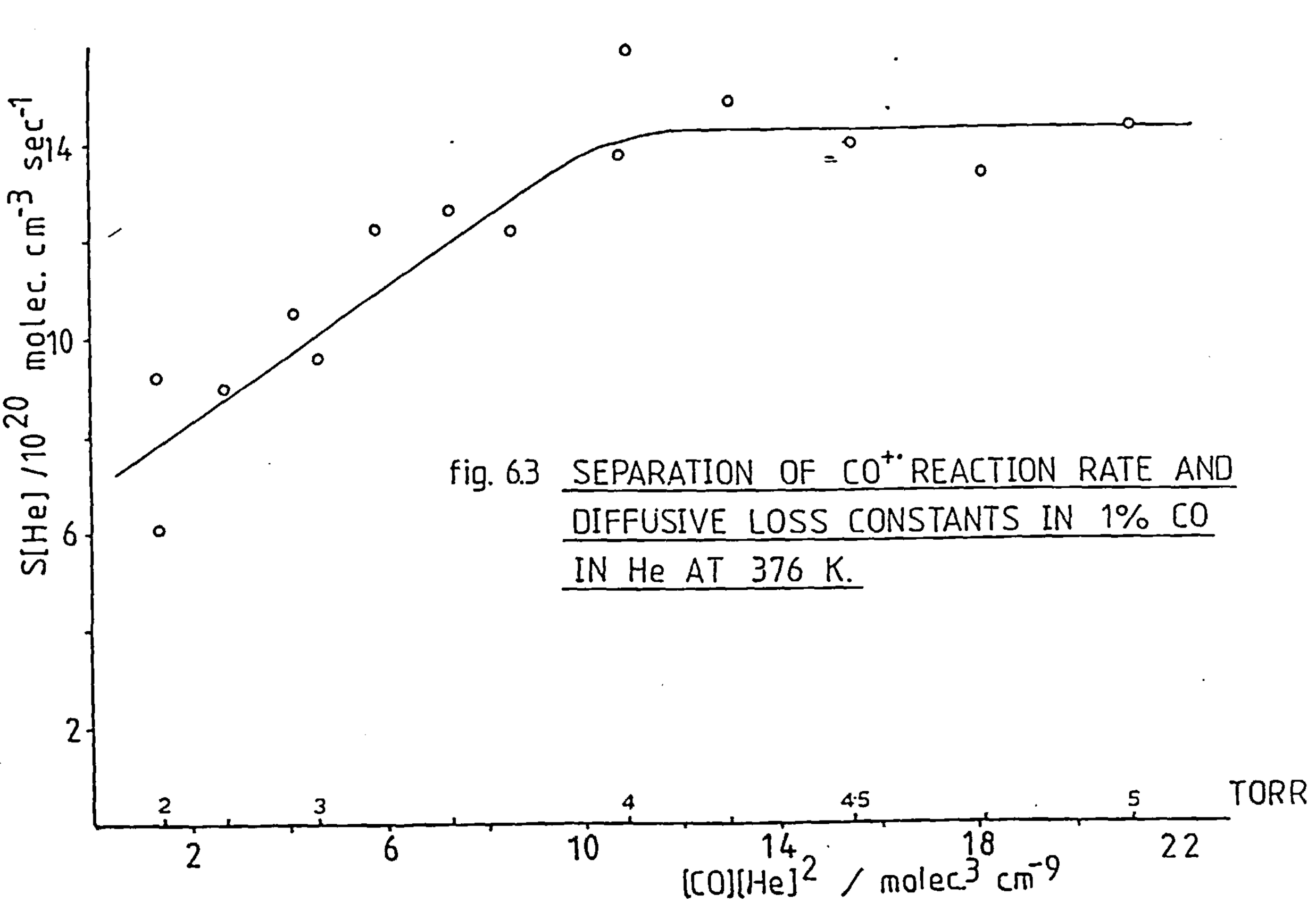

The conventional $k_f = CT^m$ form for the temperature dependence of this system was assumed and a corresponding $\log_{10}k$ versus $\log_{10}T$ plot performed as shown in Figure 6.4. The temperature dependence was measured as -1.18±0.16 by use of a least squares fit to the data. The overall rate constant dependence may be expressed in the form:

$$k_7 = 8.8.10^{-29}/(300/T)^{-1.18} \qquad (6.11)$$

The diffusion coefficient data derived subsequently are shown as a function of temperature in Chapter Seven.

6.2(ii) Carbon Monoxide/Neon System

This system was studied over a temperature range of 320 to 570K and over a pressure range of 0.5 to 5 Torr. The mass spectra shown in Figure 6.5 show that at low pressures the cluster species $(CO)_2^{+\cdot}$ and $Ne_2^{+\cdot}$ are present only in small quantitites. In fact the carbon monoxide dimer was reliably detectable only above 1.5 Torr. These spectra also illustrate clearly the isotope pattern of the parent Neon ion and its dimeric counterpart. At first this system was treated similarly to the previous one in that the forward and reverse rate constants for reaction 6.12 were monitored. However, it was soon aparent that the behaviour of this system was different from that of the previous system. Figures 6.6

$$CO^{+\cdot} + CO + Ne \underset{k_{-8}}{\overset{k_8}{\rightleftharpoons}} (CO)_2^{+\cdot} + Ne \qquad (6.12)$$

and 6.7 show example plots recorded for the measurements of these rate constants. The dissociation rate constant k_{-8} is definitely non-zero, whereas the forward reaction appears to be negligible for the 470K example shown. The lower temperature result also shown in Figure 6.7 exhibits a great deal of scatter although consideration of the high pressure section

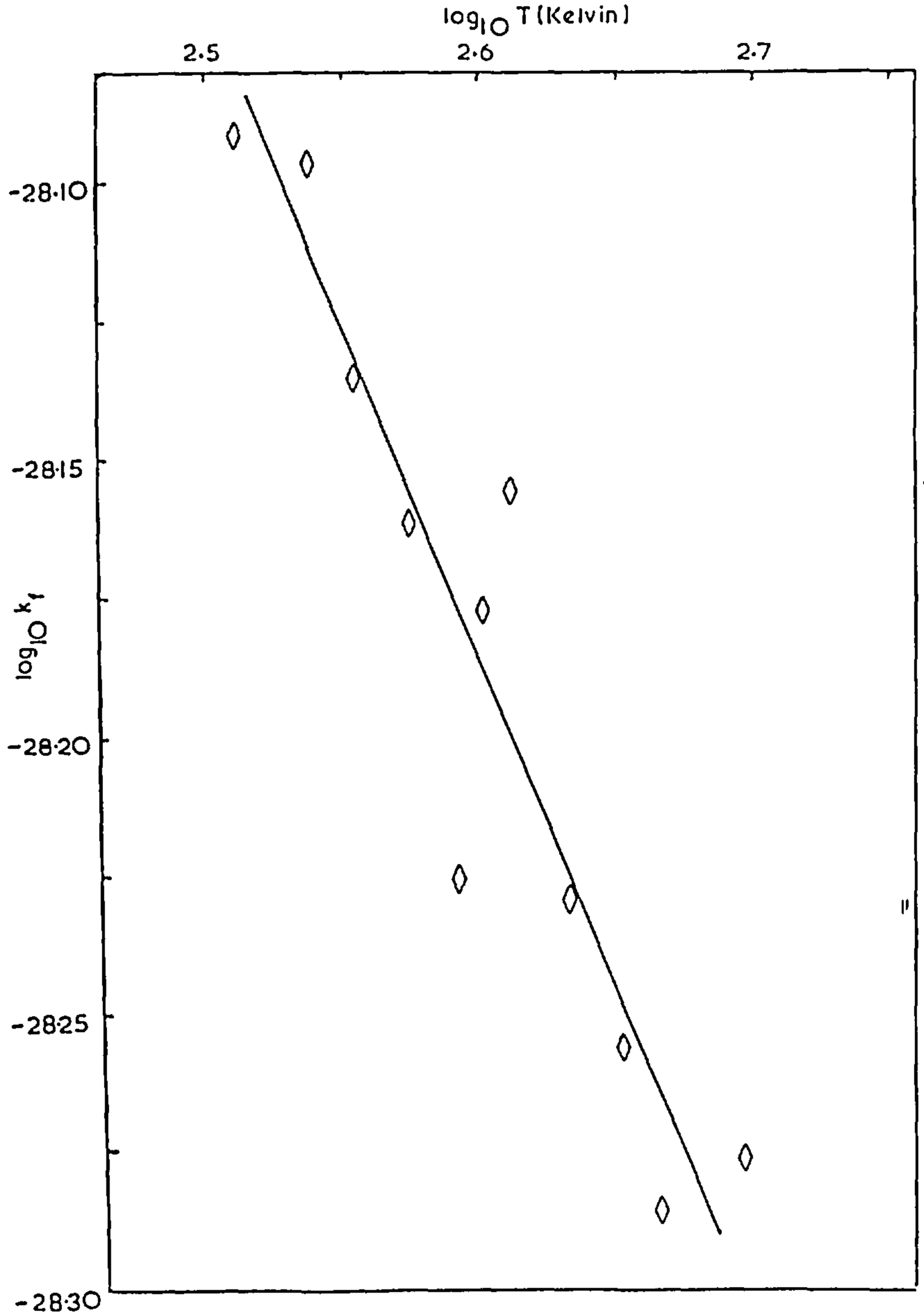

Fig. 6.4 FORWARD ASSOCIATION RATE CONSTANT AS A FUNCTION OF TEMPERATURE FOR THE SYSTEM: $CO^{+\cdot} + CO + He \longrightarrow (CO)_2^{+\cdot} + He$

fig. 6.5 HIGH PRESSURE MASS SPECTRA FOR 1% CO IN NEON

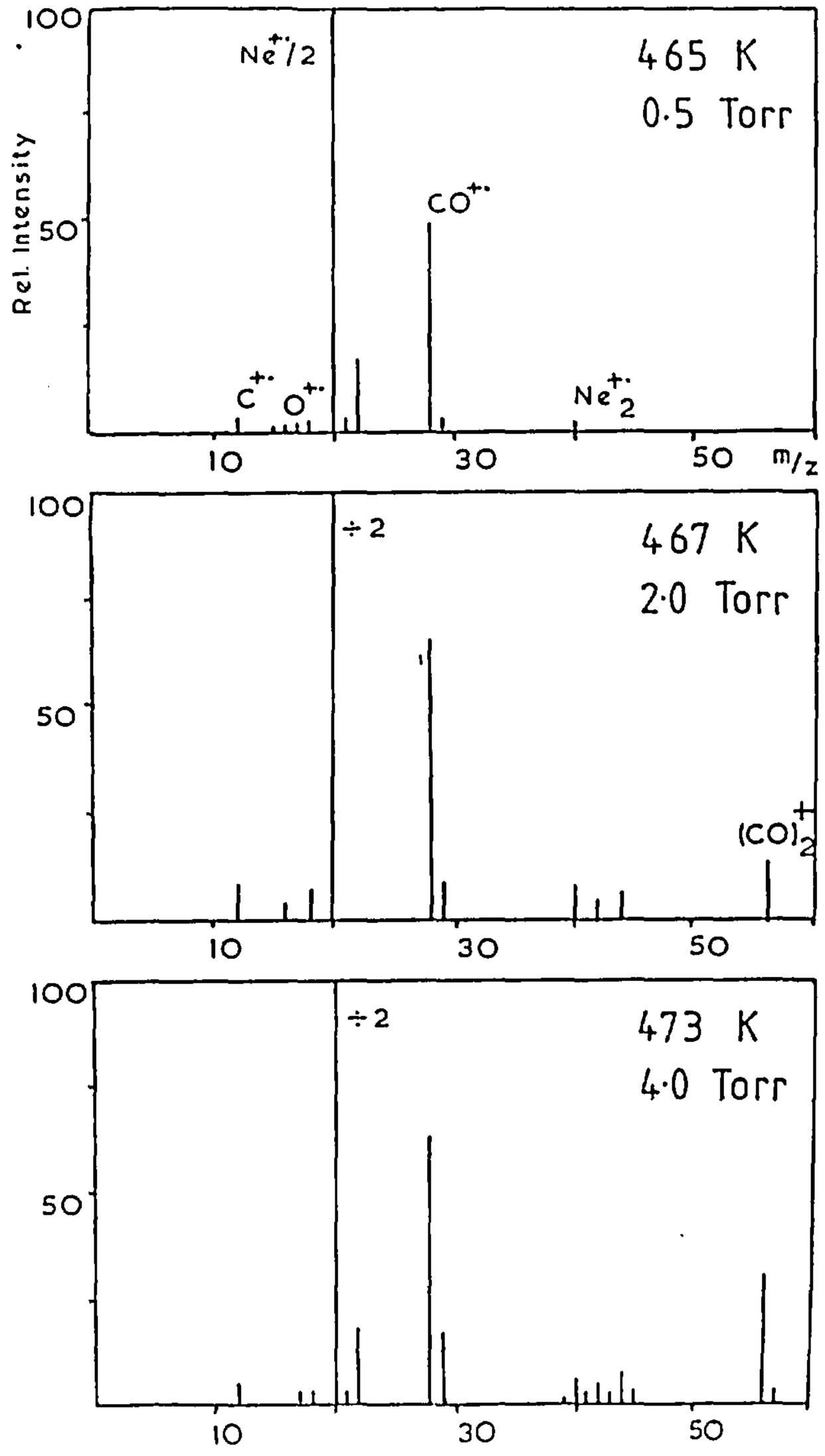

fig.6.6 PLOT OF $-S[Ne]$ vs $[Ne]^2$ FOR THE DETERMINATION OF THE RATE CONSTANT FOR THE DISSOCIATION REACTION:

$(CO)_2^{+\cdot} + Ne \longrightarrow CO^{+\cdot} + CO + Ne$

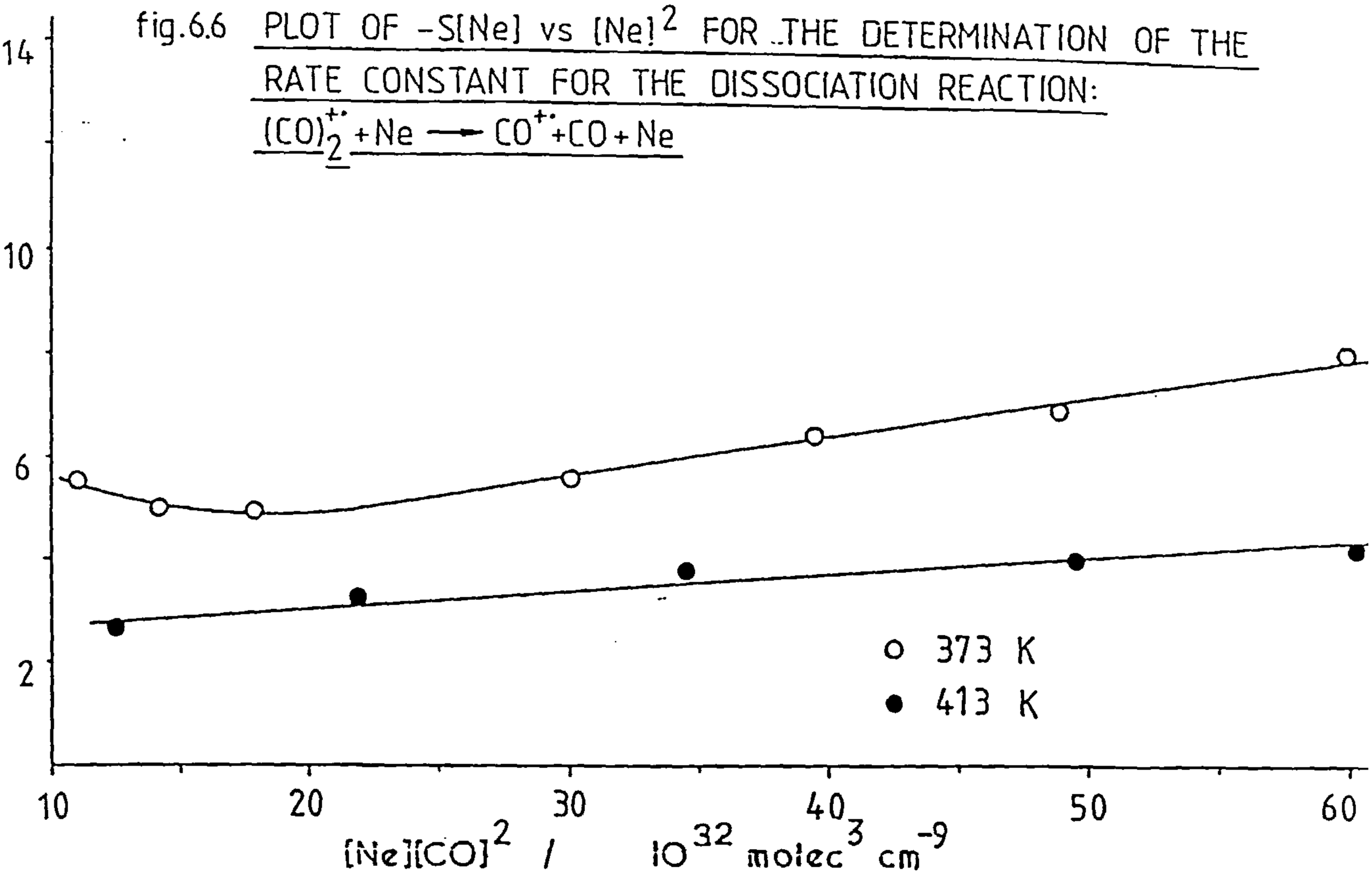

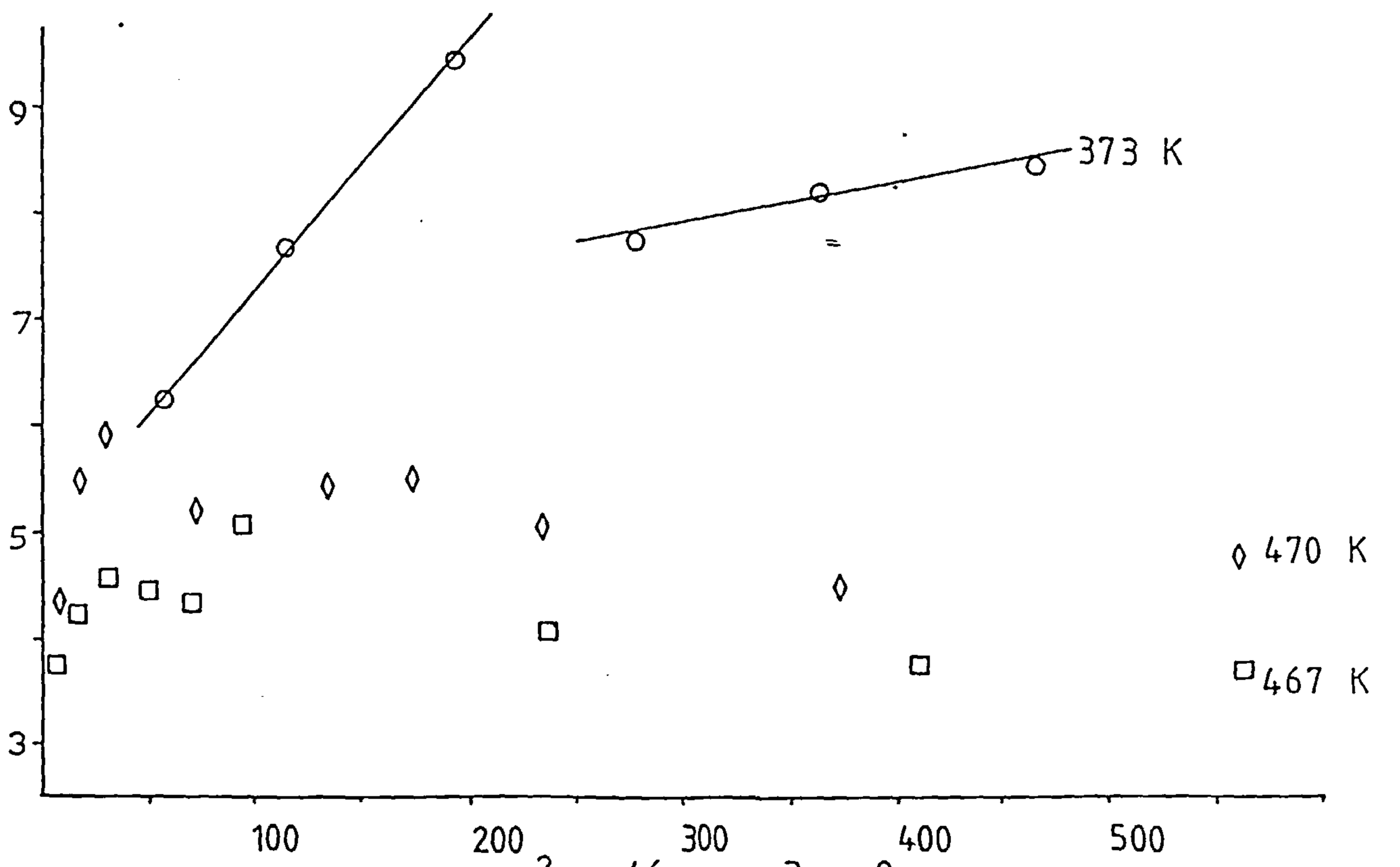

fig. 6.7 SEPARATION OF $CO^{+\cdot}$ REACTION RATE AND DIFFUSIVE LOSS CONSTANTS IN 1% CO IN Ne AT 373, 470 AND 467 K.

(the last three data points) collected over 2.5 to 3.0 Torr range, yields a k_8 value comparable to that of the system previously studied:

System;	$CO^{+\cdot}$/He	$CO^{+\cdot}$/Ne	least squares fit to:
k/molecule^{-2}	----------	$6.19.10^{-29}$	(last three data points)
cm^6sec^{-1}	$6.88.10^{-29}$	$6.30.10^{-29}$	(all data points)

This result may be just fortuitious as higher temperature results indicate a zero k_8 or it may be that we are monitoring the end of the $k_f = CT^m$ relationship validity.

If we next compare the peak profiles of the primary and secondary ions for this and the previous system it is observed that the shape of the $CO^{+\cdot}$ profile is much narrower in the helium bath gas case, Figures 6.8 and 6.9. The secondary ion $(CO)_2^{+\cdot}$ profiles are both very similar for both systems. The tailing off of the $CO^{+\cdot}$/Ne system ion profiles is similar to that obtained in the carbon dioxide equilibrium system, see Figure 3.7. An attempt to measure K_{eq} was performed by the method described in section 3.9 and the values determined are shown in Figure 6.10 as a function of pressure.

6.2(iii) Carbon Monoxide/Argon System

This system was treated in the same manner as the CO^{+}/He analog. Experiments were conducted from 328 to 497K and a pressure range of 1.0 to 3.5 Torr. As shown in Figure

$$CO^{+\cdot} + CO + Ar \underset{k_{-9}}{\overset{k_9}{\rightleftharpoons}} (CO)_2^{+\cdot} + Ar \qquad (6.13)$$

6.11, the $Ar^{+\cdot}$ ion gave the most abundant peak under low pressure conditions but decreased in relative intensity as the pressure rose. This is believed to be due to charge exchange reactions mainly between the $Ar^{+\cdot}$ and neutral CO species occurring to a greater extent as the

fig. 6.8 COMPARISON OF MONOMER AND DIMER CO ION PEAK PROFILES FOUND IN 1% CO IN He AT 376 K.

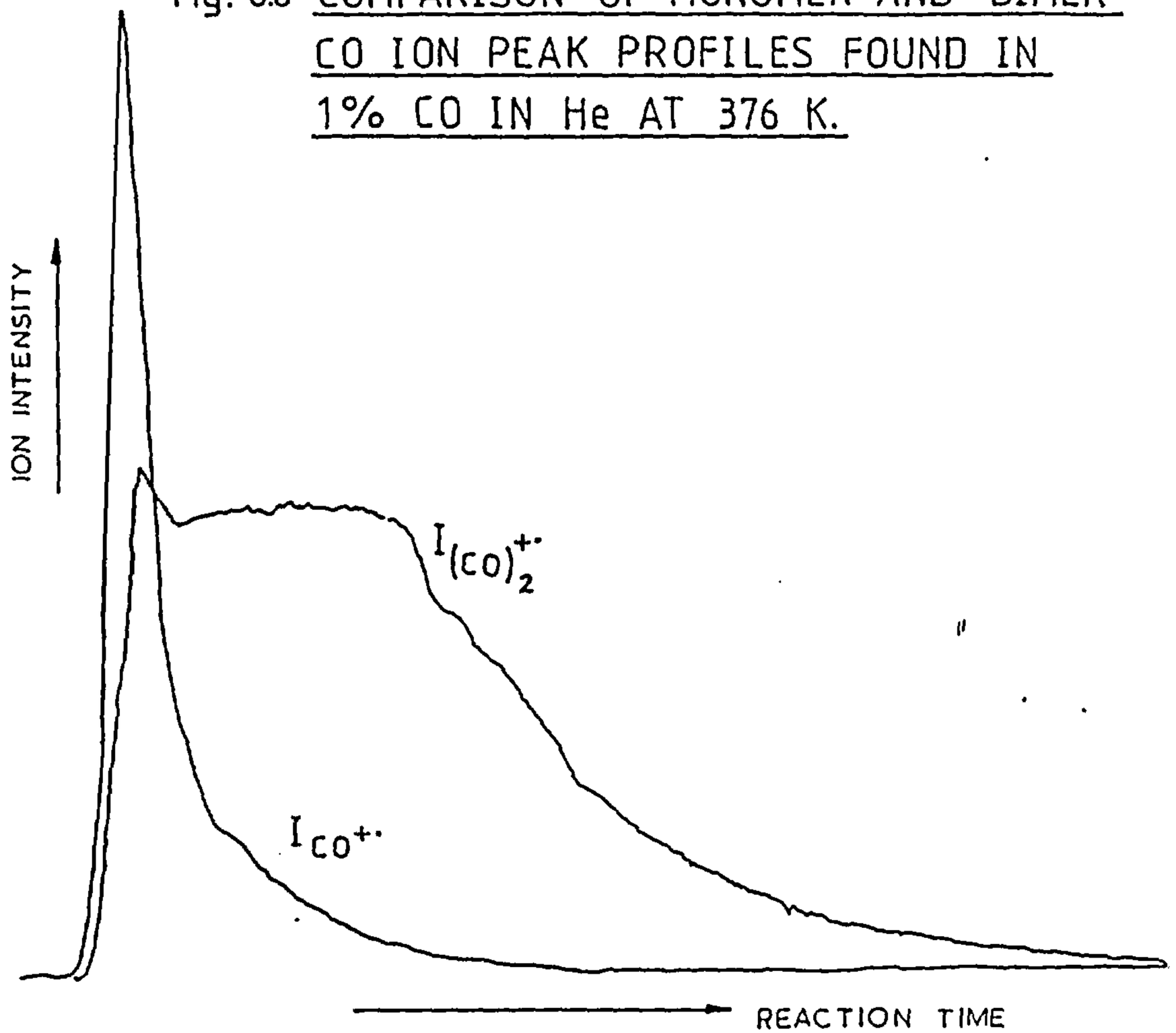

fig. 6.9 COMPARISON OF MONOMER AND DIMER IONS PEAK PROFILES FOUND IN 1% CO IN Ne (398 K, 3.5 TORR OVER 20000 CYCLES).

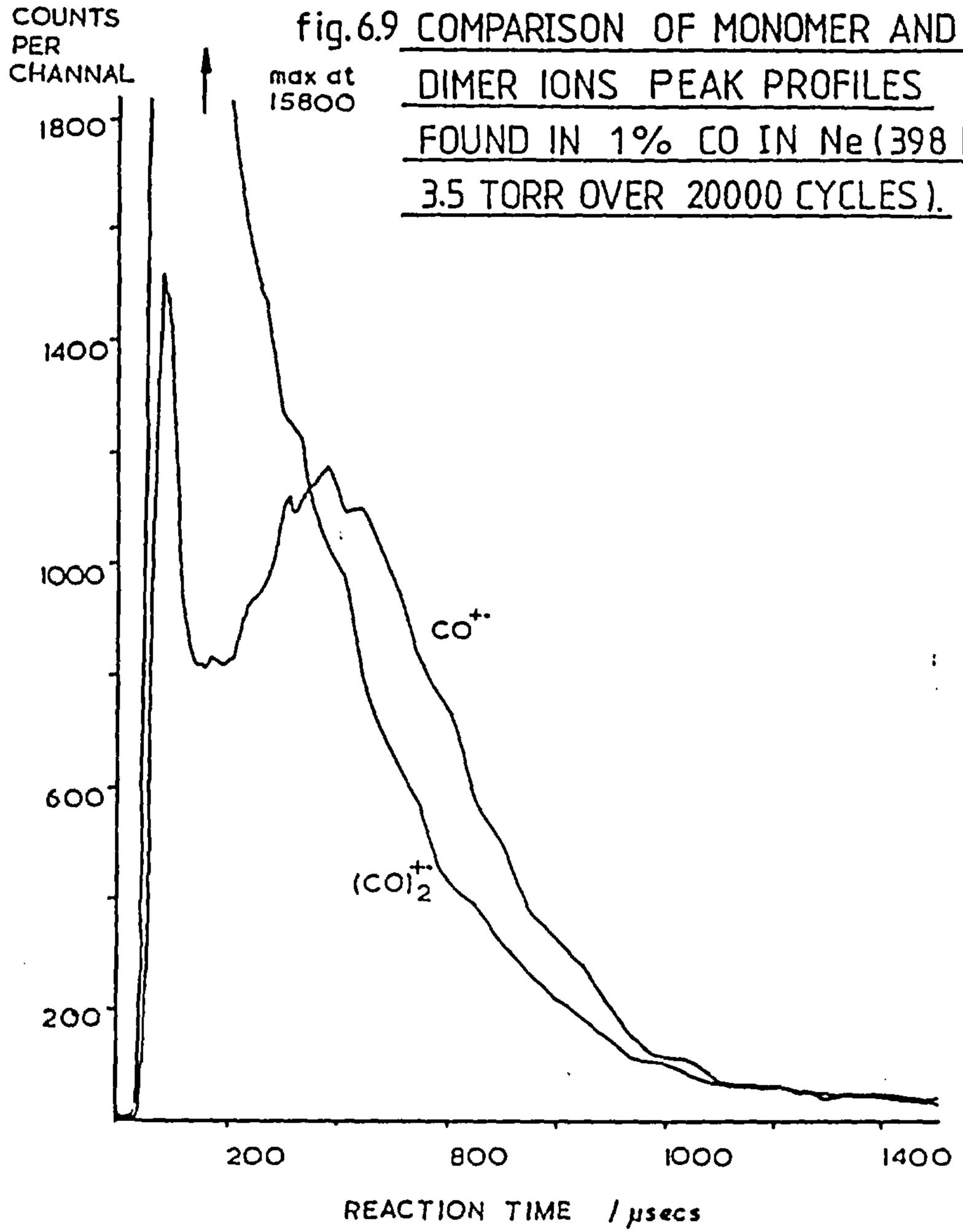

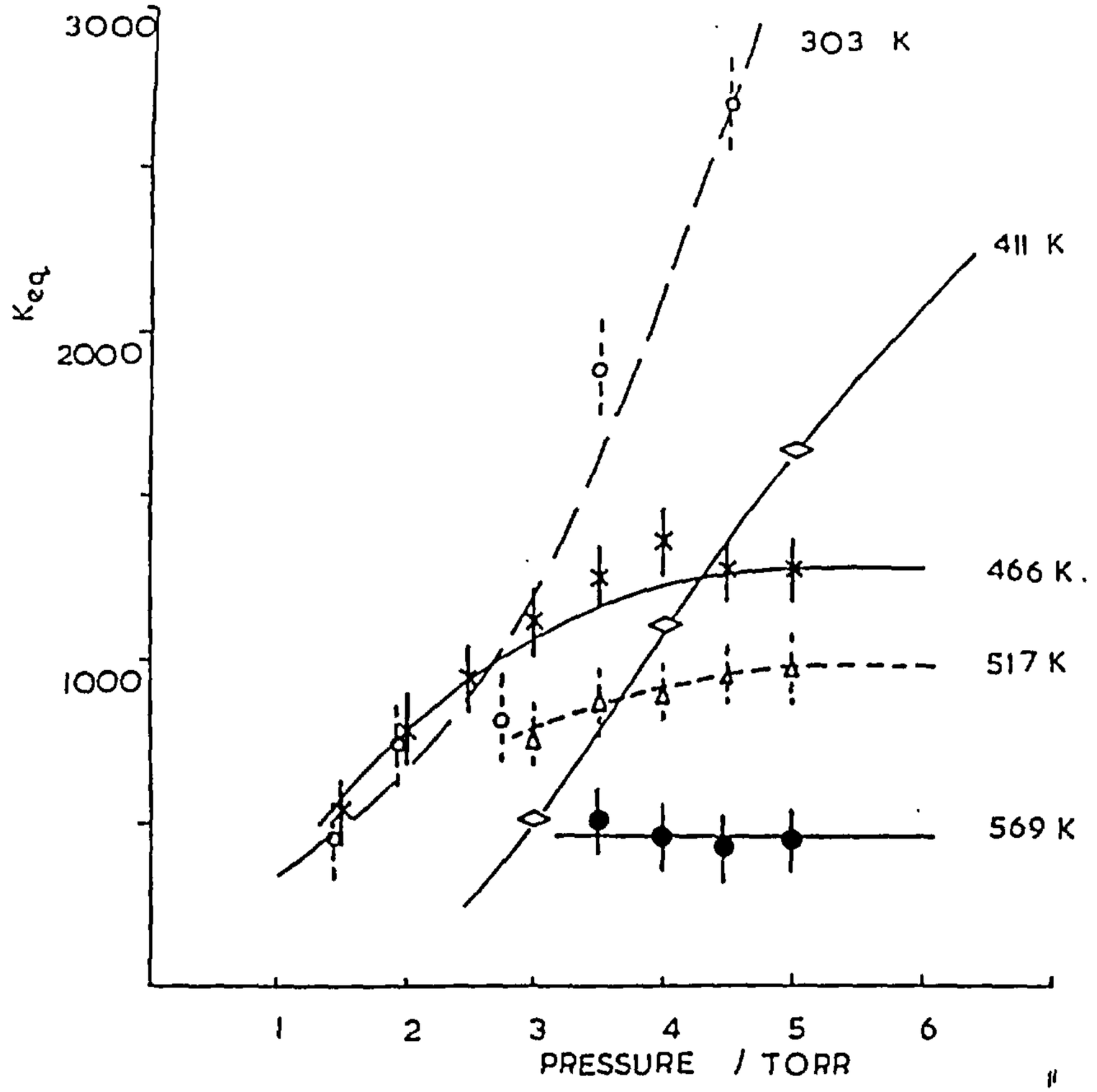

fig.6.10 VARIATION IN THE APPARANT K_{eq} WITH RESPECT TO PRESSURE FOR THE SYSTEM:
$CO^{+\cdot} + CO + Ne \rightleftharpoons (CO)_2^{+\cdot} + Ne$

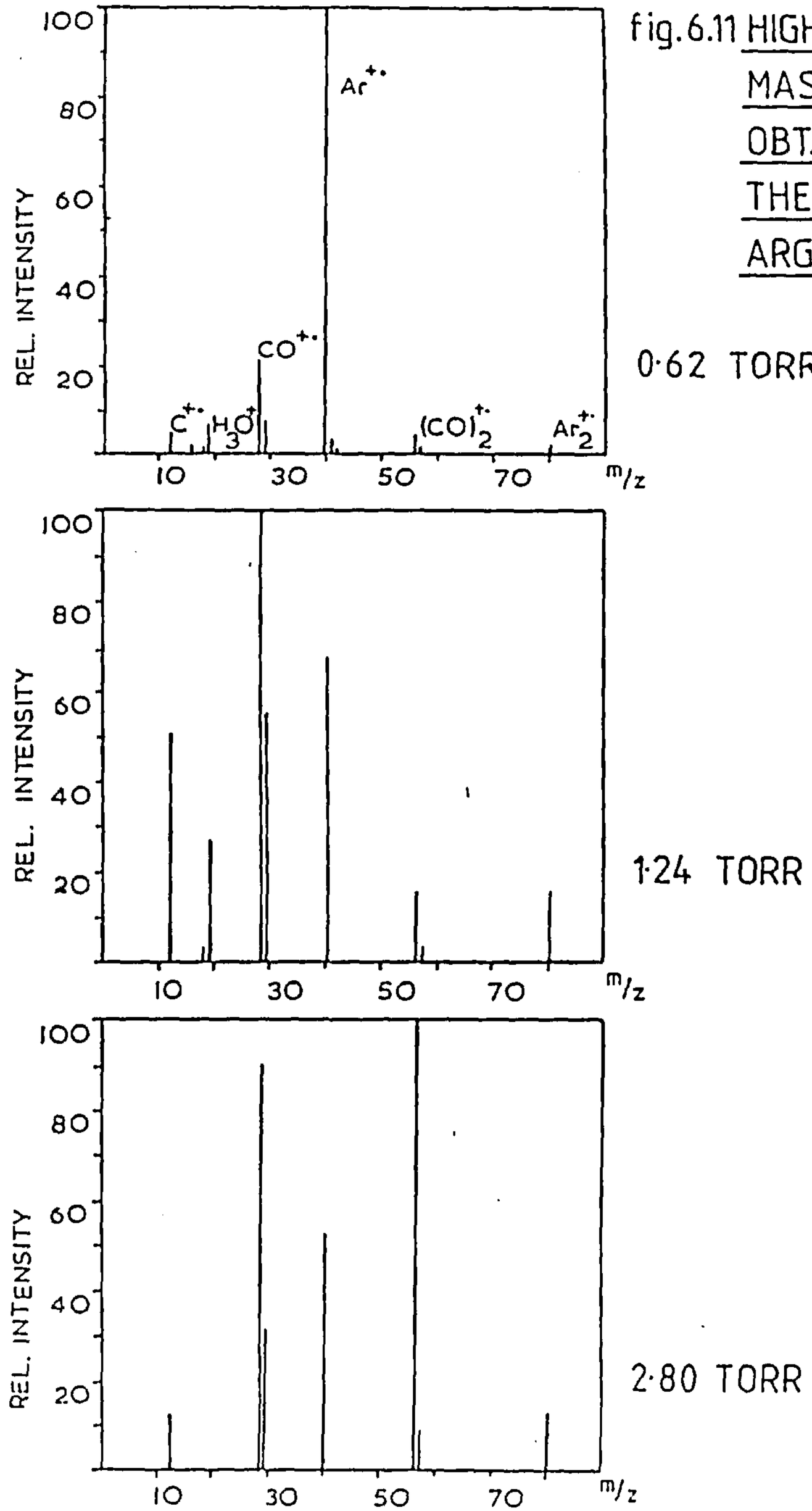

fig.6.11 HIGH PRESSURE MASS SPECTRA OBTAINED FOR THE 1% CO IN ARGON SYSTEM.

gas number density increased in the chamber. A small amount of the bath gas dimer was formed but fortunately no $(COAr)^{+\cdot}$ cluster was observed.The forward and reverse reaction was monitored and the corresponding rate constants determined. Example plots of S[Ar] versus $[CO][Ar]^2$ and S[Ar] versus $[Ar]^2$ performed on the primary and secondary ionic species are given in Figures 6.12 and 6.13. The rate constant of the dissociation reaction was established and found to be zero over the whole temperature range investigated. In the case of the association reaction no tailing off was observed in the plots used to determine the rate constants, unlike the $CO^{+\cdot}$/He system previously studied.

The temperature dependence m, of reaction 6.13 was measured by a log k vs log T plot and determined by the aid of a least squares fit as $m=-1.53\pm0.32$, see Figure 6.14. Overall the rate constant k_9 for this system can be described by the relationship below:

$$k_9 = 19.5.10^{-29}/(300/T)^{-1.53} \qquad (6.13a)$$

The diffusion coefficients were also measured and are shown along with the $CO^{+\cdot}$ in helium results in chapter seven.

6.3 Results Obtained for the Nitrogen Systems

6.3(i) Nitrogen/Helium System

Ion profiles were monitored over a temperature range of 326 to 618K and a pressure range of 0.5 to 6.0 Torr. The mass spectra obtained are essentially the same as recorded for the pure nitrogen system except for the bath gas ion at 4 daltons and a cluster ion at 32 daltons corresponding to the $(HeN_2)^{+\cdot}$ species, Figure 6.15. The gas mixture used consisted of 10% N_2 and 90% Helium by volume, and for determining k_{10}, the rate constant for reaction 6.14, a plot of $S([N_2]+[He])$ versus $[N_2][He]([N_2]+[He])$ was used where S is the slope of the ln $N_2^{+\cdot}$ ion intensity-reaction time profile, Figure 6.16. The corresponding rate

fig. 6.12 SEPARATION OF $CO^{+\cdot}$ REACTION RATE AND DIFFUSIVE LOSS CONSTANTS IN 1% CO IN ARGON.

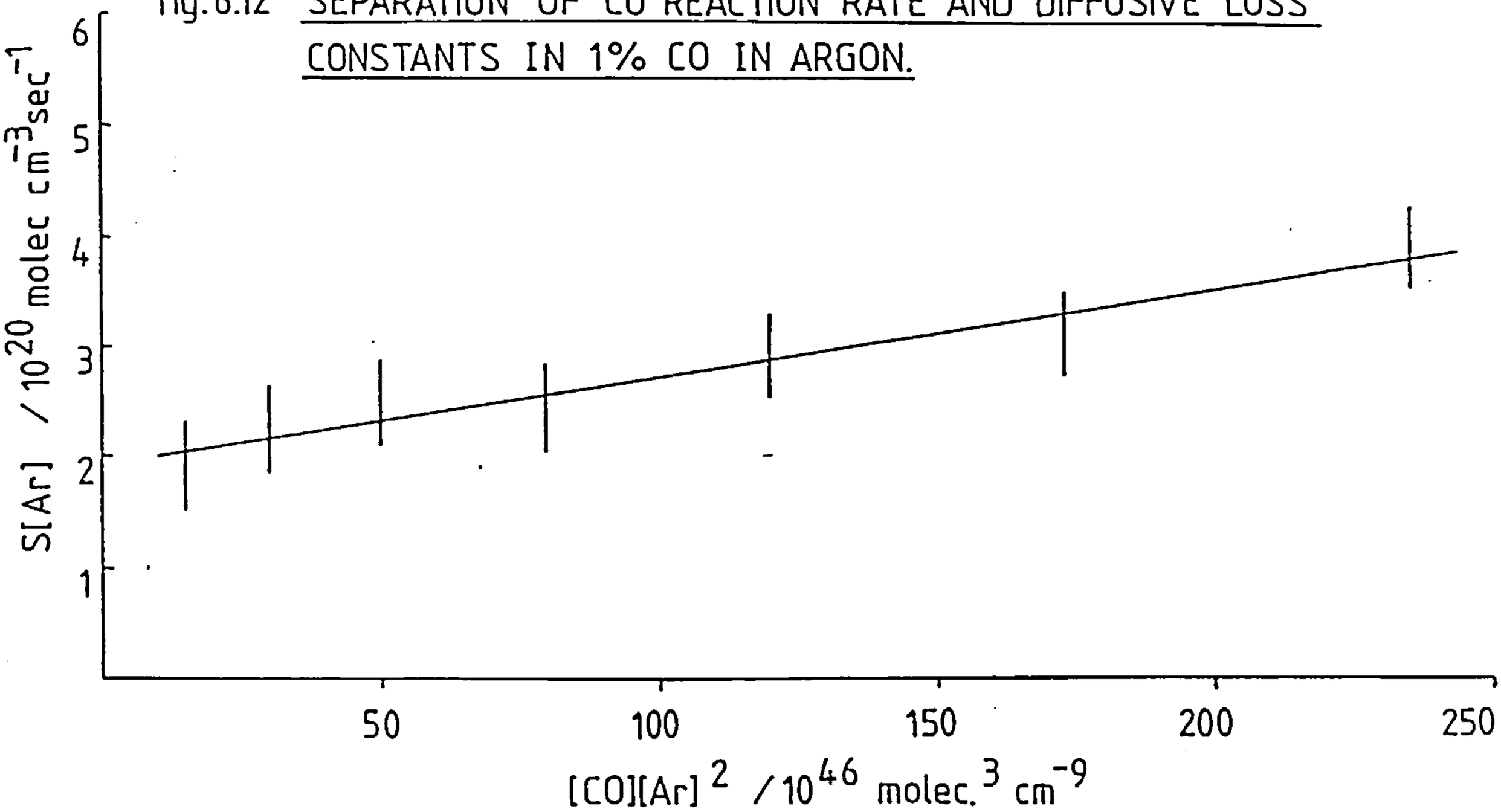

fig. 6.13 PLOT OF S[Ar] vs $[Ar]^2$ FOR THE DETERMINATION OF THE RATE CONSTANT OF THE DISSOCIATION REACTION: $(CO)_2^{+\cdot} + Ar \longrightarrow CO^{+\cdot} + CO + Ar$

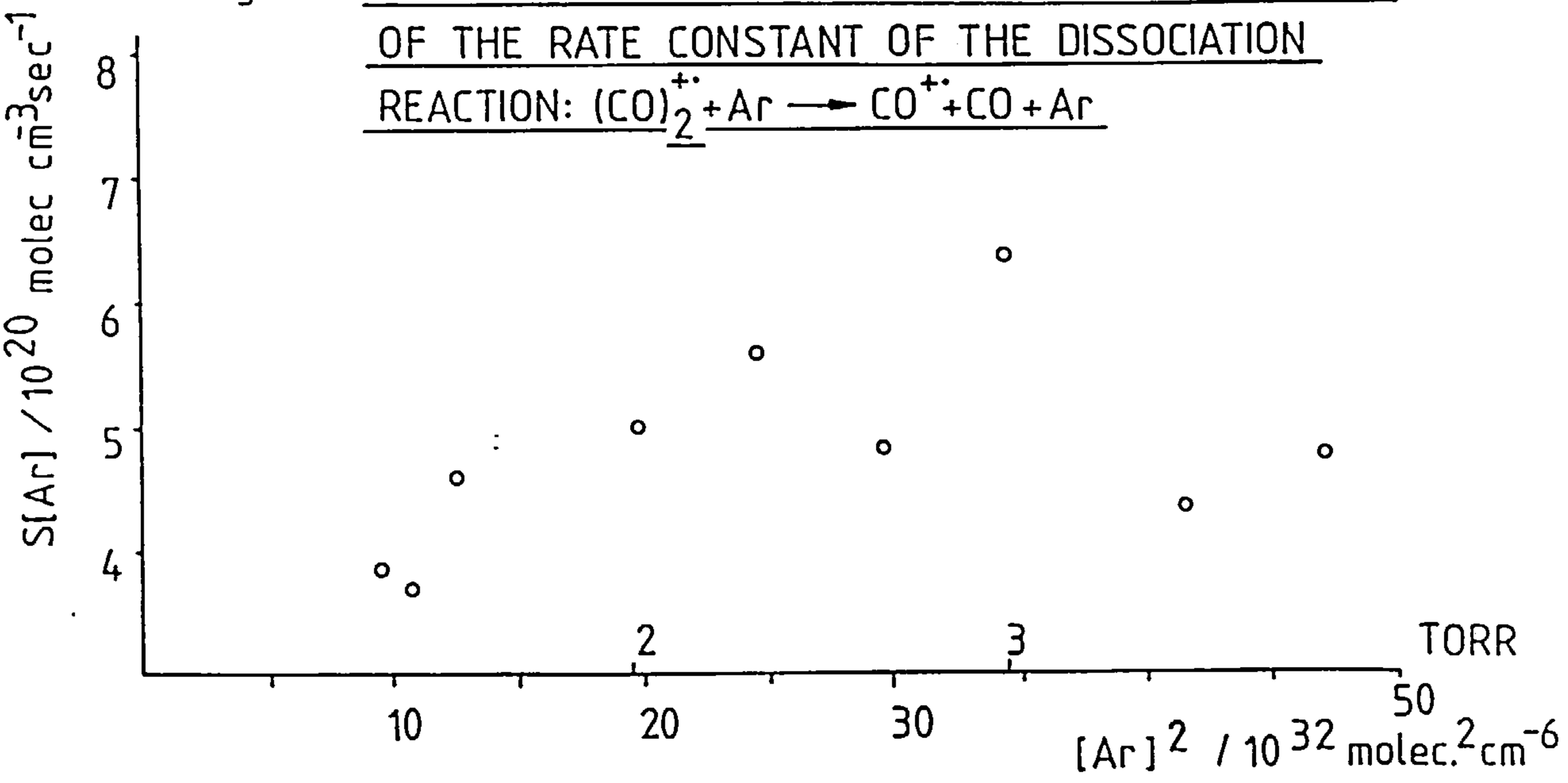

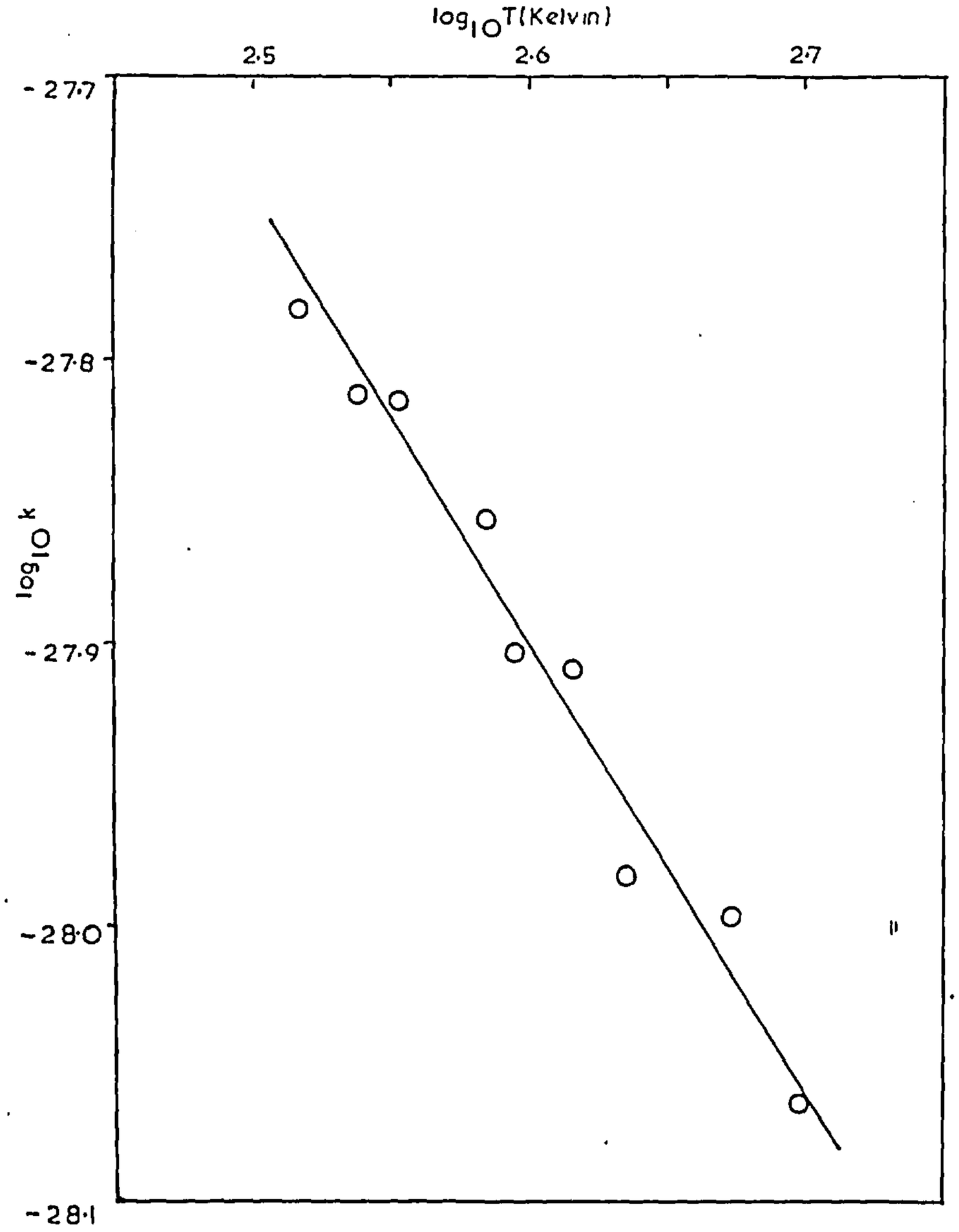

fig. 6.14 FORWARD ASSOCIATION RATE CONSTANT AS A FUNCTION OF TEMPERATURE FOR THE SYSTEM: $CO^{+\cdot} + CO + Ar \longrightarrow (CO)_2^{+\cdot} + Ar$

fig. 6.15 HIGH PRESSURE MASS SPECTRA FOR 1% N_2 IN HELIUM.

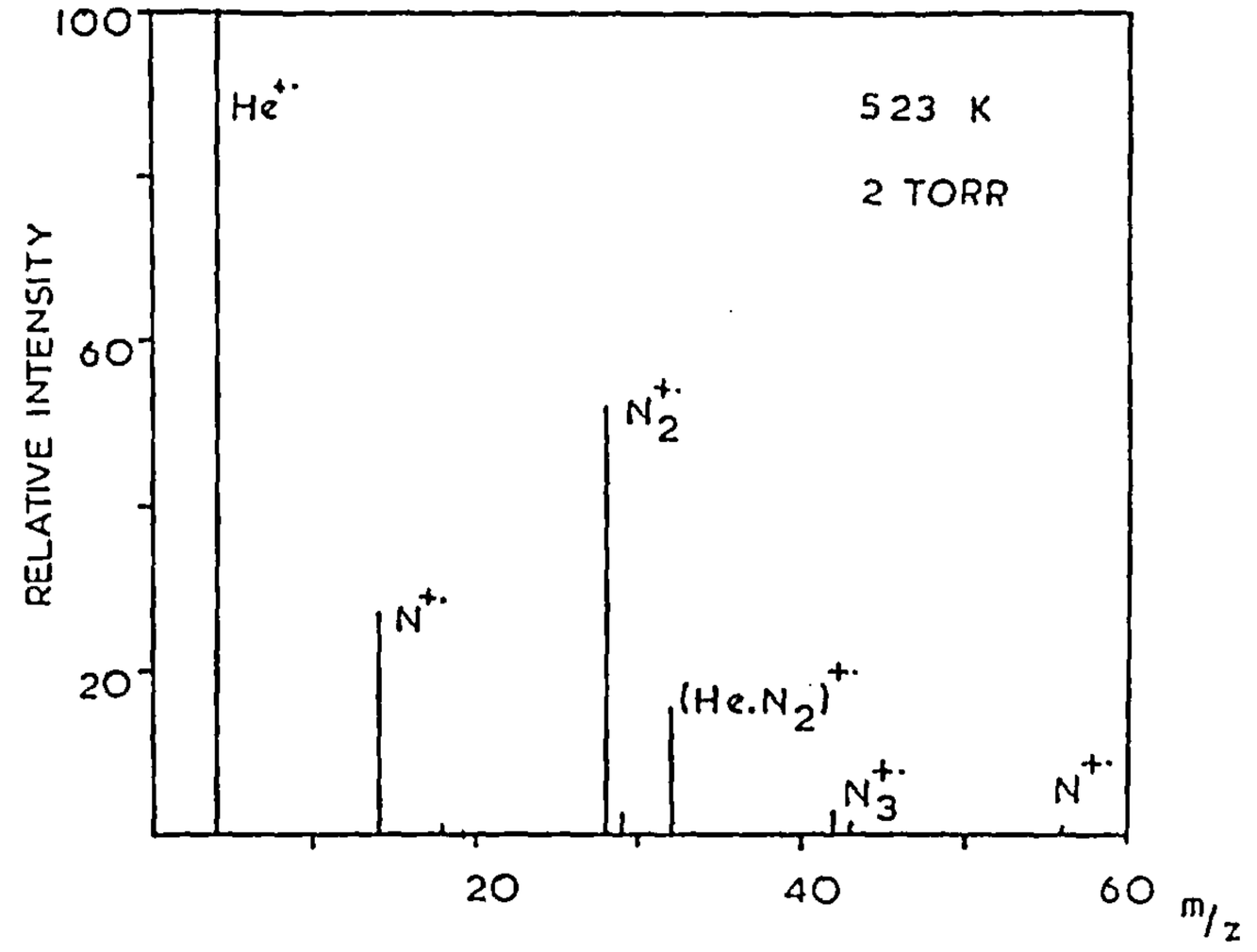

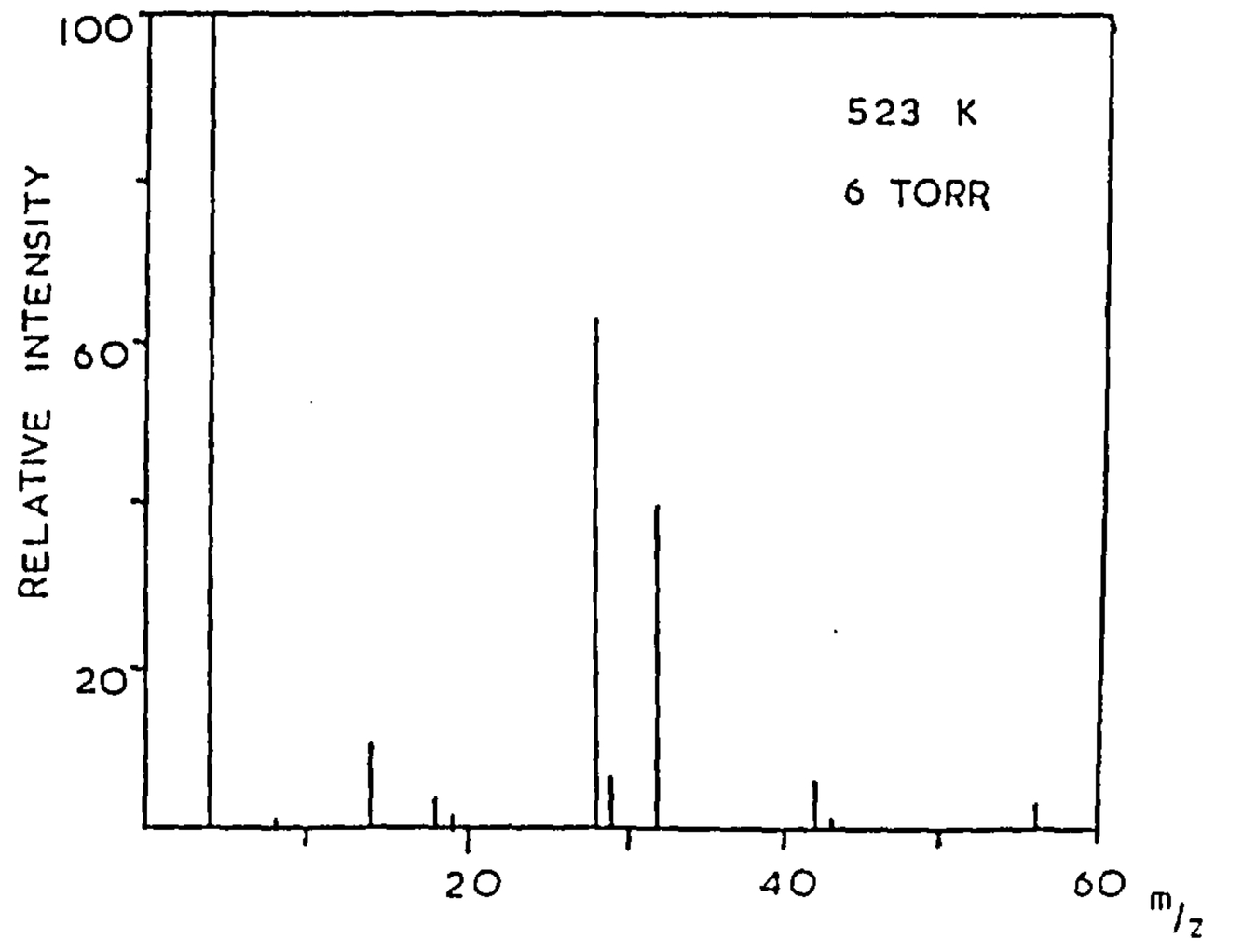

fig. 6.16 EXAMPLE OF PLOT USED TO DETERMINE THE FORWARD ASSOCIATION RATE CONSTANT OF THE REACTION: $N_2^{+\cdot} + N_2 + He \longrightarrow (N_2)_2^{+\cdot} + He$

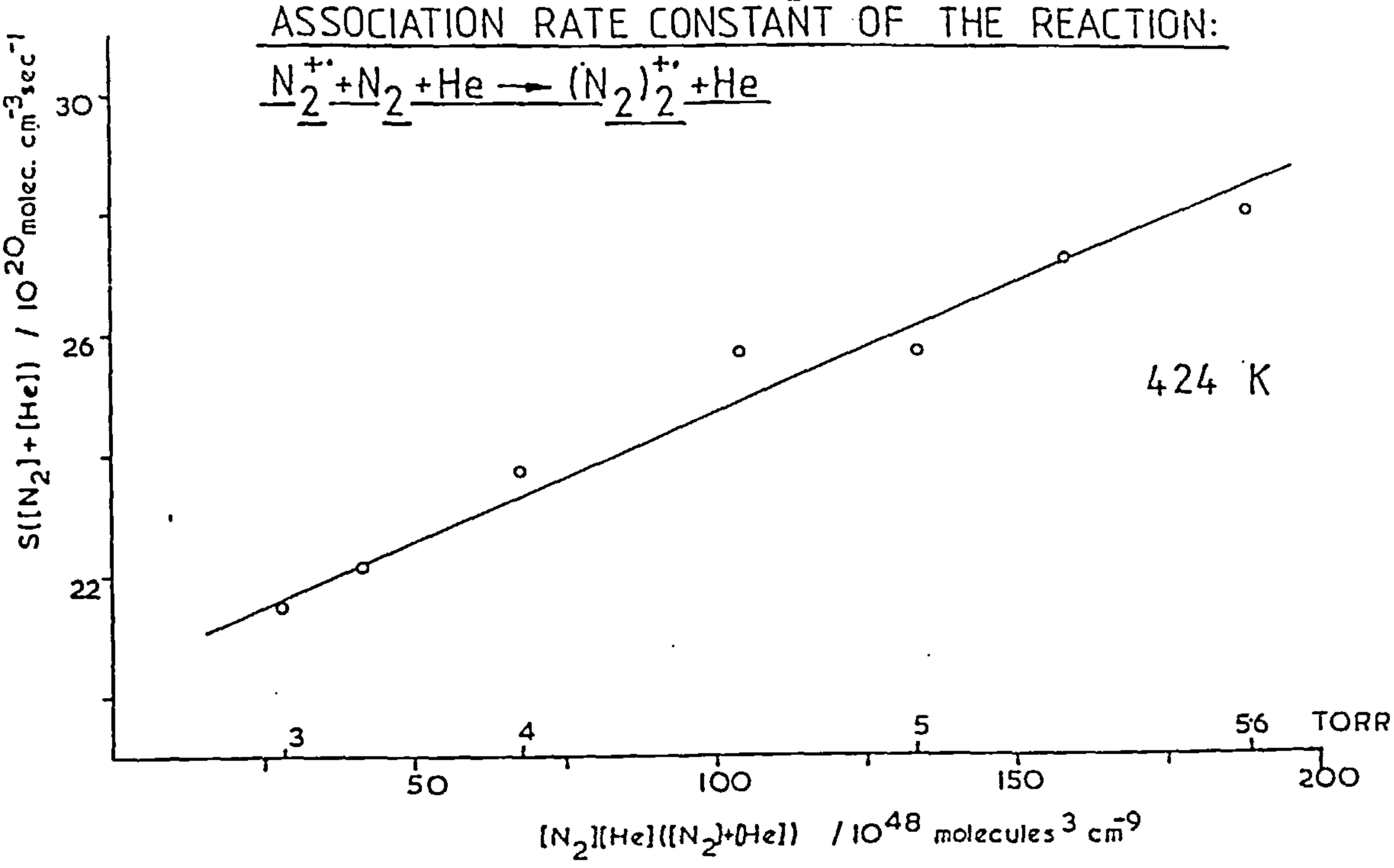

fig. 6.17 FORWARD ASSOCIATION RATE CONSTANT AS A FUNCTION OF TEMPERATURE FOR THE SYSTEM: $N_2^{+\cdot} + N_2 + He \longrightarrow (N_2)_2^{+\cdot} + He$

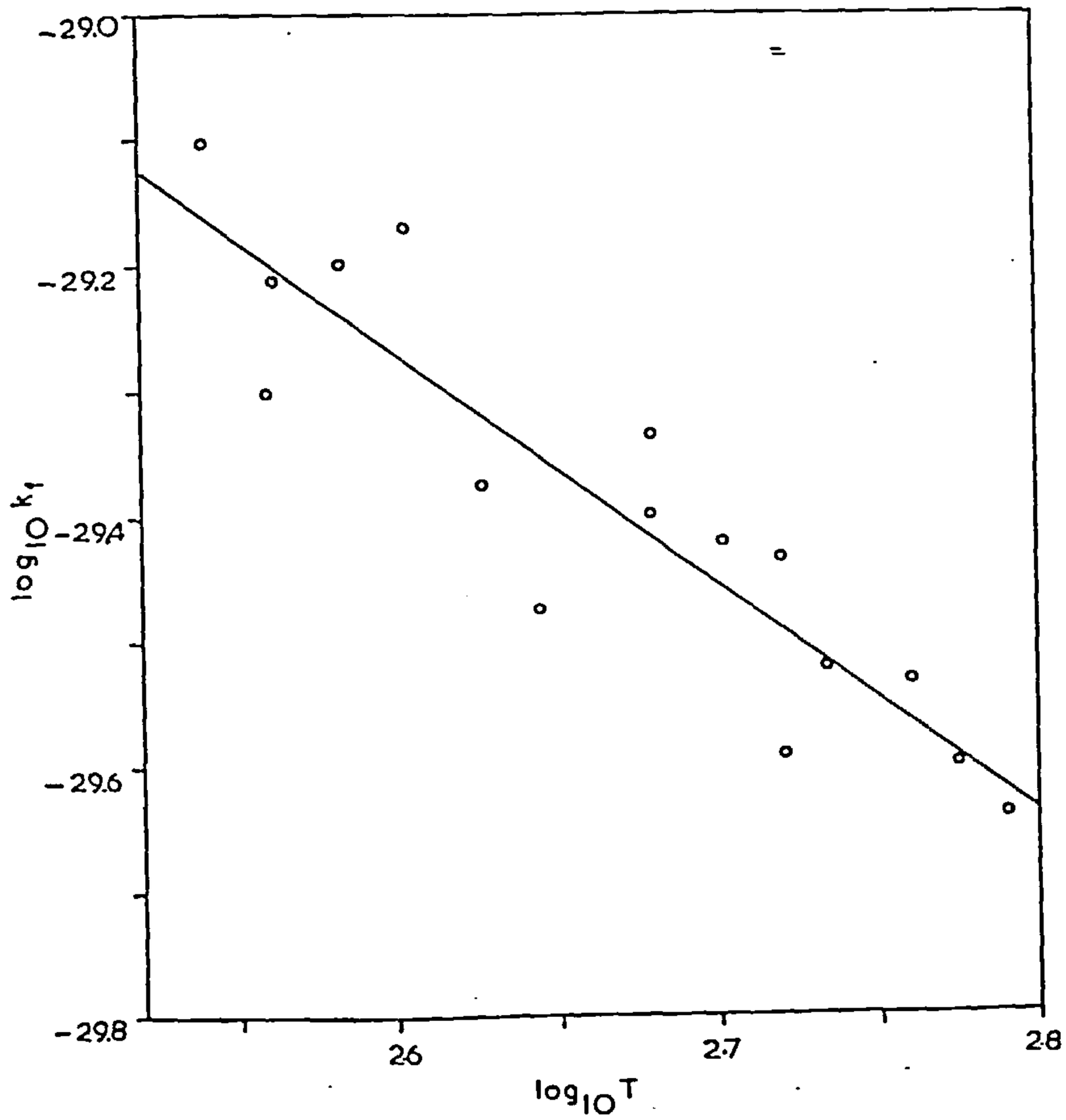

$$N_2^{+\cdot} + N_2 + He \xrightarrow{k_{10}} N_4^{+\cdot} + He \qquad (6.14)$$

and diffusion constant was measured at approximately 20K intervals over the stated temperature range. The diffusive coefficients are shown as a function of temperature in Chapter 7, and the temperature dependence of k_{10} in Figure 6.17. The results of this section can be described in the form:

$$k_{10} = 1.06.10^{-29}/(300/T)^{-1.67} \qquad (6.15)$$

6.3(ii) Nitrogen/Argon System

Investigation of this system was conducted over a temperature and pressure range of 403-575K and 0.5-2.8 Torr. The ion spectra recorded were again similar to that of the one component nitrogen system but dominated by the bath gas peak $Ar^{+\cdot}$ at m/z 40. The dimer $Ar_2^{+\cdot}$ was also observed at higher pressures and also a small amount of the $(ArN_2)^{+\cdot}$ species, but at less than 0.5% of the total ion beam current, Figure 6.18.

In order to determine rate constants for the reaction 6.16, similar plots to those used in studying the previous system were performed on a gas mixture containing 10% Nitrogen.

$$N_2^{+\cdot} + N_2 + Ar \xrightarrow{k_{11}} N_4^{+\cdot} + Ar \qquad (6.16)$$

The effect of varying the amount of each constituent in the gas mixture is shown in Figure 6.19. The resulting measured rate constants at 373K are shown in the next figure. Also shown in Figure 6.19 and 6.20 is a result obtained at high temperature, 603K; the curvature indicates that the relationship 6.17 is no longer valid. Here S is the slope of the ln $N_2^{+\cdot}$ versus reaction time profile and f is the diffusive loss constant.

fig. 6.18 HIGH PRESSURE MASS SPECTRA FOR A 10% NITROGEN IN ARGON MIXTURE AT 554 KELVIN.

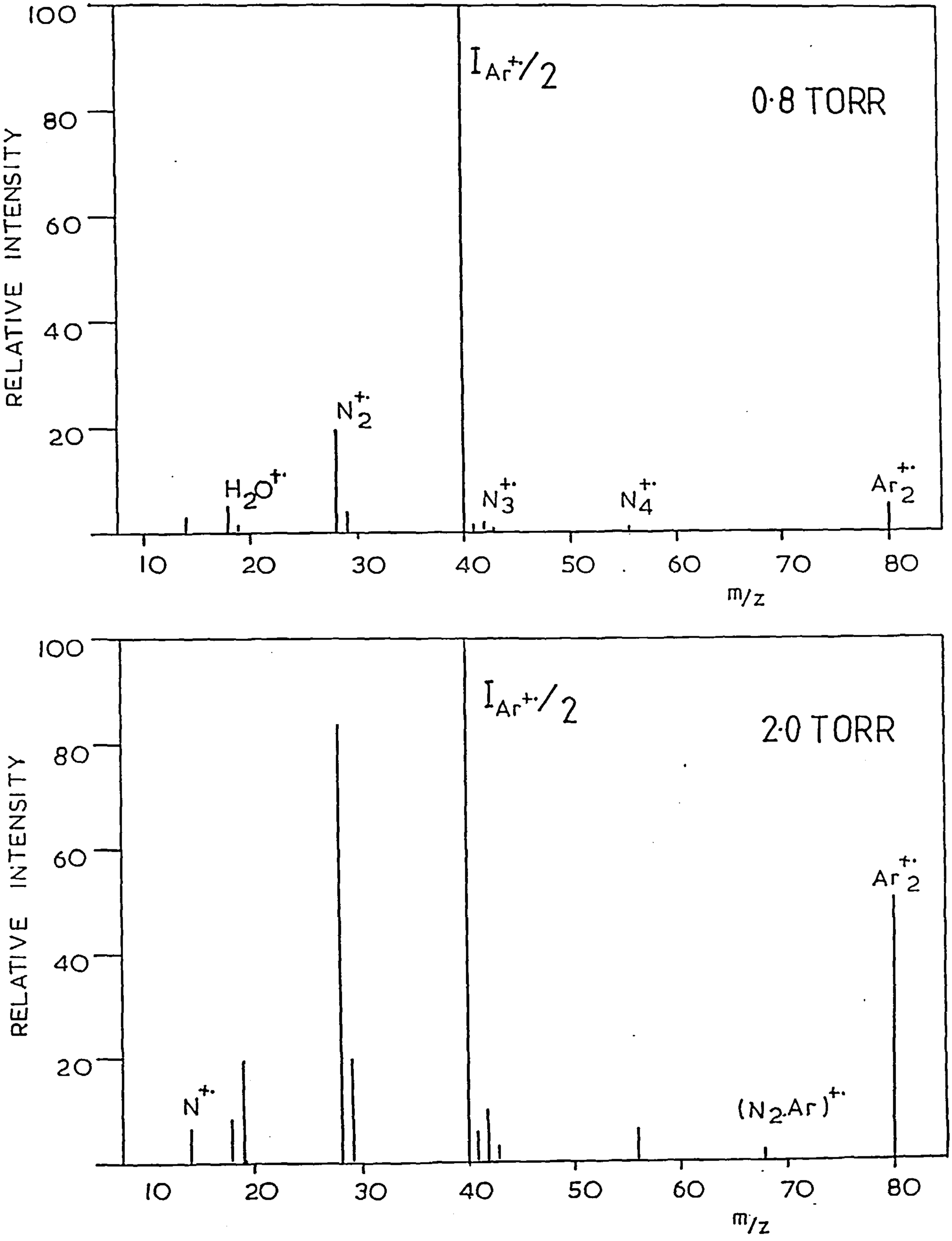

fig. 6.19 VARIATION IN THE FORWARD ASSOCIATION RATE CONSTANT AS A FUNCTION OF THE MIXTURE COMPOSITION.

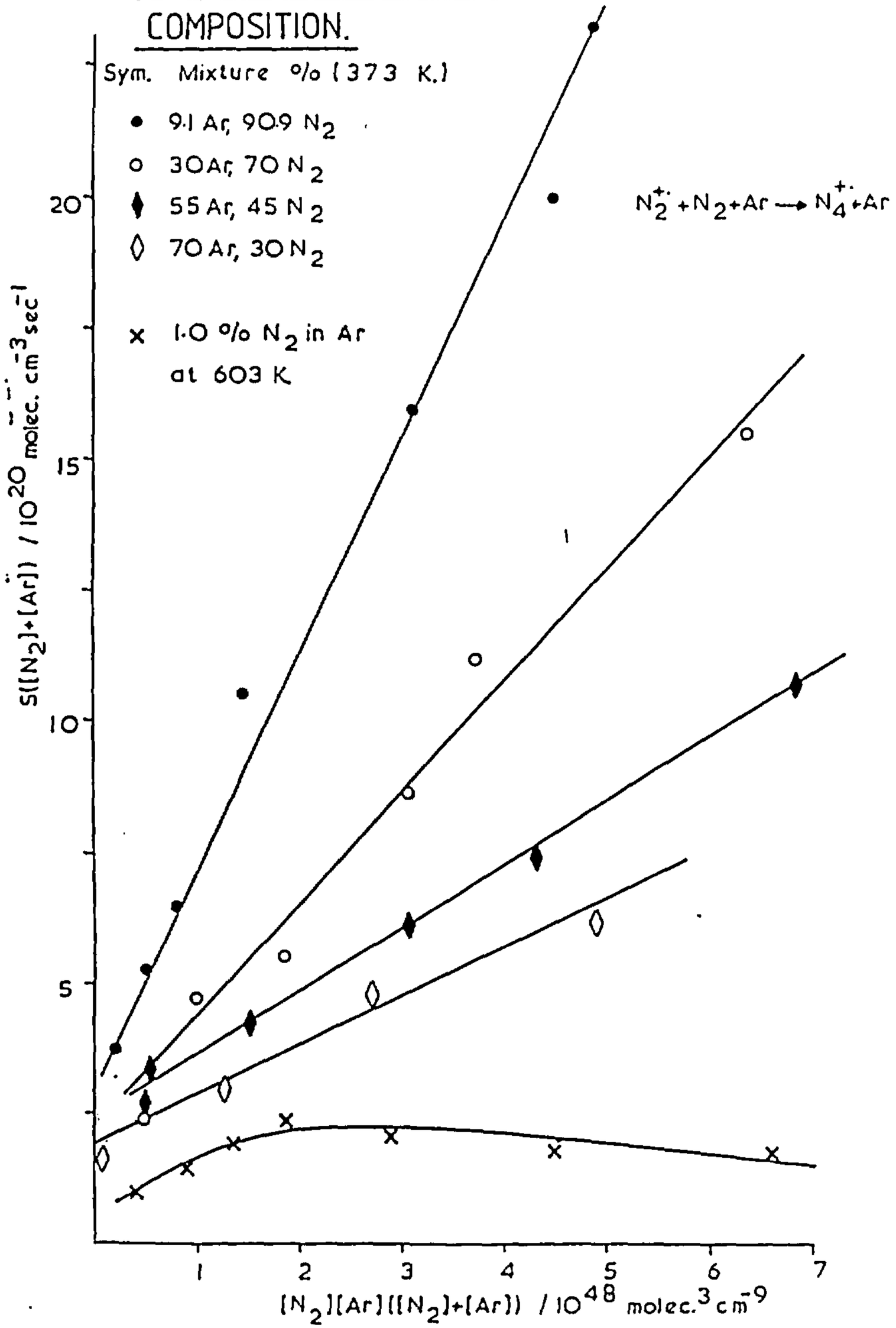

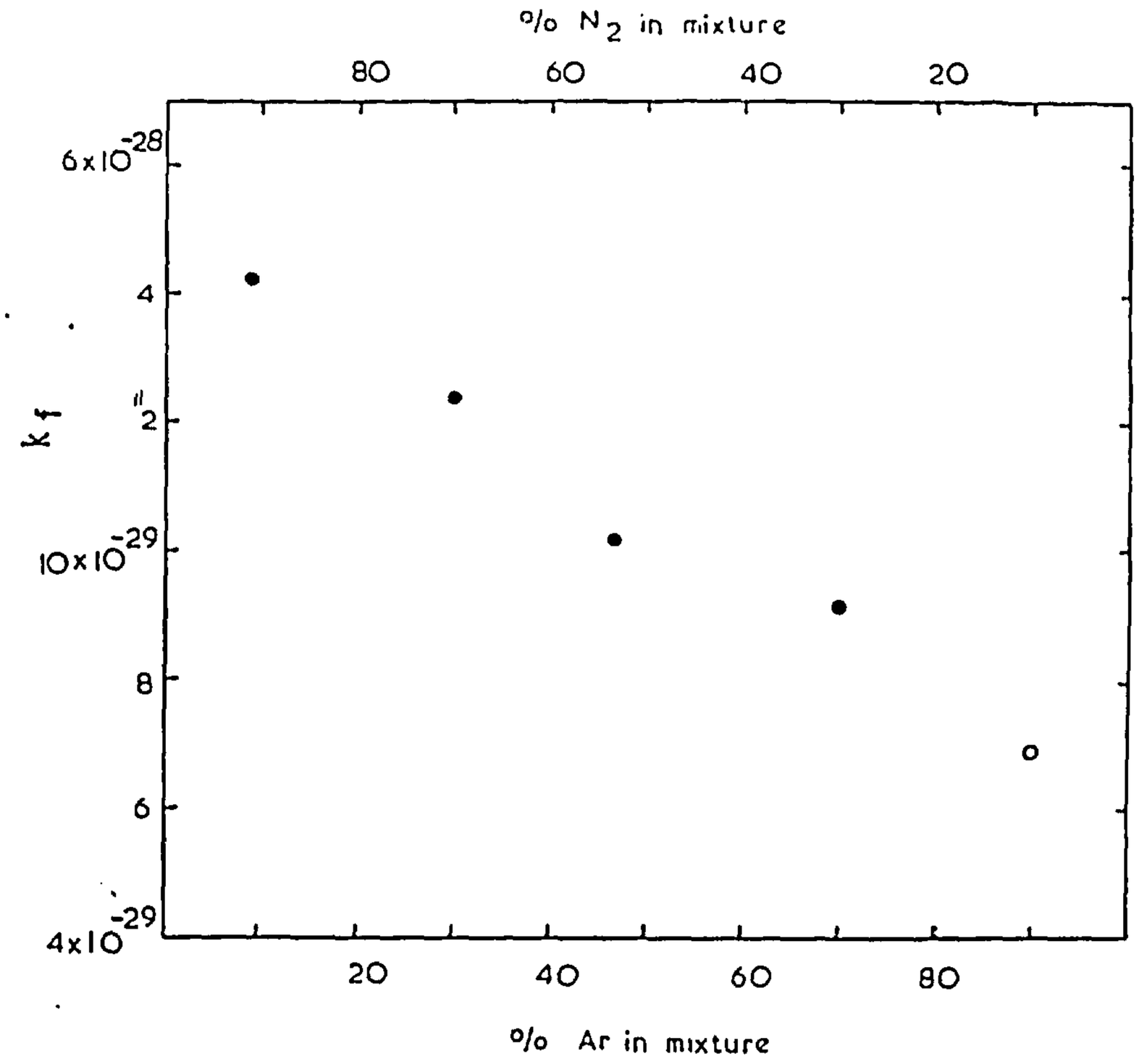

fig. 6.20 VARIATION OF THE FORWARD ASSOCIATION RATE CONSTANT, MEASURED IN VARIOUS COMPOSITION MIXTURES OF N_2 AND Ar

$$S([N_2]+[Ar]) = k_{11}([N_2][Ar])([N_2]+[Ar]) + f \qquad (6.17)$$

The temperature dependence of k_{11} was again investigated assuming a $k=CT^m$ relationship, Figure 6.21, and the resulting expression obtained is:

$$k_{11} = 8.40.10^{-29}/(300/T)^{-1.84} \qquad (6.18)$$

6.4 Theory and Discussion of Results

6.4(i) Energy Transfer/Ligand Switching Mechanism

As discussed in section 2.5, the Energy Transfer and Ligand Switching mechanisms may be distinguished by investigation of the temperature dependence of a reactive system; log k versus $\log_{10}T$ or $\log_{10}k$ versus $^1/T$ plots being respectively linear for each mechanism. In all the systems considered here an Energy Transfer mechanism was assumed. For definitive results it is necessary to measure the rate constant k over a much larger temperature range than that used in this work, particularly including low temperature ranges. For this work over a limited temperature range, $\log_{10}k$ vs $\log_{10}T$ and $^1/T$ plots are approximately linear, Figures 6.4 and 6.22. While both plots appear linear in this study, results obtained by other groups show unquestionably that over a larger temperature range a $\log_{10}k$ vs $\log_{10}T$ plot exhibits a linear behaviour, while a $\log_{10}k$ vs $^1/T$ plot is distinctly curved[82]; and thus the mechanism for reaction is best described by the Energy Transfer model.

6.4(ii) Theory

The overall process for the reactions under study is:

$$A^{+\cdot} + A \xrightarrow{k_3} A_2^{+\cdot} \qquad (6.19)$$

where;

$$d[A_2^+]/dt = k_3[A^+][A] \qquad (6.20)$$

fig. 6.21 FORWARD ASSOCIATION RATE CONSTANT AS A FUNCTION OF TEMPERATURE FOR THE SYSTEM: $N_2^{+\cdot} + N_2 + Ar \longrightarrow N_4^{+\cdot} + Ar$

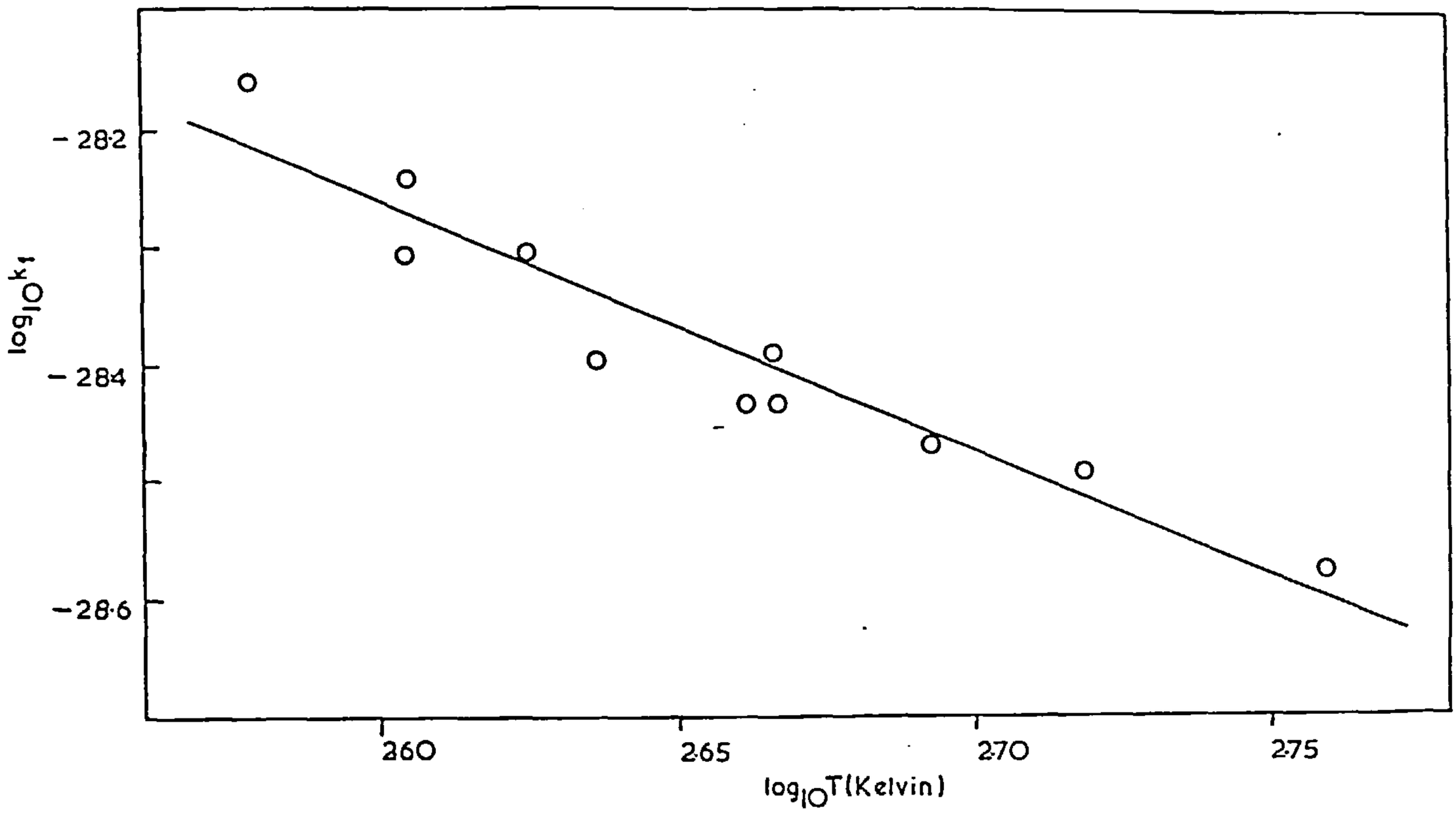

fig. 6.22 LOG k_f vs 1/T PLOT USED TO INVESTIGATE THE MECHANISM OF THE $CO^{+\cdot}$/He SYSTEM ASSOCIATION REACTION (see section 6.4(i)).

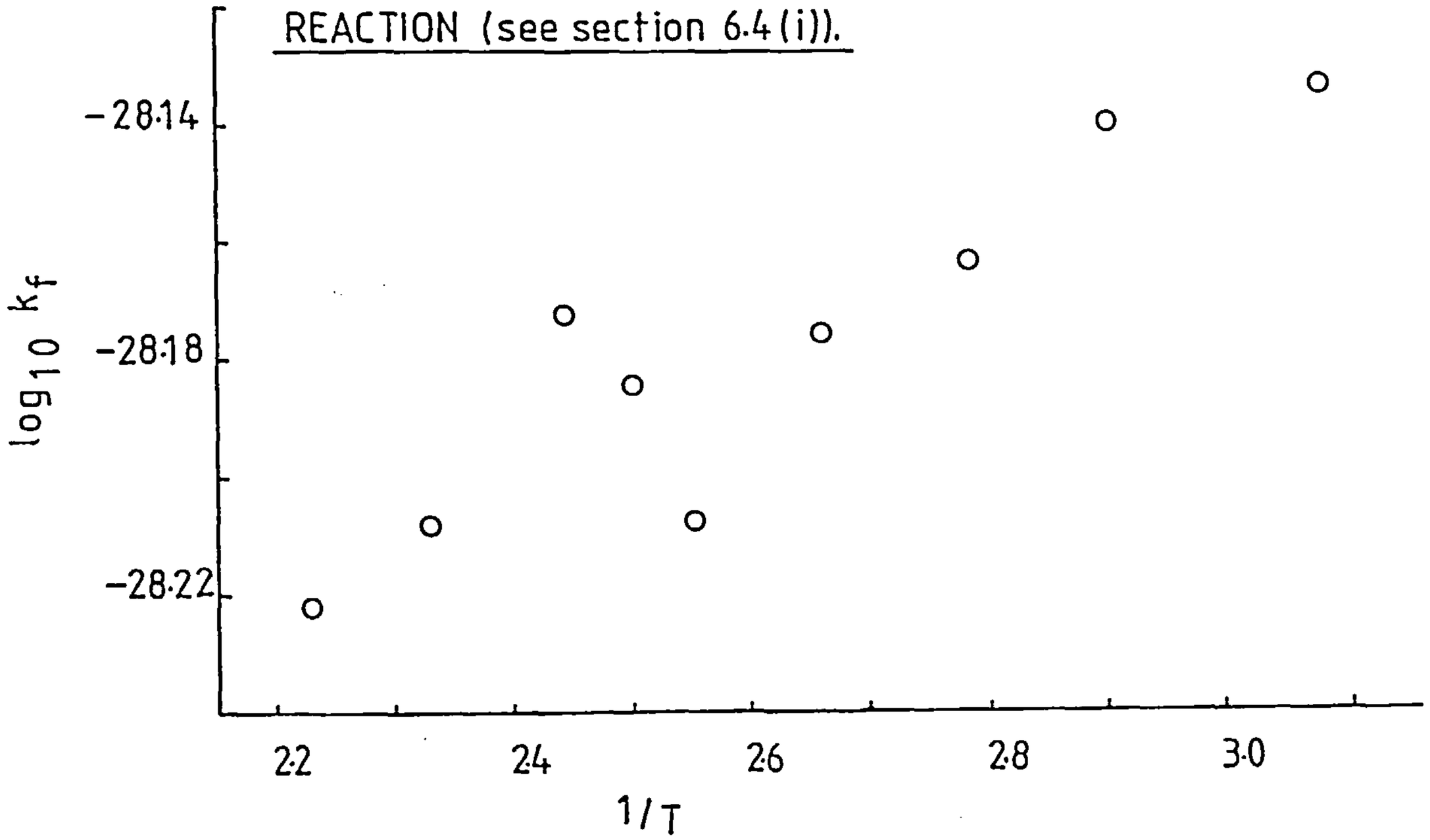

and k_3 is in general pressure dependent. A more detailed mechanism involves the energy transfer model:

$$A^{+\cdot} + A \underset{k_b}{\overset{k_a}{\rightleftharpoons}} (A_2^{+})^* \qquad (6.21)$$

$$(A_2^{+})^* + M \xrightarrow{\beta k_s} A_2^{+\cdot} + M \qquad (6.22)$$

$$(A_2^{+})^* + A \xrightarrow{\beta' k_s'} A_2^{+\cdot} + A \qquad (6.23)$$

where the asterisk denotes that the dimeric species is in some rotationally and/or vibronically excited state; β is the collisional stabilisation efficiency of the bath gas M (or β' for A). This mechanism can yield an expression for the rate of formation of the dimer:

$$d[A_2^{+}]/dt = (\beta k_s[M] + \beta' k_s[A])[A_2^{+}]^* \qquad (6.24)$$

Applying a steady-state approximation to $[(A_2^{+})^*]$ and substituting in equation 6.24 yields an expression for $d[A_2^{+}]/dt$ which may be equated with expression 6.20 and solved for k_3. The resulting expression is:

$$k_3 = \frac{k_a \beta k_s[M] + k_a' \beta' k_s'[A]}{k_b + \beta k_s[M] + \beta' k_s'[A]} \qquad (6.25)$$

For the majority of the two-component systems studied here, the concentration of A was normally < 1% of the total pressure and the relationship 6.25 may be simplified to:

$$k_3 = \frac{k_a \ k_s \beta [M]}{k_b + \beta k_s[M]} \qquad (6.26)$$

The negative temperature dependence of k_3 is expected as k_b is assumed to increase as the temperature of the reagents forming the dimer increases. The rate constants k_a and k_s are calculated by ADO theory as detailed in section 2.5. Here it is assumed that all A^+/A collisions result in the formation of the excited $(A_2^+)^*$ complex. This is in contrast to the collisional stabilisation of the complex where a fraction β of all the $(A_2^+)^*/M$ collisions only are assumed to result in a stabilised complex. The dissociation rate constant k_b for the complex is calculated from the expression:

$$k_b(E,J) = F(E,J)/\rho(E,J) \qquad (6.27)$$

where F(E,J) is the flux through the orbiting transition state, and $\rho(E,J)$ is the density of states for the $(A_2^+)^*$ ion, section 2.6(ii) gives a fuller account of the phase space theory considerations.

The calculations necessary for the determination of k_b have been performed on the CO^+/M data presented here by Bowers[101], primarily for the determination of β, the collisional efficiency of the bath gases.

6.5 Vibrational Quenching of Dimeric Ions

It was discovered as early as 1931 that neutral vibrational de-excitation by the interconversion of vibrational to rotational energy can be very inefficient[102]. For example, approximately 10^{10} collisions of CO(v=1) with CO(v=0) are required at 300K to convert the vibrational energy to translational energy. Vibrational deactivation efficiency is promoted by increasing the violence of collision, i.e. the temperature. The efficiency of such collisions is greater for cases where low frequency vibrations are required to be converted to translational energy[103,94].

In 1974, a study by Anicich and Bowers on the stabilising efficiency of bath gases on dimer ions of 1,1, difluoroethylene, found a direct corelation between the stabilising

efficiency and the reduced mass of the interacting pair[104]. The explanation of this phenomenon was attributed to a direct relationship between the duration of the dimer ion-bath gas collision and the 'active' vibrational modes of the dimer. Later work by Cates and Bowers[105], however, shows no such effect, especially when the bath gases were inert gases. For these the same efficiency was measured even though their masses range from 4 to 131 amu.

Vibrational relaxation of molecular ions by neutrals is generally more efficient because of the added electrostatic potential between ions and neutrals. A recent review by Ferguson[94] shows that the vibrational quenching of an excited ion by its parent neutral is a special case. For such systems the quenching occurs by a near-resonent charge-transfer process providing the reaction is exothermic. Both the N_2+/N_2 and CO+/CO system have been reported on [94,106] and in each system, the quenching is efficient. The latter system was investigated in the CO+(v=1) and CO+(v=4) states, both of which were quenched at near-resonant charge-transfer rates. Very recent work by Lindinger[107] has shown using a drift tube operating high E/N conditions, that N_2+ ions can be vibrationally excited and de-excited by collisions with helium.

Results obtained by Lin and Rabinovitch[108] lead to the conclusion that the collisional efficiency β, of a bath gas is dependent only on the number of transitional modes formed in a collision complex. This number corresponds to the number of translations and rotations in the colliding species that become vibrations in the complex. All monatomic species investigated by this group were found to have the same efficiency. They concluded from this work that for two stabilisers of similar mass, the more complex one will in general be more efficient. Calculations have been performed on the nitrogen association 6.3, which conclude that removal of one vibrational quantum from $N_2^{+\cdot}$ requires a minimum of 10 to 1000 collisions with most molecules[109], increasing to $>10^5$ collisions with helium. It should be noted however, that in this latter investigation measurements were made at low pressure ~ 5.10^{-4} Torr, with the aid of a Tandem Ion Cyclotron Resonance (TICR) technique.

Increasing the pressure of the collision gas in the reaction cell was found to reduce the amount of vibrational excitation of the nitrogen through collisional deactivation. Thus it may be inferred that vibrational excitation will not interfere with the systems studied here because of the much higher pressures at which these systems were investigated in the present work.

In view of the results obtained in this study for the apparent independence of the collisional stabilisation efficiency (see next section) with respect to the bath gas used, it is proposed that the important energy transfer process in these termolecular association reactions is not vibrational energy, but rather rotational or translational energy from the excited complex to the bath gas.

6.6 Comparison and Discussion of Results

Comparisons of the results obtained from the one and two component systems studied are shown in Tables 6.1, 6.2 and Figures 6.23 and 6.24. For the one component monoxide system $CO^{+\cdot}/CO$, good agreement between both HPPS and drift source results were obtained. It is interesting to note that when the results of the third order rate coefficients k_3 at 300K are compared to those of Meot-Ner and Field[82] and Bowers et al[73,87], that the values fall into two groups; the drift source data of this work and Bowers at 20.5 and $19.7.10^{-29}$ cm^6sec^{-1} respectively, and the corresponding lower HPPS results of 14.3 and $11.4.10^{-29}$ cm^6sec^{-1} obtained from this work and Meot-Ner and Field respectively. The temperature dependence m values for this system are, however, more comparable ranging from -1.50 to -1.60. Such a separation was also found in the case of the $N_2^{+\cdot}/N_2$ system, again the quoted drift source/table results are slightly lower than the comparable HPPS results, see Table 6.2.

No conclusions can be readily deduced from the $CO^{+\cdot}$/He results. Here good agreement with both comparative studies for the rate constant was obtained, with the present result for k_3 being close to the average of the literature values, Table 6.1. The temperature dependence m obtained here of value -1.12 is in good agreement with Bowers result of -1.22 but differs significantly from Meot-Ner and Field's value of -1.5. This latter result is very similar to this

Table 6.1

THIRD ORDER ASSOCIATION RATE COEFFICIENTS k_3 –

FOR CARBON MONOXIDE SYSTEMS: $CO^{+\cdot} + CO + M \xrightarrow{k_3} (CO)_2^{+\cdot} + M$

System $CO^{+\cdot}/M$	k_3 (@ 300K) molecules^{-2}cm^{6}sec^{-1}	Method	$k_3 = CT^m$ m	β	Pressure Range data collected over/Torr	Ref.
$CO^{+\cdot}/CO$	14.3×10^{-29}	HPPS	-1.50 ± 0.30	1.0	0.2 – 3.51 Torr	This work
	20.5×10^{-29}	Drift Source	-1.54 ± 0.35	1.0	0.64 Torr	This work
	19.7 c 10^{-29}	Drift Source	-1.60	1.0	~0.5 Torr	87
	11.4×10^{-29}	HPPS	-1.5	1.0	0.2 and 0.8 Torr	82
$CO^{+\cdot}/He$	8.8×10^{-29}	HPPS	-1.17 ± 0.32	1.0	2–6 Torr	This work
	4.78×10^{-29}	Drift Soruce	-1.22	0.34	~0.5 Torr	87
	14.2×10^{-29}	HPPS	-1.5	0.99	0.075 – 0.25 Torr	82
$CO^{+\cdot}/Ne$	——	HPPS	Unable to measure	rate constant		This work
	5.47×10^{-29}	Drift Source	-1.20	0.55	~0.5 Torr	87
$CO^{+\cdot}/Ar$	19.5×10^{-29}	HPPS	-1.53 ± 0.32	1.0	1 – 3.5 Torr	This work

fig 6.23. Comparison of $CO^{+\cdot}$/M Results

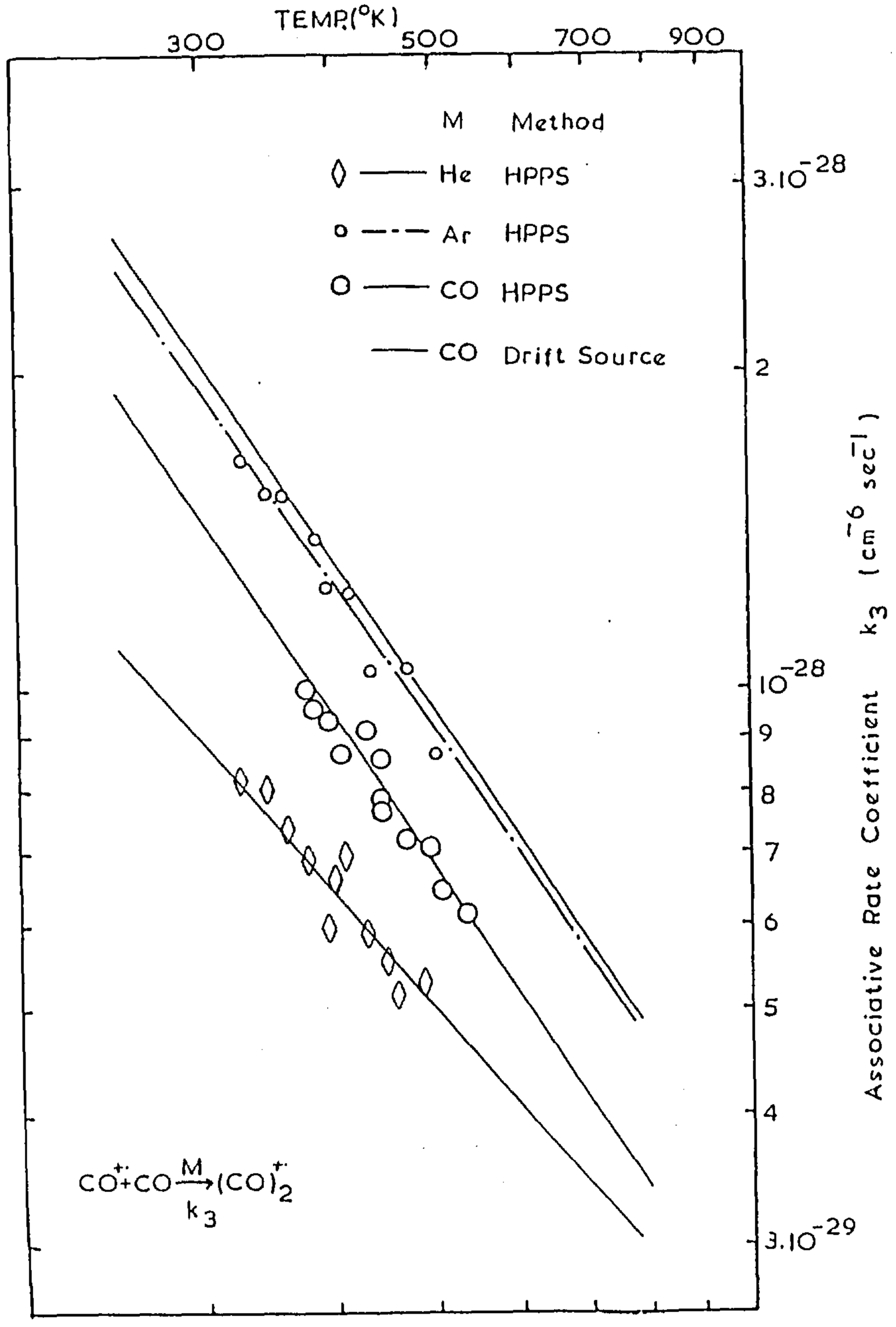

fig. 6.24. Comparison of $N_2^{+\cdot}$/M Results

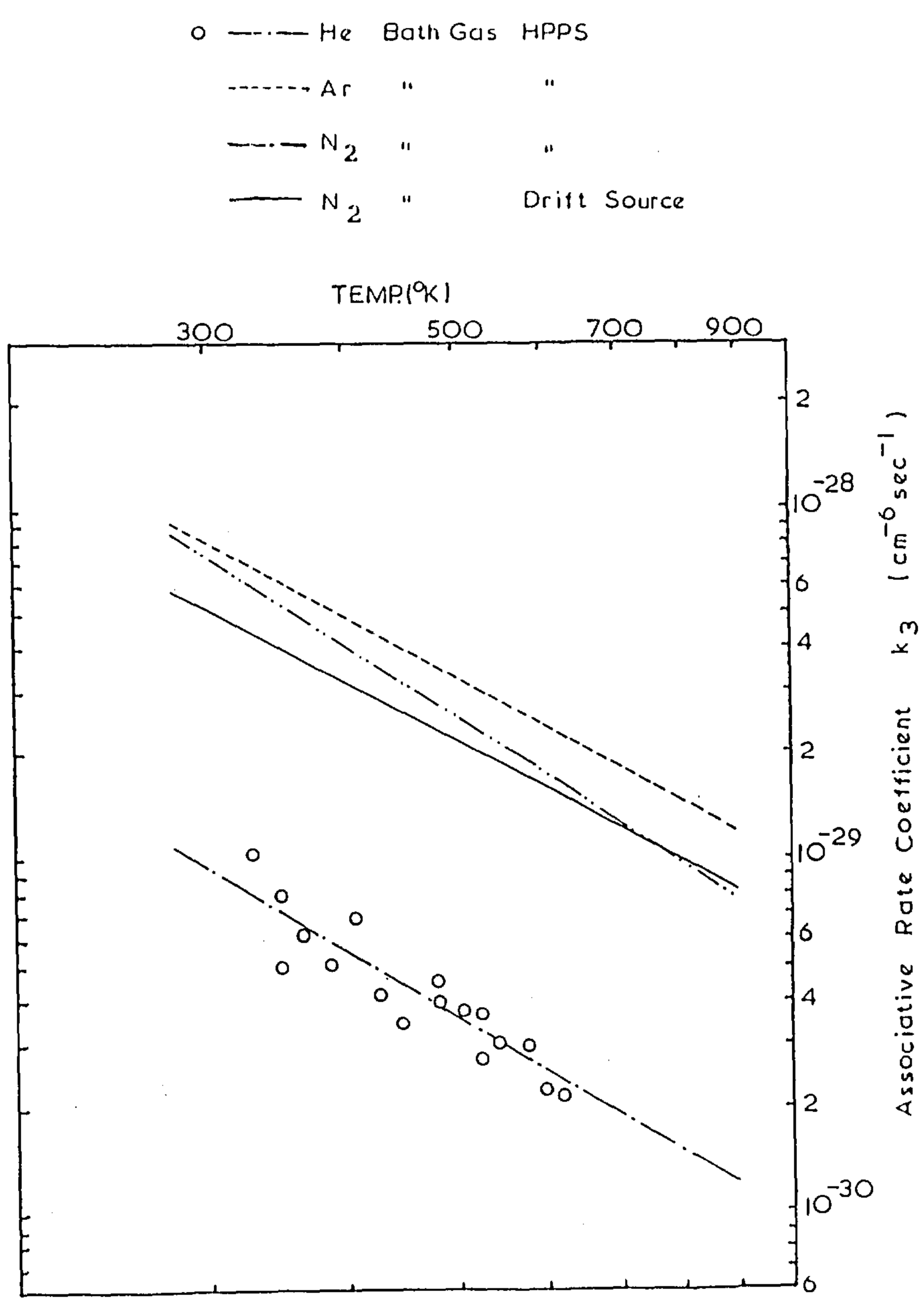

group's corresponding one component system study; k_3=11.4/14.2.10^{-29} cm^6sec^{-1} for the $CO^{+\cdot}$/CO and $CO^{+\cdot}$/He studies respectively with m equal to 1.5 found for both. However, the measured collision efficiency β for Helium relative to CO was measured as 0.99, in very good agreement with the value deduced here of 1.0, compared to a value of 0.34 for Bowers. It was shown that on investigation of the $CO^{+\cdot}$/Ar system that very similar results for both k_3 and m to those obtained for the $CO^{+\cdot}$/CO system were measured. A similar agreement was also found upon investigation of the analogous nitrogen system, Table 6.2 and Figure 6.23. It is concluded from these results that the corresponding $CO^{+\cdot}$/CO, $CO^{+\cdot}$/Ar and the $N_2^{+\cdot}$/N_2, $N_2^{+\cdot}$/Ar system are behaving in a very similar manner. Hence, the collisional stabilisation efficiency β, of both the parent gas and the inert gas argon in each group must be the same, i.e. β=1.0 for argon relative to CO or N_2. Some supporting work for this assumption that β=1.0 for argon has been given by Lindinger at al[112] where a flow drift tube was used to investigate N_2, CO and CO_2 reactive systems. Here it is suggested that argon buffer gas may 'simulate' Boltzmann equilibria better than the more commonly used helium buffer. This is believed to be a consequence of the reagent ion-buffer gas collisions being more energetic for the $M^{+\cdot}$-Ar case compared to the $M^{+\cdot}$-He analogue.

As for the carbon monoxide system, an increase in the temperature dependence of the dimer formation was seen for the N_2 analogue on changing to helium buffer gas; -1.85 (av. result from two ion sources) compared to -1.67 for the $N_2^{+\cdot}$/N_2 and $N_2^{+\cdot}$/He systems respectively. When these systems were investigated by Smith and Adams[111] a much larger negative m value was obtained for the $N_2^{+\cdot}$/N_2 study, -2.20, which changed only slightly when helium bath gas was used to -2.30. This discrepancy is further complicated as good agreement was found in the rate constant determined at 300K. Johnson and co-workers have also measured k_3 and obtained a similar result of -2.20 for the temperature dependence of the $N_2^{+\cdot}$/N_2 system, both latter results being obtained with the aid of a SIFT and drift tube apparatus.

Table 6.2

THIRD ORDER ASSOCIATION RATE COEFFICIENTS k_3 – FOR NITROGEN SYSTEMS: $N_2^{+\cdot} + N_2 + M \xrightarrow{k_3} N_4^{+\cdot} + M$

System $N_2^{+\cdot}/M$	k_3 (@ 300K) molecules^{-2}cm^{6}sec^{-1}	Method	$k_3 = CT^m$ m	β	Pressure Range data collected over/Torr	Ref.
$N_2^{+\cdot}/N_2$	5.3×10^{-29}	Drift Source	-1.75 ± 0.55	1.0		This work
	7.6×10^{-29}	HPPS	-1.95 ± 0.26	1.0		This work
	5.5×10^{-29}	Drift Source	-1.67 ± 0.07	1.0	~ 0.4 Torr	73
	6.1×10^{-29}	Drift Tube	-1.64	---		81
	7.9×10^{-29}	HPPS	-1.70	1.0	0.2 and 0.8 Torr	82
	5.0×10^{-29}	Drift Tube	-2.20	---		70, 110, 111
	4.5×10^{-29}	HPPS	-3.80 ± 0.3	---		29, 66, 67
$N_2^{+\cdot}/He$	1.1×10^{-29}	HPPS	-1.67 ± 0.21		0.5 to 6.0 Torr	This work
	0.9×10^{-29}	Drift Source	-1.54 ± 0.02	0.14		73
	1.6×10^{-29}	SIFT	-2.4	---		70, 110, 111
$N_2^{+\cdot}/Ar$	1.4×10^{-29}	Drift Source	-1.54 ± 0.07	0.36		73
$N_2^{+\cdot}/Ar$	8.4×10^{-29}	HPPS	-1.85 ± 0.25	1.0	0.5 – 2.8 Torr	This work

Our results suggest that both CO, He and Ar have the same stabilisation efficiency. Bowers was able to study successfully the CO^+/Ne system at lower temperatures and pressures than this work and obtained a β_{Ne}/β_{CO} ratio of 0.55. This indicates for the latter study that the relative stabilisation efficiencies of the bath gases to be CO>Ne>He; which is in agreement with earlier results of Bowers on the nitrogen association[73], i.e. N_2>Ne>He. Other groups have found that β for helium in the nitrogen clustering reaction to be greater than that of nitrogen itself[111]. Similar conflicting data has been reported on the HCO^+/M system[82]:

$$HCO^{+\cdot} + CO + M \longrightarrow (HCO.CO)^{+\cdot} + M \qquad (6.28)$$

where M is H_2 and CO. Results of Meot-Ner and Field[82] show that hydrogen is more efficient as a third body than carbon monoxide by a factor of two, whereas for the CO^+/M analogue, CO is more efficient than He by about 50%. These latter conclusions were deduced by comparing rate constants for the forward reaction, and not the collisional stability β. Although this data base is quite limited it appears that the changes found in the measured parameters may be dependent on the pressure at which the experiments were carried out.

Critical examination of various experimental techniques is necessary to attempt to resolve these conflicting results. For the HPPS and drift sources used here, the good agreement obtained by investigation of one-component systems with results published by other groups leads us to believe that both ion sources are operating reliably. Possible causes of error in both ion sources have been considered in earlier sections and relative conclusions drawn. A cause of error maybe due to changing the ion source pressure during rate constant determinations. The rate constant k_3 is known to be pressure dependent as shown by expression 6.26. However, this effect is believed to be significant only at low temperatures (<150K) where k_b is small and $\beta k_s[M]$ is no longer negligible with respect to k_b. This effect has been shown to be very small above 300K for the nitrogen association by Bass and

Jennings[61] and a similar behaviour can be expected with carbon monoxide. It should be noted that the latter work assumes k_3 is measured using a constant ion source pressure.

Some drift tube results must be viewed with caution, particularly so when they are used in temperature dependence studies of rate constants rather than energy dependence studies. It has been shown that rate constants measured by this experimental apparatus only approach the 'true' temperature values due to the low gas density in the reaction region[130]. The discrepancies in rate constants between drift tube results and 'true' thermal values are attributed to differences in the extent of vibrational excitation of the reactant ions under the different conditions.

The theoretically determined values of the temperature dependence $\underline{m}$ of the termolecular reactions studied are shown in Tables 6.1 and 6.2. Values of -1.5 and -1.7 for transition state theory, TST, and phase space theory, PST, are obtained respectively. These values are of particular interest as $\underline{m}$ is found to be independent of the third body used, in disagreement with the experimentally derived values. This finding is not surprising when the theoretical expressions used in relating k_3 and temperature are considered; no terms corresponding to the bath gases are found to be included, Chapter 2. Results obtained by phase space theory assume that the experiments are performed under the low pressure limit conditions where k_b is considered to be independent of pressure. From examination of this work very similar results in k_3 and $\underline{m}$ are found when either one component systems or argon is used as a bath gas. This is now believed to be a consequence of a mass effect in the colliding $(P)_2^+$/Ar species where P is the primary ion under investigation. CO^+/He and N_2^+/He systems were monitored over a pressure range which is approximately twice that used when different collision gases were investigated. These conditions were necessary to obtain large enough primary and secondary ion intensities for reliable signal monitoring. Thus the systems CO^+/M and N_2^+/M where M is either He or Ne, were studied under conditions of high gas number density and consequently high collision conditions.

This work and that performed by Meot-Ner and Field on similar systems with similar results were conducted at higher pressure than that used in the work of Bowers et al. Thus it may be considered that the change in k_3 may be due primarily to the fact that k_b is no longer pressure independent as the low pressure limit assumption is no longer valid. This may explain the apparent 'levelling out' observed in the plots used to determine k_3 at higher pressures, Figure 6.3, although this phenomenon was greatly reduced at higher temperatures. Drift source experiments do not experience this problem and may be considered more reliable. However this does not explain the apparent inability of theory to predict a change in the temperature dependence m for different bath gases. Low temperature studies of the carbon monoxide systems show deviations from linearity of the log/log plot from the $k=CT^m$ relationship. These deviations are more significant when CO is used as a bath gas as opposed to He or H_2[82]. The energy of interaction of the CO molecule with the excited complex must be significantly larger than those of He or H_2 with the complexes. No such deviations are experienced by another group however, working at very low pressure conditions. Rowe's experiments[83] conducted at a pressure of the order of 10^{-3} Torr are also assumed to be in the low pressure limit. Good agreement was found between Rowe's reported results at high temperatures and those from HPPS experiments. The low pressure assumption used at high temperatures now spans four orders of magnitude and must be considered questionable. If it is decided that this work is not in the low pressure limit, then the observed lack of change of β with different bath gases may be due to the rate of back dissociation increasing linearly as the pressure increases. A consequence of this is that all k_3 values measured are in error due to k_b varying during each determination, and hence the collision efficiency β is also in error. If the low pressure limit assumption is considered to hold under conditions where the 'levelling out' observed at high pressures is minimal (see Figure 6.3), then the apparent discrepancy in results between different groups may be due to a temperature dependence in β, a possibility which has not been investigated to date. The association reactions occurring in one component systems are sufficiently slow that on

average several hundred/thousand collisions occur before reaction is likely to occur. All the ions are thus well thermalised before reaction, and any energy quenching is also especially effective as symmetric charge-transfer can occur up to more than the Langevin rate[113,114]. Thus it may be inappropriate to compare one and two component system results due to there being a possible different deactivation mechanism for each case.

Chapter Seven

The Measurement of Mobility and Diffusion Constants

7.1 Mobility Measurements

The mobilities of some ions in gases were measured as a function of drift field and temperature. An ion mobility, as defined in section 4.4, is normally quoted as the reduced mobility[76] given by the following expression:

$$K_o = (P/760)(273/T)K \qquad (7.1)$$

where P is the pressure in Torr, T the absolute temperature and K the ion mobility as determined by equation 4.2. The reduced mobility K_o, can be directly determined from ion drift theory[76] and is given by:

$$K_o = 35.9/\sqrt{(\alpha\mu)} \qquad (cm^2V^{-1}s^{-1}) \qquad (7.2)$$

where α is the polarisability of the neutral in atomic units (Ångströms^3) and μ is the reduced mass of the ion-molecule pair in atomic mass units. Under low electric field conditions the ionic velocity distribution is very nearly Maxwellian, i.e. the drift velocity is negligible with respect to the random thermal motion of the gas, and equation 7.2 is generally valid. Under stronger field conditions the ions acquire a small drift velocity component in the direction of the applied field superimposed on their random motion. The thermal onset where all the Maxwellian motion is dominant over the drift velocity of the ions is dependent on pressure and varies for each ion-molecule pair. The theoretical basis of the applicability of this theory has been discussed[78] and is summarised elsewhere[115]. The reduced mobility is measured as a function of either E/P or E/N where E is the electric field, P the pressure of the gas and N the gas number density. An ion's mobility will become independent of this parameter E/P, as

this ratio approaches zero. Thus, the zero field reduced mobility of an ion in a gas is obtained by extrapolating a plot of K versus E/P to zero field. The reduced mobility of Ar^{+}; $CO^{+\cdot}$and $N_2^{+\cdot}$in their respective parent gases were measured as a function of E/P by use of the pulsed electron beam, high pressure drift source described in chapter 4. The results are shown in Figures 7.1, 7.2 and 7.3 for the $Ar^{+\cdot}/Ar$, $CO^{+\cdot}/CO$ and $N_2^{+\cdot}/N_2$ systems respectively. The thermal onset, where the measured mobility becomes independent of E/P, was not observed over the experimental conditions used here (E; 1 to 5 Vcm^{-1}; Pressure 0.4 or 0.5 Torr). An accurate extrapolation to zero field conditions was made using a least squares analysis fit to the data to obtain K_o for all three ions at various temperatures.

7.2 Reduced Mobility Results obtained for 300K

The mobility of $Ar^{+\cdot}$in argon has been investigated by many groups; table 7.1 The results obtained in this work show $K_o = 1.52 \pm 0.05$ $cm^2V^{-1}s^{-1}$ at 300K and is in good agreement with the other studies listed. An interesting aspect of similar systems has been reported by Helm and Elford[116,117] for neon, krypton and xenon. They observe that spin-orbit coupling occurring in an ion affects measured K_o values. In both krypton and xenon, Helm observed that the mobility of the ions in the $^2P_{1/2}$ state was higher than that in the $^2P_{3/2}$ state, the reverse being the case for neon. In this work no such effect was observed in argon although Helm has argued that the different Ar^{+} mobilities due to the $J = {}^1/_2$ and ${}^3/_2$ states occupied at unknown porportions, lie within $\pm$1.5% of the apparent mobility. This extreme closeness of the different argon ion mobilities means that they cannot be resolved in this apparatus.

The study of the mobility of $N_2^{+\cdot}$and $N_4^{+\cdot}$in nitrogen is of interest as the two ions are linked by the reaction:

$$N_2^{+\cdot} + 2N_2 \longrightarrow N_4^{+\cdot} + N_2 \qquad (7.3)$$

Fig. 7.1 MOBILITY vs E/P FOR $Ar^{+\cdot}$ IN ARGON AT VARIOUS TEMPERATURES EXTRAPOLATED TO ZERO FIELD.

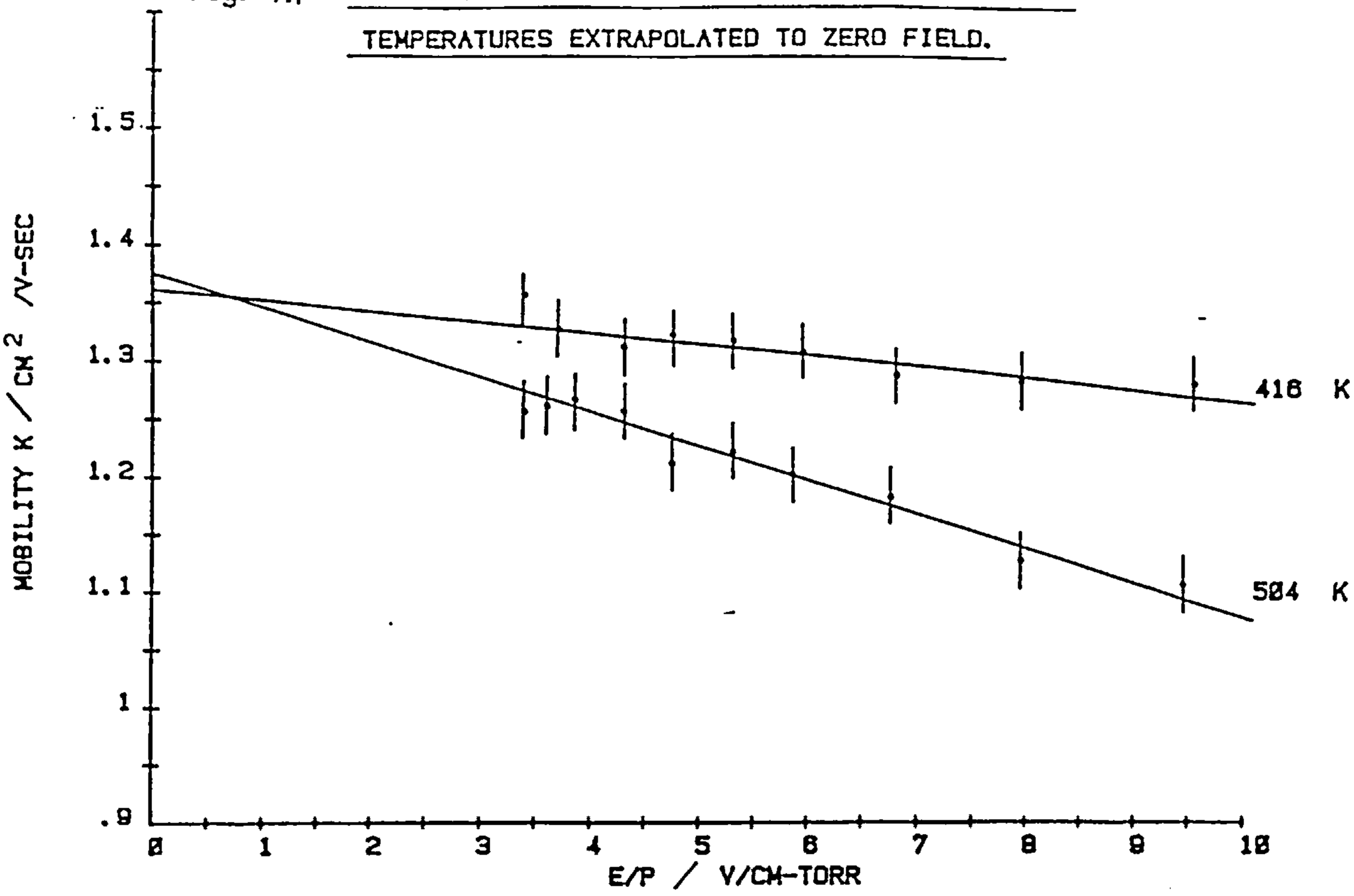

Fig. 7.2 THE MOBILITY OF $N_2^{+\cdot}$ IN NITROGEN AS A FUNCTION OF FIELD STRENGTH. THE EXTRAPOLATED ZERO-FIELD MOBILITY IS SHOWN FOR TWO TEMPERATURES: 375 AND 415 K.

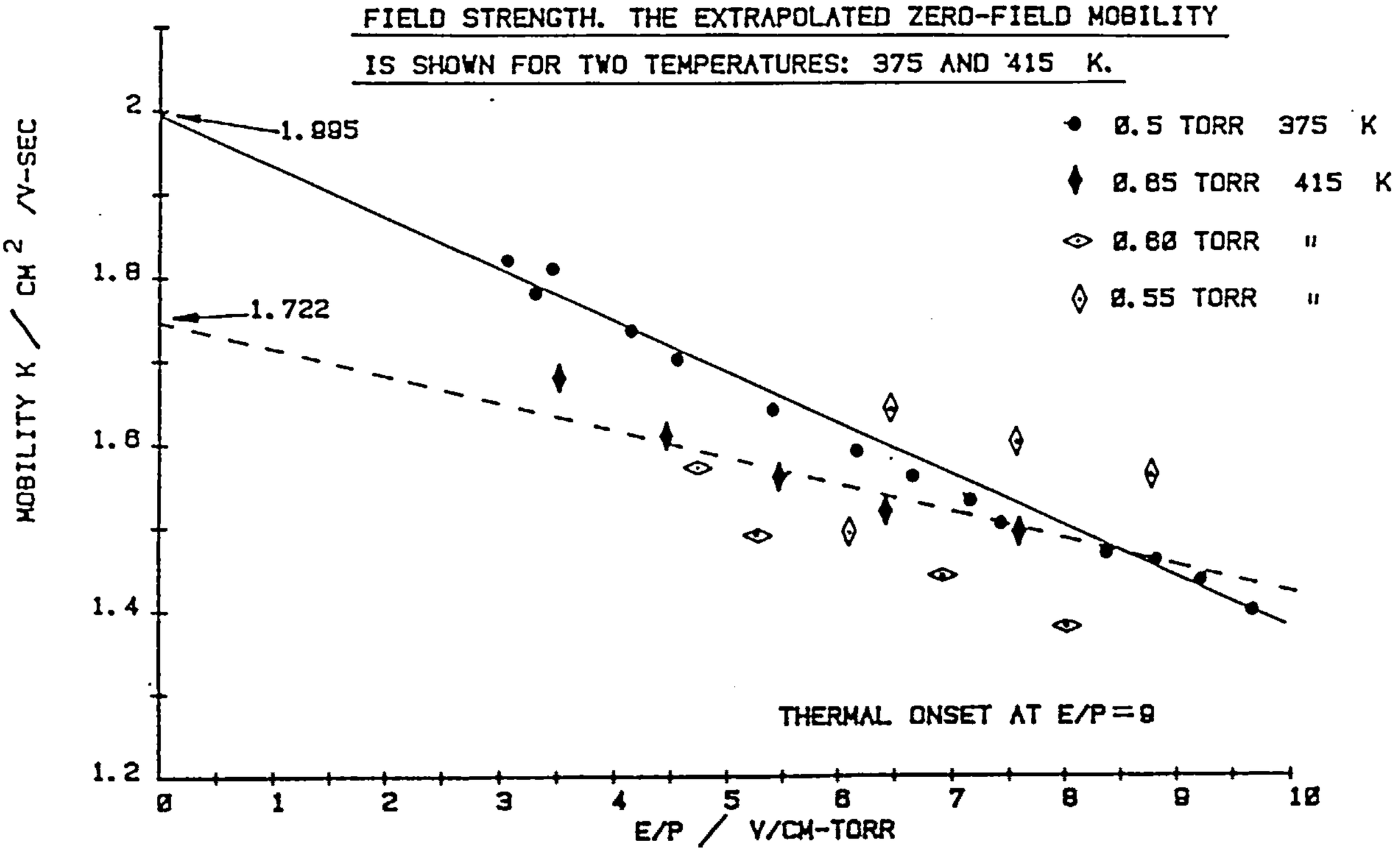

Fig. 7.3 THE MOBILITY OF $CO^{+\cdot}$ IN CARBON MONOXIDE AS A FUNCTION OF FIELD STRENGTH. THE EXTRAPOLATED ZERO-FIELD MOBILITY IS SHOWN FOR TWO TEMPERATURES: 373 AND 423 K.

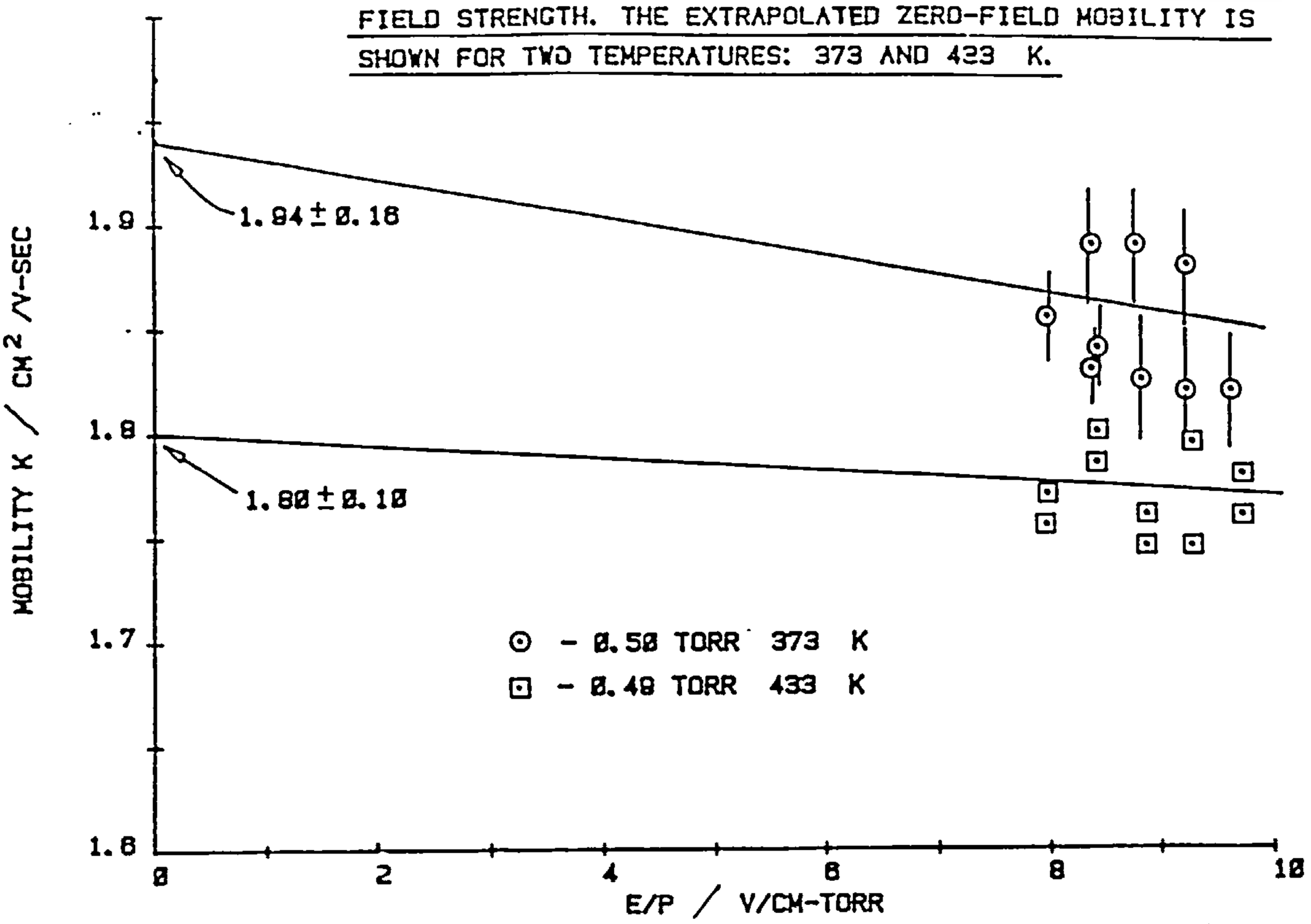

Fig. 7.4 ZERO FIELD REDUCED MOBILITY OF $Ar^{+\cdot}$ IN ARGON AS A FUNCTION OF TEMPERATURE.

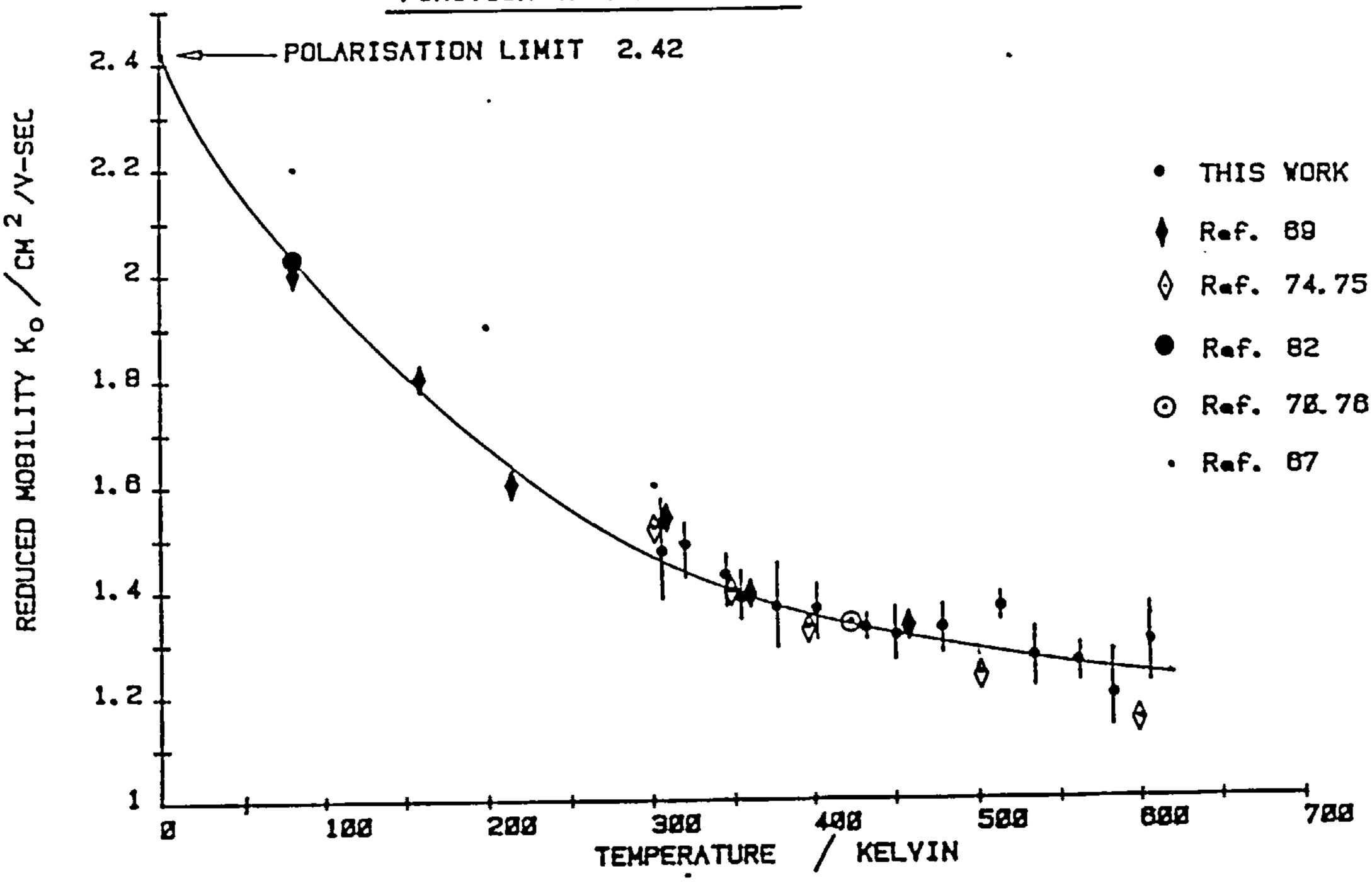

Table 7.1

Zero Field Reduced Mobility

K_o ($cm^2V^{-1}s^{-1}$)

Ion/Neutral	Ko (300K)*	Method	Reference
Ar^+/Ar	1.52±0.05	Drift Source	This work+
	1.52	Drift Source	73
	1.47	Drift Tube	70
	1.53 (318K)		118, 119
	1.35±0.01 (298K)		74, 120
	1.52 (293K)		121
	2.41 (0K)	Polarisation Limit+	
N_2^+/N_2	1.88±0.08	Drift Source	This work+
	1.87±0.06		76
	1.78±0.01		74
	1.90		122
	1.85	Drift Tube	70
	2.81 (0K)	Polarisation Limit+	
CO^+/CO	1.98±0.08	Drift Source	This work+
	1.60		123
	1.56(0K)	Polarisation Limit+	

* Measured at 300K unless otherwise stated

\+ Extrapolated result from this work

\+ Result predicted by equation (7.2)

Measurements of McDaniel on the drift velocity of these species indicate that certain previous results obtained in a drift tube mass spectrometer are in error by a factor of two[79]. This is regarded as being due to the failure to analyse properly the shapes of the arrival time spectra and to take into account the conversion of $N_2^{+\cdot}$ to N_4^{+}: Under the conditions the ion mobility measurements were conducted here, the $N_2^{+\cdot}$ ion intensity was observed to decrease with both decreasing E/P and increasing source chamber pressure P, see Figure 5.14. The origin of the nitrogen ion dimer in the drift source is unknown due to its formation according to reaction 7.3. The measured mobility of this dimer ion would be expected to fall between the true mobilities of the $N_2^{+\cdot}$ and $N_4^{+\cdot}$ ions and would show a pressure dependence. Thus, it was decided not to measure the dimer's mobility as the result would not be a true indication of the sources operating performance. The mobility of the $N_2^{+\cdot}$ ion however, measured at low pressure and low E/N, extrapolates to 1.88 ± 0.05 $cm^2V^{-1}s^{-1}$ at 300K; in good agreement with literature values of 1.78 to 1.90 $cm^2V^{-1}s^{-1}$ determined by other methods, table 7.1.

The conclusions on the results of the carbon monoxide system are mixed. Very little work has been reported on the $CO^{+\cdot}/CO$ system. The result from this work of $K_o = 1.98$ $cm^2V^{-1}s^{-1}$ is 20% larger than that obtained by Varney[123]. The accuracy of this latter result is uncertain due to the long extrapolation of the experimental data required to reach zero field conditons. Schummer's result of $K_o = 1.56$ $cm^2V^{-1}s^{-1}$ is also questionable. This value is quoted at an E/P value of 75 $Vcm^{-1}Torr^{-1}$ and shows an increasing trend in the K_o value with decreasing E/P[124]. Extrapolating this data of Schummer's to zero field conditions yields a $CO^{+\cdot}$ reduced mobility of 1.78 $cm^2V^{-1}s^{-1}$ which is still lower than this works value by 10%.

The carbon monoxide system is similar to the nitrogen system in that the $CO^{+\cdot}$ ion undergoes the association reaction:

$$CO^{+\cdot} + 2CO \longrightarrow (CO)_2^{+\cdot} + CO \qquad (7.4)$$

Figure 5.18 shows the mass spectra obtained for pure CO in the drift source at typical operating pressures. The most abundant peak at an m/z ratio of 56, corresponds to the dimer ion. The results of Schummer of K_o = 1.56 and 1.97 $cm^2V^{-1}s^{-1}$ for the $CO^{+\cdot}$ and $(CO)_2^{+\cdot}$ species respectively were obtained at much lower pressures (0.08-0.15 Torr) where the amount of dimerisation occurring would be expected to be very limited compared to this work (0.4-0.7 Torr). It is believed that under the source conditions used here, this system is able to undergo the dimerisation reaction to a much greater extent and thus the result obtained may be a misnomer. However, it should be noted that Schummer's results were obtained at a much higher effective field strength of 75 to 150 Td compared to 5 to 17 Td for this work, and may not therefore be at the true thermal value stated.

7.3 The Temperature Dependence of K_o

Ion mobilities for a large number of ions have been measured by the use of drift tubes[44,76] and flow drift technique[126]. These measurements are generally performed at, or near room temperature. The temperature dependence of the reduced mobility of several ions has been reviewed[44,76,127] but this data rarely extends beyond 300K. Karasek and co-workers have recently reported the variation of K_o for a number of reactant ions used in chemical ionisation studies over the temperature range 293 to 473K by the use of plasma chromatography[128]. Ion mobilities of several polyatomic ions have also been obtained over the temperature range of 73 to 423K from measurements of Ion Cyclotron Resonance line widths[129,130]. The latter method is particularly useful as this technique can measure momentum transfer rates and ion mobilities at very low E/P values where drift and beam methods fail.

The temperature dependence of the zero field reduced mobility for $Ar^{+\cdot}$ argon is shown in Figure 7.4 together with the results obtained by the groups of Helm[117], Ellis[118,119], Biondi[71] and Bowers[73]. The results of Ellis[118,119] are all calculated values except the 300K result which is experimental. Good agreement is shown over the entire temperature range

studied here. These results tend towards a lower limit of K_o at high temperature which can be estimated from this work as 1.23 $cm^2V^{-1}s^{-1}$. This dependence of the reduced mobility with temperature can be explained.

Literature shows a frequent discrepancy between the observed drift properties and the idealised drift properties predicted by equation 7.2, particularly so for ions moving in their parent gases where resonant charge-transfer may occur[44]. For thermal energies, the rate constant for a charge-transfer process may be much larger than that predicted by the polarisation limit. Charge-transfer may dominate all other elastic scattering processes except at very low temperatures where polarisation scattering finally limits the transport process[76,77]. Resonant charge-transfer has a profound effect on the behaviour of the mobility as a function of temperature and is dependent mainly on the cross-section of collision; a large cross-section consequently yielding a low ion mobility. Charge-transfer processes have high cross-sections because of the large internuclear distances (impact parameter) at which they occur. This causes the measured mobility to decrease smoothly with increasing temperature from the polarisation limit, estimated by equation 7.2 for the purpose of comparison, to the value dictated by the charge-transfer process, see table 7.1.

Such effects are evident in the results of this study where the reduced mobility of the ions are reduced 40 to 60% at higher temperatures compared to the values determined at the polarisation limit, Figures 7.4, 7.5 and 7.6. Furthermore, comparison of these results with literature values of K_o reveals a pronounced temperature dependence from 80 to 300K for $Ar^{+\cdot}$ in argon, but is virtually independent to temperature changes over the 400 to 600K range. In the case of $CO^{+\cdot}$ in CO, the decrease over this latter range is much more pronounced, indicating that the effects of charge-transfer in this region are much more dominant. Carbon monoxide is also a polar molecule and ion-dipole interactions may also occur to a much larger extent than experienced in the argon system.

The nitrogen system $N_2^{+\cdot}$ in N_2, has been studied extensively by d.c. mobility techniques[123] and by transient ICR Methods[122,123]. The results of this study show an

Fig. 7.5 ZERO FIELD REDUCED MOBILITY OF $N_2^{+\cdot}$ IN NITROGEN AS A FUNCTION OF TEMPERATURE (374 TO 545 K)

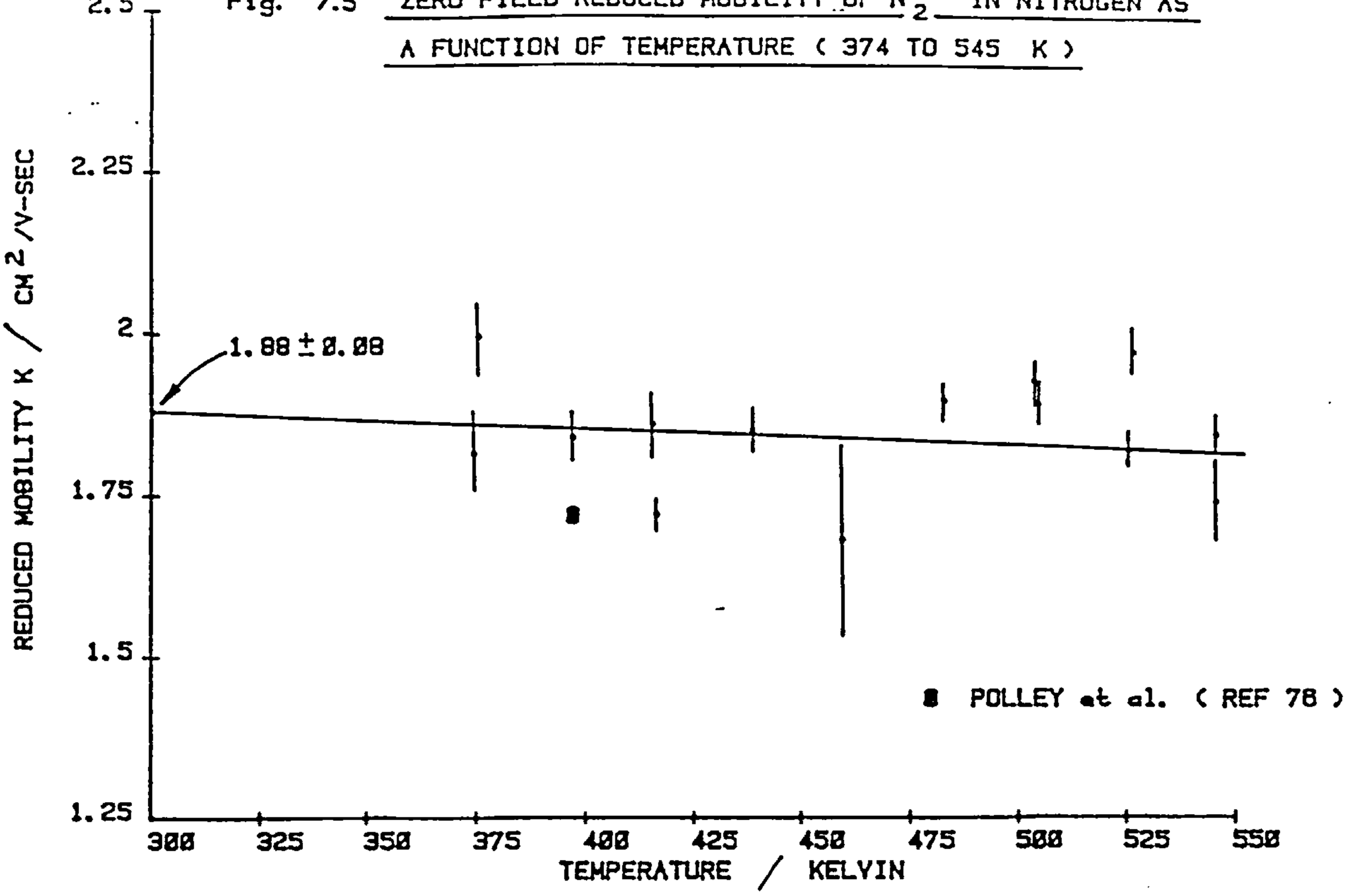

Fig. 7.6 ZERO FIELD REDUCED MOBILITY OF $CO^{+\cdot}$ IN CARBON MONOXIDE AS A FUNCTION OF TEMPERATURE.

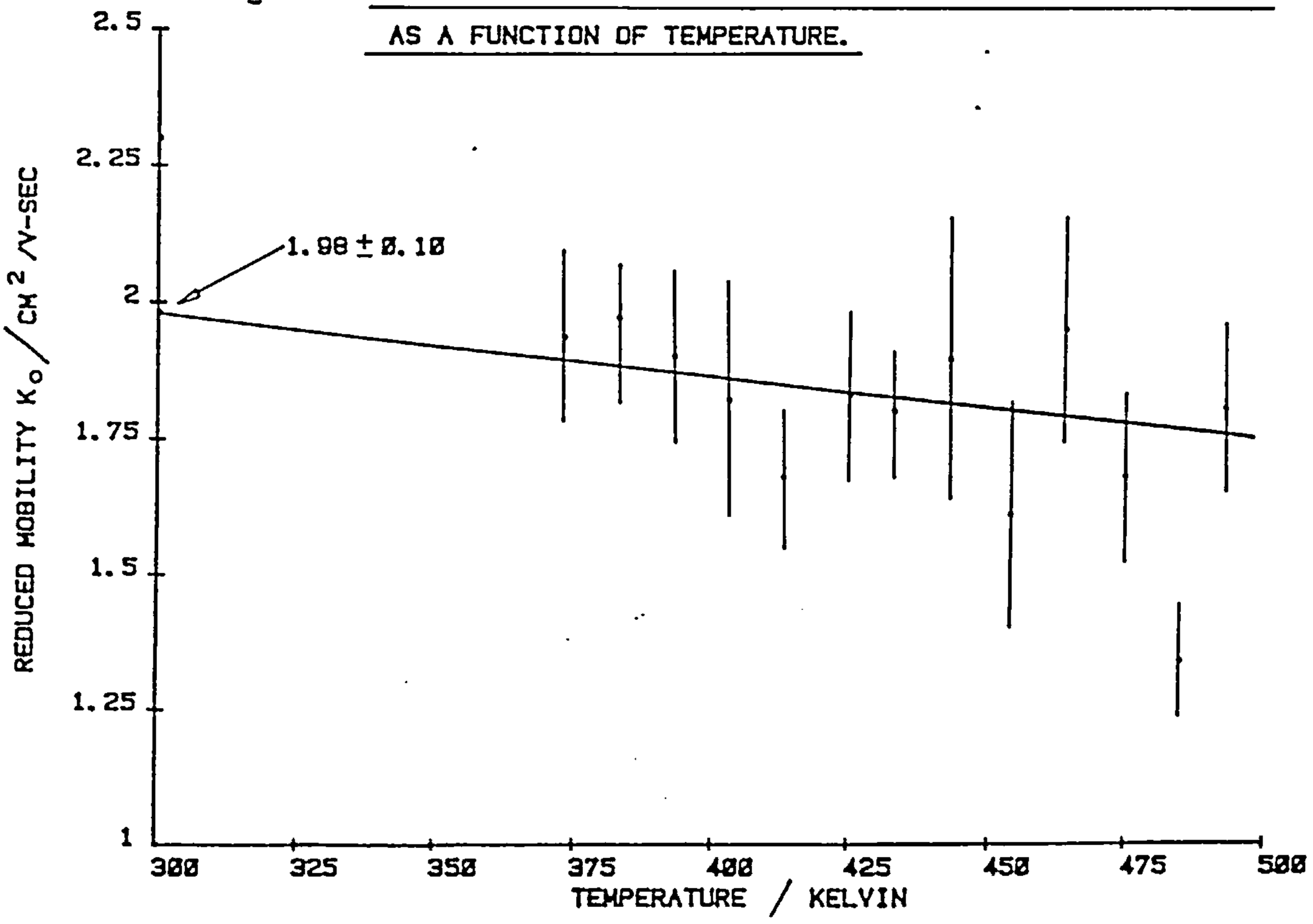

apparent low dependence of K_o with respect to temperature over the range 375 to 545K compared to the two previous studies, Figure 7.6. The low variation in the reduced mobility may be simply due to these experiments being conducted in a temperature range where the charge-transfer process is already dominating all other scattering processes. This is supported in figure 7.7 where the results of Bohringer and Arnold[70], and Ellis et al [118] are shown for comparison. Bowers[130] and Huntress[122] have reported on the temperature dependence of momentum transfer rate constants, k_{mv}, for this system. This is an indication on how the reduced mobility will vary[122], and k_{mv} was found to remain constant, within experimental error over this temperature range[129], in close agreement with this work.

In conclusion we can state that the pulsed high pressure drift source, although not an established technique for obtaining ion mobilities, does yield results in good agreement with literature values for all three systems studied, table 7.1. These comparative values, measured by a variety of techniques, leads one to assume that the source is capable of producing reliable data.

7.4 Diffusion Coefficients

Ions become dispersed throughout a gas by a process known as diffusion. This spatial transport of ions is a consequence of the variation of ionic concentration in a neutral gas environment. The diffusive flow which takes place is directly proportional to the Coulombic forces present between the ions. The constant of proportionality which relates the ionic flux density (the rate of ion flow per second)J, to the variation in ion concentration ∇n, is known as the diffusion coefficient D, as given by Fick's law of diffusion[131]:

$$J = - \nabla D n \qquad (7.5)$$

Fig. 7.7 ZERO FIELD REDUCED MOBILITY OF $N_2^{+\cdot}$ IN NITROGEN AS A FUNCTION OF TEMPERATURE.

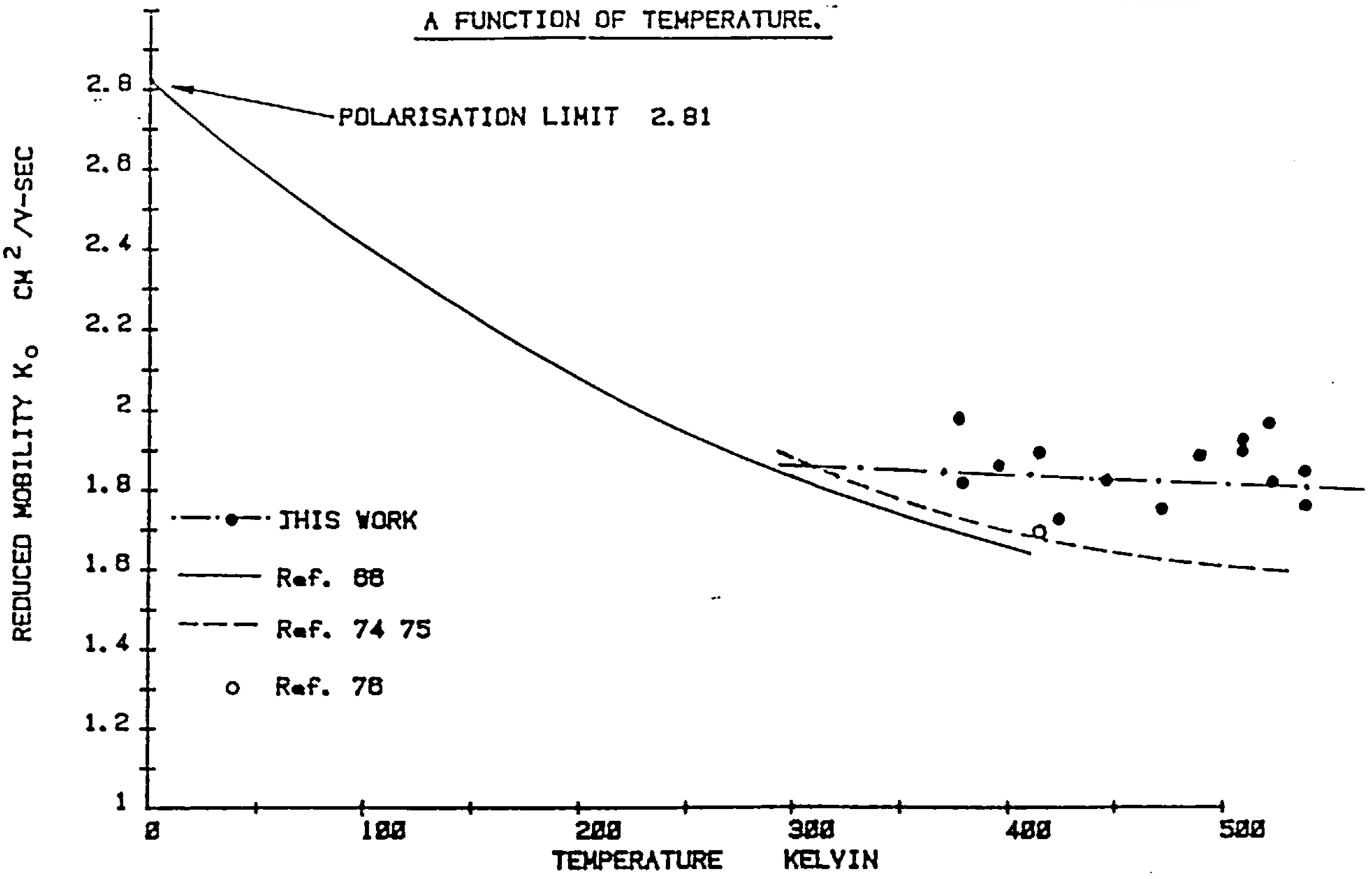

Fig. 7.8 DIFFUSION DATA PLOTTED AS LOG α_T AGAINST LOG T FOR $N_2^{+\cdot}$ IN NITROGEN OVER 388 TO 547 K.

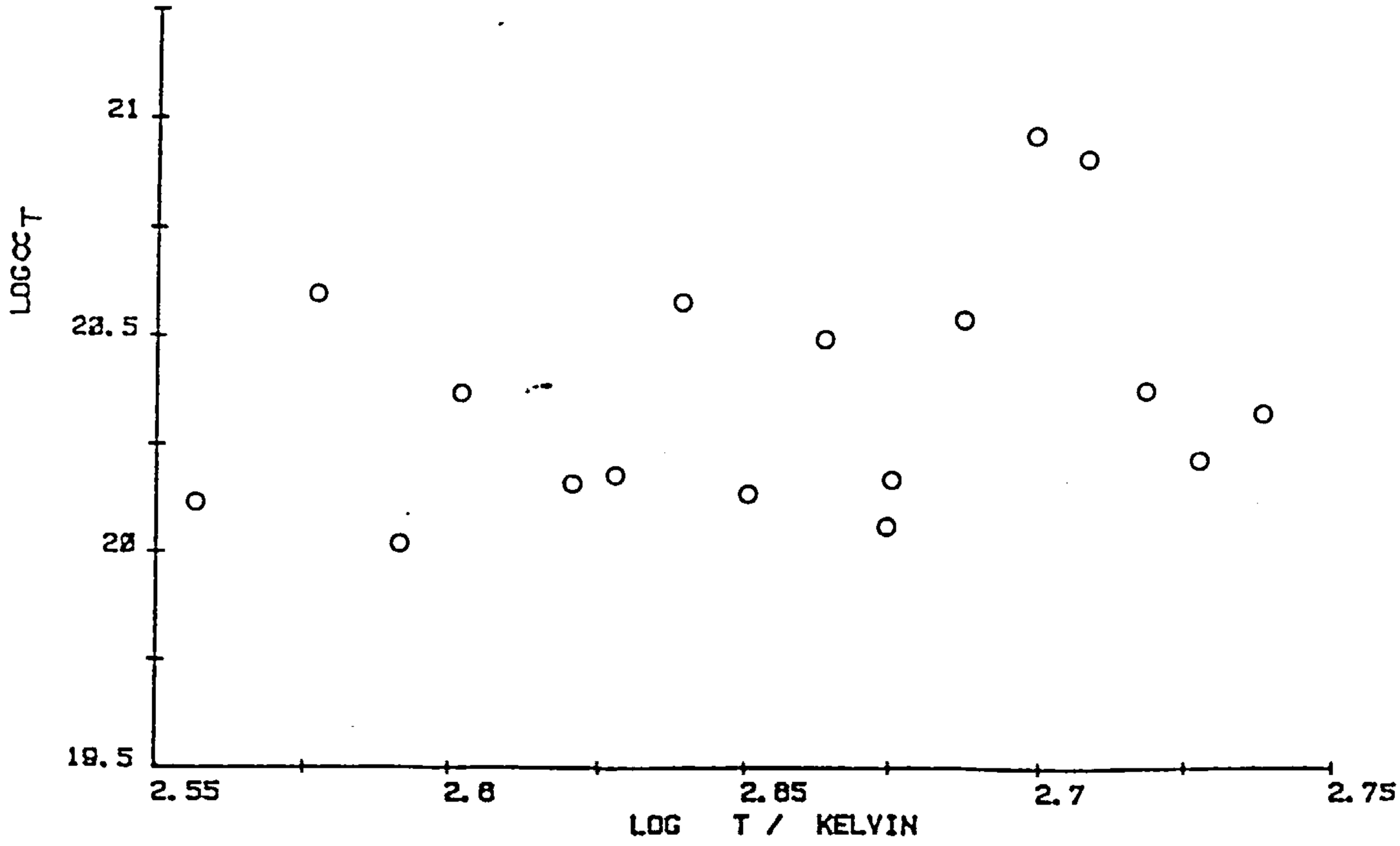

The first order decay constants α_T (denoted as a,b,c,d,e and f in chapters 5 and 6) obtained from the intercept of plots used to derive rate constants (section 3.9(i)), can be related to the diffusion coefficient by the relationship below[76]:

$$\alpha_T = Dn_T/\lambda_D^2 \text{ (molecules cm}^{-3}\text{s}^{-1}) \qquad (7.6)$$

where n_T is the total number density at temperature T. The characteristic diffusion length λ_D (cm) is dependent on the shape and size of the reaction chamber and the mode of diffusion. The reaction chamber of the high pressure ion source can be approximated to a one centimeter cube. The corresponding solution of the diffusion equation has been calculated by McDaniel[76] as:

$$1/(\lambda_{ijk}) = \pi^2[(2i-L)^2 + (2j-L)^2 + (2k-L)]/L \qquad (7.7)$$

where L is the length of the sides of the square ion chamber. As all measurements conducted here on ion peak profiles were conducted in the late afterglow region, the modes of diffusion i,j and k in each direction are assumed equal to unity. Headley has shown that λ_D may be estimated to 0.55cm if fundamental mode diffusion is assumed by using the known mobility of N_2^+ in N_2 and relationships 3.6, 7.1, 7.6 and 7.7. This is in quite good agreement with the approximate 1cm dimension of the source chamber remembering that it was not originally designed for this type of work. However, since λ_D is only approximately known values of the diffusion coefficient D can only be estimated.

7.5 The Temperature Dependence of Diffusion Coefficients

The Chapman-Enskog equation below gives to a first approximation the diffusion coefficient:

$$D = \frac{\text{constant}}{\sigma^2} \cdot \frac{1}{\mu} \cdot \frac{T}{\Omega(T)} \qquad (7.8)$$

where σ is the binary collision cross-section, μ is the reduced mass of the colliding pair and Ω is the collision integral. From this relationship we can determine that the temperature dependence of D is given by:

$$D(T) \alpha T^{1/2}/\Omega(T) \text{ -------> } D(T) \alpha T^{1/2}/\Omega(T) \qquad (7.9)$$

For a general ion-molecule interaction, the potential experienced between the 'colliding' pair is of the form $V(r) \alpha r^{-n}$. Studies into this collision theory[76] yields a temperature dependence of the collision integral of the form $T^{2/n}$. Thus equation 7.9 can be re-written as:

$$D \alpha T^{2/n}.T^{1/2} \qquad (7.10)$$

For low energy collisions the ion-molecule pair experience an attractive r^{-4} potential and thus D is directly proportional to T. At higher temperatures a repulsive r^{-12} potential will dominate and $D \alpha T^{0.67}$. Hence, all the diffusion coefficient data obtained here is presented in the form of a log α_T/log T plot to determine directly from the slope the temperature dependence of D.

The results obtained from this study are shown in Figures 7.8, 7.9 and listed in Table 7.2. The temperature dependencies of these studies were calculated using a least squares analysis fit to the data points. Although this data does show some scatter the gradient values and hence the temperature dependence of the N_2^+/N_2,N_2^+/Ar and CO^+/Ar results show good agreement with the theoretical value of 0.67. However, the CO^+/CO result is somewhat lower at 0.25 although closer to the value obtained by Headley[66] of 0.1 measured using an identical experimental method. This is probably a consequence of resonance change transfer occurring between the $CO^{+\cdot}$ species and the parent molecule. The CO^+/He and N_2^+/He

Figure 7.9 Diffusion Data Plotted as a Function of Temperature

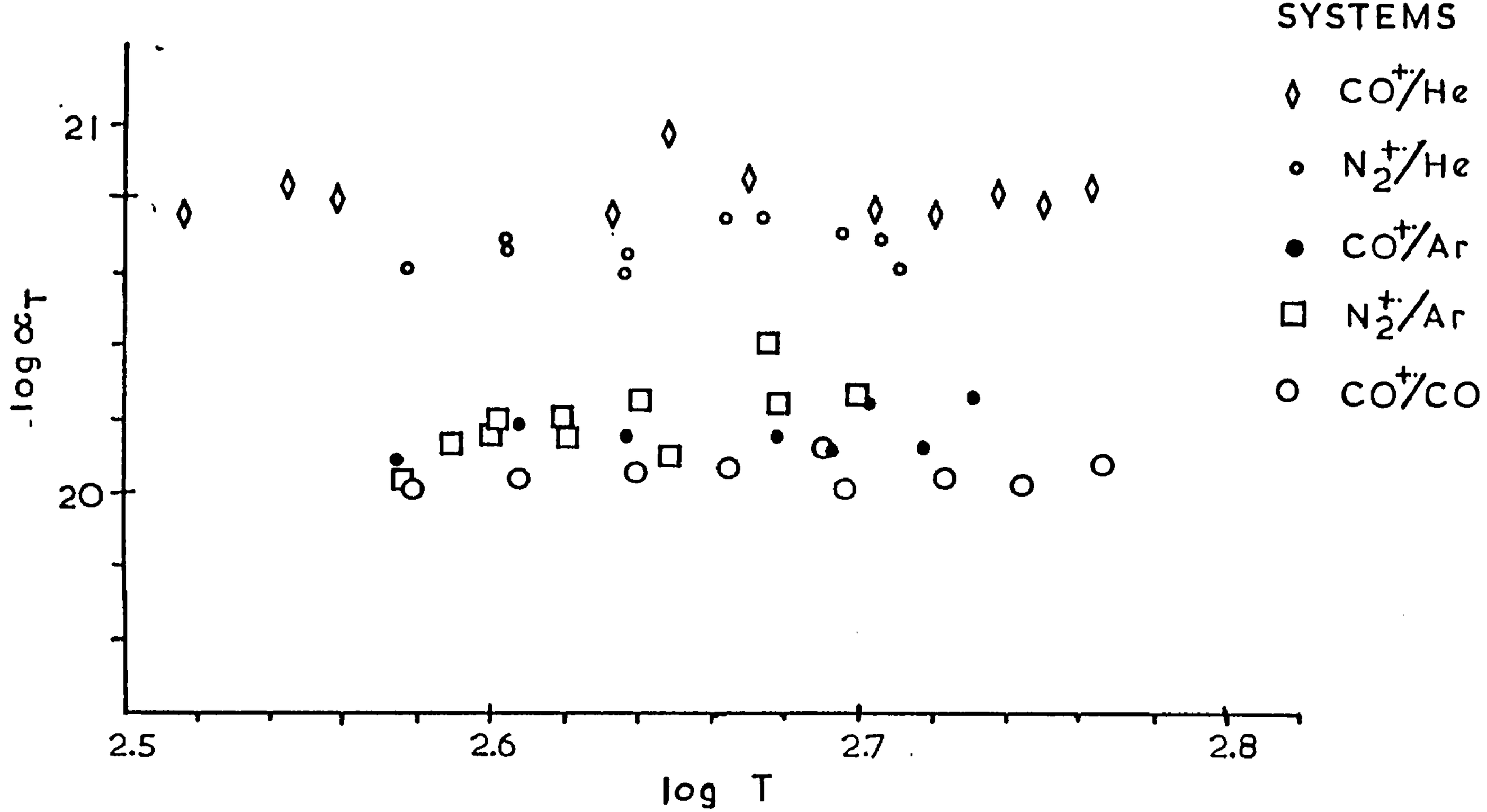

Table 7.2

Diffusion Coefficient Temperature Dependencies

where the temperature dependence x, can be expressed as: $Dn/\lambda^2 = \alpha T^x$

Ion/Neutral	Temperature Dependence x	Reference
N_2^+/N_2	0.69	This work
	0.62	66
N_2^+/Ar	0.79	This work
N_2^+/He	None	This work
CO^+/CO	0.25	This work
	0.10	66
CO^+/Ar	0.56	This work
CO^+/He	None	This work

results show an apparent temperature independence over the experimental temperature range of 370 to 520K. This may be a consequence of scatter in the data points which masks the true trend or simply that the temperature range over which these systems were studied is too short to show the very low value of x. Thus these latter results should be viewed simply as a guide to how the diffusion values may vary as a much more detailed study is required to produce definitive diffusion coefficient and temperature dependence values.

APPENDIX A

The impregnation technique used to implant a fluorescent pigment into the pores of the graphite moderator samples:

(i) The graphite sample is cut up into 4 or 5 blocks, approximately 1.5 by 1.5cm. These samples are then placed in a heated vacuum chamber (250^{o}C, < 1 Torr) for 24 hours. This is to remove all the moisture out of the graphite pore structure.

(ii) A resin (Lemix A-Hard, Emscope Lab. Ltd.) was made up following the manufacturer's instructions and saturated with a yellow dye.

(ii) In turn, each graphite sample is transferred via a butterfly valve into a plastic pot in a secondary vacuum chamber and covered with the resin mixture. The resin impregnates into the graphite and excludes any air from entering the sample.

(iv) After repeating this procedure for all samples they are then placed in an incubator oven at 60^{o}C overnight to cure.

(v) The plastic covers are then removed and the samples are ground and polished to a smooth finish using carborundum paper and diamond paste.

APPENDIX B: MICROSCOPE VIEWS OF GRAPHITE SAMPLES

B1. MP4 AT × 6

B2. MP4 AT × 64

B3. GM3 AT × 6

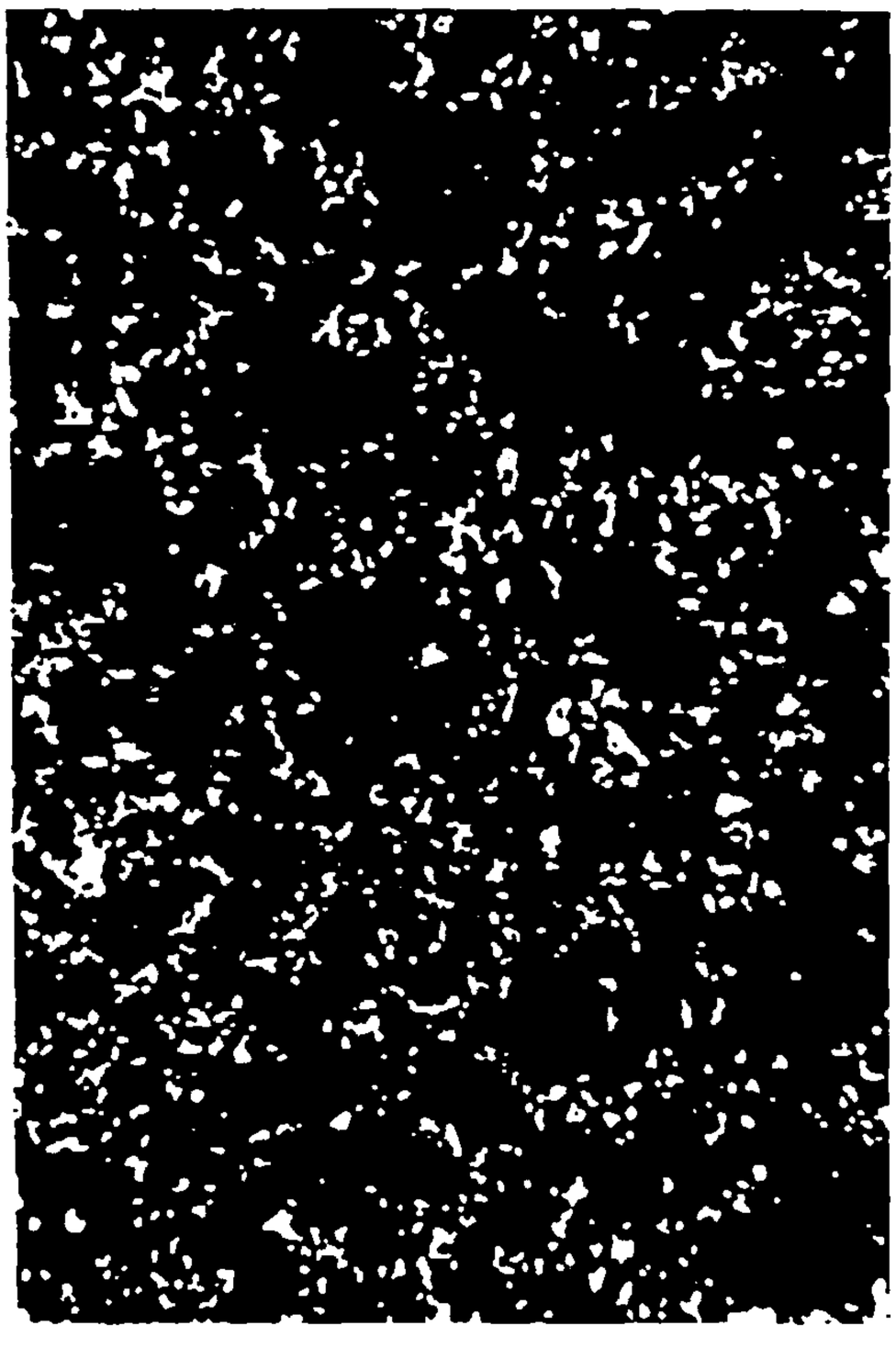

B4. GM3 AT × 64

APPENDIX C: CUMULATIVE OPEN PORE VOLUME (%) VS CHARACTERISTIC PORE DIMENSION TO EVALUATE GRAPHITE PORE SIZE DISTRIBUTION.

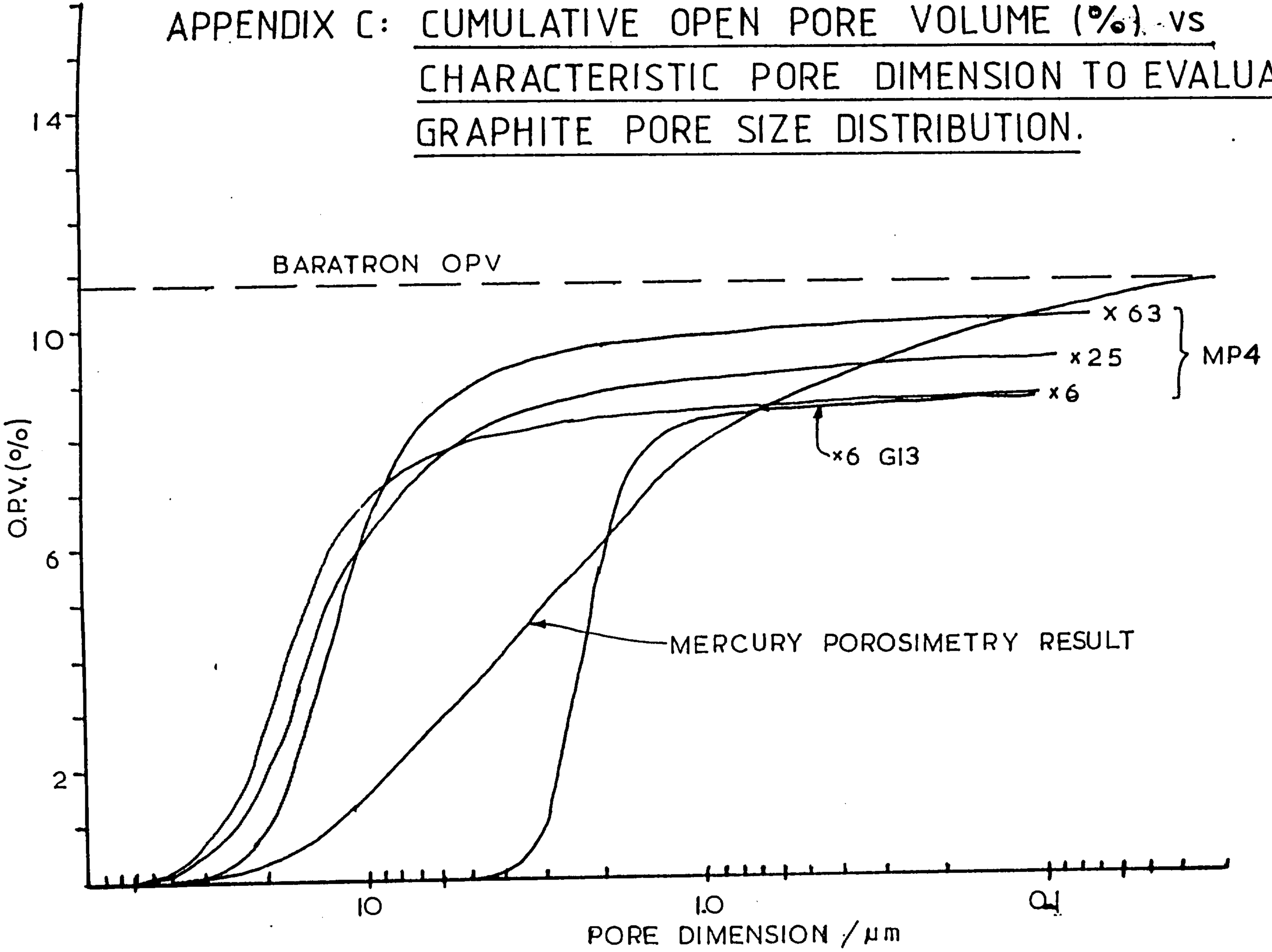

REFERENCES

1 N.G.Adams and D.Smith, 'Reactions of Small Transient Species', Academic Press, London, Chap.6, 311 (1983).

2 W.T.Huntress, Chem.Soc.Rev., 6, 295 (1977).

3 E.E.Ferguson et al, 'Gas Phase Ion Chem.', Vol 1, Academic Press, New York, 445, (1979).

4 E.E.Ferguson and F.Arnold, Acc.Chem.Res., 14, 327 (1981).

5 W.D.Watson, Ann.Rev.Astron.Astrophys., 16, 585 (1978).

6 D.Smith and N.G.Adams, Astrophys. J., 220, L87 (1978).

7 M.Meot-Ner, 'Gas Phase Ion Chem.', Vol 1, Academic Press, New York, 197 (1979).

8 A.J.Wickham, Chemistry in Britain, 15, 286 (1979).

9 J.V.Best, W.J.Stephen and A.J.Wickham, Pro.Nuc.Energy, 16 (2), 127 (1985).

10 A.B.Rakshit and P.Warneck, Int.J.Mass Spec.Ion Proc., 40, 135 (1981).

11 A.B.Rakshit and P.Warneck, Int.J.Mass Spec.Ion Proc., 35, 23 (1980).

12 P.Coxon and J.L.Moruzzi, J.Phys. (Appl.Phys.), 10, 969 (1977).

13 L.W.Sieck and R.Gorden, J.Res.Nat.Bur.Stand., 78A, 315 (1974).

14 L.W.Sieck, Int.J.Chem.Kinet., 10, 335 (1978).

15 J.V.Headley, Ph.D. Thesis, Chap.6, University of Warwick, Coventry, England.

16 A.J.Dempster, Phil.Mag., 31, 436 (1916).

17 H.D.Smith, Phys.Rev., 25, 452 (1925).

18 R.T.Hogness and E.G.Lunn, Phys.Rev., 26, 44 (1925).

19 G.G.Meisels, Radiat.Phys.Chem., 20.1, 1 (1982).

20 M.S.B.Munson and F.H.Field, J.Am.Chem.Soc., 88, 262 (1966).

21 P.Ausloos and S.G.Lias, 'Ion-Molecule Reactions - Their role in Radiation Chemistry', Am.Chem.Soc., Washington D.C., (1975).

22 E.G.Johnson and A.O.C.Nier, Phys.Rev., 91, 10 (1953).

23 W.Paul, H.P.Reinhard and U von Zahn, Z Physic., 143, 152 (1958).

24 P.Kebarle, Ann.Rev.Phys.Chem., 28, 445 (1977).

25 D.Smith and N.G.Adams, 'Gas Phase Ion Chemistry, Ed.M.T.Bowers, Vol.1, 2 (1979).

26 T.A.Lehman and M.M.Bursey, 'Ion Cyclotron Resonance Spectroscopy', New York, Wiley.

27 A.G.Marshall, Acc.Chem.Res., 18, 316 (1985).

28 A.J.Cunningham, J.Payzant and P.Kebarle, J.Am.Chem.Soc., 94, 7627 (1972).

29 K.R.Jennings, J.V.Headley and R.S.Mason, Int.J.Mass Spec.Ion Proc., 45, 315 (1982).

30 'Transient Species in the Gas Phase', Ed.Foutijna and Clyne.

31 K.R.Jennings, 'Advances in Mass Spectrometry'. Ed.Daly, 6A (1976), and references therein.

32 S.W.Rayment and J.L.Moruzzi, Int.J.Mass Spec.Ion Proc., 26, 321 (1978).

33 N.G.Adams and D.Smith, Chem.Phys.Lett., 79, 563 (1981).

34 R.T.McIver Jr., Rev.Sci.Instr., 49, 111 (1978).

35 H.R.Morris (Ed)., 'Soft Ionisation Biological Mass Spectrometry', Heyden, London, (1981).

36 F.W.McLafferty (Ed)., 'Tandem Mass Spectrometry', J.Wiley, New York.

37 R.G.Cooks (Ed)., 'Collision Spectroscopy', Plenum Press, New York, (1978).

38 K.Blemann, Anal.Chem., 58, 1289 (1986).

39 R.A.Yost and C.G.Enke, Anal.Chem., 51, 1251 (1979).

40 G.C.Didonato and K.L.Busch, Anal.Chem., 58, 231 (1986).

41 A.E.Scheon et al, Int.J.Mass Spec.Ion.Proc., 65, 125 (1985).

42 J.D.Ciupek, J.W.Amy, R.G.Cooks and A.E.Scheon, Int.J.Mass Spec.Ion.Proc., 65, 14 (1985).

43 P.K.Langevin, Ann.Chem.Phys., 5, 245 (1905).

44 E.W.McDaniel, 'Collision Phenomena in Ionised Gases', J.Wiley, New York, (1964), and references therein.

45 A.Henglein, 'Kinetics of Ion-Molecule Reactions in Molecular Beams', Academic Press, New York (1970).

46 T.Su and M.T.Bowers, 'Gas Phase Ion Chemistry', Chap.3, M.T.Bowers (Ed)., Academic Press, New York (1979).

47 J.Stevenson, J.Chem.Phys., 29 , 296 (1958).

48 F.T.Moran and W.H.Hamill, J.Chem.Phys., 39.

49 T.Su and M.T.Bowers, Int.J.Mass Spec.Ion Proc., 12, 347 (1973).

50 T.Su and M.T.Bowers, J.Chem.Phys., 58, 3027 (1973).

51 A.G.Harrison et al, Int.J.Mass Spec.Ion Proc., 19, 23 (1976).

52 T.Su, E.C.F.Su and M.T.Bowers, J.Chem.Phys., 69, 2243 (1978).

53 T.Su and M.T.Bowers, Int.J.Mass Spec.Ion Proc., 17, 309 (1975).

54 E.Rabinowitz, Trans.Far.Soc., 33, 283 (1937).

55 O.K.Rice and H.C.Ramsberger, J.Am.Chem.Soc., 49, 1616 (1927) and 50 617 (1928).

56 S.Glasstone et al, 'The Theory of Rate Processes', McGraw-Hill, (1941).

57 M.Meot-Ner and F.H.Field, J.Chem.Phys., 61, 3742 (1974).

58 L.M.Bass et al, J.Am.Chem.Soc. 103 5283 (1981).

59 E.Herbst, J.Chem.Phys, 75, 4413 (1981).

60 D.R.Bates, J.Chem.Phys., 73, 1000 (1980).

61 L.M.Bass and K.R.Jennings, Int.J.Mass Spec.Ion Proc.(1984),307,58.

62 D.K.Bohme et al, J.Chem.Phys., 52, 3133 (1970).

63 E.Herbst, Chem.Phys., 68, 323 (1982).

64 G.Porter, Disc.Faraday Soc., 33, 198 (1962).

65 V.L.Tal'roze and E.L.Frankevich, J.Phys.Chem., 34, 1275 (1960).

66 J.V.Headley, Ph.D.Thesis, Warwick University, Coventry, England, 1981.

67 J.V.Headley, R.S.Mason and K.R.Jennings, J.Chem.Soc.Faraday Trans. 1, 78, 933 (1982)

68 Gamma Ray Laboratory, CEGB, Berkeley Nuclear Laboratories, Berkeley, Glouchestershire.

69 W.Scottky, Phys.Z., 25, 635 (1924).

70 H.Bohringer and F.Arnold, Int.J.Mass Spec.Ion Proc., 49, 61 (1983).

71 Chanim and Biondi, Phys.Rev., 100, 423 (1957).

72 K.Hiraoka and K.Morise, Int.J.Mass Spec.Ion Proc., 68, 99 (1986).

73(a) P.van Koppen, P.R.Kemper, A.J.Illies and M.T.Bowers, Int.J.Mass Spec.Ion Proc., 54, 263 (1983).

(b) P.van Koppen et al, J.Chem.Phys., 81, 288 (1984).

74 A.J.Illies and G.G.Meisels, Annal.Chem., 52, 325 (1980).

75 SIMION is an electrostatic lens analysis and design program originally developed by D.C.McGilvery at Latrobe University, Department of Physics and Chemistry, Bundoora, Victoria, Australia (1977). The version of SIMION which was used had been extensively rewritten and expanded for highly interactive use on PC/AT class computers by D.A.Dahl and J.E.Delmore of Idaho National Engineering Laboratory, E.G. & G., Idaho Inc., Idaho Falls, ID.

76 E.W.McDaniel and E.A.Mason, 'The Mobility and Diffusion of Ions in Gases', J.Wiley, New York (1983).

77 G.Sroka, C.Chang and G.G.Meisels, J.Am.Chem.Soc., 94, 1052 (1972).

78 G.H.Wannier, Bell Syst.Tech.J., 32, 170 (1953).

79 E.W.McDaniel, J.Chem.Phys., 52, 3931 (1970).

80 J.T.Moseley et al, Phys.Rev., 178, 240 (1969).

81 H.Bohringer and F.Arnold, J.Chem.Phys., 77, 5534 (1982).

82 M.Meot-Ner and F.H.Field, J.Chem.Phys., 61, 3742 (1974).

83 B.R.Rowe et al, J.Chem.Phys., 80, 4915 (1984).

84 S.Dheandanoo et al, Proc. of 35th Gas Elec.Conf., Dallas, TX (1982).

85 J.D.Payzant and P.Kebarle, J.Chem.Phys., 53, 4723 (1970).

86 L.W.Sieck and R.Gordon Jr., Int.Mat.Res.Nat.Bureau Stad., Washington 784, 315 (1974).

87 P.van Koppen, R.Derai, P.Kemper, S.Liu and M.T.Bowers, Int.J.Mass Spec.Ion Phys., 73 (1986).

88 J.H.Schummer et al, Phys.Rev.A, 7, 683 (1973).
89 L.W.Sieck and R.Gordon, J.Res.Nat.Bur.Stand, Sec.A 73, 315 (1974).
90 A.B.Rakshit and P.Warneck, Int.J.Mass Spec.Ion Phys. 35, 23 (1980).
91 R.Patrick and D.M.Golden, J.Chem.Phys., 82, 75 (1984).
92 R.E.Mickens, J.Chem.Phys., 79, 1102 (1983).
93 D.R.Bates, J.Chem.Phys., 81 (1) 298 (1984).
94 E.F.Feguson, J.Phys.Chem., 90, 731 (1986).
95 A.Good, Chemical Reviews 75(5), 563 (1975).
96 P.Kebarle, Ann.Rev.Phys.Chem., 28, 445 (1977).
97 A.J.Stace and C.Moore, J.Am.Chem.Soc., 105, 1814 (1983).
98 A.J.Stace, J.Phys.Chem., 87, 2286 (1983), J.Am.Chem.Soc., 107, 755 (1985).
99 M.F.Jarrold et al, J.Phys.Chem., 89, 3269 (1979).
100 N.G.Adams et al, Chem.Phys.Lett., 61, 608 (1979).
101 Michael T.Bowers, Dept. of Chemistry, University of California, Santa Barbara, California 93106, U.S.A.
102 O.Oldenberg, Phys.Rev. 37, 556 (1931).
103 W.Federer et al, J.Phys.Chem., 83, 1032 (1985).
104 V.G.Anicich and M.T.Bowers, ibid, 102, 3994 (1980).
105 R.D.Cates and M.T.Bowers, J.Am.Chem.Soc., 96, 1279 (1974).
106 C.E.Hamilton, V.M.Bierbaum and S.R.Lowe, J.Chem.Phys., 83, 2284 (1985).
107 W.Lindinger, Communication to previous reference.
108 Y.N.Lin and B.S.Rabinovitch, J.Phys.Chem., 74, 3151 (1970).
109 P.R.Kemper and M.T.Bowers, J.Chem.Phys., 81, 2634 (1984).
110 H.Bohringer, F.Arnold, D.Smith and N.G.Adams, Int.J.Mass Spec.Ion Proc., 52, 25 (1983).
111 D.Smith, N.G.Adams and E.Alge, Chem.Phys.Lett., 105, 317 (1984).
112 W.Lindinger et al, J.Chem.Phys., 63, 5 (1975).
113 N.G.Adams and D.Smith, Astrophys.J.Lett., 247, L123 (1981).
114 I.Dotan, Chem.Phys.Lett., 75, 509 (1980).
115 C.Chang and G.G.Meisels, Int.J.Mass Spec.Ion Phys., 11, 367 (1973).
116 H.Helm, J.Phys.B.Atom.Molec.Phys., 9, 2931 (1976).
117 H.Helm and M.T.Elford, J.Phys.B., 10, 983 (1977).
118 H.W.Ellis, R.Y.Pai, E.A.Mason and L.A.Viehland, At.Nucl.Data Tables, 17, 177 (1976).
119 H.W.Ellis et al, At.Nucl.Data Tables, 22, 179 (1978).
120 C.W.Polley, A.J.Illies and G.G.Meisels, Anal.Chem., 52, 1803 (1980).
121 H.Helm and M.T.Elford, J.Phys.B.Atom.Molec.Phys., 10(18), 3849 (1977).
122 W.T.Huntress, J.Chem.Phys., 55, 2146 (1971).

123 R.N.Varney, Phys.Rev., 89, 708 (1953).

124 J.H.Schummers et al, Phys.Rev., A7, 683 (1973a).

125 J.H.Schummers et al, Phys.Rev., A7, 689, (1973b).

126 M.McFarland et al, J.Chem.Phys., 59, 6610 (1973).

127 H.E.Revercomb and E.A.Mason, Anal.Chem., 47, 970 (1975).

128 S.Kim, K.R.Betty and F.W.Karasek, Anal.Chem., 50, 2006 (1978).

129 S.E.Buttrill, J.Chem.Phys., 58, 656 (1973).

130 M.T.Bowers, P.V.Nielson, P.R.Kemper and A.G.Wren, Int.J.Mass Spec.Ion Phys., 25, 103 (1977).

131 A.Fick, Ann.Phys.Lpz., 170, 59 (1855).